ANALYSIS, DESIGN AND IMPLEMENTATION OF HIGH PERFORMANCE CONTROL SCHEMES IN RENEWABLE ENERGY SOURCE BASED DC/AC INVERTER FOR MICRO-GRID APPLICATION

SOUVIK DASGUPTA

NATIONAL UNIVERSITY OF SINGAPORE

2011

ANALYSIS, DESIGN AND IMPLEMENTATION OF HIGH PERFORMANCE CONTROL SCHEMES IN RENEWABLE ENERGY SOURCE BASED DC/AC INVERTER FOR MICRO-GRID APPLICATION

SOUVIK DASGUPTA
(M.Engg., Bengal Engineering and Science University, India)
(B.Engg.(Hons.), Jadavpur University, India)

A THESIS SUBMITTED

FOR THE DEGREE OF DOCTOR OF PHILOSOPHY

DEPARTMENT OF ELECTRICAL AND COMPUTER ENGINEERING
NATIONAL UNIVERSITY OF SINGAPORE
2011

Acknowledgments

The author wishes to record his deep sense of gratitude to his supervisor, Assoc. Prof. Sanjib Kumar Panda, who has introduced the present area of work and guided in this work. The author's thesis supervisor, Assoc. Prof. Sanjib Kumar Panda has been a source of incessant encouragement and patient guidance throughout the thesis work. The author is extremely grateful and obliged to Dr. Sanjib Kumar Sahoo for his intellectual innovative and highly investigative guidance in the thesis work. The author likes to express special thanks to Prof. Jian-Xin Xu for his valuable help in control theory and application. The author is also indebted to Assoc. Prof. Ramesh Oruganti and Assoc. Prof. Ashwin M Khambadkone for their incredible teachings in the design aspects of power electronics and drive systems. The author would also like to thank Assoc. Prof. Thong T. L. John, Assoc. Prof. Y. C. Liang and Assist. Prof. Akshay K. Rathore for their guidance as PhD Thesis Committee Members. The author wishes to express his thanks to Mr. Y. C. Woo, and Mr. M. Chandra of Electrical machines and Drives lab, NUS, for their readiness to help on any matter. The author is also grateful to his fellow research scholars, specially Mr. Parikshit Yadav, Mr. Sangit Sasidhar and Mr. Hoang Duc Chinh, for their constructive criticism in different aspects of this thesis. The author wishes to convey special thanks to Dr. Xinhui Wu, Dr. Haihua Zhou, Dr. Yenkheng Tan and Dr. Prasanna U. R. for their inspiring comments whenever the

author approached to them.

Last but not the least, the author is strongly indebted to the Almighty for presenting him the best parents of the whole of Universe. The author's father Mr. Sankar Dasgupta and the author's mother Mrs. Mamata Dasgupta have been bearing with him in different aspects of life for long time. The author wishes to dedicate this thesis to their love and support.

Contents

Summary

In traditional micro-grid application, harvested renewable energy is interfaced with the single/three-phase micro-grid using single(typical residential application)/three(typical industrial application)-phase power electronic converters/inverters (Distributed generators or DGs). Power flow control as well as shaping of the current drawn from the common AC bus (grid) of the micro-grid is primarily done by controlling the inverter currents using suitable current references, which in turn necessitates digitally implemented high-performance controllers for these applications. This thesis investigates different high-performance control schemes to control power flow as well as shaping voltages/currents under different adverse operating conditions in the micro-grid.

In the first part of the thesis, a *Lyapunov function* based current controller is proposed for a single-phase parallel connected inverter along with a local load connection. The proposed control system ensures high-performance tracking of the inverter current derived by single phase p-q theory to ensure a specific amount of active and reactive grid power consumption by the load along with maintaining grid current to be sinusoid. The proposed controller gives superior performance over conventional PI + resonant controller. In the second part of the thesis, a single-phase series connection of the DG inverter along with micro-grid and load

is proposed. The proposed method ensures rated high quality of the load voltage even in the presence of sag, swell or harmonic distortions in the micro-grid voltage, using a *Spatial Repetitive Controller*(SRC), facilitating micro-grid fundamental frequency independent performance. The total load active power is controllably shared between inverter and micro-grid with the assurance of leading micro-grid power-factor even if the load power-factor is lagging. In the last part of the thesis, DG inverter connection is considered in parallel to a generalized three-phase micro-grid along with local load. Controllable load power sharing with the control on the grid current THD is also ensured with a proposed *Lyapunov function* based current controller. The proposed method considers unbalance not only in the grid voltages but also in the line side inductances while the controller is implemented in *a-b-c* frame. The three-phase *p-q* theory and *FBD* theory based approaches are used to calculate the inverter current reference and the corresponding effects on DC link side ripples are also investigated. A *Complex Notch Filter* (CNF) based approach is proposed to extract fundamental positive as well as negative sequence components from the generalized grid voltages for the *a-b-c* frame implementation of the *p-q* theory based approach. The proposed *FBD* based approach is implemented on the grid fundamental phase domain ensuing high-performance operation even under fractional change in grid frequency. Both *b-6* (six-switch) and *b-4* (four-switch) three-phase inverter topologies are tested for such DG interconnection. The proposed control technique ensures simple Sine PWM based control of *b-4* inverter unlike the conventional adaptive SVPWM method. Detailed experimental results are provided to show the efficacy of each of the methodologies.

List of Tables

List of Figures

Acronyms

PCC	Point of Common Coupling
PFC	Power Factor Correction
THD	Total Harmonic Distortion
DG	Distribute Genartor
STS	Static Transfer Switch
DC	Direct Current
AC	Alternating Current
CCVSI	Current Controlled Voltage Source Inverter
PI	Proportional-Integral
VCVSI	Voltage Controlled Voltage Source Inverter
MPPT	Maximum Power Point Tracking
PWM	Pulse-Width-Modulation
PC	Personal Computer

PR	Proportional Resonant
DPC	Direct Power Control
MB	Mega Byte
ADC	Analog to Digital Conversion
DAC	Digital to Analog Conversion
IO	Input Output
TTL	Transistor Transistor Logic
SRC	Special Repetitive Controller
LF	Lyapunov Function
PLL	Phase Lock Loop
CNF	Complex Notch Filter
RRSC	Rotating Reference Signal Characterizer
SPWM	Sine PWM
SVM	Space Vector Modulation
FM	Fostescue's Method

Symbols

C_{DC}, C_{PV}	Different stage DC link capacitors of PV inverter
$C_{src}(z_\theta)$	SRC transfer function
C_{dc1}, C_{dc2}	DC link split capacitors
d, $\widehat{d}$	Actual and estimated disturbance terms
e	Current error
e_{1b}	Final value of converged current error
f_s, f_{sample}	Switching frequency and sampling frequency of inverter (Hz)
$G(z_\theta)$	Plant transfer function
i_c, i_c^*	Single-phase CCVSI actual and reference current
i_g, i_g^*	Actual and reference single-phase grid current
i_L	Single-phase load current
i_{Cx}	Phase-x current of three-phase CCVSI
I_p	Positive sequence fundamental grid current peak (A)
I_n	negative sequence fundamental grid current peak (A)
K_{src}	Gain of SRC
L_x, R_x	Line side inductance of phase-x of three-phase CCVSI

L	Single-phase CCVSI grid interfacing inductance
L_f, C_f	Single-phase inverter $L-C$ filter, inductor and capacitor
N	Number of position samples for SRC
N_1	Sample advancement of SRC
p_{grid}	Instantaneous power injected into the grid
P_{grid}	Average power injected into the grid
P_L, Q_L	Active and reactive power consumption of load
P_{inv}, Q_{inv}	Active and reactive power flow of inverter
P_g, Q_g	Active and reactive power consumption of grid
P_{mpp}	Power extracted at MPPT
p_{dc}	DC side instantaneous power
p_h	Harmonic power
R	Single-phase CCVSI grid interfacing resistance
$S_1 ... S_6$	Three-phase inverter switching signals
T	Inverse of fundamental grid frequency (rad/sec), $\frac{1}{\omega}$
T_s	Sampling time of the controller
U_C	Mean capacitor voltage
u_{lf}	Output of Lypunov function based controller
u_{src}	Output of spatial repetitive controller
V_{dc}	DC link voltage
v_g	Grid voltage
v_c	Single-phase inverter SPWM control signal
v_{gr}, i_{gr}	Real voltage and current of complex grid

v_{ix}	Inverter voltage of phase-x for three-phase inverter wrt N
V_L	Single-phase load voltage phasor
v_{iac}, v_{ibc}	Three-phase inverter line voltages
v_{gx}	Phase-x voltage of three-phase grid
v_{gi}, i_{gi}	Imaginary voltage and current of complex grid
$v_{cona}...v_{conb}$	Three-phase inverter SPWM control signals
v_{ixO}	Phase-x voltage wrt DC link mod-point, O of three-phase inverter
V_L	Single-phase load voltage phasor
$v_{OO'}$	DC link actual mid-point voltage wrt ideal mid-point
V_p	Positive sequence fundamental grid voltage peak (V)
V_n	Negative sequence fundamental grid voltage peak (V)
v_{dcp}, v_{dcn}	DC link split voltages
ω_{grid}	Angular frequency of grid (rad/sec)
x	Phase-x for three-phase inverter with $x \in\ a\, b\, c$
Z	Single-phase load impedance
z_θ	Digital dynamic complex frequency in position sample domain
λ	Lyapunov gain for single-phase inverter
θ	Single-phase load power factor angle
γ	Grid power angle for single-phase inverter
θ_1	Positive sequence fundamental grid voltage phase
θ_2	Negative sequence fundamental grid voltage phase

Chapter 1

Introduction

1.1 General Discussion

Electrical energy is the most important form of energy to meet the daily requirements of the human being. This is used to run all the possible appliances of residential as well as commercial application. It can be easily felt that the rate of per capita energy consumption is increasing due to the introduction of more and more electrical based systems. Normal practice is to generate electric energy through synchronous generators (mainly thermal energy by burning the natural coal), placed at different locations of a country and feeding all the power to a common grid. This facilitates the development of infinite power grid, which is used by consumers distributed all over the country. The introduction of sophisticated electronic loads also pollutes grid with harmonic distortions which also affects the other loads connected in the same grid. It can also be seen that in developing countries, due to increase of load demands, the grid voltage undergoes sag, swell etc and other types of intermittent problems. Moreover, to take care of these problems some substations of huge power capacity (of the order of 100 kVA) are

installed at different power distribution networks. These substations contain large transformers, capacitor banks etc. This calls for investment of huge capital cost.

Renewable energy research is becoming more and more popular during these days due to the fast depletion of fossil fuels. The distributed renewable energy generations are bringing in micro-grid research intensely. Micro-grid can be viewed as an integration of different types of distributed renewable energy sources. These alternative energy sources are connected to the main power grid in addition to supplying the local load demand. Conventional electric power systems are getting stressed by the exponential growth of the power demand, limit of power delivery capability, complications in building new transmission and distribution lines and blackouts [1]. Micro-grid is being applied and focused due to these reasons. Developments of power electronic converters and high performance digital controllers are enabling integration of all types of renewable energy sources to a self supported micro-grid which can operate independent of the main power grid in islanded mode. Control issues of the distributed generation unit in the micro-grid have been addressed by a number of researchers [1]-[21]. Since the micro-grid is a power grid having extensive properties of a typical weak utility system [2], different types of control methods have been reported [3]-[16] to mitigate different power quality problems associated with the micro-grid power systems. In a typical micro-grid structure, the energy sources and the load terminals are connected at the point of common coupling (PCC)[17]-[18]. Because of the nature of the weak grid, the voltage can have disturbances such as sag, swell and contamination with voltage harmonics [17], [19]-[20]. Some of the solutions to mitigate these problems (in case of three phase micro-grid) are discussed in [21]. These grid voltage disturbances as well as grid voltage harmonic contamination problems are addressed and discussed

in [21]-[22] by employing either shunt or series active filters so that these problems in grid voltage cannot affect the load. If a typical single-phase micro-grid (medium power level micro-grid) is considered, the methods applied in [21] and [22] cannot be applied because of the unavailability of the traditional "$d-q$" [21]-[67] theory in case of single phase application. It can also be noted from [21] and [22] that, the systems can only improve the disturbances in the micro-grid voltages but it is unable to control the active power flow through the power electronic converters (active power filters). So, ultimately, the active power drawn by the load from the micro-grid as well as renewable energy sources cannot be controlled. The existing literature also show that on one hand, the single phase inverter is directly connected (through an interfacing choke coil) to the point of common coupling (PCC) [3] to facilitate power flow to the PCC. On the other hand, the grid (micro-grid) and the loads are also connected to the PCC. Three phase unbalance grid interface of the micro-grid systems are well documented in [26]-[29]. In [26]-[27], hybrid series-parallel compensators are proposed to minimize the current harmonics generation effect in a typical unbalanced three phase micro-grid system. Even in the case of the unbalanced generalized grid connected renewable energy inverters, there is a problem of DC link side even harmonic ripples because of the unbalance nature of the grid [30]-[31]. These problems either can be solved using huge passive filter component or taking the help of high performance control methodology in controlling the inverter. For grid connected topology of renewable energy source based inverters, both for three-phase as well as single-phase case, the inverter is only used to pump in sinusoidal current to the grid and another inverter is connected in parallel with the load to reduce the grid current distortions due to the non-linear load current. The second inverter system is referred as *power factor correction* (PFC) circuit [32].

Therefore, the motivation behind this thesis is to develop high performance controllers for single-phase renewable energy fed voltage source inverters (VSI) so that even if the grid voltage undergoes intermittent disturbances, the single-phase residential loads can enjoy disturbance-free voltage as well as energy savings in the electricity bill. For direct grid connected conditions, in the case of single-phase residential loads, a controller for the inverter is developed that controls the power flow from the grid as well as the total harmonic distortion (THD) of the grid current. For the three-phase unbalanced and distorted grid connected inverter, a high performance control strategy is proposed to control the power flow from the grid, control the THD of the grid current as well as reducing the DC link side ripples. The thesis also investigates the possibility of reducing the three phase inverter hardware cost reduction by optimizing the power circuit with advanced non-linear controller application.

1.2 Configuration of a typical multi-bus micro-grid system

Micro-grid is generally classified as a cluster of micro-generators connected to the mains utility grid, usually through some voltage-source-inverter(VSI) based interfaces. The trend of fast depletion of fossil fuels is accelerating the advancements of micro-grid technology to manage the available electrical power efficiently. Renewable energy sources, such as PV or solar are also considered in a large way to interconnect with the micro-grid to reduce the carbon footprint to a large extent. Based on the nature of the existing loads, broadly two types of micro-grids are possible, i.e. AC and DC types. The most popular way of electrical engineering

practise leads to the formation of AC micro-grid in the present time. Different technologies of micro-grid control systems interconnecting different renewable energy sources are well discussed in [10]-[16]. Different structures of micro-grids are available. In this thesis a typical structure of multi-bus AC micro-grid is considered.

Figure 1.1 shows a typical structure of multi-bus micro-grid configuration considered in this report as also discussed in [8]-[9], [24]-[25]. The micro-grid comprises of three paralleled Distributed Generation (DG) systems, viz. DG1, DG2 and DG3. DG1 comprises of renewable energy sources along with associated power

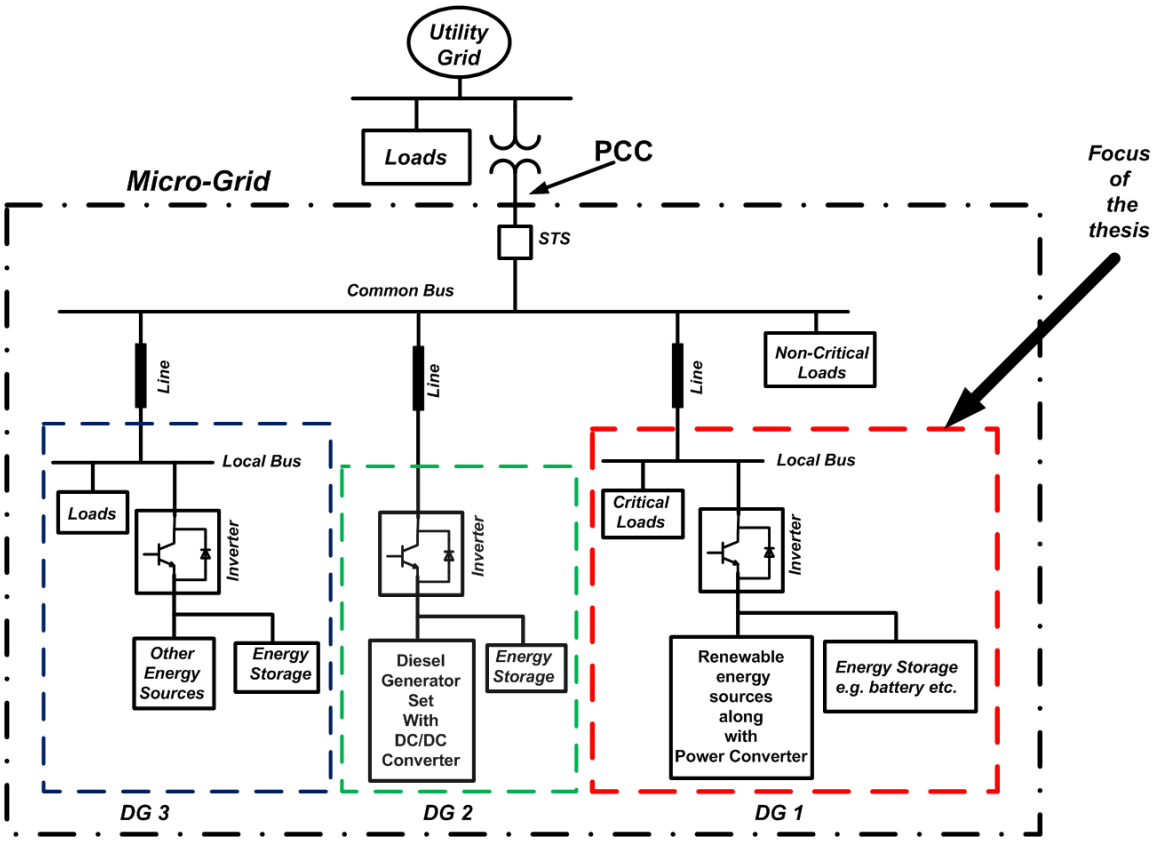

Figure 1.1: Typical configuration of inverter-based micro-grid.

electronic energy extractor and interfaced to the *Local Bus* using a parallel connected inverter topology. At the DC link of the inverter energy storage element (such as battery etc.) is also connected. In the *Local Bus*, some critical loads are

connected. The *Local Bus* is interfaced to the *Common Bus* of the micro-grid. DG2 supplies power extracted from fossil fuel based diesel generator directly to the *Common Bus*. Inside DG3, some other type of energy sources along with loads are connected to another *Local Bus* and then connected to the *Common Bus* of the micro-grid system. Some non-critical loads are also connected directly to the *Common Bus* of the micro-grid. The focus of this thesis lies in discussing the control of the parallel connected inverter inside the DG1 as indicated in Figure 1.1. Under normal mode of operation, the micro-grid is connected to the utility grid at the point of common coupling (PCC) through a static transfer switch (STS). Under this condition, the voltage of the *Common Bus* as well as *Local Bus* are mostly well regulated by the infinite source nature of the main utility grid. In this mode, inside DG1, most of the extracted renewable energy is stored in battery and the critical loads draw active power from the *Common Bus* via *Local Bus*. But if needed, certain amount of extracted or stored energy can be fed to the *Common Bus* via *Local Bus* to reduce the active power consumption from the *Local Bus*.

In the case of islanded condition, when the micro-grid is isolated from the main utility grid by means of STS switch, the power demand of all the DG systems are changed and each of the DG systems should immediately follow the changed power demand to stabilize the voltage in the *Common Bus* in the micro-grid. In this thesis, control techniques are proposed and validated by experimental studies for the inverter inside DG1. The inverter inside DG1 is operated in current controlled voltage source inverter (CCVSI) mode.

The work of the thesis is directed towards the operation of the DG1 as a part of the whole micro-grid. The desired grid current reference is calculated from

the required active and reactive power flow from the grid. The current reference for the inverter is obtained by subtracting the desired grid current from measured load current. Accurate current control of the inverter results in both desired power flow control as well as a purely sinusoidal grid current. In case there is a voltage change in the *Local Bus*, the proposed control method is capable of maintaining the required power demand by adjusting the current of the CCVSI automatically. This ensures high band-width active, reactive and harmonic power control to ensure high quality energy exchange within the micro-grid.

All the characteristics of the DG1 can also be achieved in case of utility grid connected mode. In this mode the proposed control technique also eliminates the need of external *Power Factor Correction* (PFC) circuit as the proposed current control method makes the single inverter to do both power control and local grid current THD control.

1.3 Different topologies of DC/AC inverters and controls to interface renewable energy sources to the micro-grid

Different renewable energy sources are interfaced to the micro-grid to make the micro-grid operation energy efficient and reduce the carbon footprint. Two popular renewable energy sources that have left the appreciable impact on the micro-grid application are *Solar energy* and *Wind energy* sources. Depending on the availability of the sunny or windy environment at a specific location, such renewable energy sources are known to be popular in different countries. Different energy extraction systems including the power electronic converters are available for residential as

well as commercial application. In this Section first of all a brief description of *Solar source* and *Wind energy source* are discussed and then the application of those sources in *micro-grid* formation are focused.

Solar PV source based inverters are becoming very popular for recent decades. Extensive researches are going on to develop different types of solar PV converter/inverter systems to extract the solar PV energy efficiently. Different topologies have been proposed. Significant contributions can be seen in the case of both single phase as well as three phase solar PV systems. It can be understood that the PV panel output is a DC output. The common form of power used for consumer application is AC power. This leads to the modern trend of PV converter/inverter topologies. The PV panel is normally connected to single or multiple stages of DC to DC converter. Then the output of the DC/DC converter is connected to the DC link of inverter to interface with either grid or load. The popular PV inverter topologies can be classified into two groups: ***grid connected PV inverters*** and ***stand alone PV inverters***.

The grid connected PV inverters [33]-[34] are the popular type of PV inverters used for the distributed power generation as well as micro grid application. Multiple PV panels are connected in series or parallel to form the PV string and then the PV string power is extracted by DC/DC converter distributed over three-phase or single-phase grid by three phase [34] or single phase [35] inverter respectively. The structure of the grid connected PV system is shown in Figure 1.2 as mentioned in [34]. It can be noticed from Figure 1.2, the PV module is directly connected to a DC/DC converter to operate the module in Maximum Power Point Tracking (MPPT)[36] mode. Then the output of MPP tracking DC/DC converter is

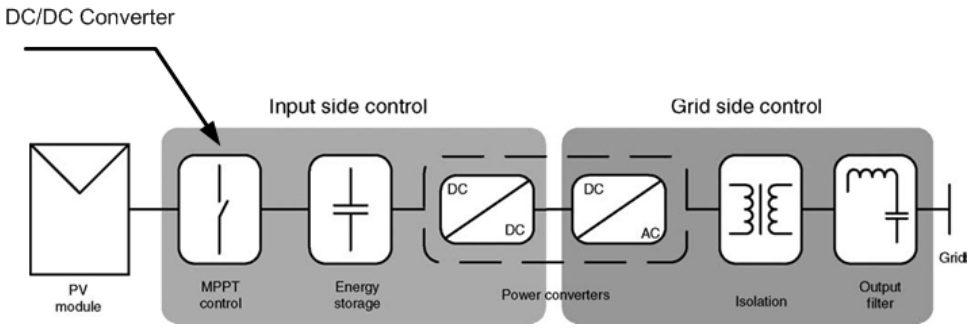

Figure 1.2: Hardware structure of three phase grid connected PV system [34].

connected to a energy storage element (say battery) and to the input of another DC/DC converter. The output of this second DC/DC converter is connected to the DC link of the PWM voltage source inverter. The inverter is connected to the grid with transformer isolation. In some topologies the isolation is also provided in the DC/DC converter just preceding the VSI. In that case the low frequency transformer on the line side is not used any more. The DC/DC converter connected to the input of the inverter is used to regulate DC link voltage of the inverter to facilitate the power flow through the inverter to the grid. The control strategy applied to the grid-side converter consists mainly of two cascaded loops. The fast internal current loop, which regulates the grid current, and an external voltage loop, which controls the DC link voltage[34, 72, 38]. The control structure is shown in Figure 1.3. The control structure is implemented in synchronously rotating reference frame (d-q frame). This requires a transformation module, e.g., $a-b-c \rightarrow d-q$, to transform the grid currents and voltages into a reference frame that rotates synchronously with the grid voltage. By means of this, the control variables become dc quantities, thus filtering becomes easier and control can be carried out using simple PI controllers. It can be seen from Figure 1.3 that the output of the DC link (of the PWM inverter) voltage controller is used as the reference of the 'd' axis current to control the active power flow through the VSI and the output

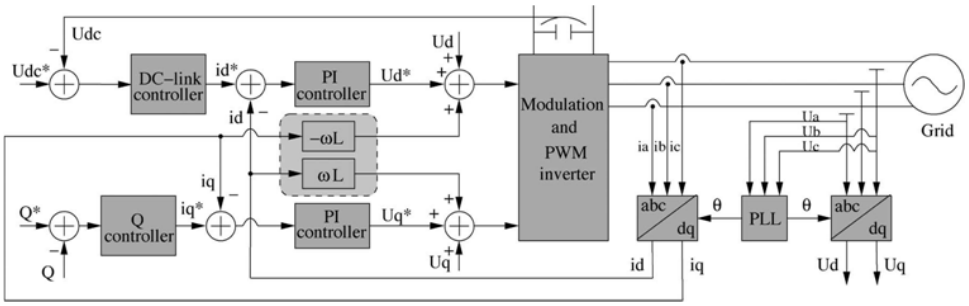

Figure 1.3: General structure for synchronous rotating frame control structure [34].

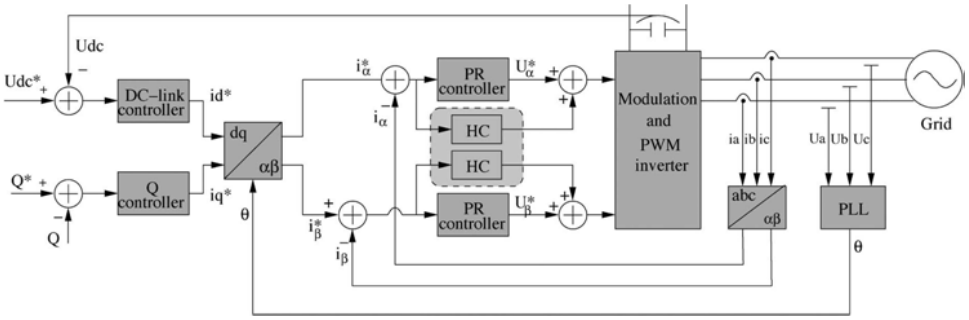

Figure 1.4: General structure for stationary frame control structure [34].

of the reactive power controller is used as the reference of the 'q' axis current to enable proper control of the reactive power flow as well. Another possible way to implement the control loops in stationary reference frame is shown in Figure 1.4. In this case, the grid currents are transformed into stationary reference frame using $a-b-c \rightarrow \alpha-\beta$ module. Since the control variables are sinusoidal in this situation, so *Proportional Resonant*[34, 39](**PR**) controller gained a large popularity in the last decade in the current regulation of the grid-tied systems. In very high power three-phase systems, multiple number of PV panels are connected to form a PV string and then power processing is carried out to distribute the PV power into three phases as discussed in [33] and shown in Figure 1.5. It can be seen from Figure 1.5(a), that each of the PV panel is connected to separate DC/DC MPPT tracker and three such outputs of the DC/DC converter are connected in parallel to form the DC link of the single phase PWM VSI for one phase. The same type of arrangement is carried out for each of the three phases. It can be seen from

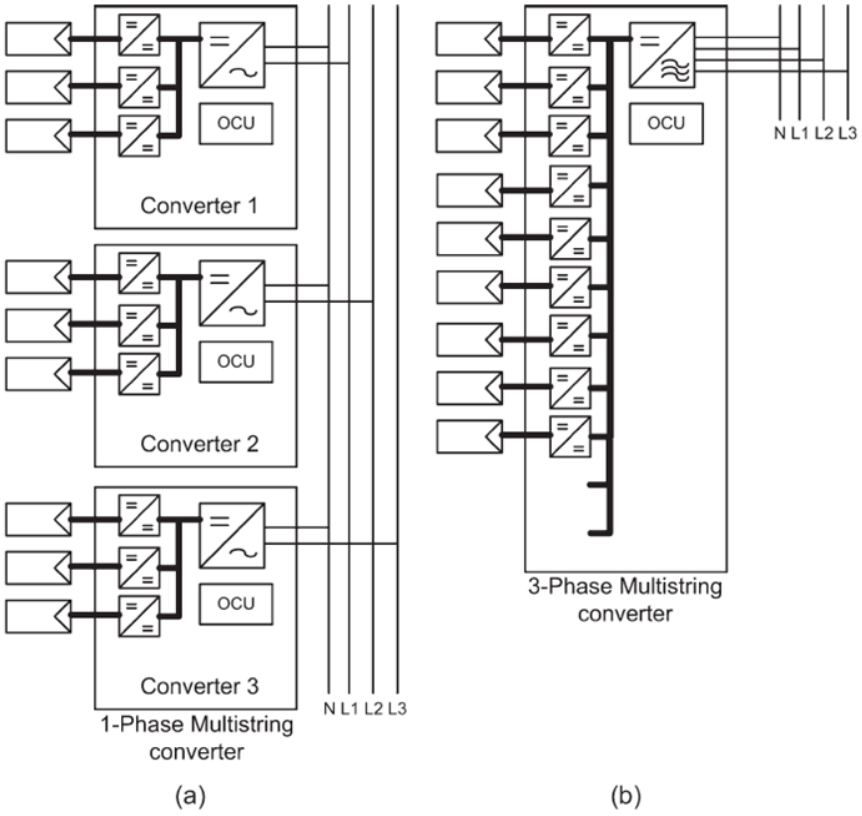

Figure 1.5: (a) One-phase each multi-string converter. (b) Three-phase combined multi-string converter [33].

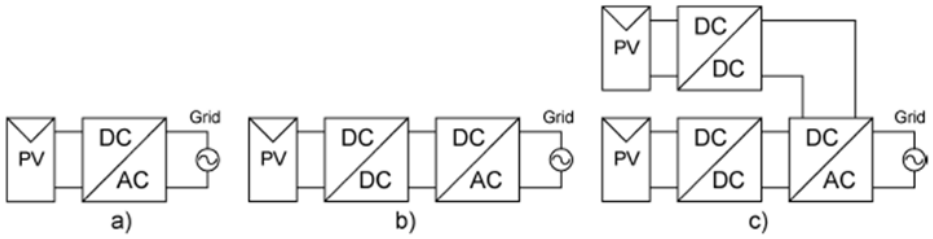

Figure 1.6: (a) Single-stage inverter (b) Dual power processing inverter, dual-stage inverter (c) Multi-string inverter [35].

Figure 1.5(b), that each of the PV panel is connected to separate DC/DC MPPT tracker and all DC/DC MPPT trackers are connected in parallel. The combined DC bus serves as the DC link of the three phase PWM VSI, which is connected to the three phase grid.

Grid connected system is well accepted in single phase PV application [35]. The broad classification of the single phase grid connected system can be seen in Figure 1.6 as classified in [35]depending on the power processing stages. The inverter in Figure 1.6(a) is a single-stage inverter. This inverter handles all the responsibilities like MPPT, voltage amplification as well as PWM inversion. Figure 1.6(b) depicts a dual-stage inverter. The DC/DC converter performs the MPPT and the DC/AC VSI performs the inversion to dump the power to the grid. Figure 1.6(c) is the solution for the multi-string inverter. Each DC/DC converter performs the MPPT and voltage boosting for each PV module/string. The DC/DC converters are connected to the dc link of a common DC/AC voltage source inverter, which takes care of the grid current control. It can be seen from Figure 1.6 that, the DC/AC VSI is interfaced with the grid. Now, considering a case that the VSI is controlled in such a way that both the grid voltage and grid current only contain the fundamental component and also they are in phase, then the instantaneous

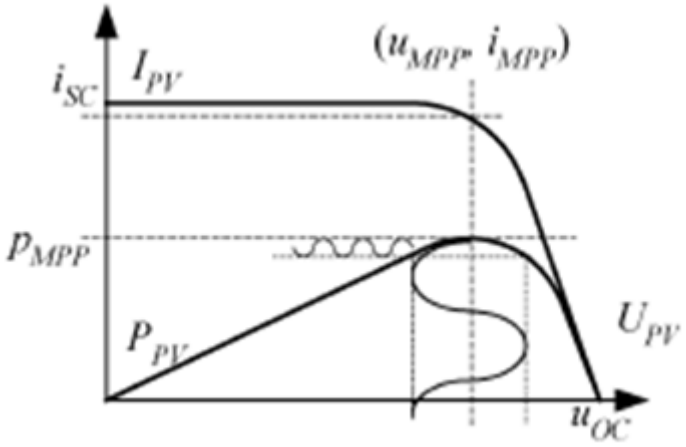

Figure 1.7: Electrical characteristics of the PV panel and the double harmonic power oscillation at the panel terminal [35].

power injected into the grid can be expressed as:

$$\begin{aligned} p_{grid} &= 2\,P_{grid}\,cos^2(\omega_{grid}\,t) \\ &= P_{grid}\,[1 + cos(2\,\omega_{grid}\,t)] \end{aligned} \tag{1.1}$$

where P_{grid} is the average injected power, ω_{grid} is the angular frequency and t is the real time. Now, it can be understood that from Figure 1.6(a) that, the PV panel needs to supply not only the average DC power, P_{grid}, but also the double harmonic oscillating power also as predicted from (1.1). The scenario can be well understood from Figure 1.7. It can be clarified from Figure 1.7 that, the operating point is oscillating around the maximum power point (P_{MPP} point as shown in Figure 1.7) and this leads to imperfect MPPT tracking. This actually makes the PV panel terminal voltage contaminated with double of grid frequency harmonic ripple. The normal solution to this problem is connecting a "decoupling capacitor, C_{PV}" at the terminal of the PV panel as shown in Figure 1.8(a). This enables the average power, P_{grid} to be supplied from the PV panel and the double harmonic power, $P_{grid}\ cos(2\,\omega_{grid}\,t)$ to be supplied by the capacitor, C_{PV}. In this case the

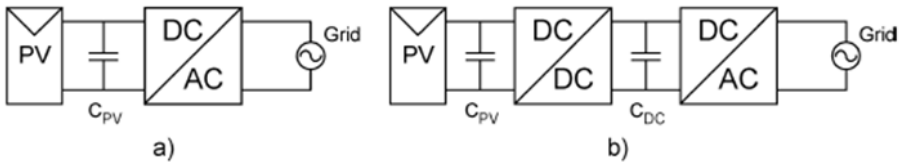

Figure 1.8: Different location of decoupling capacitor; (a) Single-stage inverter: capacitor only placed in parallel with the PV panel . (b) Multi-stage inverter: Capacitor placed in parallel to the PV panel as well as in the dc -link [35].

capacitance of the decoupling capacitor can be calculated as:

$$C_{PV} = \frac{P_{PV}}{2\,\omega_{grid}\,U_C\,\widehat{u}_C} \tag{1.2}$$

where P_{PV} is the nominal power supplied by the PV module, U_C is the mean voltage across the capacitor and $\widehat{u}_C$ is the amplitude of the voltage ripple across the PV terminals. It can be understood from (1.2) that, as ω_{grid} is of the order of 50 to 60 Hz, so for appreciably small voltage ripple, the value of the capacitor becomes very big (of the order of few hundreds of mili-farads). On the other hand in the topology shown in Figure 1.8(b), C_{DC} is placed of the order of 1000 $\mu\,F$ and the DC/DC converter is controlled in such a way that, PV terminal output voltage does not flicker with small value of C_{PV}. It can also be noted that, the DC/DC converter operates in the switching frequency range of 10's of kHz, so the size of the C_{PV} also comes out to be quite small value according to (1.2). These large capacitors placed in the DC link are the aluminium electrolytic capacitors. These capacitors are the weakest link of the inverter. It can be understood that all the inverters so far discussed are current controlled voltage source inverters. This needs a capacitor presence at the dc-link of the inverter. Recently another type of PV inverter is proposed in [40]. The power circuit of the total PV inverter is shown in Figure 1.9. It can be understood from [40] that, the inverter operates in "current source inverter" mode. It is explained in [40] that, the DC link current of the inverter is maintained to be a "rectified sinusoidal" shape by controlling the

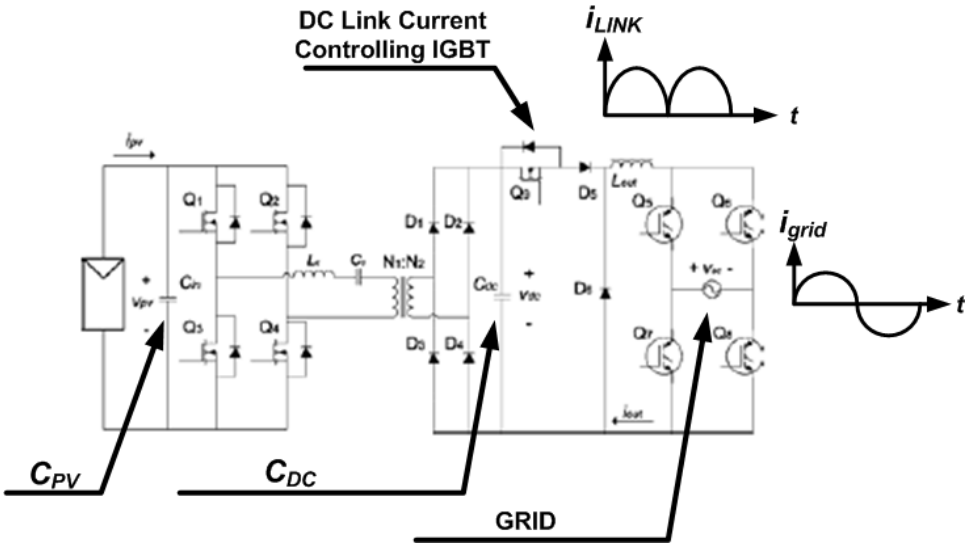

Figure 1.9: Unfolding inverter based single phase PV module inverter system [40].

dutycycle of the switch. Then the inverter switches are controlled in synchronism with the grid voltage such that, the grid current becomes sinusoidal and always in phase with the grid voltage. This topology of PV inverter is called "Unfolding Inverter" [41]. It can be seen from Figure 1.9 that, the DC link current is rectified sinusoidal shape. The shape can be approximated as:

$$i_{LINK} \simeq I_{DC} \, [1 + cos(2\,\omega_{grid}\,t)] \tag{1.3}$$

Now, using 1.1 and 1.3, it can be written that, the voltage across the capacitor C_{DC} as shown in Figure 1.9 can be written as:

$$v_{DC} = v_{LINK} = \frac{p_{grid}}{i_{LINK}} \simeq \frac{P_{grid}}{I_{DC}} \tag{1.4}$$

So, it can be seen from (1.4) that V_{DC} already has almost no ripples. This causes almost zero voltage ripple across the PV panel terminals , i.e. across the capacitor C_{PV} as shown in Figure 1.9. This results in significant low values of coupling capacitors C_{PV} as well as C_{DC}. C_{PV} is only provided to reduce the small switching frequency ripple in voltage by the DC/DC converter used for MPPT as mentioned in [40]. This method significantly increases the life span of the PV inverter systems.

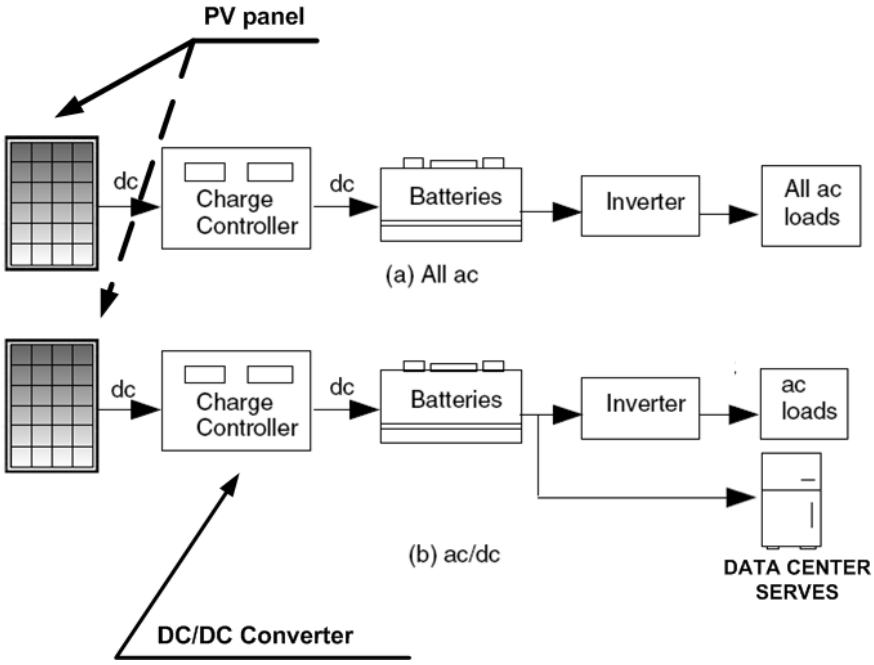

Figure 1.10: Stand alone PV inverter systems. (a) all the loads are AC loads. (b) there are both AC as well as DC loads [41].

Stand-alone PV installations are typically very common in remote applications. In most of the cases stand-alone systems are used in single phase applications. Three phase stand-alone systems are normally not used. These type of PV installations very often use batteries to provide back-up during nights as well as cloudy days [41]. Some stand-alone systems are very simple with the solar array being directly connected to the load. These are called as "Direct-coupled PV systems" [41]. A typical circuit configuration for stand-alone system for both AC as well as DC application is shown in Figure 1.10. It can be noticed from Figure 1.10(a) that, the PV energy is stored in battery using a DC/DC converter based battery charger. The battery output is then connected to the the inverter and the inverter supplies the AC loads. The capacity of the battery is designed in such a way that, it can store enough energy so that the energy demand in the night as well as during some cloudy days can be easily met. Another version of the stand-alone system is depicted in Figure 1.10(b). It can be seen that in the second case, the battery

directly feeds the DC loads (i.e. DC data center servers etc.).

Harvesting electrical energy from wind system has matured to a level of development where it is ready to become a generally accepted utility generation technology. Wind-turbine technology has undergone a dramatic change with the development of power electronic converters as well as mechanical systems in last 15 years [42]-[43]. With the introduction of power electronic converters, the wind turbines are made with different types of electrical power generators and power electronic converters, viz. Partial Power Electronic Converter and Wound Rotor Induction Generator (WRIG) with gear train, Full power Electronic converter and Slip Ring Induction Generator (SRIG) or Synchronous Generator (SG) with gear train and Full power electronic converter and Permanent Magnet Synchronous Generator (PMSG) without gear train as broadly classified in [33]-[34].

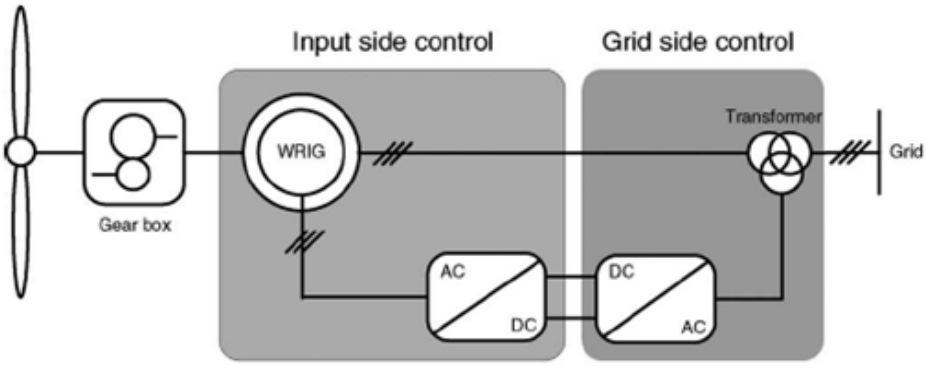

Figure 1.11: Partial Power Electronic Converter and Wound Rotor Induction Generator (WRIG) with gear train based wind energy harvester [34].

Partial Power Electronic Converter and Wound Rotor Induction Generator (WRIG) with gear train based wind turbine based system is shown in Figure 1.11. As can be found in [33]-[34], this type of wind energy harvester AC/DC followed by a DC/AC power electronic converter to harvest wind energy using the "slip power recovery" technique. The power converters connected to the rotor slip rings controls

the rotor currents to ensure "slip power recovery". If the generator is running *super-synchronously*, the electrical power is delivered through both the rotor and stator. If the generator is running *sub-synchronously*, the electrical power is only delivered into the rotor from the grid. A typical power converter of power rating around 30% around the nominal power can be used to harvest power while the variation of the motor speed can be allowed within 60% of the *synchronous* speed[44].

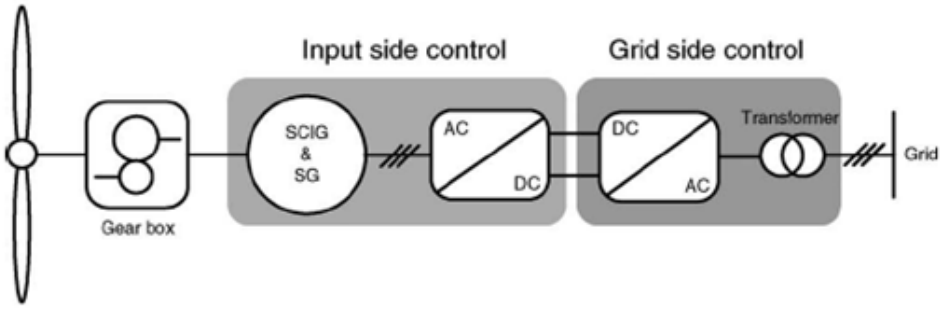

Figure 1.12: Full power Electronic converter and Slip Ring Induction Generator (SRIG) or Synchronous Generator (SG) with gear train based wind energy harvester [34].

Full power Electronic converter and Slip Ring Induction Generator (SRIG) or Synchronous Generator (SG) with gear train based wind turbine system is shown in Figure 1.12. By implementing a full-scale power converter between the generator and the utility grid, improved technical performances of the wind turbine (WT) system can be achieved, with the payback in losses in the power conversion stage as can be found in [33]-[34].

Full power electronic converter and Permanent Magnet Synchronous Generator (PMSG) without gear train based wind turbine system is shown in Figure 1.13. Use of multi-pole wound-rotor synchronous generator or permanent-magnet synchronous generator gives the flexibility of eliminating the presence of gear train as discussed in [33]-[34]. The system enables low mechanical loss in the overall

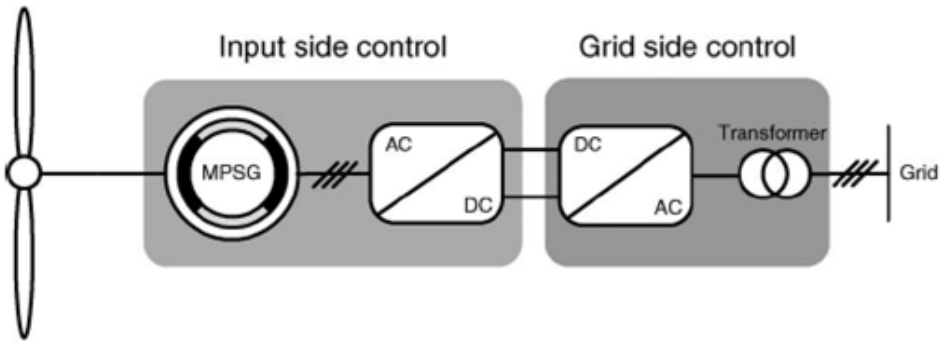

Figure 1.13: Full power electronic converter and Permanent Magnet Synchronous Generator (PMSG) without gear train based wind energy harvester [34].

conversion process.

All the power electronic converter structures presented in [33]-[34] utilize two-level pulse-width-modulation (PWM) voltage-source inverters (VSI) because this is the state-of-the-art technology used today by all manufacturers of wind systems. The possibility of high switching frequencies combined with a proper control makes these converters suitable for grid interface in the case of distributed generation, which has a large contribution to the improvement of generated power quality [34]. Three level neutral clamped VSI is used for high power wind turbine (WT) systems to reduce the voltage stress on the power semiconductor devices. Attempts of using multilevel [45] or matrix converters [46]-[47] have been made, but the use of such technologies are not validated yet in the field of distributed generation. The developed control system employed for the DC/AC grid connected wind turbine inverters are same as that of the PV inverters as discussed previously in this Section with the help of Figures 1.3 and 1.4.

The interconnection of different renewable energy sources with the micro-grid is of special interest of the recent time. The configuration of the renewable energy integrated micro-grid is well analyzed in [10]-[16]. The cited papers consider the

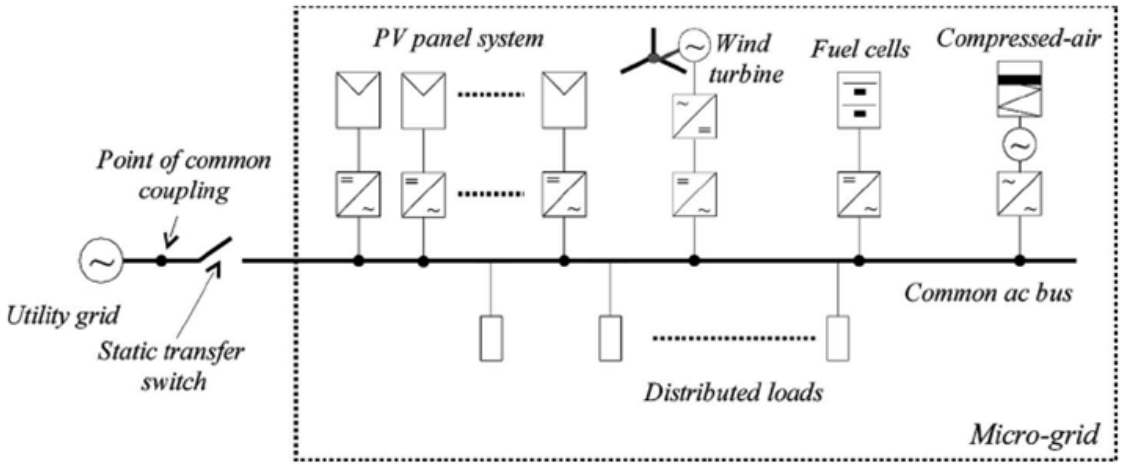

Figure 1.14: Configuration of flexible micro-grid with the interaction of different renewable energy sources [11].

multiple connections of different types of renewable energy sources utilizing the AC/AC as well as DC/AC converters as shown in Figure 1.14. The PV panels are connected to the common ac bus using DC/AC converters. The DC/AC converters should have both Maximum Power Point Tracking (MPPT) followed by grid power pump-in capability. The wind turbines are essentially gearless permanent magnet synchronous generator based systems as discussed in Figure 1.13. The AC output of the wind turbine generators are converted to DC using a AC/DC rectifier ensuring MPPT operation and followed by grid power pump-in using a DC/AC inverter. The overall execution of the power electronic converters ensures energy efficient operation of the overall micro-grid system.

1.4 Problem Statement

The thesis is directed towards the design and implementation of high-performance controllers for micro-grid application. During the execution of the thesis research work, four different problems related to both single phase residential micro-grid as

well as three phase industrial micro-grid are considered. It should be noted that, inside a typical multi-bus micro-grid, the common ac bus voltage can be referred to as the grid voltage.

1.4.1 Inverters for single-phase residential micro-grid

It can be seen from the previous Section that, the widely accepted renewable energy source based DC/AC inverters are grid connected systems in the single phase application as shown in Figure 1.8. The grid connected DC/AC inverters feed harvested power to grid directly i.e. the topology is referred to as parallel connected topology. The loads are also connected in parallel to the inverter. Most of the loads connected to the micro-grid are non-linear in nature which draws non-sinusoidal currents distorting the voltage at the point of common coupling (PCC) as shown in Figure 1.14. To solve this problem, another inverter is connected in parallel to the load to reduce the harmonic distortion in the grid currents. This extra inverter circuit is called *Power Factor Correction* (PFC) circuits. Such PFC circuits are referred as typical *active power filters* as shown in Figure 1.15. For a typical user, who has his/her own renewable energy sources and his/her own residential loads, needs two parallel connected inverter for the operation of overall system and the cost of the overall system increases. In most of the cases, the renewable energy harvested is partially stored in the battery or flywheel based systems and partially supplied to the load. Rest of the load power comes from the grid. However, if the consumer loads are not operating, the person can choose to feed all the surplus power to the grid. This calls for a high-bandwidth control of active and reactive power flow from or to the grid irrespective of the load current with unity *Displacement Power Factor* (DPF) and at the lowest possible *Total Harmonic Distortion*

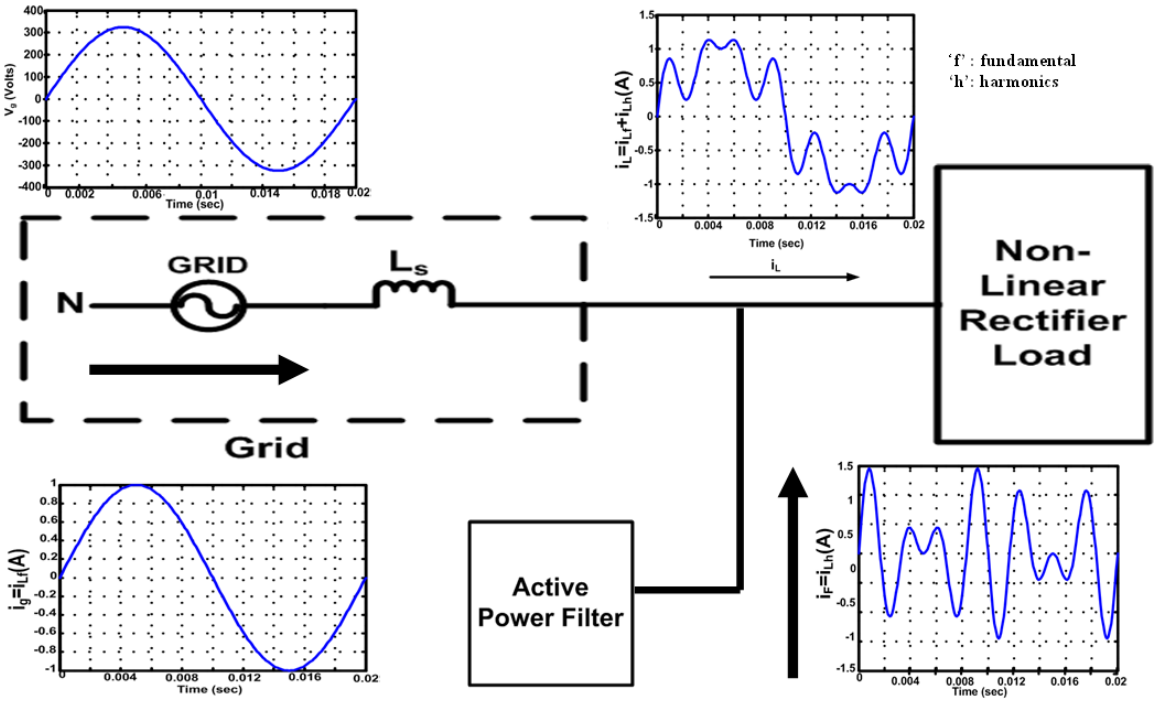

Figure 1.15: Illustration of typical PFC circuits.

(THD) in the grid current. The power control methodology by controlling the current of the inverter is a standard practice these days, however, for single phase application, the control methodology as well as control technique needs to be reformulated as the controlling quantities in synchronously rotating '$d-q$' axis frame is not directly applicable in the case of single phase inverter application.

In the parallel connected topology, the load is connected directly to the micro-grid at the PCC. So, if there is any disturbances in the micro-grid common ac bus voltage, i.e. in the grid voltage such as sag, swell or any other type of harmonic distortions due to the operation of other non-liner loads in the micro-grid, the consumer specific loads need to sustain all these disturbances. This may damage the critical sophisticated loads. Hence, there is a need for the inverter topological connection which interacts with the grid as well as load and the renewable energy

source in such a way that, not only the load power is shared between the renewable energy source and the grid, but also, the load sees high-quality voltage despite of any problems in the grid voltage.

1.4.2 Inverters for three-phase industrial micro-grid

The three-phase micro-grid system is the favorable configuration in an industrial power system. However, due to some intermediate fault or asymmetrical load sharing in the three phases, the common ac three phase bus voltages, which is also referred as grid voltage, gets distorted due to harmonic contamination as well as unbalanced. Even, in the micro-grid due to construction asymmetry, the line side inductors used for the renewable energy source connection to the grid can also be unbalanced. On the other hand, industrial non-linear loads are also connected at the PCC in parallel with the three phase renewable energy inverter. A method needs to be derived to model the control structure of such unbalanced system, thereafter current control of the inverter needs to be ensured to control the power sharing of the load power between the grid power and the renewable energy source based inverter with controlling the THD of the grid current to prevent further distortion of the grid voltages. A power control methodology and current controller need to be devised to handle such issues in such an asymmetrical and distorted three phase micro-grid system. The DC link side ripple control should also be taken as one of the criterion of the control methodology.

The six-switch (*b-6* topology) three phase voltage source inverter (VSI) based renewable energy sources are emphasized in details in [33]-[34]. It can also be highlighted that the VSI is operated in current control mode (CCVSI operation) to

ensure power balance between different elements in the micro-grid. The number of power electronic switches needed for *b-6* inverter topology is six during the overall operation. To optimize the overall power circuit of the micro-grid, a cost effective solution for the power circuit is to replace the traditional six switch (*b-6* topology) with a four switch three phase inverter topology is to be investigated. The four switch inverter topology is referred as *b-4* topology in the literature. The successful implementation of such an optimized switch inverter control is desired to reduce the implementation cost of the overall micro-grid system.

1.5 Literature Review

The grid connected inverters are popular in three-phase micro-grid to have active, reactive power flow control [1] as well as used as active filter to minimize the harmonic contents in the grid current drawn by the load [21]. Such works are well established in the field of three-phase grid connected inverters as can be observed in [32]-[56]. In [57]-[58], the current tracking is carried out using *Proportional Resonant* (PR) controllers implemented in synchronously rotating *'d-q'* frame and the current control facilitates active and reactive power flow control of the inverter to the grid. In [32], the grid current harmonics are reduced by using *P-I* and multiple *P-R* controller implemented in synchronously rotating *'d-q'* frame. Similar type of current control is also reported to be carried out by *Repetitive Controller* (RC) [59]-[62] as well as *Iterative Learning Controller* (ILC) [63]. Some improved current control techniques for three phase grid connected inverters are reported recently in [75]-[80]. All these current controls are implemented in the synchronously rotating *'d-q'* frame. In [76] a method is discussed to control active and reactive power flow

for a three phase grid connected inverters for islanded operation. *Newton-Rapshon* repetitive iteration method is used to calculate the inverter voltage magnitude and voltage angles to control the power flow. However, because of the repetitive calculation, the control process is slower than the other developed methodologies of grid power control. Besides these, in the case of single phase grid connected inverters, the well known *'a-b-c to d-q'* transformation concept cannot be used directly. An approach is proposed in [64] to facilitate current control of single phase inverters using *'a-b-c to d-q'* transformation based synchronous reference frame controllers by introducing an extra imaginary *'q'* axis. Some approaches are shown in [65]-[66], where the current of the single phase grid connected inverter is directly controlled without using imaginary *'q'* axis concept. The analysis given in [65] and [66] pronounces that, the structure of the controllers become more complex with the increase in harmonic contents in the current to be tracked. This controller structure requires the fundamental operating frequency of grid to be constant. A *Hysteresis* controller based single-phase grid connected inverter current control is proposed in [81]. *Ho et. al.* proposed a Hysteresis controller which can be implemented using constant switching frequency of the power electronics switches. However, the presented experimental results reflects the presence of chattering in the current waveforms.

In order to take care of the voltage dip problems in single phase micro-grid, a single phase inverter is needed to interface between the micro-grid, load and renewable energy sources. Such type of inverter is first proposed in by Fei Kong *et. al.* [68]. Fei Kong *et. al.* proposed a single phase series connected PV inverter to mitigate the sag and swell problems in weak power grids in developing countries like P. R. of China or India. The series inverter discussed in [68] uses PV energy

to regulate the load voltage under the voltage disturbances in the grid, with some energy savings (using PV energy) as an extra benefit. The basic structure of the proposed series inverter [68], is a two level inverter structure utilizing costly *bi-directional power switches*. The series connected inverter works in two modes: during day time if there is voltage sag or swell in the grid voltage, the inverter would add or subtract a compensating voltage (in phase with the grid voltage) component to maintain the load voltage constant. During night time, when there is a voltage swell, the same inverter operates like a voltage regulator (AC/AC converter[69]) by tapping the grid voltage itself using the technique discussed in [70]. This type of grid voltage disturbance problems are very common in case of micro-grid application. So, the same series inverter is applicable to interface AC loads with renewable energy sources as well as micro-grid. The total load power is shared by the renewable energy source based inverter and in micro-grid, with an additional benefit of load voltage regulation. In the control strategy proposed in [68], the compensation voltage, which is in phase of the grid voltage is added in series with the grid voltage. This results in the condition that the same load current flows through the inverter, grid and load. The series inverter compensation voltage is used to regulate the load voltage but the active power flow through the series inverter as well as the grid cannot be controlled. Besides this, the power factor seen by the grid terminal is same as that of the connected load [68]-[70]. It should also be noted that during conditions, when the grid voltage does not undergo sag or swell, the series inverter does not provide any compensation voltage which leads to the condition that the series inverter behaves like an *idle element* under healthy condition in the grid. So, load power cannot be shared by renewable sources if the grid is at healthy condition.

These disadvantages associated with the preliminary series inverter control mentioned in [68]-[70] can be resolved using the vectorial addition of inverter voltage with grid voltage to ensure both load voltage regulation and inverter power flow control. The load voltage controller of the proposed series inverter system has two tasks: (1) to maintain a load voltage with a specific magnitude and a specific phase in relation with the micro-grid voltage - which can be classified as a *voltage tracking* problem, (2) the load voltage should be free of *grid voltage harmonics* - which can be classified as a *grid voltage harmonics elimination* problem. An additional problem associated with the micro-grid is that due to the unpredictable loading condition in the total micro-grid network, the frequency of the grid can change suddenly. But, the series inverter voltage has to synchronize instantly with the grid voltage to avoid any power line oscillations [71] and [72]. Both the problems, i.e. tracking a sinusoid and eliminating harmonics can be seen like eliminating steady state error at selected frequencies, with the fundamental frequency itself has a possibility of varying. These problems have been reported in the literature and solved using nonlinear controllers, i.e. *resonant controller* [32], [39], *repetitive controller* [59] and [60] and *iterative learning controller* [63]. A typical work in the similar line as harmonic elimination of voltage source inverter is also reported in [73]. Chen *et. al.* [73] mainly dealt with the elimination of harmonics in the load voltage due to non-linearity associated with the PWM process and other nonlinear phenomena related with the circuit. In this stand-alone inverter application, both the inverter voltage frequency and the repetitive controller tuning frequency is decided by the internal timer placed in the controller, resulting no chance of frequency mismatch. But in the series connected inverter, the load voltage phase reference is taken from the fundamental component of the grid voltage using the phase-lock-loop. So, if resonant controller, repetitive controller or time domain iterative learning

controller are used and the fundamental tuning frequency of those controllers are fixed at rated frequency 50 Hz and if there is a sudden change of grid fundamental frequency from its rated value, the control system suffers from synchronization problem and load voltage becomes oscillatory.

Grid connected renewable energy source based three-phase inverters are well documented in the literature [33]-[34] to facilitate renewable energy usage globally. The most popular topology is Current Controller Voltage Source Inverter (CCVSI) mode to control the active and reactive power flow of the grid as reported in [34]. It is discussed also in the cited papers that high band-width grid active, reactive power control and unbalanced grid current shaping are facilitated by directly controlling the currents of the CCVSI system. The thesis is directed towards the proposition of a high-performance current controller for such type of three phase unbalance grid connected renewable energy inverters. High band-width current control for three phase grid connected CCVSI is reported in [32], [34] and in [84]-[86]. The controllers are implemented in *synchronously rotating reference* frame using PI controller or *stationary reference* frame using *Proportional Resonant* (PR) controller or in *a-b-c* frame using *Hysteresis* controller or *Deadbeat* controller. A *Predictive* controller based current control scheme implemented in *synchronously rotating* reference frame is proposed in [87]. It is well known that current controllers implemented in *synchronously rotating reference* frame suffer form the problem of grid frequency drift and *hysteresis* type controllers face the problem of finite sampling frequency if implemented in digital controllers or suffer from the problem of high semiconductor device switching loss if implemented using analog controller. *Predictive Controller* is also proposed in [88] for balanced grid connected active filter application. These research works only take care of the bal-

anced grid and balanced inverter line side impedance interactions. However, with the increasing research in the field of micro-grid, unbalanced grids are the focus of research[29].

Current control of unbalanced grid connected DC/AC inverters is reported in [89]-[91] and the same for AC/DC rectifiers is reported in [59]-[60]. In these papers, *dual synchronously rotating frame* based current control is proposed and different high performance controllers are used to have high bandwidth current control in the case of unbalanced grid conditions. However, the methods used in these papers deal with symmetrical unbalance (absence of zero sequence component), balanced three phase choke connection between the inverter and grid and also no compensation for the unbalanced non-linear current drawn by the loads connected in the grid. Besides these, implementation of such controllers needs the feedback variables in both +ve and -ve rotating synchronous reference frames. Which in turn necessities the dual frame Park transformation process using the *Software Phase Lock Loop* (SPLL) [33], [92]. This faces the problem of huge online computation of the overall system and delay due to the dynamics associated with the SPLL block under sudden changes in grid phase in case of intermittent fault inside the micro-grid.

The most popular power control method for grid connected three phase inverters is known to be the *Direct Power Control*(DPC). In DPC, an optimal switching table is utilized to generate the PWM voltage references in order to minimize the error in average active power demand and reactive power demand[93]. However, this results in varying switching frequency of the power electronics devices restricting the use of circuit components and fixed bandwidth digital signal processor for controller application. A constant switching frequency based DPC is reported in

[94]-[96] to apparently solve the varying switching frequency problem. However, the method suffers from delay as well as parameter uncertainty problem in the grid connected application. Active and reactive power control for three phase inverter connected to the unbalanced grid is also reported in [97]. In [97], a method is described by *Garcia et. al.* to compensate for the harmonic active as well as reactive power. The method calculates the active as well as reactive power by means of dot and cross product of instantaneous voltage and current vectors and compensates for the oscillatory component of both active as well as reactive power by isolating the oscillatory component using finite mean value technique. However, this method shows harmonics in actual active as well as reactive power along with harmonic contamination in grid currents because of the interaction of instantaneous currents and voltages. It is also mentioned in [97] that minimizing oscillations in any one component of power(active or reactive) results in increased oscillations in the other, while suppressing oscillations in both the power components tends to distort the current waveform. The conclusions can be explained in a more generalized way by the analysis provided in [98]. It can be seen from [93]-[98] that, the VSI system is directly connected to the three phase grid. Any loads connected to the point of common coupling (PCC) at the three phase grid are not addressed in these papers. However, loads connected in PCC is considered in [76]. The method described in [76] utilizes separate controller for each of the line current harmonics to improve the current and voltage THD as well as uses *Newton-Rapson* based iterative method to facilitate control action. These leads to further more computation loads on the processor and its associated delay in the overall system dynamics.

Power control of unbalanced grid connected VSI is also reported in [30], [59]-[60] and [99]-[100]. These papers use three phase p-q theory based approach to

deal with the VSI current estimation. In [30], [59]-[60], the authors describe how *p-q* theory based method can be used to reduce the even harmonic component [31] of active as well as reactive power in case of three phase PWM rectifier to eliminate the DC link voltage ripples and unwanted current harmonics. Whereas, in [99]-[100], the proposed method deal with the elimination of double frequency harmonics in active as well as reactive power in the application of three phase grid connected inverter for unbalanced grid condition using the same *p-q* theory approach. It can be noted that in these references, the current calculation is carried out in *dual frame synchronously rotating reference frame* utilizing *dual frame d-q* theory to deal with unbalance in the grid voltage. It can be understood that, calculation in dual frame *d-q* needs computation of *Park's Transformation* and its inverse in realtime along with the *positive sequence grid voltage phase*. In [59]-[60], it is well described that, the *positive sequence grid voltage phase* is estimated using a *software based phase lock loop* (SPLL) [101] placed after the extraction of the positive sequence component of grid voltage. It can be understood that these calculations require significant mathematical computation burden on the processor and specially, the SPLL needs a dynamic computation time delay to get in operation under sudden change in grid frequency. The dedicated *p-q-r* theory, which is an extension of traditional *p-q* theory, is also proposed in [102]-[103] to take care of the zero sequence active power components.

An attractive alternative method of CCVSI current reference calculation, namely *FBD*, is discussed in [104]-[108]. *FBD* method is significantly different from the traditional *p-q* method and the current reference directly can be calculated in the *a-b-c* frame as described in the cited papers. Even in the case of unbalanced grid voltage, the grid voltages need not to be split into *positive* and

negative sequences space vectors unlike the case in *p-q* theory. However, a large number of online memory allocation is needed to store the squared voltage quantity samples over half electrical cycle of the fundamental grid voltage to correctly implement *FBD* method of calculating current reference. Moreover, in the *FBD* method, each grid phase current reference is in phase with corresponding grid phase fundamental voltage resulting in the presence of a huge double harmonic power in the instantaneous power in the case of unbalanced grid condition. This double harmonic instantaneous power manifest as the double harmonic quantity in the DC link increasing the value of capacitor in DC link. It can also be noted that, in the implementation of *FBD* method, the need of *SPLL* is also not there. However, if there is a change in grid fundamental frequency, the number of samples needs to be changed. In the present form of *FBD*, the dynamic change of number of samples is not provisioned in the case of grid fundamental frequency change.

Besides these techniques, a significantly different technique for calculating inverter current reference is analyzed in [109]-[110], namely *CPC* method. It is also reported that the *CPC* method utilizes *Recursive Discrete Fourier Transform* to calculate equivalent conductance and susceptance of the asymmetrical load to compensate for the reactive power as well as harmonic power. As mentioned in [109], that the method is hugely computational intensive and difficult to implement in real time. Hence, this method is also not investigated in details in the report.

The six-switch (*b-6* topology) three-phase voltage source inverter (VSI) based renewable energy source based inverters are emphasized in details in [33]-[34]. It is also highlighted that the VSI is operated in current control mode (CCVSI operation) to ensure power balance between different elements in the micro-grid. The

number of power electronic switches needed for *b-6* inverter topology is six during the overall operation. To optimize the overall power circuit of the micro-grid, a cost effective solution for the power circuit is to replace the traditional six switch (*b-6* topology) with a four switch three phase inverter topology is proposed. The four-switch inverter topology is also known as *b-4* topology as discussed in [111]-[119]. In the four-switch inverter, one of the grid terminal is connected to the the center tap of the DC-link capacitors so that the overall operation needs two less numbers of IGBTs as also highlighted in the cited literature. The peak voltage of the four switch inverter is reduced to $\frac{V_{dc}}{2\sqrt{3}}$ whereas the same quantity for the six switch inverter is $\frac{V_{dc}}{2}$ reducing the overall voltage utilization factor of the power circuit. Other than that, the DC link center tap voltage also fluctuates at the fundamental frequency of the phase current due to the flow of AC current through the center tap point of the DC link causing fluctuation of the inverter voltages around the steady value. Besides these, if the DC link split capacitors are not equal (which is the case always), there is a possibility of over-modulation of switch PWM process to take care of this DC link mid point voltage.

The four-switch inverters (*b-4* topology) are used previously for developing cost effective induction motor drives which can run both in single-phase as well as three-phase power supply as reported in [111]-[119]. In the papers [114]-[119], different methods are discussed to perform asymmetrical Space Vector Modulation (SVM) to take care of the DC-link mid point voltage fluctuation. Different type space vector modulation techniques for the four switch inverters for induction motor drive application is also proposed by Blaabjerg *et al.* in [111]. This process ensures the inverter voltage vector to follow a desired space vector. The PWM method is further modified in [112]. In this modified method, the voltages of each of the

half DC link capacitors are measured and the difference is directly included in the modulation process. This method needs extra voltage sensors to measure the half DC link voltages. Besides, if the voltage sensors have phase delay associated with the measurement process, the compensation sufferers from inaccuracy. *Kim et. al.* in [113] discusses an alternative method to compensate for the DC link mid point voltage fluctuation by inserting a virtual equivalent impedance in the phases which are not connected to the DC link mid-point to compensate for DC link mid-point voltage fluctuation. This method also needs the information of instantaneous value of current of the phase which is connected to DC link mid-point. This current measurement error also effects the performance. Other than that if the DC link split capacitor values are not known perfectly, the impedance injection becomes erroneous.

1.6 Contribution of this thesis

The problem statement of this thesis covers different aspects of single-phase and three-phase micro-grid systems. The Section, '*Literature survey*', states several similar solutions relating to those problems; however none of the papers or articles describes concrete solutions for those problems related to the micro-grids. The thesis is directed towards investigations of different terminal problems of the loads related to the micro-grids. In the presence of harmonic distortions or other types of disturbances in the grid, the proposed power electronic solutions reduce the power consumptions of the load from the grid with renewable energy penetration while load operation is not affected by the grid voltage disturbances as well as load operation cannot further deteriorate the grid voltage quality. The contributions of

this thesis are as following:

- Control methodology of single-phase parallel connected renewable energy source based inverter connecting to micro-grid to control active and reactive power flow with grid current shaping.
- Control methodology of single-phase series connected renewable energy source based inverter connecting to micro-grid to mitigate voltage related problems along with active power flow control.
- A Lyapunov function based current controller to control active and reactive power flow from a renewable energy source to a generalized three-phase micro-grid system.
- Derivation of instantaneous current references for multi-phase PWM inverter to control active and reactive power flow from a renewable energy source to a generalized multi-phase micro-grid system: the p-q theory based approach.
- Derivation of instantaneous current references for multi-phase PWM inverter to control active and reactive power flow from a renewable energy source to a generalized multi-phase micro-grid system: the FBD theory based approach,
- Application of four-switch based three-phase grid connected inverter to connect renewable energy source to a generalized unbalanced micro-grid system

Brief description of each of the contributions of this thesis is given in Appendix I.

1.7 Organization of this Thesis

Chapter 1 is presented to introduce the background and motivation of the thesis work. The basic operation of the multi-bus micro-grid and the associated single phase and three phase PWM DC/AC inverters to interconnect renewable energy sources to the micro-grid is explained. Problems associated to the disturbed grid as well as unbalanced grid are identified. Motivation behind the selected work is also explained. A brief literature review is also provided to highlight the past works to solve similar problems. Contributions of the thesis work is listed to differentiate from existing solutions.

Chapter 2 describes the state-space modeling of the parallel connected single phase renewable energy source based inverter with grid as well as non-linear load. The inverter operates in current controlled voltage sources inverter (CCVSI) mode. The aim of operation of the inverter is that the single inverter operates in such a way that, the total load power is shared between the grid and the renewable energy sources along with maintaining unity DPF of the grid current with minimum possible THD of the grid current at the presence of non-linear load connected at the PCC. A novel method of calculating current references for the CCVSI using the single phase p-q theory is proposed to control the grid active as well as reactive power flow with minimum grid current THD assurance.

Chapter 3 discusses about the current controller for the single phase parallel grid connected inverter to ensure grid active as well as reactive power along with minimum THD of grid current at the presence of the non-linear load at the grid PCC. A *Lyapunov function* based current tracking controller is designed and

implemented. The current controller is special in comparison with conventional current controllers because of the reason that , the CCVSI current reference is a non-sinusoidal periodic wave because of the two fold work as mentioned before. A SRC is also used to estimate the grid and other periodic disturbances such as inverter non-linearity due to blanking time etc to further improve the operation of the current controller. Detailed experimental results are provided to emphasize the efficacy of the proposed system.

Chapter 4 presents the analysis and design of the single phase series connected renewable energy inverter. The PWM inverter operates in voltage controlled mode (VCVSI) unlike the parallel connected inverter. How the vectorial addition of the inverter voltage with the grid voltage non only regulates the load voltage under grid voltage disturbances but also shares the active power required by the load with the grid is described in this Chapter. A detailed vector analysis is provided to facilitate the design of the DC link voltage requirement and other circuit restrictions.

Chapter 5 describes the control methodology for the series inverter to regulate the load voltage as well as control the active power flow through the inverter. The proposed control system ensures high quality sinusoidal load voltage across the load in the presence of grid voltage disturbances such as sag or swell or severe harmonic distortion along with controlling the active power flow from the renewable energy sources through the inverter. A *Spatial Repetitive Controller*(SRC) is proposed for this operation. The proposed SRC operates to ensure the rated undistorted load voltage in the presence of any grid voltage disturbances. The proposed SRC also operates in the case of sudden change in the grid frequency as well. Another *Lyapunov function* based load voltage controller is also analyzed and designed for

the series inverter configuration. The operation of the *Lyapunov function* based controller is shown to be faster than the SRC. A detailed analysis as well as experimental results are provided to test the efficacy of the proposed series inverter and the control system under different operating conditions.

Chapter 6 deals with modeling of the three-phase grid connected renewable inverter under generalized grid voltage condition and unbalanced line side inductance connection. The modeling is carried out in state-space domain to facilitate the direct control inverter currents in the *a-b-c* frame. The modeling method can take the symmetrical as well as asymmetrical unbalance of the three-phase grid voltage. The modeling method can also take into account arbitrary distortions in the three phase grid voltages also. The modeling method can be applied in the case for both three phase six switch grid connected inverter topology (*b-6* topology) as well as three phase four switch grid connected inverter topology (*b-4* topology). The modeling method is used to formulate the control input to facilitate the current control of the three phase inverter. This Chapter is directed towards the formulation of a *Lyapunov function* based controller utilizing the state-space model of the three phase generalized grid connected renewable energy source based inverter to control the inverter currents directly in the *a-b-c* frame. The proposed controller ensures high band-width active and reactive power flow control from the grid with minimum possible THD of the grid current even in the presence of non-linear load at the grid. The control methodology ensures energy savings of grid power consumption by the load by compensating with the renewable energy source based inverter power flow. A SRC is also proposed to improve the performance of the proposed *Lyapunov function* based current controller for grid current tracking.

Chapter 7 deals with the current reference generation methods of a multi-phase renewable energy inverter to ensure specific active and reactive power flow along with minimum possible grid current THD in the presence of non-linear load at the grid. The grid can be any distorted, unbalanced generalized multi-phase grid. Different power control methodologies, i.e. *p-q* and *FBD* methods are used to generate the grid current references. The effect of these current reference generation methods on the DC link side ripple is also investigated. The details implementation methods of these systems are described. The proposed method is shown to be grid fundamental frequency independent. A *Complex Notch Filter* is designed to extract the +ve as well as -ve sequence components of the grid voltages. A *Rotating Reference Signal Characterizer* (RRSC) method is also proposed to estimate the magnitude, frequency and phase of the positive and negative sequence voltages is also proposed. Detailed experimental results are provided during the tracking of inverter currents to control the grid active as well as reactive power along with controlling grid current THD under different operating condition as well as grid with different grid current generation schemes. Experimental studies are carried out on a three phase inverter system connected to a three phase grid in the presence of three-phase non-linear load.

Chapter 8 deals with application of four switch three phase inverter (*b-4* topology) in generalized grid connected condition. The grid active as well as reactive power control in presence of non-linear loads at the PCC with grid current THD control by controlling the CCVSI currents with the same controller proposed in Chapter 6 is investigated for *b-4* inverter topology of the grid connected inverter. Sine PWM is used instead of the complex four switch space-vector PWM methods. The problems of DC link mid-point voltage fluctuation as well as unbalance

DC link split capacitors are also addressed. The proposed controller is capable of handing all these well known *b-4* inverter problems for three phase grid connected application. Detailed experimental results are provided to show the efficacy of the proposed method.

Chapter 9 summarizes the concluding studies of the work described in this report and some new dimensions are discussed that can be undertaken in future.

1.8 Summary

This Chapter introduces the performance related problems of single-phase as well as three-phase renewable energy source based DC/AC PWM inverters for micro-grid application. The operation of the inverters are considered under distorted, unbalanced grid condition as well as in the the presence of non-linear load. The main contribution of the thesis are then listed. The structure of the thesis is provided along with the focus of each of the Chapters. The experimental platforms used for validating the proposed methods are also described in this Chapter.

Chapter 2

Mathematical model, active and reactive power flow control of single-phase parallel connected renewable energy source based inverter

All the controller design methodologies for any system need a good understanding of the dynamic behavior of the plant. Representation of the plant in a mathematical form leads to the convenience of analysis and controller design. In this Chapter, firstly a mathematical model of the parallel connected single phase renewable energy source based inverter is discussed. The model is used to derive the state-space model of the overall system. The PWM inverter is connected in parallel with the common AC bus of the micro-grid and the load is also connected to the same point of common coupling. For typical non-linear loads, the current drawn from the common AC bus is non-sinusoidal leading to distortions of the AC bus voltage. So, there is a two fold requirements of controlling the active and reactive power flow from the grid while maintaining the grid current drawn from the common AC bus

to be sinusoidal. A *single-phase p-q theory* [120]-[121] based approach is used to perform both the functions together using only one inverter. The *single-phase p-q theory* based approach is used to derive suitable current reference for the parallel inverter so that, the total load power is partially supplied by the renewable energy source based parallel inverter and partially from the common AC bus with sinusoidal current and controllable power factor condition.

2.1 Description of the inverter configuration and its control

2.1.1 Description of the inverter assembly

The highlighted part in Figure 1.1 is further analyzed in this Section. Figure 2.1 shows the schematic diagram of the power circuit of the parallel connected inverter assembly interconnecting the load and the micro-grid. The inverter power circuit is preceded by a set of renewable energy extracting apparatus as can be seen in Figure 2.1. Figure 2.1 also shows that, the renewable energy extractor is directly connected to power electronic converter, *PEC*. The *PEC* is a typical DC/DC converter if the renewable energy extractor is a PV panel or a fuel cell based system and a typical AC/DC converter if the renewable energy extractor is a permanent magnet or induction machine based wind turbine. The *PEC* output is connected to the DC link of the PWM voltage source inverter (VSI). At the DC link of the PWM VSI, an energy storage element, battery is also connected in parallel with the *PEC* converter output. As depicted in Figure 2.1, the PWM VSI, is directly connected in parallel with the micro-grid, operating in CCVSI mode. The load is directly connected to the micro-grid. The *PEC* converter is operated in such a way that

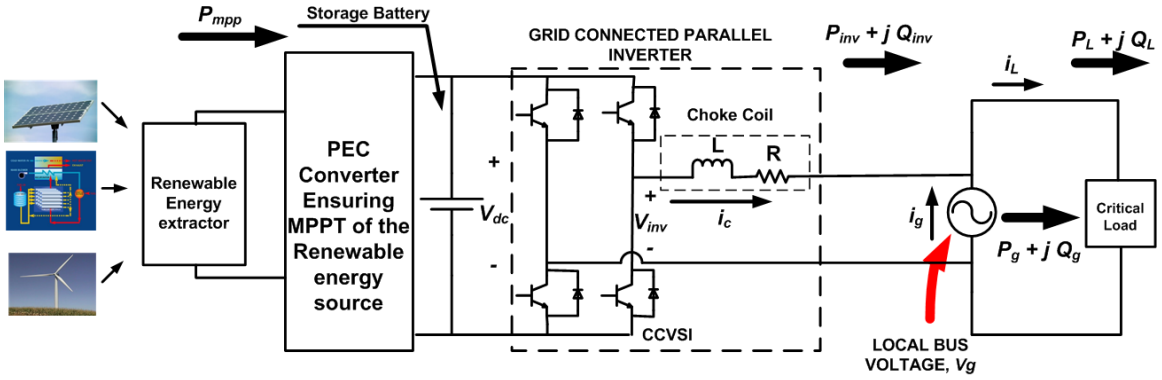

Figure 2.1: Power circuit of the single-phase micro-grid connected inverter.

the renewable energy source operates at Maximum Power Point (MPP) [36], [74] and the MPP active power, P_{mpp} is extracted from the renewable energy source. The details of the MPPT circuit in the case of PV system is explained in Figure B.1 in Appendix B.

2.1.2 Control strategy of the inverter

In Figure 2.1 it is shown that, the load requires the active power, P_L and the reactive power, Q_L (load complex power $S_L = P_L + j\,Q_L$). If the inverter is not operated, load draws the full complex power, S_L from the *Local Bus*. In reality, the inverter is connected in parallel to the micro-grid, with *local bus* voltage, v_g. The current, i_c of the CCVSI is controlled in such a way that, the inverter supplies active power, P_{inv} and reactive power, Q_{inv} to the *Local Bus* of the micro-grid (the *Local Bus* is getting complex power $S_{inv} = P_{inv} + j\,Q_{inv}$ from the inverter). In normal operating conditions, the active power, P_{inv}, supplied by the CCVSI, is less than the extracted renewable power, P_{mpp} ($P_{inv} \leq P_{mpp}$) and the rest of the renewable power is stored in the battery ($P_{bat} = P_{mpp} - P_{inv}$). The discussions here make it clear that, only part of the load power demand: active power, $P_g = P_L - P_{inv}$

and reactive power, $Q_g = Q_L - Q_{inv}$ are drawn from the *Local Bus* connected to the micro-grid. Initially P_{inv} is controlled in such a way that P_{bat} is positive to charge the battery. When battery is fully charged $P_{inv} = P_{mpp}$ is maintained to transfer the entire extracted renewable power, P_{mpp} to the load. The battery energy is used to feed the load if the renewable energy is not sufficient to supply the load during intermittent grid failure condition. In the actual system, the values of P_g and P_{inv} under different operating conditions are to be set by an automatic controller but in the laboratory prototype, P_g and P_{inv} are manually changed to test the proposed control strategy in the laboratory environment. The reference of the current, i_g^*, drawn from the *Local Bus*, is derived from P_g and Q_g using the single-phase *p-q theory* approach [120]-[121] to ensure specific active and reactive power flow ($S_g = P_g + j\,Q_g$) from the *Local Bus* connected to the *Common Bus* (as shown in Figure 1.1) of the micro-grid. The details of the current reference calculation is discussed in the next few Sections in this Chapter. If the active energy storage elements are not present at the DC link of the inverter, the inverter active power flow, P_{inv} command is controlled to stabilize the voltage of the DC link capacitor as discussed in Appendix C. However, it is considered in here and in the subsequent chapters that, the inverter DC link voltage is stabilized by the active energy storage element.

2.2 Modeling of the CCVSI system

Assuming that the *PEC* converter is extracting MPP power from the renewable energy source and the storage element battery is operating properly, the inverter dc link can be modeled as a DC power source. From this stage onwards, the *Local Bus*

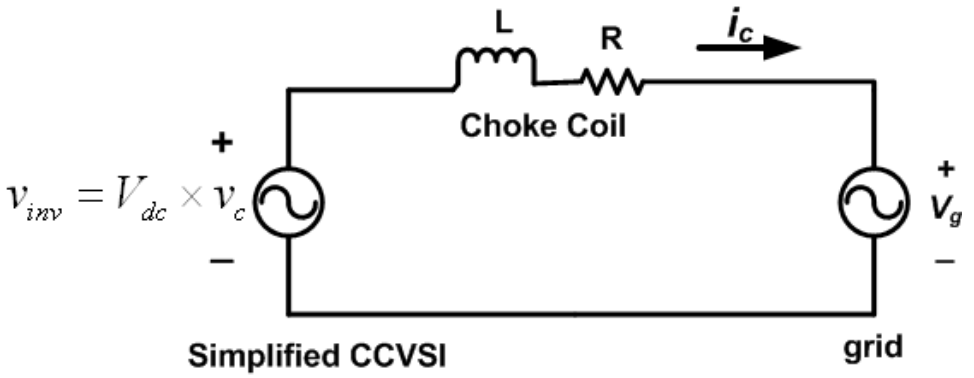

Figure 2.2: Simplified power circuit for the single-phase parallel CCVSI.

voltage, where the targeted load and the renewable energy source based inverter are connected, is called the grid voltage, v_g. In order to ensure proper power flow, a fast current tracking controller is needed. The current tracking system of the CCVSI can be modeled as a first order system as shown in Figure 2.2. Neglecting the switching frequency related harmonics voltages, the voltage source inverter is modelled as a dependent voltage source, $v_{inv} = V_{dc} \times v_c$, where, v_c is the control signal of the sine PWM process. The dynamic equation of the CCVSI current, i_c can be written as,

$$\frac{di_c}{dt} = -\frac{R}{L}i_c + \frac{V_{dc}}{L}v_c - \frac{1}{L}v_g \tag{2.1}$$

To analyze the system from control point of view, the state of the system is chosen as: $x = i_c$, control input, $u = v_c$, disturbance input $d = -\frac{1}{L}v_g$, state function $f(x) = -\frac{R}{L}i_c$ and the input function $b(x) = \frac{V_{dc}}{L}$. So the state equation of the system can be written as,

$$\frac{dx}{dt} = f(x) + b(x)\,u + d \tag{2.2}$$

However, the considered model of the SPWM inverter is simple and it does not consider any unpredictable non-linear periodic disturbances d_{up} (one such possible source is the blanking time in the inverter driver circuit). In actual circuit, these non-linear periodic disturbances play important roles. In practical cases, the dis-

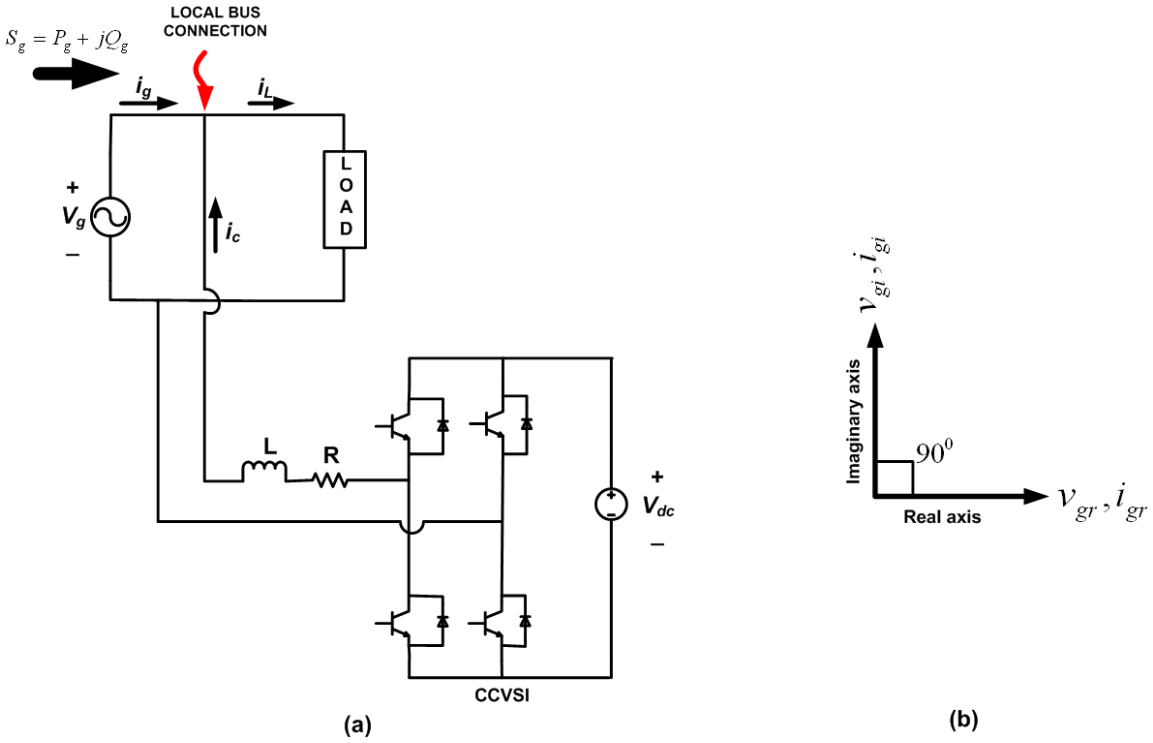

Figure 2.3: (a) Simplified power circuit of the single-phase micro-grid connected inverter and (b) real, imaginary axis quantity.

turbance term d in (2.2) consists not only grid voltage disturbance, $-\frac{1}{L}v_g$ but also the unpredictable non-linear disturbances as

$$d = -\frac{1}{L}v_g + d_{up} \tag{2.3}$$

2.3 Deriving the current reference of the inverter

2.3.1 Using conventional single-phase *p-q* theory

CCVSI current reference, i_c^* can have any type of periodic shape (i.e. sinusoidal or non-sinusoidal shape) depending on the load. The full inverter assembly can be re-drawn as shown in Figure 2.3(a). The load is connected to the grid voltage, v_g and the parallel CCVSI can be regarded as the the shunt active current, i_c

compensator. If the required amount of active and reactive power flow from the grid are P_g and Q_g respectively, then the reference grid current magnitude, i_g^*, can be found by applying *p-q* theory as mentioned in [120] and [121]. To apply *p-q* theory, concept of real and imaginary axis is introduced as shown in Figure 2.3(b). The real axis grid voltage is $v_{gr} = v_g$ and the real axis grid current reference is, $i_{gr} = i_g^*$. The corresponding imaginary axis grid voltage and the imaginary axis grid current references are v_{gi} and i_{gi} respectively. If the instantaneous value of a quantity in real axis is known, the instantaneous value of the corresponding quantity in the imaginary axis can be estimated by passing the real axis quantity value through the Hilbert transform (providing 90^0 phase lead to all the frequencies) as mentioned in [121]. In [120], the Hilbert transform operation is approximated as passing the real axis quantity through the all pass filter $H(s) = \frac{1-T\,s}{1+T\,s}$, where $T = \frac{1}{\omega}$ and ω is the fundamental power frequency in rad/s. By using this technique, v_{gi} is estimated from the instantaneous measurement of v_{gr}. So, in terms of time domain convolution, $v_{gi}(t) = h(t) * v_{gr}(t)$. The frequency characteristics of this all pass filter can be noticed as:

$$\begin{aligned} H(j\,\omega) &= \frac{1 - j\,T\,\omega}{1 + j\,T\,\omega} \\ &= 1 \angle -2\,tan^{-1}(T\,\omega) \end{aligned} \tag{2.4}$$

It can be noted from (2.4) that at $\omega = \frac{1}{T}$, $H(j\,\omega) = 1 \angle -\frac{\pi}{2}$. So, the *voltage space vector* formed in this system can be expressed as:

$$\overrightarrow{V} = v_{gr} + j\,v_{gi} \tag{2.5}$$

The *current space vector* formed in this system can be expressed as:

$$\overrightarrow{I} = i_{gr} + j\,i_{gi} \tag{2.6}$$

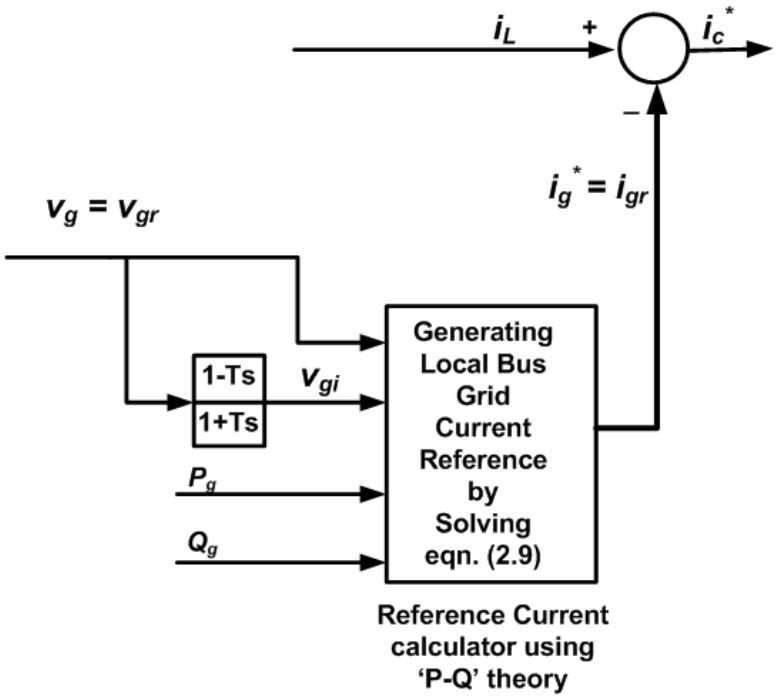

Figure 2.4: Block diagram of the calculation of CCVSI current reference.

Now by using (2.5) and (2.6), the complex power, S, drawn by this virtual two phase system can be calculated as:

$$\begin{aligned} S_g &= \overrightarrow{V}\ \overrightarrow{I}^* \\ &= (v_{gr} + j\, v_{gi})\,(i_{gr} - j\, i_{gi}) \\ &= (v_{gr}\, i_{gr} + v_{gi}\, i_{gi}) + j\,(v_{gi}\, i_{gr} - v_{gr}\, i_{gi}) \\ &= 2P_g + j\, 2Q_g \end{aligned} \tag{2.7}$$

Using p-q theory, the instantaneous active and reactive power flow balance equation at the grid can be written as,

$$\begin{bmatrix} 2\,P_g \\ 2\,Q_g \end{bmatrix} = \begin{bmatrix} v_{gr} & v_{gi} \\ v_{gi} & -v_{gr} \end{bmatrix} \begin{bmatrix} i_{gr} \\ i_{gi} \end{bmatrix} \tag{2.8}$$

The multiple of '2' in left side of (2.8) is due to the fact that, to use the space vector concept in power calculations, the imaginary axis is introduced, so the total power shown in left side of (2.8) is taking care of the total power handled by both

the real and as well as imaginary axis. By inverting the matrix in (2.8), the i_{gr} and i_{gi} can be solved. The real grid current reference, i_g^* can be calculated as,

$$i_g^* = i_{gr} = \frac{2\, v_{gr}\, P_g + 2\, v_{gi}\, Q_g}{v_{gr}^2 + v_{gi}^2} \tag{2.9}$$

If Krichoff's Current Law (KCL) is applied at the PCC terminal, the reference current for the CCVSI is found by measuring the load current, i_L as given by,

$$i_c^* = i_L - i_g^* \tag{2.10}$$

So, by sensing the instantaneous load current, i_L and the grid voltage, v_g, the instantaneous value of the CCVSI current reference, i_c^* can be found using (2.9) and (2.10) depending on the micro-grid active as well as reactive power flow requirements, P_g and Q_g respectively as shown in Figure 2.4. If grid voltage, v_{gr} contains harmonics, the grid voltage is pre-processed through a notch filter tuned at grid fundamental frequency before passing into the current reference calculation block shown in Figure 2.4. More analysis on single phase p-q theory is given in Appendix E.

2.4 Summary

This Chapter deals with the formulation of state-apace modeling of the parallel connected renewable energy source inverter. The state-space model derived in this Chapter is used to formulate the high-performance control law to control the CCVSI current as discussed in details in the next Chapter. The proposed method of deriving the CCVSI current reference in this Chapter is to ensure the proper active and reactive power from the grid along with current shaping of the grid current. The current reference for the CCVSI derived with the method discussed in this Chapter

is tracked by the high-performance controller described in the next Chapter to meet the power flow and grid current THD requirements. Detailed experimental results are provided in the next Chapter along with the current tracking to ensure the proper control of the CCVSI current in order to ensure the proper grid active and reactive power flow along with grid current shaping.

Chapter 3

Implementation of control strategy for the single-phase parallel connected renewable energy source based inverter

Renewable energy sources are interfaced to the micro-grid using the parallel connected inverters connected to the common AC bus. The load is also connected in parallel to the common AC bus in the micro-grid. Total active and reactive power drawn from the common AC bus by the load is partially supplied by the inverter and rest is supplied by the common AC bus. The control methodology is executed by deriving the suitable current reference for the PWM DC/AC inverter using the single-phase p-q theory based approach as discussed in Chapter 2. However, because of the variable nature of the load, the current reference of the PWM inverter is a typical periodic non-sinusoidal wave. This Chapter focuses on designing an accurate and non-linear high-performance current controller to ensure proper PWM inverter current tracking. The stability analysis of the entire control system is also analyzed and the efficacy of the proposed control system is supported by adequate

experimental results under different operating conditions.

3.1 Design of Non-Linear Control Law based on Lyapunov function

3.1.1 Determining the Lyapunov function based control law to ensure current control

It is needed to generate the control input, $u(t)$ so that, $x = i_c$ tracks the reference value, $x_d = i_c^*$. The dynamic tracking error can be written as $e = x_d - x$. It is required to find a control input $u(t)$ such that tracking error $e(t)$ asymptotically converges to zero. *Lyapunov* direct method is used to find out the control input $u(t)$ for the specific application.

The *Lyapunov function* is taken as,

$$V = \frac{1}{2} e^2 \tag{3.1}$$

According to the property of *Lyapunov function*, $V > 0$ for all the conditions except $e = 0$ in this case. Thus, the selected V can be mentioned to be a *positive definite* function. Differentiating (3.1) wrt time,

$$\frac{dV}{dt} = e \frac{de}{dt} = e \left(\frac{dx_d}{dt} - \frac{dx}{dt} \right) \tag{3.2}$$

Substituting (2.2) into (3.2), the resulting equation becomes as,

$$\frac{dV}{dt} = e \frac{de}{dt} = e \left(\frac{dx_d}{dt} - f(x) - b(x)\, u - d \right) \tag{3.3}$$

In order to make the control input, u effective enough to force the tracking error, e to converge to zero, the first derivative of the chosen *Lyapunov function* needs to

be *negative definite*. For the present case, the first time derivative of the *Lyapunov function* is chosen as,

$$\frac{dV}{dt} \;=\; -\,\lambda\, e^2 \tag{3.4}$$

where, λ *is a strictly positive* number. Comparing (3.3) and (3.4), the relationship can be written as,

$$\begin{aligned} -\,\lambda\, e \;&=\; \left(\frac{dx_d}{dt} \;-\; f(x) \;-\; b(x)\, u \;-\; d\right) \\ \Rightarrow\; u(t) \;&=\; b(x)^{-1}\left(\frac{dx_d}{dt} \;-\; f(x) \;+\; \lambda\, e \;-\; d\right) \end{aligned} \tag{3.5}$$

3.1.2 Estimation of the disturbance term 'd' to facilitate the control action

The control law shown in (3.5) can be divided into two parts as,

$$\begin{aligned} u(t) \;&=\; b(x)^{-1}\left(\frac{dx_d}{dt} \;-\; f(x) \;+\; \lambda\, e\right) \;-\; \left(b(x)^{-1}\, d\right) \\ u(t) \;&=\; u_1(t) \;+\; u_2(t) \end{aligned} \tag{3.6}$$

(3.6) shows that the term $u_2(t) \;=\; (-\,b(x)^{-1}\, d)$ is dependent on the grid voltage as well as other unpredictable periodic disturbance terms as shown in (2.3). In this case, part of d dependent on v_g can be obtained by sensing the micro-grid voltage, v_g using voltage sensor but the unpredictable part d_{up} (as shown in (2.3)) cannot be measured but can be estimated if the proper non-linear model of the inverter is known. Irrespective of all these, d cannot be estimated properly due to the phase lag associated with the voltage sensor (specially in the case of harmonic presence in v_g) and model inaccuracy of the inverter. Considering this, the estimated value of disturbance term is $\widehat{d}$ is different from actual value d; and the control input can

be re-written as,

$$u(t) \;=\; b(x)^{-1}\left(\frac{dx_d}{dt} \;-\; f(x) \;+\; \lambda\, e\right) \;-\; \left(b(x)^{-1}\,\widehat{d}\right) \tag{3.7}$$

Plugging in (3.7) in (3.3), the equation can be modified as,

$$\frac{dV}{dt} \;=\; -\,\lambda\, e^2 \;+\; e\,(\widehat{d} \;-\; d) \tag{3.8}$$

Thus the tracking error, e converges to a value e_{1b} if $\widehat{d} \neq d$ as,

$$\begin{aligned} \frac{dV}{dt} \;&=\; 0 \\ \Rightarrow\; e \;=\; e_{1b} \;&=\; \frac{\widehat{d} \;-\; d}{\lambda} \end{aligned} \tag{3.9}$$

Under this circumstance, if the disturbance $\widehat{d}$ is estimated using a SRC based on the residual tacking error, then at steady state, $\widehat{d} \;=\; d$ and current tracking becomes perfect with $e \;=\; 0$ (as per (3.9)). So, the second part of the control signal in (3.6) is denoted as $u_2(t) \;=\; u_{src}(t)$ and the first part of the control signal is called $u_1(t) \;=\; u_{lf}(t)$. For the micro-grid conditions, the inverter unpredictable non-linearities as well as grid voltage do not change very often, so the slow dynamics of the SRC control law $u_{src}(t)$ is dominated by the fast dynamics of feedback *Lyapunov function* based control law $u_{lf}(t)$. In this condition, if there is a sudden change in current reference i_c^*, the actual CCVSI current, i_c is observed to follow i_c^* almost in no time with *Lyapunov function* based controller unlike the slow condition in the case of SRC as shown later. The block diagram of the control system is shown in Figure 3.1.

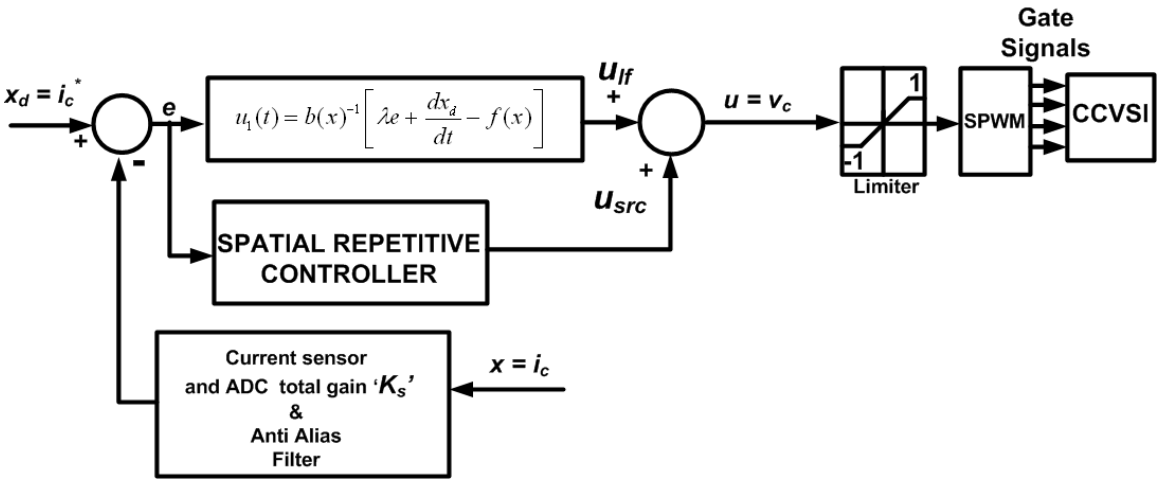

Figure 3.1: Schematic of the proposed control system.

3.1.3 Ensuring the stability of the plugged-in Spatial Repetitive Controller in parallel with the *Lyapunov Function* based controller

As mentioned before, the dynamics of the SRC is slower than the *Lyapunov function* based controller. In this case, it is required to judge the stability of the SRC when it is plugged-in in the presence of *Lyapunov Function* based controller as shown in Figure 3.1. Following the discussions in the previous paragraph, the control signal $u = v_c$ can be written as (using (2.1) and (3.6)),

$$u = v_c = \frac{L}{V_{dc}}\lambda\, e + \frac{L}{V_{dc}}\frac{di_c^*}{dt} + \frac{R}{V_{dc}}\, i_c + u_{src} \tag{3.10}$$

Using (3.10) in (2.1), the modified differential equation of the system is,

$$L\frac{di_c}{dt} + R\, i_c = L\,\lambda\, e + L\frac{di_c^*}{dt} + R\, i_c + V_{dc}\, u_{src} - v_g \tag{3.11}$$

Using the fact $e = i_c^* - i_c$, (3.11) can be re-written as,

$$\begin{aligned} L\frac{di_c}{dt} + L\,\lambda\, i_c &= V_{dc}\, u_{src} + \left[L\,\lambda\, i_c^* + L\frac{di_c^*}{dt} - v_g\right] \\ \Rightarrow L\frac{di_c}{dt} + R_{eff}\, i_c &= V_{dc}\, u_{src} + d_{mod} \end{aligned} \tag{3.12}$$

where, $d_{mod} = \left[L\,\lambda\,i_c^* + L\,\frac{di_c^*}{dt} - v_g \right]$. In this application, i_c^*, $\frac{di_c^*}{dt}$ and v_g are the periodic quantities with the period of the fundamental grid frequency. Hence, d_{mod} is a periodic disturbance seen by the SRC. If (3.12) is compared with (2.1), with *Lyapunov function* based controller, the *Spatial Repetitive* controller can be concluded to see the effective resistance $R_{eff} = L\,\lambda$ unlike the actual resistance of the choke coil R. The discussions on (3.12) clarify that, with *Lyapunov Function* based controller, the design of the SRC is to be done using the modified transfer function of the plant $G_{mod}(s) = \frac{1}{s\,L + R_{eff}}$.

3.1.4 Effect of parameter uncertainty on the convergence

It is considered that the disturbance term 'd' in (3.5) is estimated. However, functions $f(x)$ and $b(x)$ are dependent on system parameters such as inductance, L and resistance, R. The parameters L and R of the chock coil can not be determined accurately. As there is uncertainty in the estimation of the system parameters, then the estimated value of the system parameters are $\widehat{f}(x)$ and $\widehat{b}(x)$ instead of actual $f(x)$ and $b(x)$ respectively. Under such circumstances, the control input shown in (3.5) is modified as,

$$u(t) = \widehat{b}(x)^{-1} \left(\frac{dx_d}{dt} - \widehat{f}(x) + \lambda\,e - d \right) \tag{3.13}$$

Plugging in (3.13) in (3.3), the resulting equation can be found as,

$$\begin{aligned} \frac{dV}{dt} &= -\,b\,\widehat{b}^{-1}\,\lambda\,e^2 - e\left[(f - \widehat{f}\,b\,\widehat{b}^{-1}) + d\,(1 - b\widehat{b}^{-1}) - \frac{dx_d}{dt}\,(1 - b\widehat{b}^{-1}) \right] \\ \Rightarrow \frac{dV}{dt} &= -\,b\,\widehat{b}^{-1}\,\lambda\,e^2 - e\,D(.) \end{aligned} \tag{3.14}$$

where $D(.) = \left[(f - \widehat{f}\, b\, \widehat{b}^{-1}) + d\,(1 - b\widehat{b}^{-1}) - \frac{dx_d}{dt}\,(1 - b\widehat{b}^{-1})\right]$

(3.14) depicts that, to make $\frac{dV}{dt}$ *negative definite* the condition can be written as,

$$|b\,\widehat{b}^{-1}\lambda\, e^2| > |e\, D(.)| \tag{3.15}$$

(3.15) shows that, the quantity λ needs to be big enough to satisfy (3.15) within the appreciable range. If it is designed that the absolute value of error converges to error bound e_b, which is closer to 0, the value of λ needs to follow the condition,

$$\lambda > \frac{|D(.)|_{max}}{|b\widehat{b}^{-1}|_{min}\, e_b} \tag{3.16}$$

3.1.5 Design of the Lyapunov Function based control law, $u_{lf}(t)$

The parameters used for testing the proposed control system are: the DC link voltage $V_{dc} = 100V$, the maximum value of grid voltage $|V_g|_{max} = 50\times\sqrt{2} = 70.7V$, choke coil inductance $L = 6\,mH$, resistance $R = 1\Omega$, inductance and resistance uncertainties are considered to be 10% in each case. For the simplicity of design, the peak value of the tracked current is considered to be $|i_c|_{peak} = 6\,A$, and the maximum rate of change present in the reference current, $\frac{di_c^*}{dt}$ is considered to be the product of peak current, $|i_c|_{peak}$ with maximum frequency component present in the reference current, ω_{es}. In this case it is considered that the load current contains harmonic up to 200^{th} order, i.e. $\omega_{es} = 1\,kHz$ is assumed. This condition is further ensured by putting an anti-alias filter of cut-off frequency around $1\,kHz$ in the feedback path. Considering these conditions, the maximum value of $D(.)$

(shown in (3.14)) can be calculated as,

$$\begin{aligned} |D(.)|_{max} &= \left(\frac{\widehat{R}}{\widehat{L}} - \frac{R}{L}\frac{\widehat{L}}{L}\right)|i_c|_{peak} + \frac{|V_g|_{max}}{L}\left(1 - \frac{\widehat{L}}{L}\right) + (|i_c|_{peak}\,\omega_{es})\left(1 - \frac{\widehat{L}}{L}\right) \\ &= 1214 \end{aligned} \tag{3.17}$$

Considering absolute error bound $e_b = 0.01$ and using (3.16), the controller parameter is found to be as,

$$\lambda > \frac{1214}{0.5 \times 0.01} = 242,800 \tag{3.18}$$

3.1.6 Design of the Spatial Repetitive Controller based disturbance estimation control law, $u_{src}(t)$

As discussed before in (3.12), that the effective plant transfer function is changed as seen by the SRC. The overall block diagram of the system in the grid fundamental phase domain with both the controllers in operation as shown in Figure 3.2. z_θ

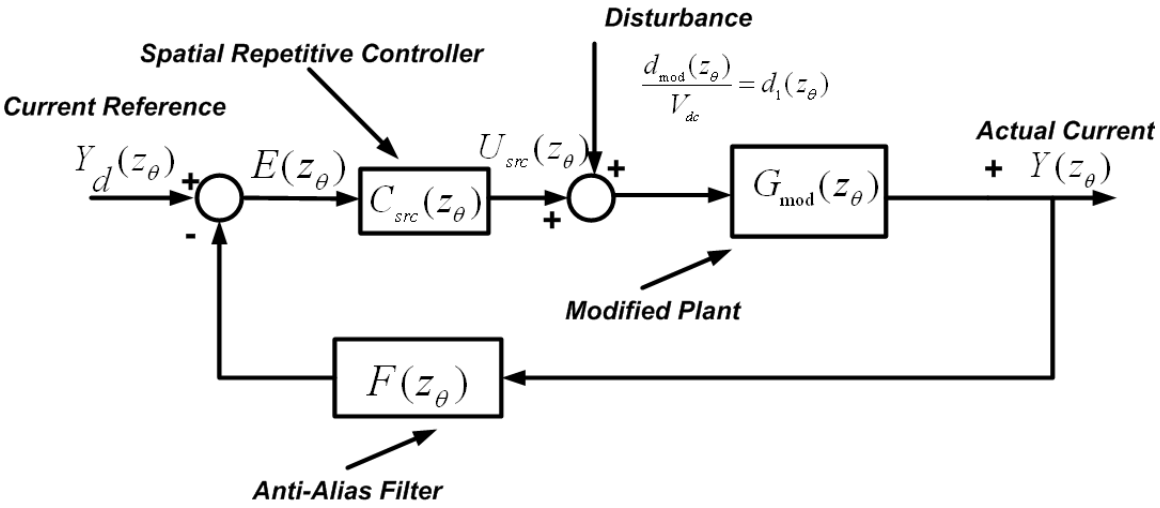

Figure 3.2: Schematics control system seen by the *Spatial Repetitive Controller*.

is defined to be the complex frequency of the system in position sample domain . Further in the analysis, any dynamic complex quantity '$X(z_\theta)$' is expressed as

'X'. The output equation of the control system can be written as,

$$Y \;=\; \frac{C_{src}\,G}{1 \;+\; C_{src}\,G_{mod}\,F}\,Y_d \;+\; \frac{G_{mod}}{1 \;+\; C_{src}\,G_{mod}\,F}\,d_1 \tag{3.19}$$

The error equation (using (3.19)) can be written as,

$$\begin{aligned} E \;&=\; Y_d \;-\; Y \\ &=\; \frac{Y_d\,(1 \;+\; C_{src}\,G_{mod}\,F \;-\, C_{src}\,G_{mod}) \;-\; G_{mod}\,d_1}{1 \;+\; C_{src}\,G_{mod}\,F} \end{aligned} \tag{3.20}$$

As the analysis repeated in [59]-[62] that, the stability of the overall repetitive control system can be ensured if the following condition is satisfied,

$$|1 \;+\; C_{src}(z_\theta)\,C_{eff}(z_\theta)| \;\neq\; 0 \tag{3.21}$$

where $C_{eff}(z_\theta) \;=\; G_{mod}(z_\theta)\,F(z_\theta)$. To design the SRC for the control, the design method is followed as mentioned in Chapter 5. The time domain dynamic equation of the modified CCVSI system is shown in (3.12). The time derivative of any variable, x, can be represented in terms of space derivative, the space variable θ is the phase position;

$$\frac{dx}{dt} = \frac{dx}{d\theta} \times \frac{d\theta}{dt} \tag{3.22}$$

As, $\frac{d\theta}{dt} = \omega$, electrical angular fundamental frequency (in rad/sec) of the micro-grid and $dx = x(\theta_{k+1}) - x(\theta_k)$, where $x(\theta_k)$ is the variable x at k^{th} sample position, θ_k. Additionally, $d\theta = \Delta\theta = \theta_{k+1} - \theta_k$ is the step size of position sampling. So, first time derivative of variable x can be rewritten, using a new variable, $m \;=\; \frac{\omega}{\Delta\theta}$ as:

$$\frac{dx}{dt} \;=\; \frac{x(\theta_{k+1}) - x(\theta_k)}{\Delta\theta} \times \omega = m\;[x(\theta_{k+1}) - x(\theta_k)] \tag{3.23}$$

In the actual implementation, the total 2π radian of fundamental grid phase is divided in N position steps resulting $\Delta\theta \;=\; \frac{2\,\pi}{N}$.

In *grid phase sample domain*, the spatial repetitive control law can be written as,

$$u_{src}(i, \theta_k) = u_{src}(i-1, \theta_k) \;+\; K_{src}\,e(i-1, \theta_{k+N_1}) \tag{3.24}$$

Where, $u_{src}(i, \theta_k)$ is the control output of SRC at the k^{th} position sample in the i^{th} iteration cycle, $e(i-1, \theta_{k+N_1})$ is the error at $(k+N_1)^{th}$ position sample in $(i-1)^{th}$ iteration cycle, K_{src} is the positive gain of repetitive controller and N_1 ($N_1 < N$) is the number of advancement samples given to take care of the phase delay in the plant and feedback filter path. One cycle consists of N samples in fundamental grid phase position. The modified plant transfer function in grid fundamental phase sampling domain is represented as,

$$G_{mod}(z_\theta) \;=\; \frac{c_p}{z_\theta \;-\; a_p} \tag{3.25}$$

where, $a_p \;=\; 1 \;-\; \frac{\lambda}{m}$, $c_p \;=\; \frac{K_s\, V_{dc}}{m\, L}$ and $K_s \;=\; 0.033$ considering the gain of current sensor (0.33) and gain of ADC (0.1) in cascaded path (as shown in Figure 3.1).

The anti-alias (second order butterworth) filter cut-off frequency is considered to be $f_c \;=\; 1000\, Hz$ and the quality factor $Q \;=\; \frac{\sqrt{2}}{\sqrt{3}}$ is considered.

Any harmonic frequency (ω_1 in rad/sec) appearing in the micro-grid system can be represented as $\omega_1 = p\omega$, where ω is the fundamental micro-grid frequency in rad/sec and p is an integer. Any arbitrary frequency ω_1 in steady state, $z_\theta \;=\; e^{j\, p\, \Delta\theta}$ and this results in $z_\theta^N \;=\; e^{j\; p\, 2\pi} \;=\; 1$ for p as integers. At steady state, $C_{eff}\,(z_\theta) \;=\; C_{eff}\left(e^{j\, p\, \Delta\theta}\right) \;=\; A_{eff}\,(p\,\Delta\theta)\, e^{j\,\phi_c(p\,\Delta\theta)}$ with $A_{eff}\,(p\,\Delta\theta)$ being its magnitude and $\phi_c\,(p\,\Delta\theta)$ being its phase. Considering the phase advancement samples in the SRC, N_1, another variable α is derived as,

$$\alpha\,(p\,\Delta\theta) \;=\; p\,N_1 \times \Delta\theta \;+\; \phi_c\,(p\,\Delta\theta) \tag{3.26}$$

Further analysis on (3.21)unfolds that, the stability condition boils down to,

$$\begin{aligned} K_{src} \quad &< \quad \frac{2\; min\,[\cos\alpha]}{max\,[A_{eff}] \;+\; \delta} \\ |\alpha| \quad &= \quad |p\,N_1 \frac{2\,\pi}{N} \;+\; \phi_c| \;<\; \frac{\pi}{2} \end{aligned} \tag{3.27}$$

where δ is the parameter uncertainty of the system considered. To ensure stability, (3.27) are to be satisfied for the entire range of frequencies of interest. Now, if the SRC is opened and it is tried to find the phase delay associated with this control action activation, the phase delay path looks like the picture shown in Figure 3.3. It is also depicted in Figure 3.3 that, the predefined angle α can also be defined

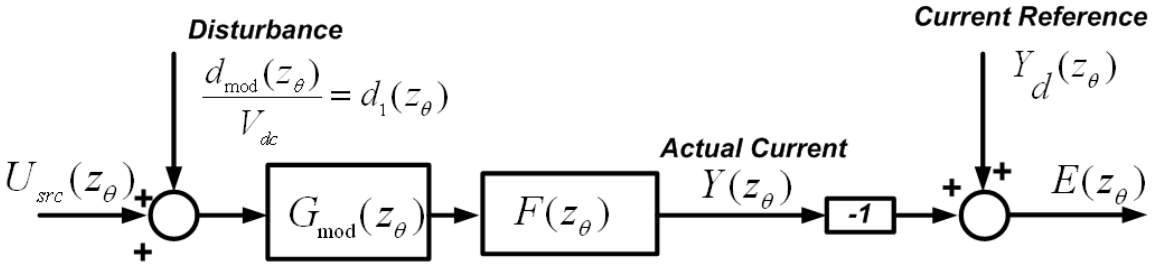

Figure 3.3: The block diagram showing the phase delay provided by the modified plant and anti-alias filter signal transmission.

as the phase delay provided by the modified plant and the anti-alias filter signal transmission and the phase lead provided by the *SRC*. The phase lead of repetitive controller ϕ_l is designed to nullify the signal transmission delay due to plant and analog filter ϕ_c to enhance the tracking performance as,

$$\begin{aligned} \alpha &= \phi_l + \phi_c\,(p\,\Delta\theta) > 0 \\ \Rightarrow \alpha &= p\,N_1\frac{2\,\pi}{N} + \phi_c > 0 \end{aligned} \tag{3.28}$$

The gain of the SRC is found to be $k_{srcmax} = 60$ (considering frequency up to $1\,kHz$ due to the presence of anti-alias filter), total sample positions in full 360^0 of fundamental grid phase is $N = 200$, the sample advancement of the controller is taken as $N_1 = 4$ with fundamental grid frequency $f_f = 50\,Hz$. The gain as well as phase plot of C_{eff} for different frequencies (upto cut-off frequency of the anti-alias filter) are shown in Figure 3.4. The parameter uncertainty of the system, δ is taken as 10% of the estimated value. The angle, α is also plotted for

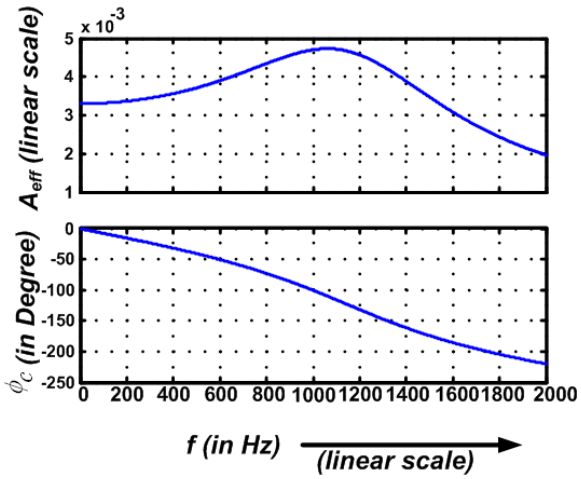

Figure 3.4: The amplitude plot (A_{eff}) and phase plot (ϕ_c) with different frequency (f) for $C_{eff}(z_\theta)$ with fundamental micro-grid frequency $f_f = 50\ Hz$ with *Lyapunov Function* based controller gain $\lambda\frac{L}{V_{dc}} = 10$.

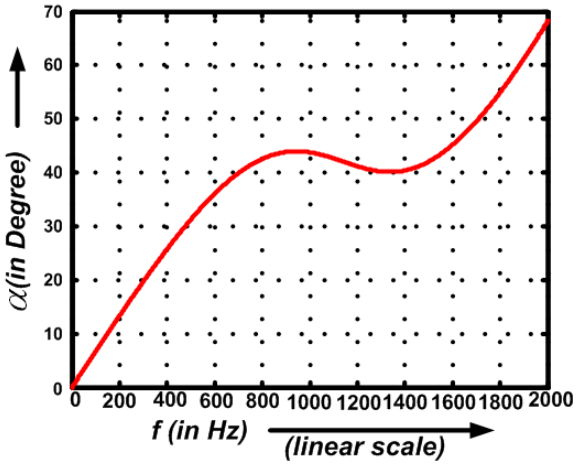

Figure 3.5: Plot of phase angle, α for different frequencies, f with phase angle compensating term, $N_1 = 4$ of the *Spatial Repetitive Controller* with fundamental micro-grid frequency $f_f = 50\,Hz$ with *Lyapunov Function* based controller gain $\lambda\frac{L}{V_{dc}} = 10$.

different frequencies. Conclusions can be drawn from Figures 3.4 and 3.5 that, the designed *SRC* is stable enough to operate in parallel with the *Lyapunov function* based controller.

3.1.7 Implementation of the proposed control system

The control system shown in Figure 3.1 is implemented in DS1104 dSPACE controller board with sampling frequency $f_{sample} = 10\,kHz$. The SPWM switching frequency is taken as $f_s = 10\,kHz$. The first time derivative term in u_{fb} is replaced by its backward approximation rule. Considering (2.1), (2.2) and (3.6), the *Lyapunov Function* based control law for PWM(control input) at k^{th} sampling instant

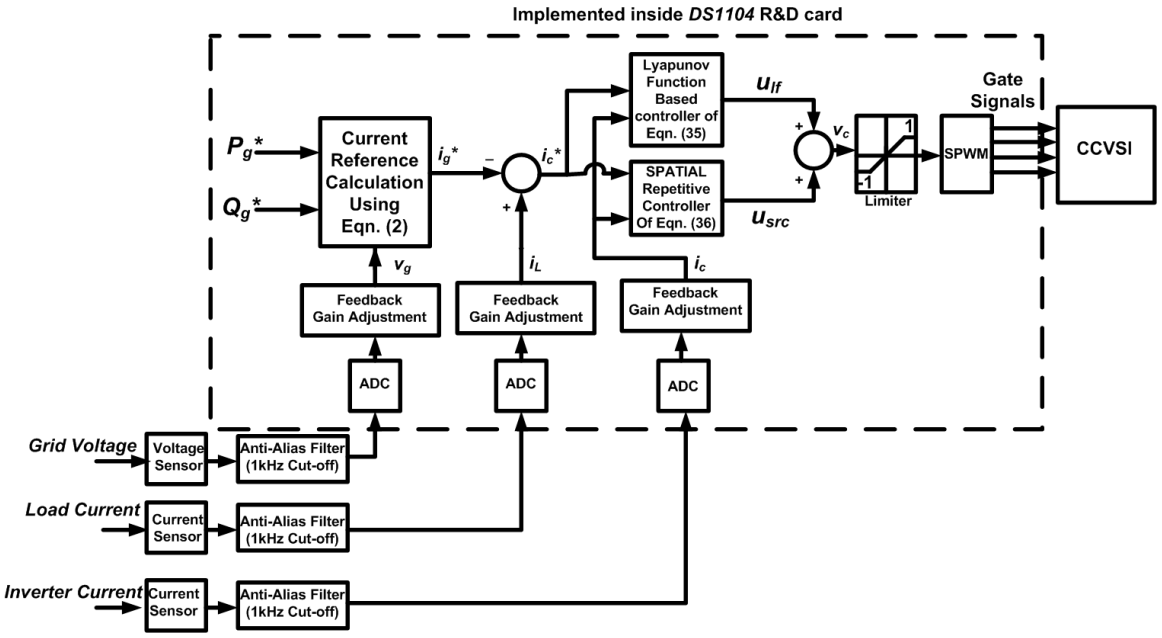

Figure 3.6: Details of the implementation method of the proposed control strategy.

can be written as,

$$\begin{aligned} u_{lf}(k) &= \frac{L}{V_{dc}}\left[\frac{[i_c^*(k) - i_c^*(k-1)]}{T_s} + \frac{R}{L} i_c^*(k)\right] \\ &+ \frac{L}{V_{dc}}\left[\lambda\left(i_c^*(k) - i_c(k)\right)\right] \end{aligned} \tag{3.29}$$

where, $T_s = \frac{1}{f_{sample}}$ is the sampling time of the control system. The block diagram of the implemented reference current calculator followed by the current controller is shown in Figure 3.1. It is also shown in Figure 3.1 that, the output of the controller is clamped by a saturation block, in actual experiment. This always ensures linear range of operation of SPWM process.

The *SRC* control law is implemented as the same form as discussed in (3.24). The detailed control system implementation is shown in Figure 3.6. The rapid prototyping DSP dSPACE ds1104 card makes it possible to implement the proposed control strategy efficiently.

3.2 Experimental Results

3.2.1 Steady-state experimental waveforms

The proposed controller is validated by extensive testing on a developed prototype. The prototype is made out of a micro-grid voltage, $V_g = 50\,V$ rms and the DC link voltage level of the *CCVSI* is taken to be $V_{dc} = 100\,V$. The load is taken to be a single-phase rectifier terminated to a resistive, capacitive assembly. In this control topology, the single parallel inverter is not only controlling the active and reactive power flow from the grid but also compensating for the non-linear current drawn by the load from the grid terminal. So, inverter current consists of both sinusoidal power current and the inverse non-linear load current. The non-linear load current has substantial $\frac{di}{dt}$ due to the capacitor termination at the DC side of the rectifier load. To take care of the substantial voltage drop in the chock coil of the CCVSI, the DC link voltage is taken as more than the required value. This higher DC link voltage also ensures better transient of the proposed current controller because of inverter PWM phenomena. The details of the power circuit used in this work is shown in Figure 3.7. The parameters of the power circuit are also given in Table 3.1. The load current i_L is seen to be highly non-sinusoidal as shown in the experimental results provided in Figures 3.8 - 3.13. At the specified grid voltage level ($50\,V$ rms), the load draws active power, $P_L = 35\,W$ with unknown reactive as well as harmonic power.

At first, the active and reactive power commands to the grid are given to be $P_g = 0\,W$ and $Q_g = 0\,Vars$. This ensures that, the grid current, i_g is zero and the load current is contributed by the CCVSI current, i_c. The experimental results for

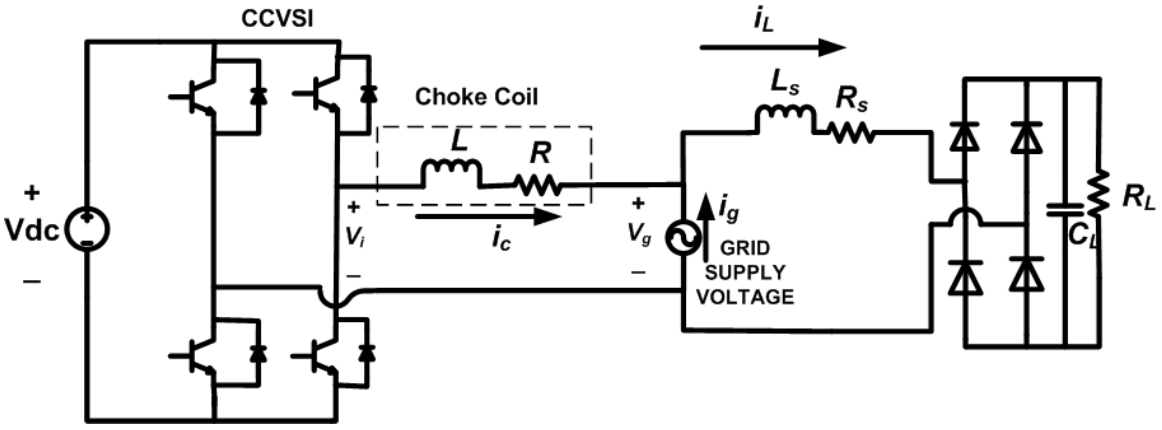

Figure 3.7: Details of the power circuit used in the experiment.

Table 3.1: Parameters of the experimental power circuit

Parameter	**Value**
DC link voltage, V_{dc}	$100\,V$
RMS of nominal grid voltage, v_g	$50\,V$
CCVSI choke inductance, L	$6\,mH$
CCVSI choke resistance, R	$1\,\Omega$
Rectifier link inductance, L_s	$3\,mH$
Rectifier link resistance, R_s	$0.3\,\Omega$
Rectifier DC side capacitor, C_L	$2200\,\mu F$
Rectifier DC side resistance, R_L	$140\,\Omega$

this condition are shown in Figures 3.8 and 3.9. Both the figures depicts that, as $P_g = 0\,W$ and $Q_g = 0\,Vars$, the CCVSI current $i_c = i_L$ as expected from (2.9) and (2.10). Figure 3.9 also verifies that the grid current $i_g = 0\,A$ as ensured by the *p-q* calculator block. Only some small EMI flickering are seen around i_g waveform due to the interaction of the inverter and AC power supply used as grid. The DC link current meter is shown to draw $0.35\,A$ under this operating condition.

The control system is further tested by changing the grid power command as shown in Figures 3.10 and 3.11. It is shown in Figure 3.10 that, when the grid power command $P_g = 30\,W$ and $Q_g = 0\,Var$ are given, the proposed controller controls the CCVSI current i_c in such a way (according to (2.9) and (2.10)) that, the grid current i_g becomes sinusoidal with peak $0.85\,A$ and rms $0.6\,A$. The grid current i_g is free of harmonics of the load current, i_L. Figure 3.11 shows that,

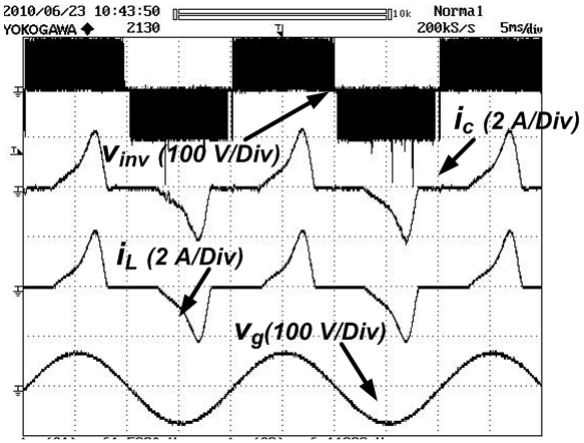

Figure 3.8: Experimental results of inverter output voltage v_{inv}, CCVSI current i_c, load current i_L and the grid voltage v_g at grid power command $P_g = 0\,W$ and $Q_g = 0\,Var$.

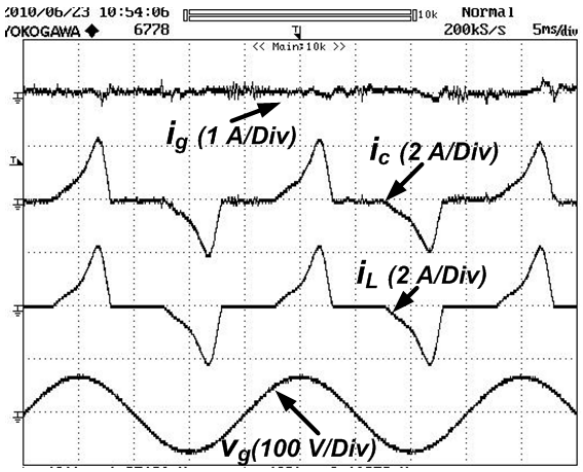

Figure 3.9: Experimental results of grid current i_g, CCVSI current i_c, load current i_L and the grid voltage v_g at grid power command $P_g = 0\,W$ and $Q_g = 0\,Var$.

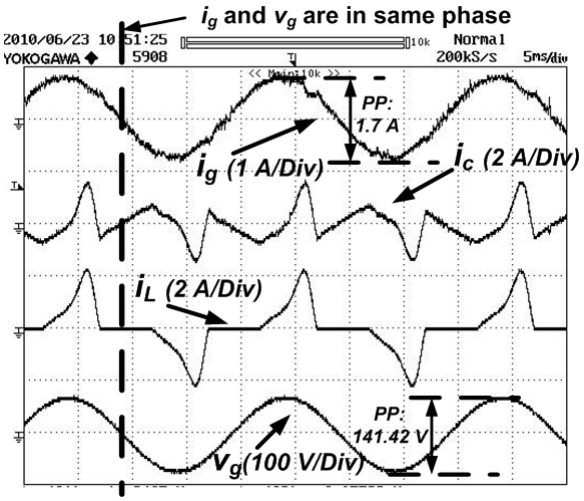

Figure 3.10: Experimental results of grid current i_g, CCVSI current i_c, load current i_L and the grid voltage v_g at grid power command $P_g = 30\,W$ and $Q_g = 0\,Var$.

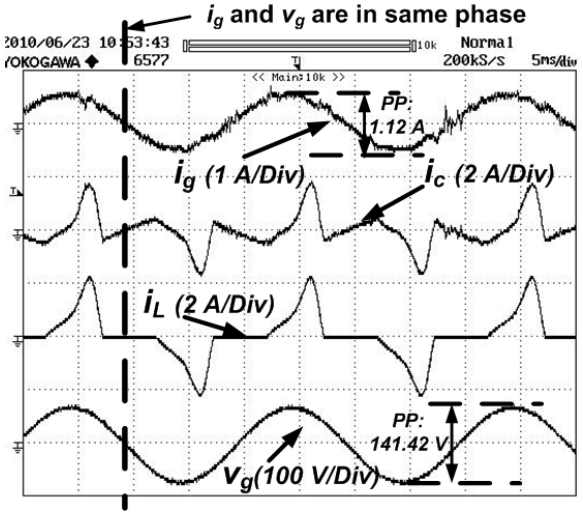

Figure 3.11: Experimental results of grid current i_g, CCVSI current i_c, load current i_L and the grid voltage v_g at grid power command $P_g = 20\,W$ and $Q_g = 0\,Var$.

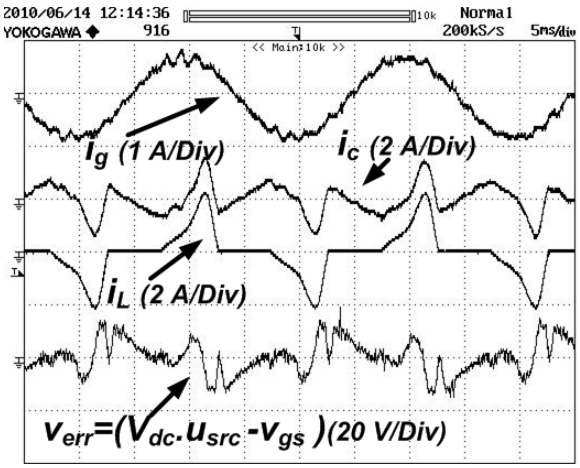

Figure 3.12: Experimental results of grid current i_g, CCVSI current i_c, load current i_L and voltage error v_{err} at grid power command $P_g = 30\,W$ and $Q_g = 0\,Var$.

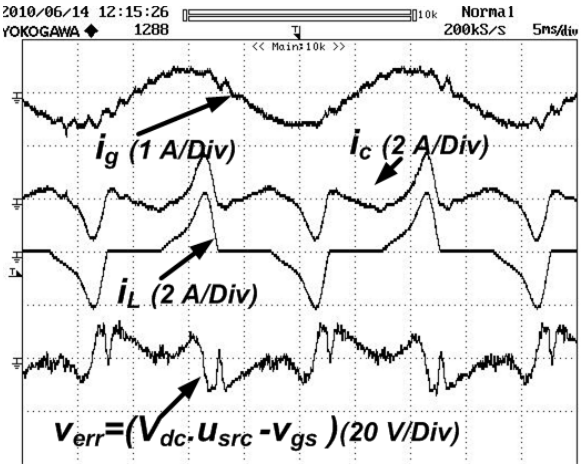

Figure 3.13: Experimental results of grid current i_g, CCVSI current i_c, load current i_L and voltage error v_{err} at grid power command $P_g = 20\,W$ and $Q_g = 0\,Var$.

when grid power command $P_g = 20\,W$ and $Q_g = 0$ given, the CCVSI current i_c is adjusted automatically by the proposed controller making the grid current i_g in phase with grid voltage v_g with magnitude $0.56\,A$ and rms value $0.4\,A$ ensuring proper grid power flow.

As discussed before, the SRC is used to sense the disturbance component control signal u_{src} (as shown in Figure 3.1). It is mentioned before that this grid voltage v_g can be sensed using a voltage sensor. As mentioned before, during the experiment one variable is defined called voltage error $v_{err} = (V_{dc} \times u_{src}) - v_{gs}$, where v_{gs} is the sensed quantity of the grid voltage. This voltage error quantity v_{err} is also investigated for different grid power command. In Figure 3.12, it is depicted that during the grid power command $P_g = 30\,W$ and $Q_g = 0\,Var$, the quantity v_{err} has significant distortion in the signal. The same error signal v_{err} can also be seen for grid power command $P_g = 20\,W$ and $Q_g = 0\,Var$ in Figure 3.13. Figures 3.12 and 3.13 make it clear that the disturbance term '$b(x)^{-1}\,d$' shown in (3.5)

and (3.6) cannot be calculated by sensing the grid voltage v_g using voltage sensors (otherwise v_{err} would be flat zero in Figures 3.12 and 3.13). This indicates the need of estimation of '$b(x)^{-1}\, d$' term by putting the SRC (the estimated voltage is indicated as u_{src} in (3.10)) in parallel with the *Lyapunov Function* based controller as shown in Figure 3.1.

3.2.2 Experimental waveforms to show the transients associated with Lyapunov Function based controller

The transient effect of suddenly changing the grid power command is shown in Figures 3.14 and 3.15.

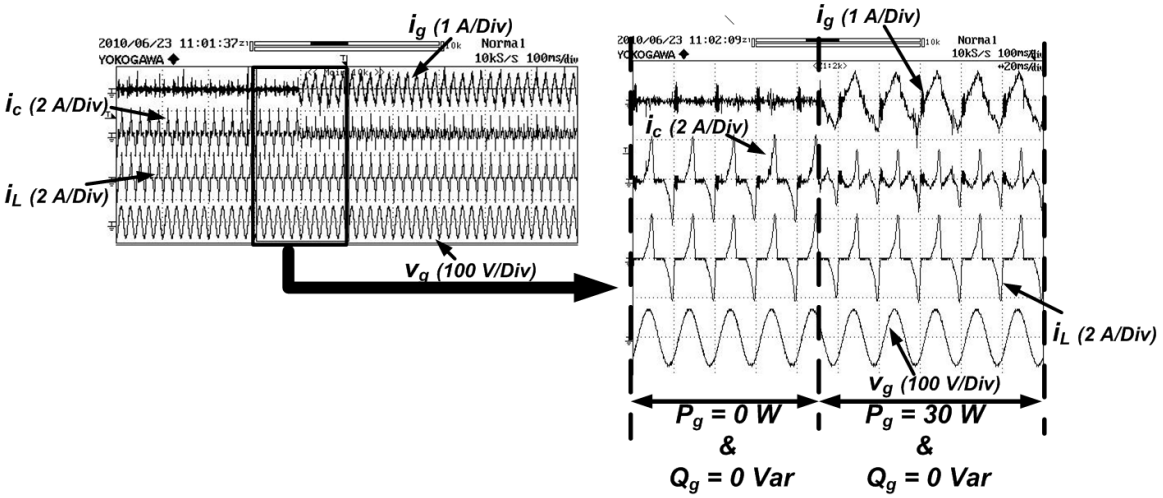

Figure 3.14: Experimental results of grid current i_g, CCVSI current i_c, load current i_L and the grid voltage v_g when the grid power command is suddenly changed from $P_g = 0\,W$ and $Q_g = 0\,Vars$ to $P_g = 30\,W$ and $Q_g = 0\,Vars$:(left fig) time scale: 100ms/div, (right fig) time scale: 20ms/div.

Figure 3.14 reflects the fact that, when $P_g = 0\,W$ and $Q_g = 0\,Vars$, the grid current is zero. But when suddenly the grid power command is changed to $P_g = 30\,W$ and $Q_g = 0\,Vars$, the grid current in almost instantaneously reached

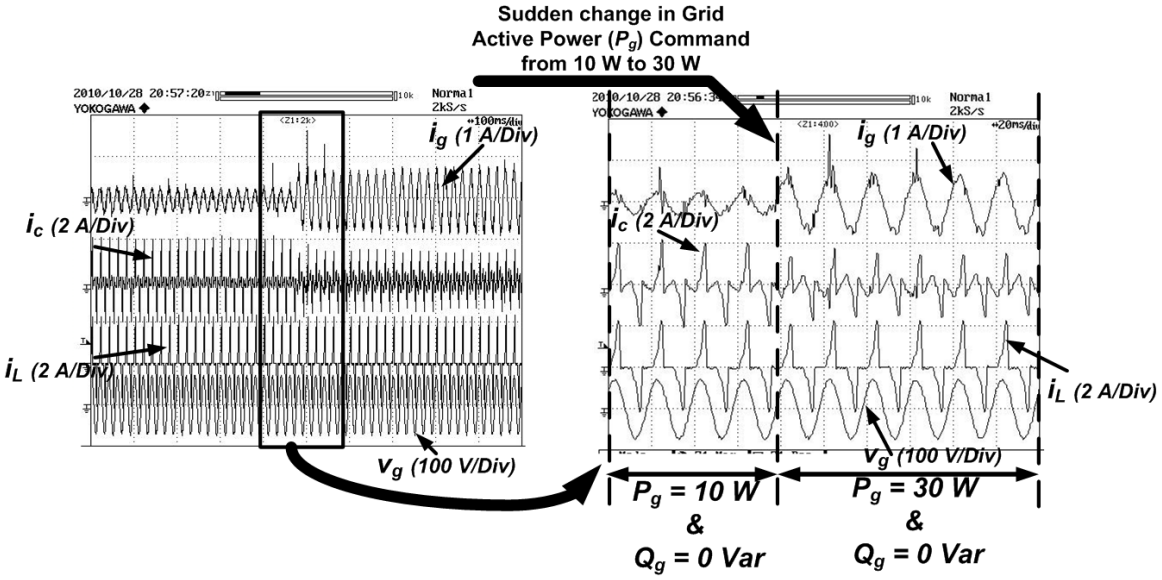

Figure 3.15: Experimental results of grid current i_g, CCVSI current i_c, load current i_L and the grid voltage v_g when the grid power command is suddenly changed from $P_g = 10\,W$ and $Q_g = 0\,Vars$ to $P_g = 30\,W$ and $Q_g = 0\,Vars$:(left fig) time scale: 100ms/div, (right fig) time scale: 20ms/div.

the peak current level $0.84\,A$ at grid voltage $v_g = 50\,V$ rms. Figure 3.15 shows the dynamics of sudden change of grid power command from $P_g = 10\,W$ and $Q_g = 0\,Vars$ to $P_g = 30\,W$ and $Q_g = 0\,Vars$. It should be clear from Figure 3.15 that when grid power command is at $P_g = 10\,W$ and $Q_g = 0\,Vars$, the grid current (i_g) peak is at $0.3A$ at grid voltage (v_g) 50 level. However when the grid power command is changed to $P_g = 30\,W$ and $Q_g = 0\,Vars$, the grid current (i_g peak almost immediately jumped to $0.84A$. This transient time to make the grid power change over possible is taken care of by the fast dynamics of the *Lyapunov Function* based controller.

3.2.3 Experimental waveforms to show the transients associated with plugged-in Spatial Repetitive controller

The dynamics associated with the sudden changes in grid voltages (v_g) is also studied. The experimental results associated with such a dynamic phenomena are shown in Figure 3.16. The active and reactive power flow from the grid are kept fixed at $P_g = 10\,W$ and $Q_g = 0\,Vars$ and the grid voltage is suddenly decreased from $v_g = 40\,Vrms$ to $v_g = 30\,Vrms$ as shown in the zoomed transient waveform in Figure 3.16(a). Figure 3.16(d) clarifies that, during the condition when grid voltage (v_g) is $40\,Vrms$, the grid current (i_g) has reached a peak value of $0.35\,A$ and in phase with the grid voltage , v_g to ensure active and reactive grid power flow of $P_g = 10W$ and $Q_g = 0Vars$ respectively. Figure 3.16(e) depicts that when grid voltage, v_g is reduced to $30\,Vrms$, the grid current, i_g is increased to $0.47\,A$ peak (from $0.35\,A$ peak) to ensure $P_g = 10\,W$ and $Q_g = 0\,Vars$. However, the transient waveforms to show the grid voltage change over phenomena is shown in Figures 3.16(a), (b) and (c). As discussed before with the help of (3.12) that change in grid voltage is taken care of by plugged-in *SRC* based disturbance estimation block resulting in noticeable amount of transient time (about 3 sec) to reach steady state. Whenever there is a change is the grid voltage, there is an error in current tracking. The *SRC* based grid voltage estimator, u_{src} is re-tuned based on the new value of d_{mod} while looking at the current error as can be explained using (3.12).

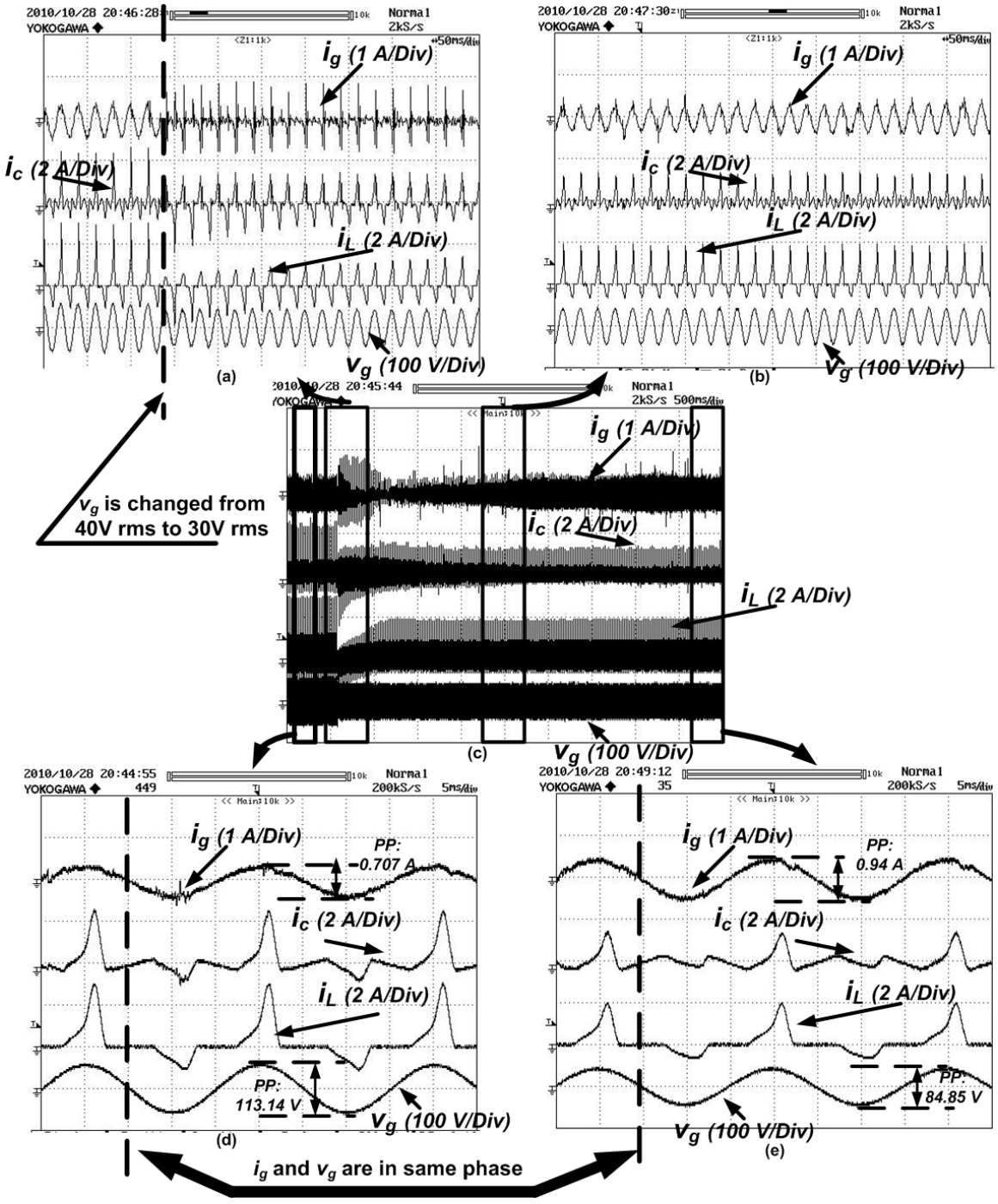

Figure 3.16: Experimental results of grid current i_g, CCVSI current i_c, load current i_L and the grid voltage v_g when the grid power command is kept fixed at $P_g = 10W$ and $Q_g = 0\,Vars$ and grid voltage v_g is changed from $40\,V$ to $30\,V$: (a)-(b) time scale: 50ms/div, (c) time scale: 500ms/div, (d)-(e) time scale: 5ms/div.

3.3 Summary

A new current control strategy for the parallel connected inverter connected to micro-grid is proposed. The current reference calculator uses the 'p-q' theory in place of the conventional one step ahead integrator block [127] making the reference current estimation faster. The proposed Lyapunov function based non-linear controller provides superior performance over conventional controllers such as rotating frame PI controller. The control law is implemented in digital domain over the other established rotating frame controllers [32]. The experimental results show that the proposed controller along with the 'P-Q' current calculator is capable of controlling the active and reactive power flow from the micro-grid in a de-coupled manner along with controlling the THD of the grid current. This power control property facilitates the efficient usage of renewable energy in a micro-grid.

Chapter 4

Voltage regulation and active power flow control of single-phase series connected renewable energy source based inverter

The traditional parallel inverters are very popular to interface renewable energy source to the grid. The topology is quite popular in the case of both residential as well as industrial applications. Due to unusual loading of the power system network during peak hours in the weak grid system in developing countries like PR of China or India and also due to unusual active power unbalance in the micro-grid, the common AC bus voltage undergoes sag, swell or other types of problems. Even because of the presence of the non-linear load, the common AC bus voltage also undergoes harmonic distortion. The domesticated electronic loads when connected to these distorted and weak grid system, the loads malfunction and some may fail to operate. Sometime a sudden frequency drift is also visible in the grid voltage as a result of active power unbalance in the power system network. So, the connected power converters also need to be auto-synchronized and operate in a proper way

to ensure same performance at the drifted grid frequency as well.

To solve all these problems, a series connected inverter topology is investigated in this Chapter. The renewable energy source based inverter is connected in series with the common AC bus and the load. The control strategy of the inverter is designed in such a way that, the inverter operation ensures load voltage regulation as well as utilization of the renewable energy to reduce the grid power consumption under all sorts of grid common AC bus voltage disturbances. The control strategy of the proposed inverter topology is analyzed in details and the feasibility study of the proposed hardware is also carried out.

4.1 Description of the inverter configuration and its control strategy

4.1.1 Description of the power circuit of the series inverter

The structure of the multi-bus micro-grid considered in this work is discussed in details in Chapter 1 and [9]-[24]. The power circuit is shown in Figure 4.1 and the inverter is connected in series with the load. The control strategy of the series inverter is designed to mitigate the voltage related problems at the *local bus* of the micro-grid mainly during *islanded* mode. The same inverter can also be used in *grid-connected* mode to enjoy grid power consumption savings and load voltage regulation, if the utility-grid also fluctuates (as normally happens in the utility grids of P.R. of China or India). The inverter block typically consists of a Sine PWM inverter followed by a high frequency transformer and a power L-C filter to eliminate the high frequency PWM signal. The high-frequency transformer is used after the

PWM inverter to boost the inverter voltage and to provide electrical isolation between renewable energy source side and the micro-grid side. However to validate the series inverter operation in laboratory environment both the requirements are optional. So, for the present scope of the report, transformer is not used to avoid the complexity in the inverter power circuit.

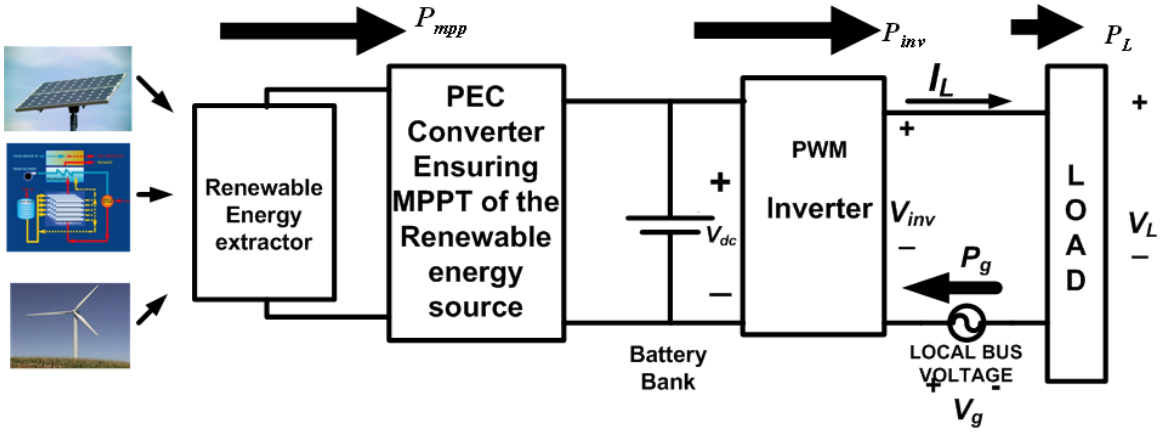

Figure 4.1: Schematic diagram of the series inverter assembly.

4.1.2 Control strategy of the series inverter under common operating conditions

For the sake of analysis of the control strategy of the inverter, it is assumed that, the renewable energy extractor is assumed to be operating steadily. So, the DC link voltage, V_{dc} is at the steady state level and the inverter output power, P_{inv} is maintained at a steady-state value. Thus, the DC link (i.e. renewable energy extractor along with *PEC* converter together with the battery) can be modeled as a DC power supply. The load is assumed to be a linear *R-L* load. The *local bus* voltage, where the targeted load and the renewable source based inverter is connected, is defined as grid voltage, v_g. The power circuit of the series inverter is shown in Figure 4.2(a). The inverter is essentially a Sine PWM (SPWM) voltage

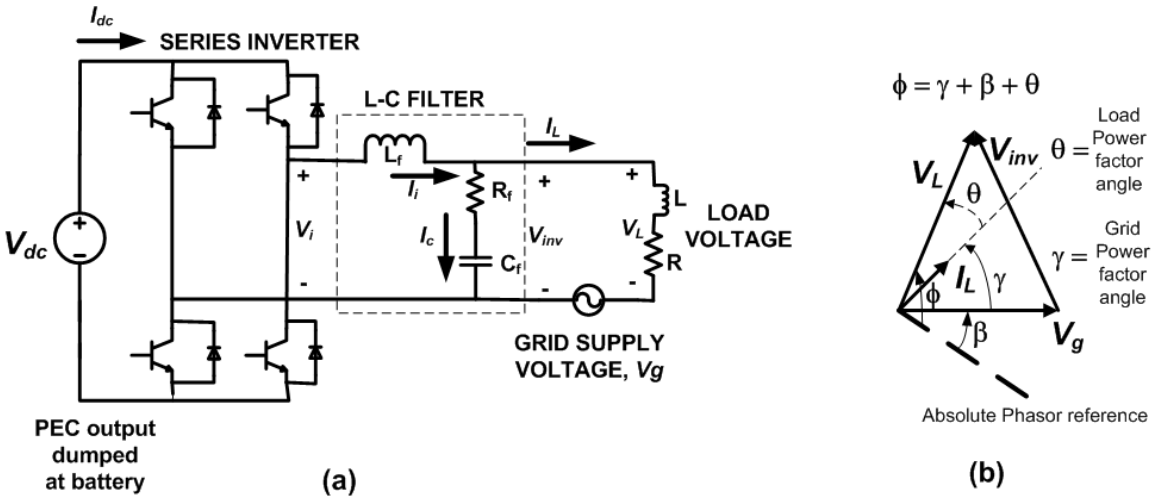

Figure 4.2: (a) Simplified Power Circuit of the series inverter and (b)Proposed control phasor diagram of the series inverter.

source inverter. The raw output voltage of the inverter contains not only fundamental power frequency voltage component but also the switching frequency based harmonic voltage components. The L-C filter as shown in Figure 4.2(a), is connected to filter the switching frequency components of the voltage harmonics, so that the inverter output voltage, v_{inv}, only contains fundamental power frequency component. The filter resistance R_f, placed in series with the filter capacitor C_f, to limit the inrush current from the inverter. It can also be noted that the inverter output is connected in series with the grid and also to the load. Both the inverter as well as the grid act as voltage sources to supply the load. The inverter operates to transfer renewable power to the load and the rest of the load power comes from grid along with the voltage regulation of the load. In the proposed control strategy in this Chapter, the inverter voltage, v_{inv}, is added vectorially in series with the grid voltage, v_g, to form the load voltage, v_L, to facilitate both the load voltage regulation as well as the inverter output power flow control unlike the condition proposed in [68] to regulate only the load voltage. The control phasor diagram of the series inverter is shown in Figure 4.2(b).

At steady state, different phasors are marked in the phasor diagram shown in Figure 4.2(b). The power needed from the grid, P_g can be calculated as,

$$P_g = P_L - P_{inv} \tag{4.1}$$

where, total load power, $P_L = |V_L| \times |I_L| \times \cos(\theta)$, where θ is the power factor angle of the load. The load current, $|I_L| = \frac{|V_L|}{|Z|}$ (where $|Z|$ is the impedance of the load at line frequency) at steady state with voltage regulated at nominal rms value $|V_L|$. Thus, (4.1) can be rewritten in the following form:

$$P_g = \frac{|V_L|^2}{|Z|}\cos(\theta) - P_{inv} \tag{4.2}$$

From grid point of view, the active power, P_g drawn from grid can be written as,

$$\begin{aligned} P_g &= |V_g| \times |I_L| \times \cos(\gamma) \\ &= |V_g| \times \frac{|V_L|}{|Z|}\cos(\gamma) \end{aligned} \tag{4.3}$$

From (4.2) and (4.3), the angle between grid voltage and load current, γ can be found out as,

$$\cos(\gamma) = \frac{\frac{|V_L|^2}{|Z|}\cos(\theta) - P_{inv}}{|V_g|.\frac{|V_L|}{|Z|}} \tag{4.4}$$

It can be noted that, if the grid voltage is $v_g(t) = |V_g|\sqrt{2}\cos(\beta)$, where $\beta = (\int \omega\, dt) + \delta$, ω is the grid frequency and by estimating the requirement of γ using (4.4), the load voltage can be forced to be $v_L(t) = |V_L|\sqrt{2}\cos(\beta + \gamma + \theta)$. The grid voltage angle β is estimated by using PLL. By this process, not only is the load voltage regulated at nominal rms value, $|V_L|$ but a specific amount of active power flow, P_{inv} can also be supplied to the load at steady state. The operation is possible irrespective of the voltage condition in the grid. It is also possible to supply the full maximum power of the renewable energy extractor to the load under all conditions of the grid voltage, along with the proper regulation of the load voltage just by

making the condition $P_{inv} = P_{mpp}$. It can also be observed from Figure 4.2(b) that under any condition of the grid voltage, the grid current (which is also load current), I_L, leads the grid voltage, V_g by the angle, γ under lagging power factor ($cos(\theta)$) load presence.

4.1.3 Constraint on the series inverter system under common operating conditions

(4.4) depicts that for an acceptable value of power angle γ, (4.5) and (4.6) have to be satisfied as (here extreme condition is shown where $P_{inv} = P_{mpp}$),

$$0 \leq \cos(\gamma) \leq 1 \tag{4.5}$$

$$|V_g| \geq \frac{\frac{|V_L|^2}{|Z|}\cos(\theta) - P_{mpp}}{\frac{|V_L|}{|Z|}} \tag{4.6}$$

(4.6) is true at steady state when the battery is fully charged and the full Maximum Power Point (MPP) power [36], [74], P_{mpp} is transferred to the load through the inverter, i.e. $P_{inv} = P_{mpp}$. In this case, the renewable energy source is considered to be solar but the analysis can be extended for any renewable energy source without the loss of generality. Then for a specific solar insolation level, the maximum dip in the grid voltage, i.e. the minimum rms value of grid voltage can be calculated from (4.6). It is assumed that, the inverter, operates with SPWM. Therefore, in order to maintain the SPWM in the linear range, there should be certain level of minimum DC link voltage required. In the extreme condition, it is assumed that, no power is taken from the grid, i.e. $\gamma = 90^0$. The phasor diagram of this condition is shown in Figure 4.3. From Figure 4.3, the phasor equation of the inverter voltage can be

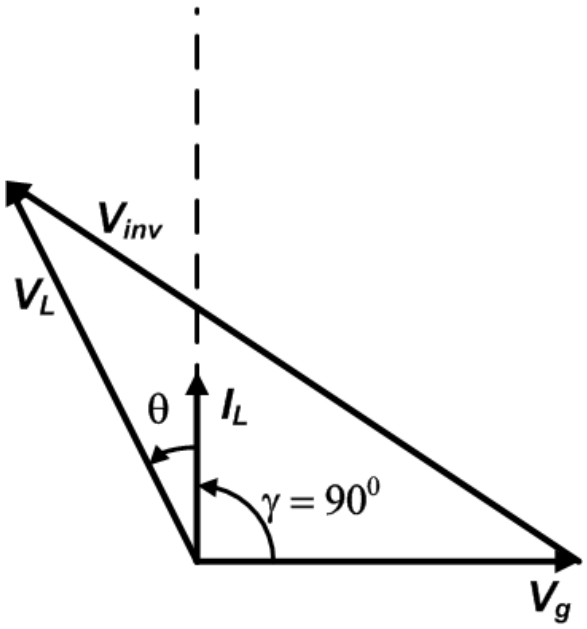

Figure 4.3: Phasors diagram of the inverter quantities when $P_g = 0$.

written as,

$$\overrightarrow{V}_{inv} = \overrightarrow{V}_L - \overrightarrow{V}_g \implies \overrightarrow{V}_{inv} = [-|V_g| - |V_L|\sin(\theta)] + j\,[|V_L|\cos(\theta)] \tag{4.7}$$

(4.7) gives the inverter voltage having the maximum rms magnitude. Beyond this point, the operation of the inverter is restricted. So, the maximum rms value of the inverter voltage is written as,

$$|V_{inv}|_{max} = \sqrt{|V_g|^2 + 2|V_g||V_L|\sin(\theta) + |V_L|^2} \tag{4.8}$$

If the DC link voltage is maintained at the level V_{dc}, the maximum rms value of the output voltage of the constant triangular voltage SPWM inverter [128] in linear range is given as,

$$|V_{inv}|_{max} = \frac{V_{dc}}{\sqrt{2}} \tag{4.9}$$

So, from (4.9) and (4.8) the minimum value of the DC link voltage needed for this application can be found as,

$$V_{dc}|_{min} = \sqrt{2 \times\ [|V_g|^2 + 2|V_g||V_L|\sin(\theta) + |V_L|^2]} \tag{4.10}$$

So, if the MPP power of the panel, P_{mpp} and the maximum dc link voltage that can be developed, V_{dc}, are known, then from (4.6), the minimum possible grid voltage dip and from (4.10), maximum possible grid voltage swell, that can be regulated by this inverter system can be estimated. Accordingly, the inverter operating conditions, like DC link voltage, maximum grid sag and swell that can be compensated, are to be designed. Observations from (4.10) and Figure 4.2(a) lead to the comment that, if a high-frequency step-up transformer is placed between the PWM inverter and the L-C power filter, the DC link voltage requirements derived by (4.10) can be reduced in proportion to the step-up turns-ratio of the transformer used. The

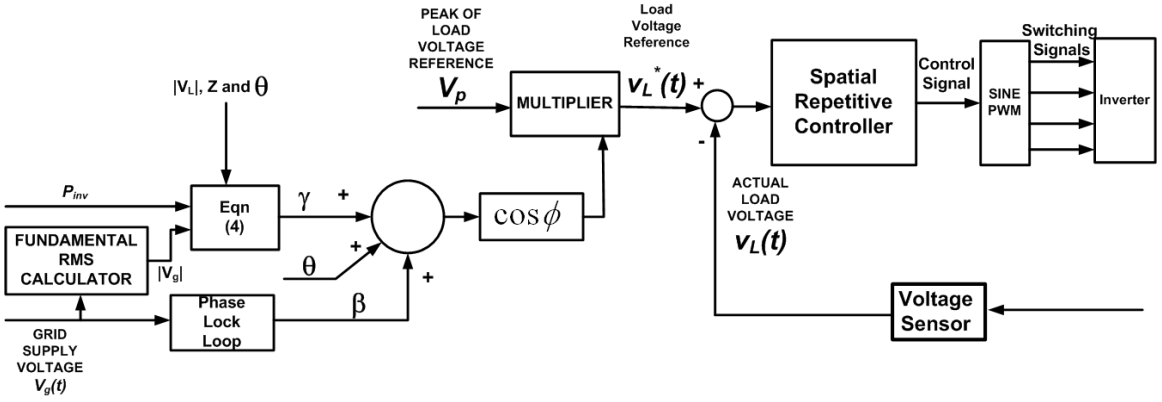

Figure 4.4: The general control diagram of the proposed inverter.

implementation diagram of the proposed control strategy of the series inverter is shown in Figure 4.4. As discussed, the proposed control strategy ensures a specific inverter active power flow, P_{inv} along with load voltage, v_L are maintained at rated level (in the present case it is $110\,V$ rms). As shown in Figure 4.4, based on the requirements of the P_{inv}, the power angle γ is calculated using (4.4). Then γ is added with the grid phase angle, β (found from PLL) and load power factor angle, θ. This gives the total reference load voltage angle, $\phi = \gamma + \beta + \theta$ (as shown in Figure 4.2(b)). Then the rated load voltage peak ($V_p = \sqrt{2}|V_L|$) is multiplied with $\cos\phi$ and the load voltage reference, $v_L^*(t)$ is generated. This load voltage

reference, $v_L^*(t)$ is tracked at steady state by using the proposed SRC. The design as well as the implementation details of the SRC are discussed in Chapter 5. Control strategies of the series inverter under other operating conditions are given in Appendix F.

4.2 Design of a typical prototype system

In the report the prototype series inverter is designed for a PV system based residential application. The parameters of the system used are, Load resistance, $R = 150\,\Omega$, Load inductance, $L = 0.1\,H$, the nominal rms load voltage requirement, $|V_L| = 110\,V$. The solar panel used for typical residential application usually provides Maximum Power Point Power, $P_{mpp} = 50\,W$ at $1kW/m^2$ solar insolation at 25^0C temperature. The system design is carried out with the inverter output power, $P_{inv} = 50\,W$. This condition ensures that, battery is fully charged and the full panel MPP power, P_{mpp} is transferred to the load side through P_{inv}.

The load impedance is $|Z| = \sqrt{R^2 + (2\pi fL)^2} = 153.25\,\Omega$. So, $|I_L| = \frac{110}{153.25} = 0.718\,A$ and the power factor angle $\theta = tan^{-1}\frac{2\pi fL}{R} = 11.83^0$. Minimum grid voltage that can be regulated by this system is calculated using (4.6) and the value is $|V_g|_{min} = 38\,V$, which is equivalent to 65% sag in grid voltage. It is considered to have maximum 18% (typical value for the prototype test) swell in grid voltage, i.e. $|V_g|_{max} = 130\,V$. The minimum level DC link voltage needed for this prototype is calculated using (4.10), $V_{dc} \geq 264.06V$. For the experiment, DC link voltage level is set at $V_{dc} = 270\,V$. Using (4.4), different values of power angle γ are

calculated, as shown in Table 4.1, under different conditions of grid voltage and for $P_{inv} = 50\,W$ as well as $P_{inv} = 40\,W$. These power angle values are used in simulation as well as in experiment. The SPWM switching frequency of the PWM inverter is maintained at $10\,kHz$. So, the power L-C filter cut-off frequency is to set less than $1\,kHz$. The parameters of the L-C filter used are: value of filter inductor, $L_f = 10mH$, value of filter capacitor, $C_f = 3.3\mu F$, filter current limiting resistance, $R_f = 10\Omega$. The actual implemented cut-off frequency of the power L-C filter is set at $f_{cut-off} = \frac{1}{2\pi}\frac{1}{\sqrt{L_f C_f}} = 876\,Hz$. The data calculated in Table 4.1

Table 4.1: Different values of Power Angle, γ

Inverter active power flow, P_{inv} (W)	**rms of Grid Voltage, $\|V_g\|$ (Volts)**	**Remark**	**value of Power Angle, γ**
50	110	Normal condition at grid	69.788^0
50	90	18% sag at grid	65.022^0
50	130	18% swell at grid	73^0
40	70.7	36% sag at grid	48^0

is used to show the effectiveness of the series inverter in the experimental results presented in the next Chapter.

4.3 Summary

This Chapter deals with the operating principles of the series connected renewable energy inverter interfacing renewable energy sources with load and common AC bus. The series inverter voltage is added in series with the common AC bus voltage to form the load voltage. The proposed control strategy ensures regulation of the load voltage with proper control on the active power flow ensuring the reduction

of grid active power consumption. In this Chapter, it is explained how the load voltage is maintained at high quality by controlling the inverter reference voltage. The proposed control strategy ensures the proper active power control by ensuring relative phase angle between the load voltage and the common AC bus voltage. In the next Chapter, the Spatial Repetitive Controller is designed to ensure high quality of load voltage under the presence of common AC bus voltage disturbances with proper active power control from the renewable energy source.

Chapter 5

Implementation of control strategy for the single-phase series connected renewable energy source based inverter

Chapter 4 discusses a control strategy of finding a relative phase between the grid voltage and the load voltage to control the power flow of the inverter as well as regulating the load voltages to the nominal condition even in the presence of huge grid voltage disturbances. The present Chapter is dedicated to designing of different non-linear high performance controllers to regulate such nice load voltage in the presence of grid voltage disturbances. The controllers are also able to maintain the same performance even during sudden change of the grid fundamental frequency. The stability analysis of the controllers are provided and the controllers are designed for the series connected inverter application. Adequate experimental results are provided to test the feasibility of the proposed control schemes.

5.1 Design of Spatial Repetitive Controller

5.1.1 General discussion on Spatial Repetitive Controller

Repetitive control is specially designed to remove the periodic errors at integral fractions of sampling frequency due to the reference tracking as well as periodic disturbance inputs. The idea of repetitive control is based on the internal model principle [82]. The underlined concept of a typical repetitive controller is to use the information of the preceding cycle to improve the control performance in the present cycle and ultimately reach the desired steady state. Design methods of fixed sampling frequency plug-in repetitive controller are discussed in [59] and [60]. Discussions in [59] and [60] depict that, the fixed sampling frequency repetitive controllers can mainly eliminate steady state errors at multiples of fundamental frequencies with fundamental frequency being an integral fraction of the sampling frequency. However, in the micro-grid application, as discussed before, the fundamental grid frequency can vary suddenly but the same control performance (load voltage having a specific phase relation with the grid voltage with no voltage harmonics present) is expected. This is possible only if the sampling frequency, f_s of the overall control system is varied according to the fundamental grid frequency, f_f (so that $\frac{f_s}{f_f} = N$, where N is a large integer). In steady state, the discrete complex frequency at fundamental micro-grid frequency (f_f) can be expressed as $z = e^{j\omega T_s}$, where $\omega = 2\pi f_f$ and $T_s = \frac{1}{f_s}$. If f_s is varied according to the variation of f_f with the relation $\frac{f_s}{f_f} = N$, the same complex frequency (for fundamental micro-grid frequency) at steady state becomes $z = z_\theta = e^{j\frac{2\pi}{N}} = e^{j\Delta\theta}$. The analysis explains that the effect of the dynamic change is sampling frequency can be achieved by sampling the system at the multiples of grid fundamental space

phase $\Delta\theta = \frac{2\pi}{N}$. So, a SRC is proposed in this report. In the proposed SRC, the control action is taken at discrete samples of fundamental grid phase $\theta = n\,\frac{2\pi}{N}$, where, $n = 1\,,\ 2\,,\ 3\,, ... N$.

The above analysis coveys that, the proposed SRC is basically a typical plug-in repetitive controller where the sampling frequency changes dynamically with the fundamental grid frequency. The dynamic behavior of the SRC is expressed with digital dynamic complex frequency $z_\theta = e^{j\,s\,T}$, where T is the variable sampling time unlike the case for fixed sampling frequency T_s, where the digital dynamic complex frequency is expressed as $z = e^{j\,s\,T_s}$. The block diagram of the closed

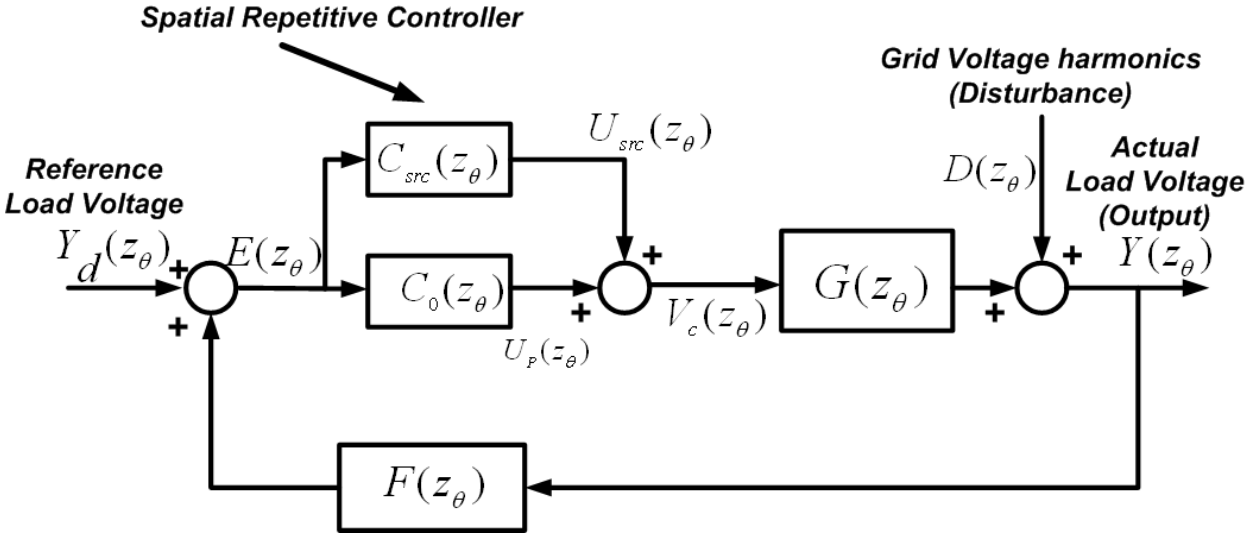

Figure 5.1: The block diagram of the proposed control system.

loop system *sampled* in *grid fundamental phase* domain is shown in Figure 5.1. The block diagram of the plug-in SRC based closed-loop control system is drawn following the guidelines presented in [61] and [62]. In Figure 5.1, $Y_d\,(z_\theta)$ is the reference signal (rated load voltage), $Y\,(z_\theta)$ is the output signal (actual load voltage), $E\,(z_\theta)$ is the tracking error, $D\,(z_\theta)$ is the disturbance input (micro-grid voltage harmonics), $G\,(z_\theta)$ is the plant transfer function (PWM inverter along with the

L-C filter), $C_0(z_\theta)$ is the feedback controller, $C_{src}(z_\theta)$ is the plugged in *Spatial repetitive Controller*, $F(z_\theta)$ is the analog filter to remove the high frequency noise at the interface between the system output and the digital controller and $V_c(z_\theta)$ is the control signal coming out of the digital controller. The total effect of the two controllers can be defined as $C(z_\theta) = C_0(z_\theta) + C_{src}(z_\theta)$.

The reference $Y_d(z_\theta)$ is a sinusoidal wave. The $C_0(z_\theta)$ is a proportional controller (K_p) and the proportional gain K_p is chosen to ensure that the characteristic polynomial of the close-loop system, $1 + K_pG(z_\theta)F(z_\theta)$, meets the stability conditions.

Following the analysis shown in [60] and [62], the transfer function of the proposed SRC is shown in (5.1).

$$C_{src}(z_\theta) = \frac{U_{src}(z_\theta)}{E(z_\theta)} = K_{src}\frac{z_\theta^{-(N-N_1)}}{1-z_\theta^{-N}} \tag{5.1}$$

where, K_{src} is positive gain of repetitive controller and N_1 is the number of advancement in samples with $N_1 < N$.

In *grid phase sample domain*, the same control law can be written as,

$$u_{src}(i,\theta_k) = u_{src}(i-1,\theta_k) + K_{src}\,e(i-1,\theta_{k+N_1}) \tag{5.2}$$

Where, $u_{src}(i,\theta_k)$ is the control output of SRC at the k^{th} position sample in the i^{th} iteration cycle, $e(i-1,\theta_{k+N_1})$ is the error of the reference and output at $(k+N_1)^{th}$ position sample in $(i-1)^{th}$ iteration cycle, K_{src} is the positive gain of repetitive controller and N_1 ($N_1 < N$) is the number of advancement samples given to take care of the phase delay in the plant and feedback filter path. One cycle consists of N samples in fundamental grid phase position. The total control action can be

expressed as,

$$\begin{aligned} C(z_\theta) &= C_0(z_\theta) + C_{src}(z_\theta) \\ &= K_p + C_{src}(z_\theta) \end{aligned} \tag{5.3}$$

From Figure 5.1, the output $Y(z_\theta)$ can be expressed by the reference $Y_d(z_\theta)$ and the disturbance $D(z_\theta)$ as shown in (5.4).

$$Y(z_\theta) = \frac{C(z_\theta)\,G(z_\theta)}{1 + C(z_\theta)\,G(z_\theta)\,F(z_\theta)} Y_d(z_\theta) + \frac{1}{1 + C(z_\theta)\,G(z_\theta)\,F(z_\theta)} D(z_\theta) \tag{5.4}$$

Further in the analysis, any dynamic complex quantity '$X(z_\theta)$' is expressed as 'X'. The dynamic tracking error can be derived as using (5.4),

$$\begin{aligned} E &= Y_d - Y \\ &= \frac{Y_d\,(1 + C\,G\,F - C\,G) - D}{1 + C\,G\,F} \end{aligned} \tag{5.5}$$

From (5.5), the characteristics polynomial of the overall repetitive control system can be written as,

$$\begin{aligned} 1 + C\,G\,F &= 1 + C_0\,G\,F + C_{src}\,G\,F \\ &= [1 + C_0\,G\,F]\left[1 + \frac{C_{src}\,G\,F}{1 + C_0\,G\,F}\right] \\ &= [1 + C_0\,G\,F]\,[1 + C_{src}\,C_{cl}] \end{aligned} \tag{5.6}$$

where, $C_{cl} = \frac{G\,F}{1 + C_0\,G\,F}$ is the transfer function from D to Y without the SRC. The observation from (5.6) is that the stability of the overall repetitive control system requires that the roots of the polynomial $1 + C_0\,G\,F = 0$ are inside the unit circle with additional condition [62] as,

$$|1 + C_{src}\,C_{cl}| \neq 0 \tag{5.7}$$

The requirement on the roots $1 + C_0\,G\,F\;=\;0$ can be met by choosing appropriate proportional gain $C_0\;=\;K_p$.

Using (5.1), (5.7) can be modified to,

$$|1\;-\;z_\theta^{-N}\;+\;K_{src}\,z_\theta^{-(N-N_1)}\,C_{cl}\,(z_\theta)\,|\;\neq\;0 \tag{5.8}$$

(5.8) can be guaranteed by satisfying the following condition:

$$|\,z_\theta^{-N}\;-\;K_{src}\,z_\theta^{-(N-N_1)}\,C_{cl}\,(z_\theta)\,|\;<\;1 \tag{5.9}$$

Any harmonic frequency (ω_1 in rad/sec) appearing in the micro-grid system can be represented as $\omega_1\;=\;p\,\omega$, where ω is the fundamental micro-grid frequency in rad/sec and p is an integer. Any arbitrary frequency ω_1 in steady state, $z_\theta\;=\;e^{j\,p\,\Delta\theta}$ and this results in $z_\theta^N\;=\;e^{j\;p\,2\pi}\;=\;1$ for p as integers. Using this result, (5.9) can be modified as,

$$|1\;-\;K_{src}\,z_\theta^{N_1}\,C_{cl}\,(z_\theta)\,|\;<\;1 \tag{5.10}$$

At steady state, $C_{cl}\,(z_\theta)\;=\;C_{cl}\left(e^{j\,p\,\Delta\theta}\right)\;=\;A_{cl}\,(p\,\Delta\theta)\,e^{j\;\phi_c(p\,\Delta\theta)}$ with $A_{cl}\,(p\,\Delta\theta)$ being its magnitude and $\phi_c\,(p\,\Delta\theta)$ being its phase. Using this information, (5.10) can be further simplified as,

$$|1\;-\;K_{src}\,A_{cl}\,(p\,\Delta\theta)\,e^{j\alpha(p\,\Delta\theta)}|\;<\;1 \tag{5.11}$$

where, $\alpha\,(p\,\Delta\theta)\;=\;p\,N_1\times\Delta\theta\;+\;\phi_c\,(p\,\Delta\theta)$. (5.11) can be expanded as,

$$|1\;-\;K_{src}\,A_{cl}\;\cos\alpha\;-\;j\,K_{src}\,A_{cl}\;\sin\alpha|\;<\;1 \tag{5.12}$$

Squaring both sides of (5.12), the equivalent form is found as,

$$K_{src}^2\,A_{cl}^2\;<\;2\,K_{src}\,A_{cl}\;\cos\alpha \tag{5.13}$$

Since the gain of the controller $K_{src}\;>\;0$ and the system gain $A_{cl}\;>\;0$, (5.13) yields:

$$K_{src}\,A_{cl}\;<\;2\;\cos\alpha \tag{5.14}$$

Stability of the overall close-loop system can be guaranteed for the entire range of frequency of reference input as well as disturbance input if,

$$K_{src} \;<\; \frac{2\,min\,[\cos\alpha]}{max\,[A_{cl}]} \tag{5.15}$$

where '$min\,[\cos\alpha]$' depicts the minimum value of $\cos\alpha$ considering all the frequencies of interest and similarly '$max\,[A_{cl}]$' depicts the maximum value of A_{cl} considering all the frequencies of interest. Since both K_{src} and A_{cl} are positive, (5.14) implies the condition shown in (5.16).

$$\cos\alpha \;>\; 0 \tag{5.16}$$

The range of phase-angle α is,

$$|\alpha| \;=\; |p\,N_1\frac{2\,\pi}{N} \;+\; \phi_c| \;<\; \frac{\pi}{2} \tag{5.17}$$

Theoretically speaking, (5.15) and (5.17) need to be satisfied throughout the infinite frequency range to make the control system stable. However Figure 5.1 shows that, F is an anti-alias filter placed to filter high frequencies in the feedback process. So, effectively, (5.15) and (5.17) are designed here to satisfy upto the cutoff frequency of the low-pass anti alias filter F only. Frequencies beyond the cut-off frequency of the anti-alias filter are neglected in the present case of design of SRC.

(5.17) provides the constraint on the choice of sample advancement parameter N_1 of the SRC for the stability point of view of the overall control system. But in this case, there is a phase delay associated with the plant and the anti-alias filter which provides the delay in effecting the repetitive controller on the error correction. This point is well explained in Figure 5.2. Figure 5.1 shows that, the output of the SRC, U_{src} acts to converge the error, E to zero. If the SRC is opened and it is tried to find the phase delay associated with this control action activation,

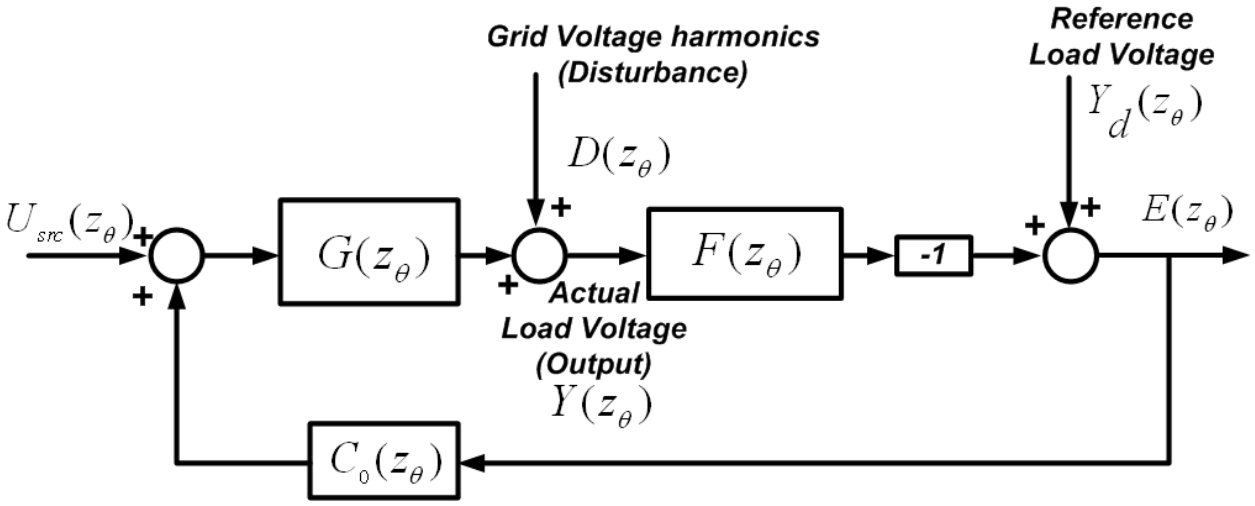

Figure 5.2: The block diagram showing the phase delay provided by plant and anti-alias filter signal transmission.

the phase delay path looks like the picture shown in Figure 5.2. If Figure 5.2 is concerned, the phase delay transfer function is shown as,

$$\begin{aligned} C_d(z_\theta) &= \frac{E(z_\theta)}{U_{src}(z_\theta)} \\ &= -\frac{G(z_\theta)\ F(z_\theta)}{1 + C_0(z_\theta)\ G(z_\theta)\ F(z_\theta)} \\ &= -C_{cl}(z_\theta) \end{aligned} \tag{5.18}$$

At steady state ($z_\theta = e^{j\,p\,\Delta\theta}$), the delay transfer function takes the form shown as,

$$C_d\left(e^{j\,p\,\Delta\theta}\right) = A_{cl}(p\,\Delta\theta)\ e^{j(\pi + \phi_c(p\,\Delta\theta))} \tag{5.19}$$

Both (5.19) and Figure 5.2 show that, SRC output, U_{src} acts on the error E with a phase lead of ϕ_c. It is shown later that, for normal power electronic systems, ϕ_c is a negative quantity which leads to a phase delay of SRC action.

(5.1) indicates that, the phase lead provided by the SRC is ϕ_l (due to phase lead provided by the term $z_\theta^{N_1} = e^{j\,p\,N_1\,\Delta\theta} = e^{j\,p\,N_1\,\frac{2\pi}{N}}$ at steady state, in the numerator of $C_{src}(z_\theta)$). The phase lead by the repetitive controller is expressed as,

$$\phi_l \;=\; p\, N_1\, \frac{2\,\pi}{N} \tag{5.20}$$

The phase lead of repetitive controller ϕ_l is designed to nullify the signal transmission delay due to plant and analog filter ϕ_c to enhance the tracking performance as,

$$\begin{aligned} \alpha \;&=\; \phi_l \;\;+\;\; \phi_c\,(p\,\Delta\theta) \;\;>\;\; 0 \\ \Rightarrow \alpha \;&=\; p\, N_1 \frac{2\,\pi}{N} \;\;+\;\; \phi_c \;\;>\;\; 0 \end{aligned} \tag{5.21}$$

(5.17) and (5.21) together decide the value of phase sample advancement parameter N_1. The gain of the SRC, K_{src} is obtained considering some model uncertainty, δ in (5.15).

$$K_{src} \;\;<\;\; \frac{2\,min\,[\cos\alpha]}{max\,[A_{cl}] \;+\; \delta} \tag{5.22}$$

Using (5.6), (5.5) is expanded as,

$$E(z_\theta) = \left(1 \;-\; z_\theta^{-N}\right) \frac{Y_d(z_\theta)\;\left(1 \;+\; C(z_\theta)\,G(z_\theta)\,F(z_\theta) \;-\; C(z_\theta)\,G(z_\theta)\right) \;-\; D(z_\theta)}{\left(1 \;+\; C_0(z_\theta)\,G(z_\theta)\,F(z_\theta)\right)\,\left(1 \;-\; z_\theta^{-N} \;+\; K_{src}\, z_\theta^{-(N-N_1)}\, C_{cl}\,(z_\theta)\right)} \tag{5.23}$$

As explained before, at steady state $z_\theta^N \;=\; e^{j\,p\,2\pi} \;=\; 1$ at integral values of p, so from (5.23) at steady state the error is derived to be zero at the multiple frequencies of the fundamental grid frequency of micro-grid, i.e.

$$E(e^{j\,p\,\Delta\theta}) \;=\; 0 \tag{5.24}$$

Hence, (5.24) concludes that at steady state, the tracking error is zero at integral multiples frequencies of the fundamental frequency of the micro-grid. The same property is also observed to exist if the fundamental grid frequency $\omega \;=\; 2\,\pi\,f_f$ varies as well. In this case, the eligible values of p can be derived from the fact

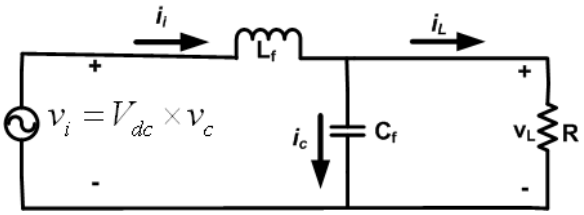

Figure 5.3: Simplified sub-circuit investigating the effect of inverter on load voltage.

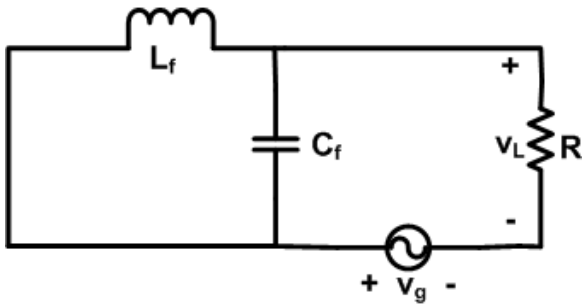

Figure 5.4: Simplified sub-circuit investigating the effect of micro-grid on load voltage.

that, the effective maximum frequency of signal can appear in the control system is $\omega_{1max} = \frac{\omega_s}{2}$, where, $\omega_s = 2\,\pi\,\frac{1}{T}$ is the effective sampling frequency in rad/sec. Comparing this analysis with the earlier discussion, the derivation says that $p_{max} = \frac{N}{2}$. Hence, the proposed SRC is able to remove the steady state error at multiples of fundamental micro-grid frequencies with multiplying factor $p = 1\ , 2\ , ..., \frac{N}{2}$ with the advantage that the fundamental grid frequency itself can vary as expected the actual micro-grid operation.

5.1.2 Position domain modeling of the inverter L-C filter assembly with load and micro-grid interconnection

The power circuit configuration of the series connected inverter is shown in Figure 4.2. For designing the controller, the power circuit is further simplified and used for reference as shown in Figures 5.3 and 5.4. Neglecting the high frequency switching terms of SPWM and considering only the fundamental component of the output, the inverter output voltage can be expressed as $v_i = V_{dc} \times v_c$ [128], where, v_c is the control voltage of the SPWM and V_{dc} is the DC link voltage of the inverter. Now, *superposition* principle is applied to find out the effect of control input (control signal, v_c) and disturbance input (micro-grid voltage, v_g) on the load voltage, v_L

separately. Considering the absence of the grid voltage, the circuit can be redrawn as shown in Figure 5.3. Considering the voltage and current across each component (filter inductance L_f, filter capacitor C_f and load resistance R) in Figure 5.3, the equations can be written as:

$$\begin{aligned} v_i - v_L &= L_f \frac{di_i}{dt} \\ i_i &= i_c + i_L \\ i_c &= C_f \frac{dv_L}{dt} \\ v_L &= i_L \times R \\ v_i &= V_{dc} \times v_c \end{aligned} \tag{5.25}$$

Putting all the equations shown in (5.25) together, the resultant dynamic behavior can be put as,

$$(V_{dc} \times v_c) - v_L = L_f \frac{d}{dt}\left(C_f \frac{dv_L}{dt} + \frac{v_L}{R}\right) \tag{5.26}$$

Now, the control system is implemented in position domain. As (5.26) is in time domain, the equivalent discrete form of the plant equation sampled in phase position domain is derived. The time derivative of any variable, x, can be represented in terms of space derivative, the space variable θ is the phase position;

$$\frac{dx}{dt} = \frac{dx}{d\theta} \times \frac{d\theta}{dt} \tag{5.27}$$

As, $\frac{d\theta}{dt} = \omega$, electrical angular fundamental frequency (in rad/sec) of the micro-grid and $dx = x(\theta_{k+1}) - x(\theta_k)$, where $x(\theta_k)$ is the variable x at k^{th} sample position, θ_k. Additionally, $d\theta = \Delta\theta = \theta_{k+1} - \theta_k$ is the step size of position sampling. So, first and second time derivative of variable x can be rewritten, using a new variable as: $m = \frac{\omega}{\Delta\theta}$ is also used.

$$\begin{aligned} \frac{dx}{dt} &= \frac{x(\theta_{k+1}) - x(\theta_k)}{\Delta\theta} \times \omega = m\ [x(\theta_{k+1}) - x(\theta_k)] \\ \frac{d^2x}{dt^2} &= m^2\ [x(\theta_{k+2}) - 2x(\theta_{k+1}) + x(\theta_k)] \end{aligned} \tag{5.28}$$

Using (5.28), (5.26) can be rewritten in position sampled domain as,

$$\begin{aligned}[V_{dc} \times v_c(\theta_k)] - v_L(\theta_k) &= L_f m \left[C_f m \{ v_L(\theta_{k+2}) - v_L(\theta_{k+1}) \} + \frac{v_L(\theta_{k+1})}{R} \right] \\ &\quad - L_f m \left[C_f m \{ v_L(\theta_{k+1}) - v_L(\theta_k) \} \right] \\ &\quad - L_f m \left[\frac{v_L(\theta_k)}{R} \right] \end{aligned} \tag{5.29}$$

Rearranging all the terms in (5.29),the circuit equation in position domain can be rewritten as,

$$v_L(\theta_{k+2}) + a\, v_L(\theta_{k+1}) + b\, v_L(\theta_k) = c\, v_c(\theta_k) \tag{5.30}$$

where, $a = \frac{\frac{1}{R} - 2\, m\, C_f}{m\, C_f}$, $b = \frac{C_f\, m - \frac{1}{R} + \frac{1}{L_f\, m}}{m\, C_f}$ and $c = \frac{\frac{V_{dc}}{m\, L_f}}{m\, C_f} = \frac{V_{dc}}{L_f\, C_f\, m^2}$

Considering the absence of the inverter voltage, the circuit can be redrawn as shown in Figure 5.4. The voltage equation then would be;

$$v_L = v_g \tag{5.31}$$

Using (5.30) and (5.31), in discrete position sample domain, the inverter characteristics can be written as (using *super-position principle*),

$$V_L(z_\theta) \;=\; \frac{c}{z_\theta^2 \;+\; a\, z_\theta \;+\; b}\, V_c(z_\theta) \;+\; V_g(z_\theta) \tag{5.32}$$

Using (5.32) and Figure 5.1, where $Y(z_\theta) \;=\; V_L(z_\theta)$, $D(z_\theta) \;=\; V_g(z_\theta)$, the plant transfer function can be written as:

$$G(z_\theta) \;=\; \frac{c}{z_\theta^2 \;+\; a\, z_\theta \;+\; b} \tag{5.33}$$

5.1.3 Position domain modeling of the anti-alias filter

The *anti-alias* filter is depicted as $F(z_\theta)$ in Figure 5.1. The *anti-alias* filter is put to filter higher order harmonic frequencies from entering into the digital controller

interface. This *anti-alias* filter is essentially an *analog 2nd order Butterworth* filter implemented with digital discrete circuit components. Let the input and output of this *anti-alias* filter be $u_f(t)$ and $y_f(t)$ in time domain. The differential equation of such filter can be represented as,

$$\frac{d^2 y_f}{dt^2} \; + \; a_f \, \frac{dy_f}{dt} \; + \; b_f \, y_f \; = \; b_f \, u_f \tag{5.34}$$

where, $b_f = (2\,\pi\,f_c)^2$ and $a_f = \frac{2\,\pi\,f_c}{Q}$ with $f_c = Cut{-}off\ frequency of\ filter in Hz$ and $Q = designed\ quality\ factor\ of\ the\ filter$. Using (5.28) in (5.34) to get the sampling equivalent of the filter:

$$F(z_\theta) \; = \; \frac{Y_f(z_\theta)}{U_f(z_\theta)} \; = \; \frac{c_2}{z_\theta^2 \; + \; a_2\, z_\theta \; + \; b_2} \tag{5.35}$$

where, $c_2 \; = \; \frac{b_f}{m^2}$, $a_2 \; = \; \frac{a_f - 2\,m}{m}$ and $b_2 \; = \; \frac{m^2 - a_f\, m + b_f}{m^2}$. The *anti-alias* filter is designed with cut-off frequency, $f_c \; = \; 400\,Hz$ and quality factor, $Q \; = \; \frac{\sqrt{2}}{\sqrt{3}}$.

5.1.4 Design of the Spatial Repetitive Controller for the series inverter

The design of the SRC is dependent on the actual parameters of the series inverter configuration as well as the control considerations as mentioned before. The actual parameters of the series inverter are discussed in the Chapter 4 before. In the experimental implementation of the controller, the plant output voltage is fed back to the *anti-alias* filter through a voltage sensor of gain, k_v, around $\frac{1}{100}$ (refer to Figure 5.1). The *anti-alias* filter output is fed to the ADC (Analog to Digital Converter) of the DSP to enable the control computation. Due to this ADC conversion, another equivalent gain, k_{ADC}, $\frac{1}{10}$ is inserted in the feedback path. The total gain (including voltage sensor as well as the ADC gain) is lumped into the plant transfer function as an additional gain of $k_s \; = \; k_v \times k_{ADC} \; = \; \frac{1}{1000}$ for the

calculation of parameters of the SRC as discussed in the later part of this Section. The details of the implementation is shown in Figure 5.5. It can be observed that the proposed control system is implemented inside DS1104 DSP card. In the design

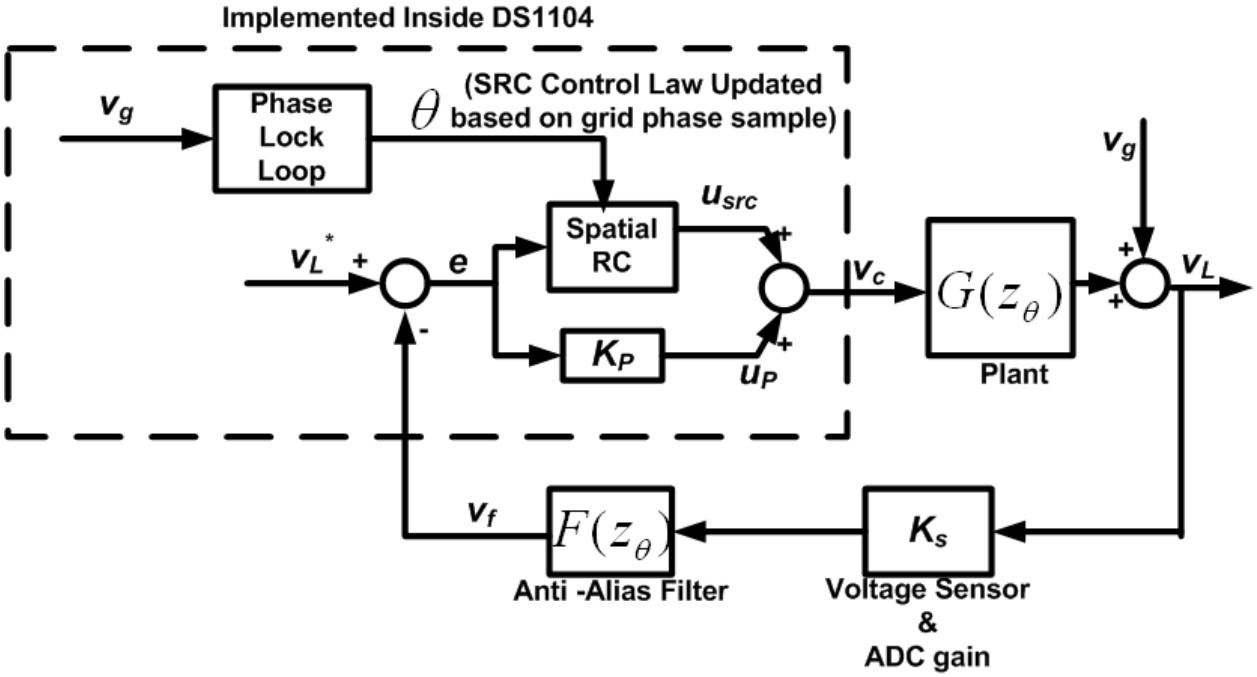

Figure 5.5: Schematics of the digital implementation of the SRC.

of the controller, the fundamental grid phase span ($2\,\pi$) is divided into 200 position samples, i.e. the $N = 200$ is taken. The cut-off frequency of the *anti-alias* filter is set at $400\,Hz$. So, the characteristics of the plant, filter as well as SRC are studied up to frequency $f = 400\,Hz$ and the parameters of the SRC (K_{src} and N_1) are obtained. In the present scope of the report, it is considered that the micro-grid voltage can be contaminated with substantial 3^{rd} and 5^{th} harmonics. The control system is designed for fundamental micro-grid frequency variation from $f_f = 40\,Hz$ to $f_f = 60\,Hz$. It should be mentioned that the micro-grid frequency consideration is taken into account due to the selection of the *anti-alias* filter but not due to the controller selection. The K_{src} and N_1 are designed by considering the effective frequency range of $0 - 300\,Hz$ ($5 \times 60 = 300$) with fundamental micro-grid frequency

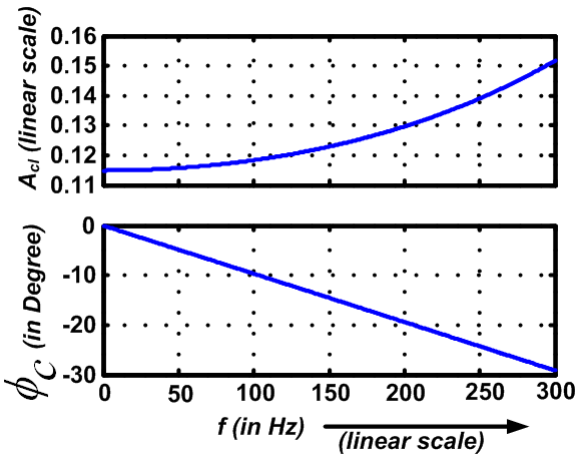

Figure 5.6: The amplitude plot (A_{cl}) and phase plot (ϕ_c) with different frequency (f) for $C_{cl}(z_\theta)$ with fundamental micro-grid frequency $f_f = 50\,Hz$.

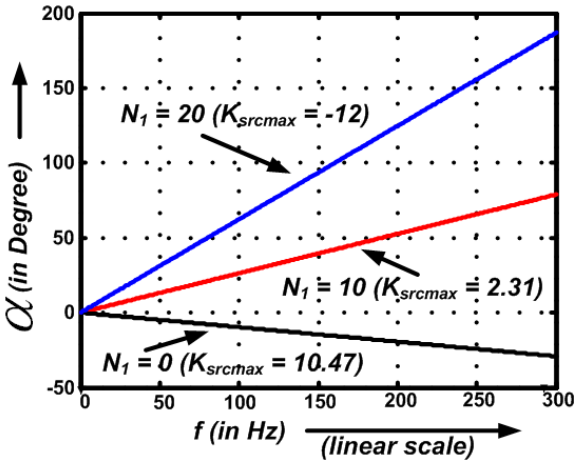

Figure 5.7: Plot of phase angle, α for different frequencies, f under different phase angle compensating term, N_1 of the SRC with fundamental micro-grid frequency $f_f = 50\,Hz$.

kept at typically three different frequencies, $f_f = 50Hz$, $f_f = 60Hz$ and $f_f = 40Hz$.

The gain as well as phase plot of C_{cl} for different frequencies under micro-grid fundamental frequencies $f_f = 50\,Hz$, $f_f = 60\,Hz$ and $f_f = 40\,Hz$ are shown in Figures 5.6, 5.8 and 5.10 respectively. In Figures 5.6, 5.8 and 5.10 that, the frequency is plotted in linear scale as well as the amplitude plot is given in absolute value. In this case, for a specific N_1, the maximum gain of the spatial repetitive controller, $K_{src} = K_{srcmax}$ can be found out from (5.22). The parameter uncertainty of the system, δ is taken as 10% of the estimated value. The angle, α (as mentioned in (5.17) and (5.21)) is plotted with different frequencies for three typical extreme values of N_1 and the corresponding values of K_{srcmax} are also calculated and shown in Figures 5.7, 5.9 and 5.11 for fundamental grid frequency, $f_f = 50\,Hz$, $f_f = 60\,Hz$ and $f_f = 40\,Hz$ respectively. Figures 5.7, 5.9 and 5.11 show that, for both $N_1 = 0$ and $N_1 = 10$, angle α is satisfying (5.17) leading

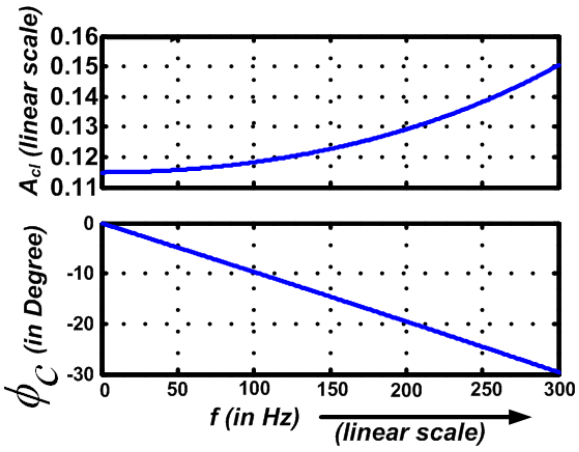

Figure 5.8: The amplitude plot (A_{cl}) and phase plot (ϕ_c) with different frequency (f) for $C_{cl}(z_\theta)$ with fundamental micro-grid frequency $f_f = 60\,Hz$.

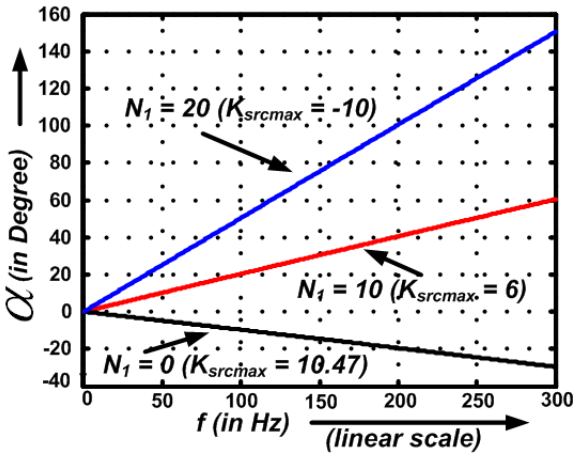

Figure 5.9: Plot of phase angle, α for different frequencies, f under different phase angle compensating term, N_1 of the SRC with fundamental micro-grid frequency $f_f = 60\,Hz$.

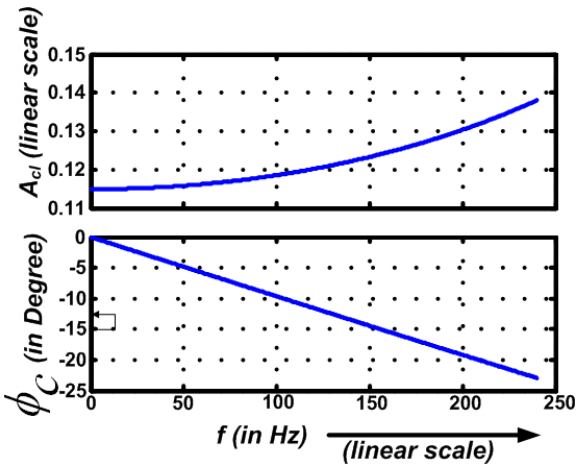

Figure 5.10: The amplitude plot (A_{cl}) and phase plot (ϕ_c) with different frequency (f) for $C_{cl}(z_\theta)$ with fundamental micro-grid frequency $f_f = 40\,Hz$.

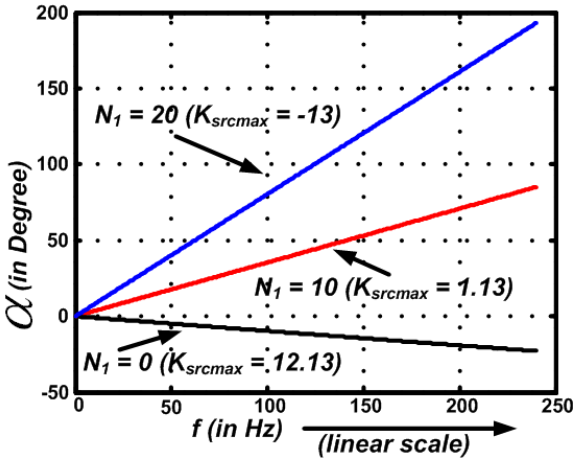

Figure 5.11: Plot of phase angle, α for different frequencies, f under different phase angle compensating term, N_1 of the SRC with fundamental micro-grid frequency $f_f = 40\,Hz$.

to a stable closed loop system for the frequency range of interest. Figures 5.7, 5.9 and 5.11 also depict that, for $N_1 = 20$, angle $\alpha > 90^0$ for $f > 100\,Hz$ under all three fundamental grid frequencies, violating (5.17), which leads to an unstable close loop system. On the other hand, it can also be observed from Figures 5.7, 5.9 and 5.11 that, for $N_1 = 0$, angle $\alpha < 0^0$, violating (5.21). Considering all these issues, for the SRC, the selected value is taken as $N_1 = 10$. Now, observing all the cases of $N_1 = 10$ with different grid fundamental frequencies, the gain of the controller is selected as $K_{src} = 1$. These settings of the controller are used for simulations as well as experimental studies of the proposed series inverter system.

5.2 Experimental Results of the proposed series inverter system with Spatial Repetitive Controller operation

In order to verify the feasibility of the proposed scheme, experiments are carried out under normal grid condition, grid sag condition as well as grid swell condition. The control system as shown in Figure 5.5, is implemented inside a dSPACE platform (DS1104) with Matlab/Simulink Real Time Interface (RTI) toolbox. The inverter sine pwm switching frequency as well as the control system sampling frequency are kept at 10 kHz.

In the control program, a single-phase PLL is used to sense the absolute phase (angle β as shown in Figure 4.4) of the fundamental component of the micro-grid voltage and corresponding phase leads are given to the load voltage reference to facilitate the proper active power flow through the series inverter along with load voltage regulation.

The steady state experimental results are shown in Figures 5.12, 5.13 and 5.14.

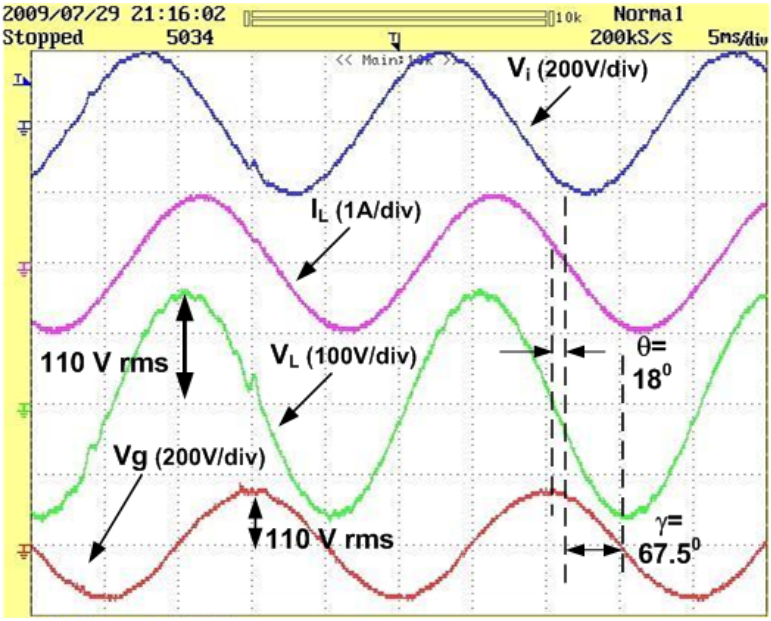

Figure 5.12: Experimental results at normal grid condition, of grid voltage v_g, load voltage v_L, load current i_L and inverter voltage v_i with $P + SRC$ controller working.

Figure 5.12 shows the steady state experimental waveform of inverter voltage (v_i), load current (i_L), load voltage (v_L) and grid voltage (v_g) under the normal condition of the grid voltage. It can be observed that the load voltage is maintained at its nominal value (110 V) and to ensure the required power flow through the inverter, the load current, i_L is forced to be leading from grid voltage, v_g by the required amount of angle ($\gamma = 67.5^0$) as calculated in Table 4.1.

Figure 5.13 shows the steady state experimental waveform of inverter voltage (v_i), load current (i_L), load voltage (v_L) and grid voltage (v_g) under the under 18% sag in the grid voltage. It can be observed that the load voltage can be maintained at its nominal value (110 V) and to ensure the required power flow through the inverter, the load current, i_L is forced to be leading from grid voltage, v_g by the

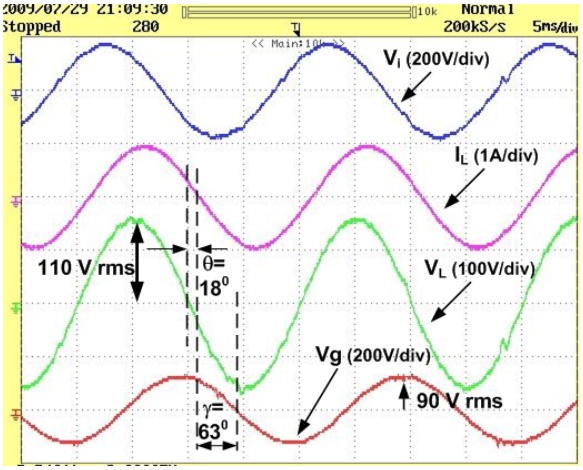

Figure 5.13: Experimental results under 18% grid voltage sag condition, of grid voltage v_g, load voltage v_L, load current i_L and inverter voltage v_i with $P + SRC$ controller working.

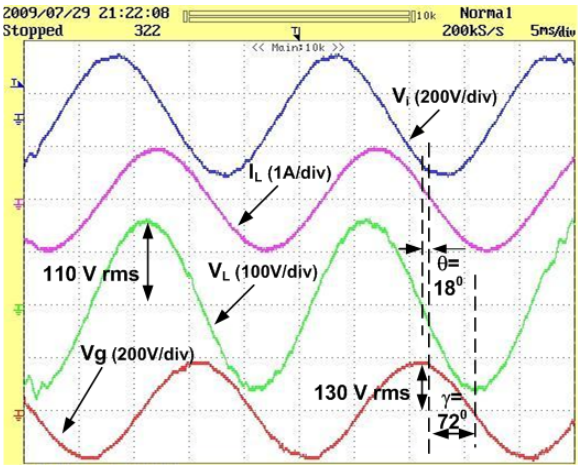

Figure 5.14: Experimental results under 18% grid voltage swell condition, of grid voltage v_g, load voltage v_L, load current i_L and inverter voltage v_i with $P + SRC$ controller working.

required amount of angle ($\gamma = 63^0$) as calculated in Table 4.1.

Figure 5.14 shows the steady state experimental waveform of inverter voltage (v_i), load current (i_L), load voltage (v_L) and grid voltage (v_g) under the under 18% swell in the grid voltage. It can be observed that the load voltage can be maintained at its nominal value (110 V) and to ensure the required power flow through the inverter, the load current, i_L is forced to be leading from grid voltage, v_g by the required amount of angle ($\gamma = 72^0$) as calculated in Table 4.1.

The following remarks can be drawn from the steady state experimental waveforms:

- Under all the conditions of the grid (normal condition, grid voltage sag as well as grid voltage swell condition), the load voltage (V_L) is maintained at nominal level 110 V.

- If the experimental phase angle between load voltage V_L and load current I_L (power factor angle θ) as well as phase angle between load current I_L and grid voltage V_g (power angle γ) are concerned, the control system can be remarked to be successful in maintaining the corresponding power angle requirements (γ) for different conditions of grid (as the power angle requirement given in Table 1). The slight mismatch between the theoretical and experimental values can be justified by considering the experimental restrictions. As mentioned before, in the control desk, the load voltage reference, V_L^* is given with magnitude reference $110\,V$ and phase angle reference as $\gamma+\theta$. As can be seen from the experimental results, the actual power factor angle (at $f_f = 50\,Hz$, the calculated value of power factor angle is $\theta_{th} = 11.83^0$ and the experimental value of power factor angle is $\theta_{ex} = 18^0$) is slightly different from the theoretical value due to slight uncertainty of load parameters as well as grid frequency. Moreover the experimental power factor is slightly more that the theoretical value, so in all the conditions of grid, the experimental value of power angle γ is slightly less than the corresponding theoretical value.

- If the power provided by the inverter is calculated as $P_{inv} = |V_L||I_L|\cos(\theta) - |V_g||I_L|\cos(\gamma)$ and all the experimental values are used to find out the result of the expression, it can be seen that $P_{inv} = 45.74\,W$, $45.08\,W$, $46.28\,W$ respectively for normal grid condition, grid voltage sag condition and grid voltage swell condition respectively. The inverter power is slightly lower than the reference power $50\,W$ because of the slightly lower value of power angle, γ (power angle lower causes more power drawn from grid and less power drawn from the inverter). In spite of this mismatch, the phase shifting of V_L with respect to V_g (as explained in Figure 4.2(b)) can be remarked to be successful.

- It can also be noted that, under all the conditions of grid, the power angle, γ is a leading angle. This is forced to create leading power factor operation from grid side even at lagging power factor load.

To test the performance of the SRC over harmonic rejection a set of experiments are carried out and the experimental results are shown in Figures 5.15-5.20. During these experiments it is considered that, the grid has a 36% dip in the fundamental grid voltage and also the grid is contaminated with 50% third harmonic voltage as well as 30% fifth harmonic voltages. It is considered in these cases that the inverter supplies $40\,W$ active power ($p_{inv} = 40\,W$) to load and rest of the load power is shared by the grid. So, the power angle, γ (using (4.4))is found to be $\gamma = 48^0$ (shown in Table 4.1) and the load voltage, v_L leads fundamental grid voltage, v_{gf} by angle $\gamma + \theta = 60^0$. So, the load voltage is forced to lead the fundamental grid voltage by 60^0 by using SRC.

Figure 5.15 shows the steady state experimental waveform of load voltage, v_L and the grid voltage, v_g with *Proportional* controller application. Due to lack of tracking and harmonic rejection capability, the load voltage becomes extremely distorted as well as in erroneous phase relation with grid voltage as shown in the experimental waveform in this condition.

Figure 5.16 shows that, when the SRC is plugged in , the load voltage, v_L becomes at rated value ($110\,V$) , maintains 60^0 phase lead with the fundamental grid voltage, v_{gf} and the voltage harmonics (50% third harmonics as well as 30% fifth harmonics) are not present in load voltage, v_L. The inverter voltage, v_i is adjusted automatically by the controller in such a way that, inverter voltage gen-

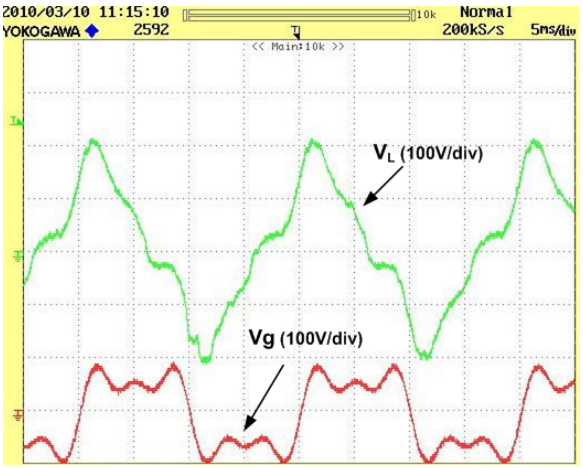

Figure 5.15: Experimental results under 36% grid voltage sag condition with 50% contamination of 3rd harmonics and 30% contamination of 5th harmonics at grid frequency $f_f = 50\ Hz$, of grid voltage v_g, load voltage v_L with *Proportional* controller working.

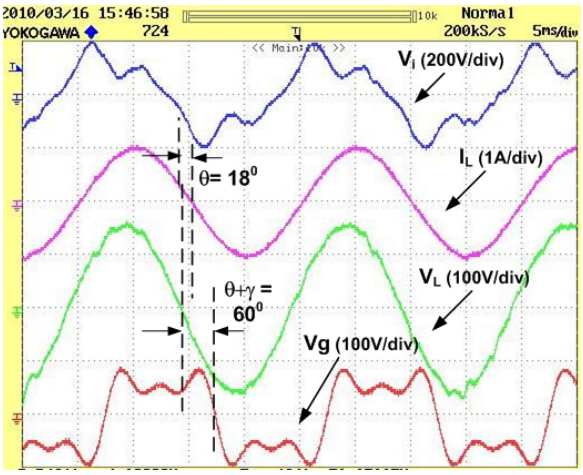

Figure 5.16: Experimental results under 36% grid voltage sag condition with 50% contamination of 3rd harmonics and 30% contamination of 5th harmonics at grid frequency $f_f = 50\ Hz$, of grid voltage v_g, load voltage v_L, load current i_L and inverter voltage v_i with $P + SRC$ controller working.

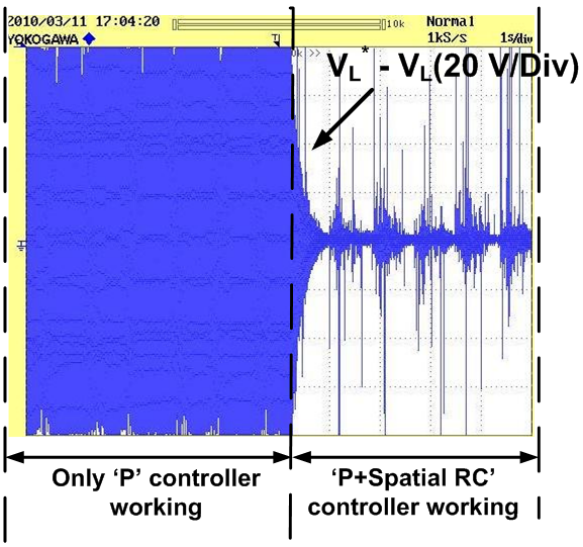

Figure 5.17: Experimental results convergence of load voltage error, $(v_L^* - v_L)$ with $P + SRC$ controller working.

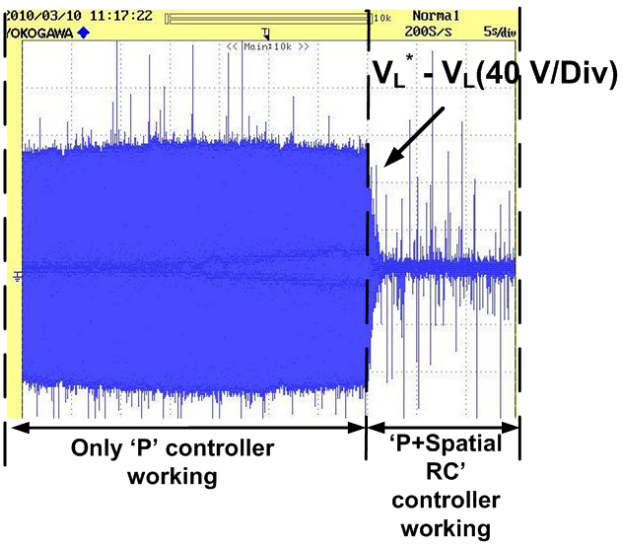

Figure 5.18: Experimental results convergence of load voltage error, $(v_L^* - v_L)$ with $P + SRC$ controller working.

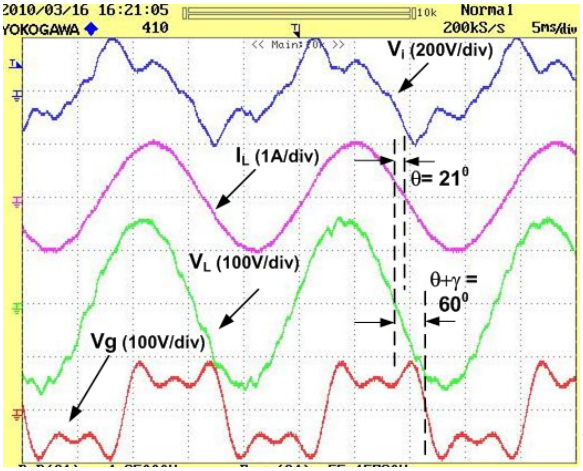

Figure 5.19: Experimental results under 36% grid voltage sag condition with 50% contamination of 3rd harmonics and 30% contamination of 5th harmonics at grid frequency $f_f = 55\,Hz$, of grid voltage v_g, load voltage v_L, load current i_L and inverter voltage v_i with $P + SRC$ controller working.

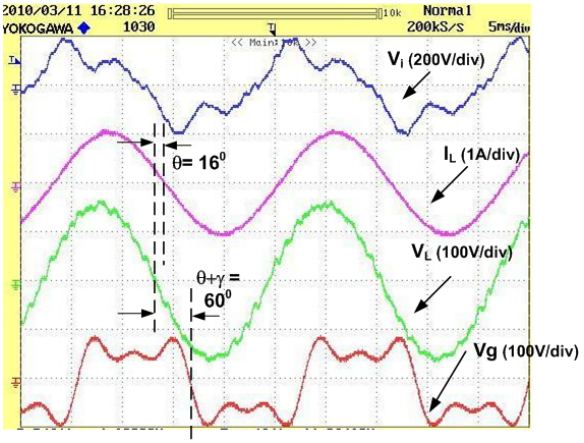

Figure 5.20: Experimental results under 36% grid voltage sag condition with 50% contamination of 3rd harmonics and 30% contamination of 5th harmonics at grid frequency $f_f = 45\,Hz$, of grid voltage v_g, load voltage v_L, load current i_L and inverter voltage v_i with $P + SRC$ controller working.

erates harmonic voltages to counter these grid voltage harmonics as can be seen in Figure 5.16. The transient performance of the SRC to converge the voltage error, $(v_L^* - v_L)$, is shown in Figures 5.17 and 5.18 (two waveforms are given with different voltage and time scale). Figures 5.17 and 5.18 show that the load voltage error is high when only *Proportional* controller is working and when the SRC is plugged in, the load voltage error gradually converges to zero. Thus it can be concluded that, it is possible to maintain rated quality load voltage in the presence of grid disturbances as well as grid distortions with proper inverter power control.

To test the *auto-synchronization with the grid* frequency property, the grid frequency is suddenly changed to $f_g = 55\,Hz$ and $f_g = 45\,Hz$ and the experimental steady state waveforms are shown in Figures 5.19 and 5.20 respectively. In both the cases, the load voltage, v_L is seen to maintain the same 60^0 phase lead relation

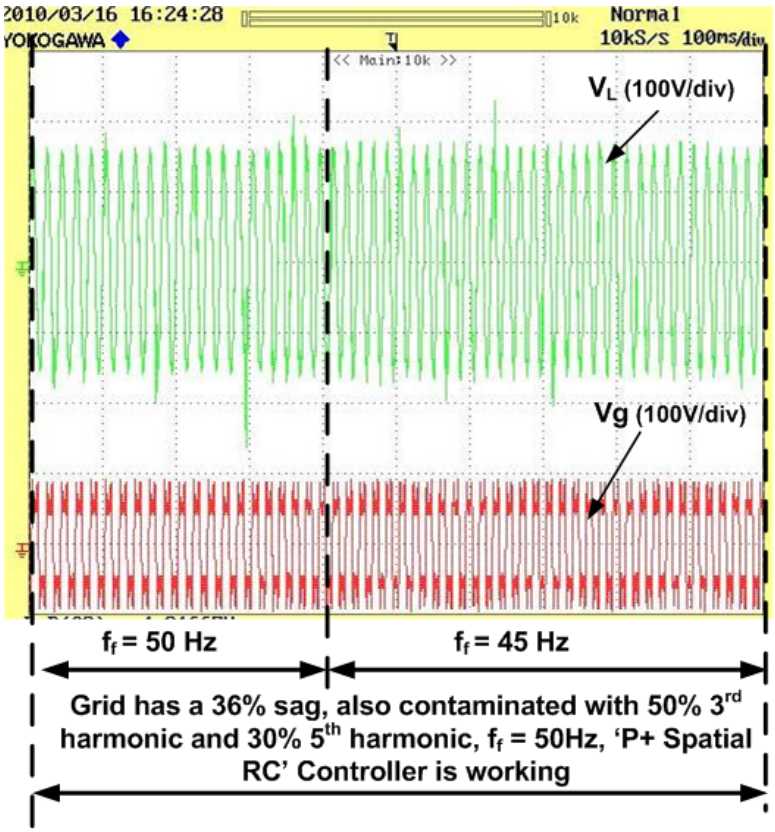

Figure 5.21: Experimental results of load voltage v_L and grid voltage v_g under 36% grid voltage sag condition with 50% contamination of 3rd harmonics and 30% contamination of 5th harmonics and sudden change of grid voltage from $f_f = 50\,Hz$ to $f_f = 45\,Hz$,with $P + SRC$ controller working.

with the grid voltage, v_g at steady state and the load voltage is not contaminated with grid voltage harmonics and maintained at rated value. The transient effect of grid frequency change on load voltage is shown in Figure 5.21. The effect of this dynamics associated with the PLL can be seen in experimental waveform Figure 5.21. Figure 5.21 shows that, when there is a sudden change of grid frequency from $f_f = 50\,Hz$ to $f_f = 45\,Hz$, there is slight increase in magnitude in load voltage and after that, the load voltage again goes back to the rated magnitude. The reason of dynamic increase in load voltage can be explained by the fact that, during the time when PLL is undergoing dynamics, the inverter voltage is tuned at $50\,Hz$ and the grid voltage is tuned at $45\,Hz$, leading to a power oscillation between inverter

and grid. But, the dynamic phase is small enough (almost undistinguishable from Figure 5.21) to destroy the power system stability.

A *Lyapunov function* based voltage controller is also investigated to overcome the slow dynamic operation of the SRC. The tracking performance of the *Lyapunov function* based controller is found to be satisfactory, however to reject the grid voltage disturbances, a huge gain is needed for the *Lyapunov function* based controller. This constraint still votes for the SRC application for this case. The details of the *Lyapunov function* based controller is provided in Appendix G.

5.3 Summary

A new control strategy for a single phase series connected inverter to interconnect AC loads with the micro-grid is proposed in Chapter 4. The control strategy is designed to stabilize the load voltage irrespective of the grid voltage magnitude as well as transfers a specific amount of renewable source based power to the load. Besides, the inverter is forced to operate in such a way that, grid always sees a leading power factor load even at the presence of lagging power factor load. A non-linear SRC is proposed in this Chapter which tracks as well as eliminates the harmonics in the load voltage facilitating the control strategy. The controller is implemented based on position domain of the fundamental micro-grid phase angle. A position domain modeling of inverter and L-C filter assembly with load and grid interconnection is also presented to facilitate the design procedure of the proposed SRC. The inverter along with the control strategy is effective in stabilizing the load voltage in the interconnection of renewable energy source as well as micro-

grid. Micro-grid voltage magnitude may vary around nominal value as well as the grid voltage may have been contaminated with harmonics. Additionally, the frequency of the micro grid voltage can also vary with time, but the load voltage is always synchronized with the fundamental phase of the grid. The proposed controller is implemented in grid phase domain, which facilitates the requirement of auto synchronization issue of maintaining undistorted nominal load voltage, with the grid voltage. The experimental test results presented validate that proposed concept of the controller.

Chapter 6

Analysis and control of a three-phase renewable energy source based inverter connected to a generalized micro-grid system

This Chapter deals with the analysis and modeling of a three phase renewable energy source based inverter interconnecting with three phase generalized micro-grid system. A detailed analysis is provided for the inverter modeling to take care of the unbalance in the line side inductors as well as unbalance and harmonic contamination in the common AC thee-phase bus inside the micro-grid. The modeling is done in the state-space domain to derive a dedicated control law to control the inverter current with arbitrary reference shape to ensure proper active and reactive power to the point of common coupling (PCC) in the micro-grid. A *Lypunov function* based current controller is proposed in this Chapter for a three-phase inverter along with its all types of unbalance. The current controller is implemented directly in the *a-b-c* frame unlike the conventional current controller.

6.1 General description of the renewable energy source based inverter: interface between micro-grid and utility grid

6.1.1 Description of the inverter interaction with the micro-grid

Figure 6.1 shows the configuration of the three-phase multi-bus micro-grid considered in this Chapter. The details of this micro-grid structure can be found in [24]-[27] and Chapter 1. The three-phase micro-grid is connected to the mains utility grid at the point of common coupling (PCC) using a circuit breaker as shown in Figure 6.1. It can also be noticed that the targeted renewable energy source

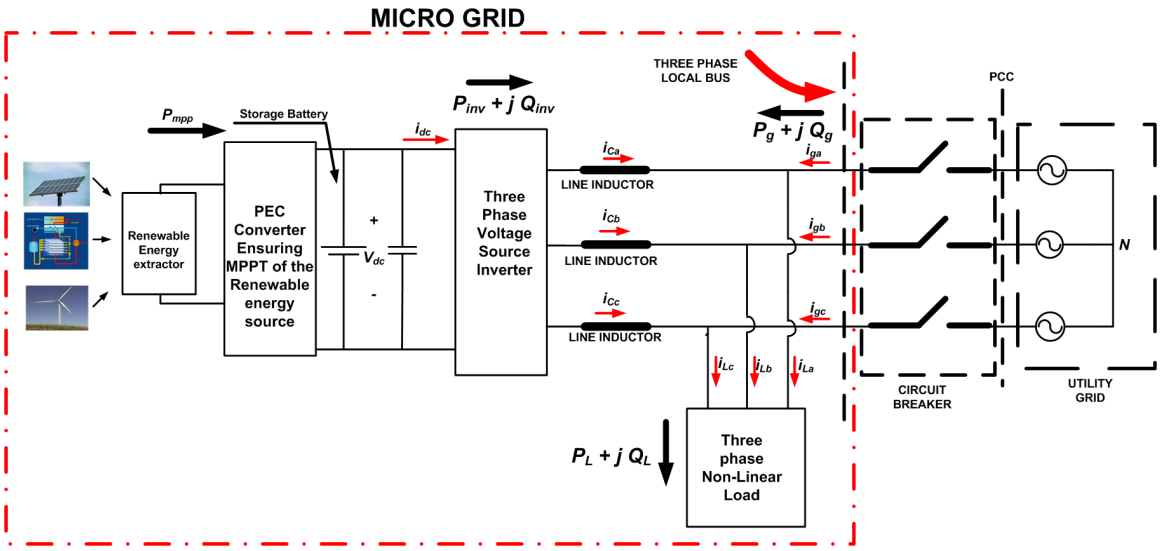

Figure 6.1: Typical configuration of a renewable energy fed three-phase micro-grid.

based inverter is connected at the three-phase local bus directly using a set of line side inductors (choke coil). At the same local bus point, a three-phase non-linear load is also connected. The non-linear load draws non-sinusoidal current from the local bus. As discussed in Chapter 2 and 4, the *power electronic converter* (PEC)

extracts power from the renewable energy sources (may be solar, wind or fuel cell based energy harvester) at Maximum Power Point (MPP) operation (extracting P_{mpp} from the renewable energy sources). The details of the MPPT circuit in the case of PV system is explained in Figure B.1 in Appendix B. The output of the *PEC* is connected to an energy storage device such as battery, which is connected to the inverter DC link. The voltage source inverter (VSI) operates in CCVSI mode to have flexible power flow control through the inverter.

6.1.2 Control methodology of the inverter current

In this work, the three-phase local bus voltage is referred to as grid voltage v_{ga}, v_{gb} and v_{gc} with respect to the utility grid neutral, N. It can be understood from Figure 6.1 that the *PEC* converter extracts maximum power, P_{mpp} from the renewable energy source. The load draws average active power, P_L and average reactive power, Q_L from the grid (i.e complex load power, $S_L = P_L + j\,Q_L$). The total load active power is shared by the grid average active power, P_g and the average active power provided by the inverter, P_{inv}. The inverter active power flow is controlled in such a way that when the DC link battery is not fully charged, certain amount of active power $P_{bat} = P_{mpp} - P_{inv}$ is pumped into the battery and when the battery is fully charged, the full harvested power, P_{mpp} is fed to the grid by the inverter. So, it can be understood that based on the amount of the harvested renewable energy, there can be savings on the power consumption from the grid by the load. The CCVSI is controlled in such a way that the three-phase inverter currents (i_{Ca}, i_{Cb} and i_{Cc}) follow their corresponding references to ensure a specific grid power consumption along with maintaining the grid currents (i_{ga}, i_{gb} and i_{gc}) to be sinusoidal and drawing zero average reactive power from

the grid. The CCVSI current references are calculated using *p-q* theory based approach to ensure minimum low frequency DC link voltage ripple to reduce the size of the electrolytic capacitor at the inverter DC link. The details of different current reference estimation methods are analyzed in details in Chapter 7. The present Chapter focuses on the current control methodology of the CCVSI.

6.2 State-space modeling of the three-phase unbalanced grid connected inverter in the a-b-c frame

Assuming that the *PEC* converter is extracting maximum power from the renewable energy source and the storage element battery is operating properly, the inverter dc link can be modeled as a DC power source. The full inverter assembly can be redrawn as shown in Figure 6.2. It can be noted that the DC link mid-point **O**

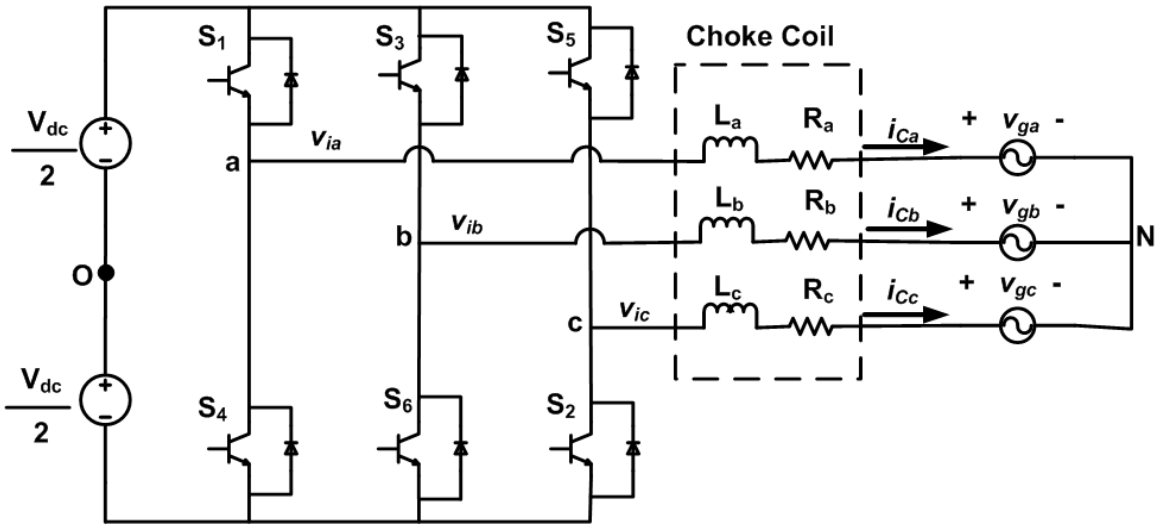

Figure 6.2: Simplified power circuit of the three-phase grid connected renewable energy inverter.

is electrically isolated from three-phase grid neutral **N**. The line side inductors as

well as the grid can have unbalance and harmonics together. The three-phase line side inductances are characterized with inductance and resistance, (L_a, R_a), (L_b, R_b) and (L_c, R_c). The parameters of the line side inductances do not necessarily have identical values in this case. The phase current of each of the phases can be written as:

$$\begin{aligned} L_a \frac{di_{Ca}}{dt} + R_a\, i_{Ca} &= v_{ia} - v_{ga} \\ L_b \frac{di_{Cb}}{dt} + R_b\, i_{Cb} &= v_{ib} - v_{gb} \\ L_c \frac{di_{Cc}}{dt} + R_c\, i_{Cc} &= v_{ic} - v_{gc} \end{aligned} \tag{6.1}$$

where, v_{ia}, v_{ib} and v_{ic} are the respective inverter phase voltages with respect to the grid neutral, **N** and v_{ga}, v_{gb} and v_{gc} are the respective grid phase voltages with respect to the grid neutral, **N**. As grid neutral **N** is isolated from the DC link mid point **O**, the three-phase currents are related as:

$$i_{Ca} + i_{Cb} + i_{Cc} = 0 \tag{6.2}$$

Subtracting phase-c equation from phase-a and phase-b equations from (6.1), following equations including line quantities are derived:

$$\begin{aligned} v_{iac} - v_{gac} &= L_a \frac{di_{Ca}}{dt} - L_c \frac{di_{Cc}}{dt} + R_a i_{Ca} - R_c i_{Cc} \\ v_{ibc} - v_{gbc} &= L_b \frac{di_{Cb}}{dt} - L_c \frac{di_{Cc}}{dt} + R_b i_{Cb} - R_c i_{Cc} \end{aligned} \tag{6.3}$$

where, v_{imn} and v_{gmn} are the respective inverter and grid line voltages between phases m and n respectively with $m, n \in a, b, c$.

Rewriting (6.3) with (6.2) by using $i_{Cc} = -(i_{Ca} + i_{Cb})$, it is found that:

$$\begin{aligned} v_{iac} - v_{gac} &= (L_a + L_c) \frac{di_{Ca}}{dt} + L_c \frac{di_{Cb}}{dt} + (R_a + R_c)\, i_{Ca} + R_c i_{Cb} \\ v_{ibc} - v_{gbc} &= (L_b + L_c) \frac{di_{Cb}}{dt} + L_c \frac{di_{Ca}}{dt} + (R_b + R_c)\, i_{Cb} + R_c i_{Ca} \end{aligned} \tag{6.4}$$

Addressing the independent states as $i_{Ca} = x_1$ and $i_{Cb} = x_2$ and solving (6.4) for $\frac{di_{Ca}}{dt}$ and $\frac{di_{Cb}}{dt}$, the following equations are found:

$$\begin{aligned} \frac{dx_1}{dt} &= a_{11}x_1 + a_{12}x_2 + b_{11}v_{iac} + b_{12}v_{ibc} + d_1 \\ \frac{dx_2}{dt} &= a_{21}x_1 + a_{22}x_2 + b_{21}v_{iac} + b_{22}v_{ibc} + d_2 \end{aligned} \tag{6.5}$$

where, $a_{11} = -\frac{R_aL_b + R_cL_b + R_aL_c}{L_aL_b + L_bL_c + L_cL_a}$, $a_{12} = -\frac{R_cL_b - R_bL_c}{L_aL_b + L_bL_c + L_cL_a}$, $a_{22} = -\frac{R_bL_a + R_cL_a + R_bL_c}{L_aL_b + L_bL_c + L_cL_a}$, $a_{21} = \frac{R_cL_a - R_aL_c}{L_aL_b + L_bL_c + L_cL_a}$, $b_{11} = \frac{L_b + L_c}{L_aL_b + L_bL_c + L_cL_a}$, $b_{12} = -\frac{L_c}{L_aL_b + L_bL_c + L_cL_a}$, $b_{21} = -\frac{L_c}{L_aL_b + L_bL_c + L_cL_a}$, $b_{22} = \frac{L_a + L_c}{L_aL_b + L_bL_c + L_cL_a}$, $d_1 = -\frac{(L_b + L_c)v_{gac} - L_cv_{gbc}}{L_aL_b + L_bL_c + L_cL_a}$, $d_2 = -\frac{-L_cv_{gac} + (L_a + L_c)v_{gbc}}{L_aL_b + L_bL_c + L_cL_a}$.

(6.5) can be further modified to (6.6) as:

$$\begin{aligned} \frac{dx_1}{dt} &= a_{11}x_1 + a_{12}x_2 + u_1 + d_1 \\ \frac{dx_2}{dt} &= a_{21}x_1 + a_{22}x_2 + u_2 + d_2 \end{aligned} \tag{6.6}$$

The control inputs u_1 and u_2 can be expressed in terms of line voltages v_{iac} and v_{ibc} are shown as:

$$\begin{aligned} \begin{bmatrix} u_1 \\ u_2 \end{bmatrix} &= \begin{bmatrix} b_{11} & b_{12} \\ b_{21} & b_{22} \end{bmatrix} \begin{bmatrix} v_{iac} \\ v_{ibc} \end{bmatrix} \\ \Rightarrow \begin{bmatrix} v_{iac} \\ v_{ibc} \end{bmatrix} &= \begin{bmatrix} b_{11} & b_{12} \\ b_{21} & b_{22} \end{bmatrix}^{-1} \begin{bmatrix} u_1 \\ u_2 \end{bmatrix} \end{aligned} \tag{6.7}$$

where d_1 and d_2 can be regarded as the disturbance inputs to the state equations shown in (6.6). In practical cases, the disturbance terms d_1 and d_2 in (6.6) consist of not only grid voltage disturbances (which is predictable by (6.5) and (6.6) but unpredictable non-linear periodic disturbances such as voltage drops due to inverter blanking time etc, as explained in details in Chapter 3.

6.3 Design of Non-Linear Control Law based on Lyapunov Function

6.3.1 Determining the Lyapunov function based control law to ensure current control

It can be seen from (6.6), that the three-phase grid connected inverter consists of two states, x_1 and x_2. So, for arbitrary waveform tracking in these two states, a non-linear control law is derived based on the *Lyapunov function* method, i.e. the first principle of absolute stability.

Considering the *Lyapunov function* as:

$$V = \frac{1}{2} e^T e \tag{6.8}$$

where error array e is represented as:

$$e = \begin{bmatrix} e_1 \\ e_2 \end{bmatrix} = \begin{bmatrix} x_1^* - x_1 \\ x_2^* - x_2 \end{bmatrix} \tag{6.9}$$

where, x_1^* and x_2^* are the tracking references of x_1 and x_2 respectively.

According to the property of *Lyapunov function*, $V > 0$ for all the conditions except $e = 0$ in this case. Thus, the selected V can be mentioned to be a *positive definite* function. It is required to find out control inputs $u_1(t)$ and $u_2(t)$ such that tracking error matrix $e(t)$ asymptotically converges to zero. *Lyapunov* direct method is used to find the control inputs $u_1(t)$ and $u_2(t)$ for the specific application.

The first time derivative of V is shown as:

$$\frac{dV}{dt} = e^T \frac{de}{dt} \tag{6.10}$$

Substituting (6.6), in (6.10), the results manifest as:

$$\frac{dV}{dt} = e^T \begin{bmatrix} \frac{dx_1^*}{dt} - a_{11}x_1 - a_{12}x_2 - u_1 - d_1 \\ \frac{dx_2^*}{dt} - a_{21}x_1 - a_{22}x_2 - u_2 - d_2 \end{bmatrix} \tag{6.11}$$

From *Lyapunov function* method of finding the stability, the first derivative should be a negative definite function as:

$$\frac{dV}{dt} = -e^T \Gamma e \tag{6.12}$$

where $\Gamma = \begin{bmatrix} \lambda_1 & 0 \\ 0 & \lambda_2 \end{bmatrix}$ with λ_1 and λ_2 are to be a positive quantity.

Comparing (6.11) and (6.12), the control variables can be solved as shown in (6.13).

$$\begin{aligned} u_1 &= \frac{dx_1^*}{dt} - a_{11}x_1 - a_{12}x_2 + \lambda_1 e_1 - d_1 \\ u_2 &= \frac{dx_2^*}{dt} - a_{21}x_1 - a_{22}x_2 + \lambda_2 e_2 - d_2 \end{aligned} \tag{6.13}$$

6.3.2 Estimation of the disturbance terms d_1 and d_2 to facilitate successful current tracking

As explained in details in Chapter 3 that, using voltage sensors, it is impossible to accurately estimate the disturbance terms in d_1 and d_2 because of the delays associated in the voltage sensors (specifically in the presence of harmonics in grid voltages) and also the unpredictable nature of the disturbances due to different non-linear phenomena in the inverter. If the estimates of the disturbance terms, $\widehat{d_1}$ and $\widehat{d_2}$ are different from its actual values, the control signals are affected accordingly. Using the improper values of disturbance terms, if the control laws in (6.13) are modified and plugged-in (6.11), (6.12) are modified as:

$$\frac{dV}{dt} = -e^T \Gamma e + e^T \begin{bmatrix} (\widehat{d_1} - d_1) \\ (\widehat{d_2} - d_2) \end{bmatrix} \tag{6.14}$$

Thus, the tracking error matrix, e converges to a value $e = \begin{bmatrix} e_{1b} \\ e_{2b} \end{bmatrix}$ with $\frac{dV}{dt} = 0$ as:

$$\begin{bmatrix} e_1 \\ e_2 \end{bmatrix} = \begin{bmatrix} e_{1b} \\ e_{2b} \end{bmatrix} = \begin{bmatrix} \frac{\widehat{d}_1 - d_1}{\lambda_1} \\ \frac{\widehat{d}_2 - d_2}{\lambda_2} \end{bmatrix} \tag{6.15}$$

Hence, to ensure perfect current tracking, the two disturbance terms are estimated by the SRC based on the residual current errors as also done in Chapter 2. Following this analysis, the control laws in (6.13) are modified as:

$$\begin{bmatrix} u_1(t) \\ u_2(t) \end{bmatrix} = \begin{bmatrix} u_{lf1}(t) + u_{src1}(t) \\ u_{lf2}(t) + u_{src2}(t) \end{bmatrix} \tag{6.16}$$

where, *Lyapuov function* based control laws are represented as:

$$\begin{bmatrix} u_{lf1}(t) \\ u_{lf2}(t) \end{bmatrix} = \begin{bmatrix} \frac{dx_1^*}{dt} - a_{11}x_1 - a_{12}x_2 + \lambda_1 e_1 \\ \frac{dx_2^*}{dt} - a_{21}x_1 - a_{22}x_2 + \lambda_2 e_2 \end{bmatrix} \tag{6.17}$$

However, the disturbance terms are estimated using SRC as:

$$\begin{bmatrix} u_{src1}(t) \\ u_{src2}(t) \end{bmatrix} = \begin{bmatrix} -d_1 \\ -d_2 \end{bmatrix} \tag{6.18}$$

For a typical micro-grid application, the grid voltage as well as inverter unpredictable non-linearities do not change very frequently, so the slow dynamics of SRC control laws are dominated by the fast dynamics of *Lyapunov function* control laws in the case of sudden change in current references as also discussed in Chapter 2. The details of the overall control system is shown in Figure 6.3.

6.3.3 Ensuring the stability of the plugged-in spatial repetitive controller in parallel with the Lyapunov function based controller

The stability of the overall system can be judged, by substituting (6.16) in (6.6) and the resulting state equations are as follows:

$$\begin{bmatrix} \dot{x_1} \\ \dot{x_2} \end{bmatrix} = \begin{bmatrix} \frac{dx_1^*}{dt} + \lambda_1 (x_1^* - x_1) + d_1 + u_{src1} \\ \frac{dx_2^*}{dt} + \lambda_2 (x_2^* - x_2) + d_2 + u_{src2} \end{bmatrix} \tag{6.19}$$

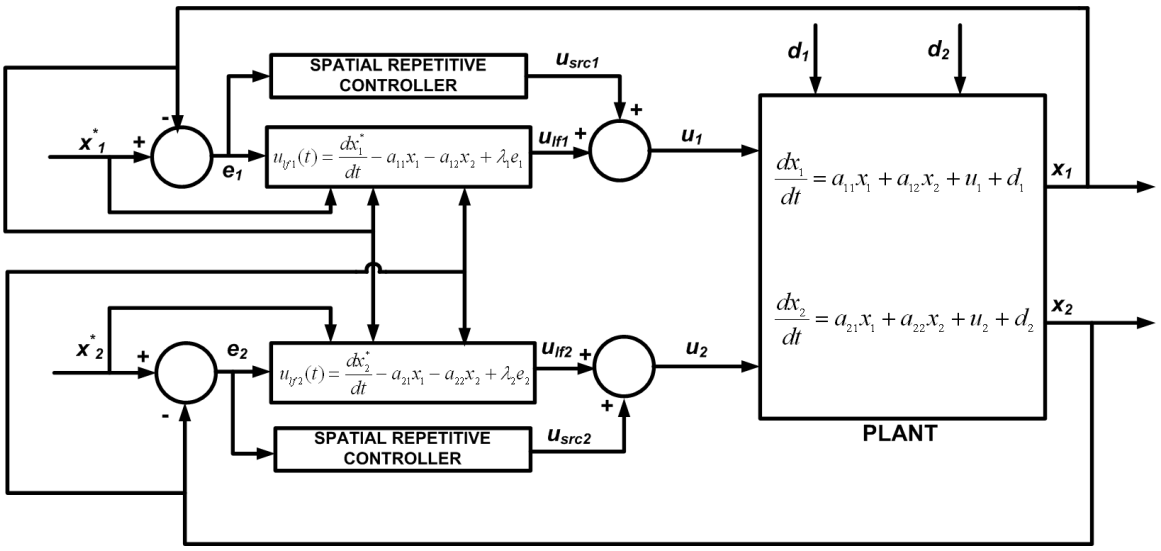

Figure 6.3: Schematics of overall control system.

(6.19) can be re-arranged as:

$$\begin{bmatrix} \dot{x_1} + \lambda_1 x_1 \\ \dot{x_2} + \lambda_2 x_2 \end{bmatrix} = \begin{bmatrix} \frac{dx_1^*}{dt} + \lambda_1 x_1^* + d_1 + u_{src1} \\ \frac{dx_2^*}{dt} + \lambda_2 x_2^* + d_2 + u_{src2} \end{bmatrix} = \begin{bmatrix} d_{mod1} + u_{src1} \\ d_{mod2} + u_{src2} \end{bmatrix} \quad (6.20)$$

where, $d_{mod1} = \left[\frac{dx_1^*}{dt} + \lambda_1 x_1^* + d_1\right]$ and $d_{mod2} = \left[\frac{dx_1^*}{dt} + \lambda_1 x_1^* + d_1\right]$ are regarded as the periodic disturbances with the period of the fundamental grid frequency seen by the repetitive controllers SRC1 and SRC2 respectively. So, each of the SRCs are designed using the modified plant transfer functions $G_{mod1}(s) = \frac{1}{s+\lambda_1}$ and $G_{mod2}(s) = \frac{1}{s+\lambda_2}$, engaging the design technique proposed in Chapter 2. The design method of plugged-in SRC is not further exaggerated in this Chapter.

6.3.4 Effect of parameter uncertainty on the error convergence

If (6.13) are observed carefully, it is seen that the parameters of the control laws, a_{11}, a_{12}, a_{21} and a_{22} are dependent on the actual values of the resistances and inductances of the line side inductors in the system. However, the resistances and

inductances of the line side inductors cannot be estimated accurately. If the estimated values (different from the actual values) of the system parameters are mentioned as: $\widehat{a}_{11}$, $\widehat{a}_{12}$, $\widehat{a}_{21}$ and $\widehat{a}_{22}$ respectively, the control laws can be re-structured as:

$$\begin{aligned} u_1 &= \frac{dx_1^*}{dt} - \widehat{a}_{11}x_1 - \widehat{a}_{12}x_2 + \lambda_1 e_1 - d_1 \\ u_2 &= \frac{dx_2^*}{dt} - \widehat{a}_{21}x_1 - \widehat{a}_{22}x_2 + \lambda_2 e_2 - d_2 \end{aligned} \tag{6.21}$$

Plugging in (6.21) in (6.11), the resulting equations can be written as:

$$\begin{aligned} \frac{dV}{dt} &= -e^T \Gamma e + e^T \begin{bmatrix} (\widehat{a}_{11} - a_{11})\, x_1 + (\widehat{a}_{12} - a_{12})\, x_2 \\ (\widehat{a}_{21} - a_{21})\, x_1 + (\widehat{a}_{22} - a_{22})\, x_2 \end{bmatrix} \\ \Rightarrow \frac{dV}{dt} &= \left(-\lambda_1 e_1^2 + e_1 D_1(.)\right) + \left(-\lambda_2 e_2^2 + e_2 D_2(.)\right) \end{aligned} \tag{6.22}$$

where, $D_1(.) = [(\widehat{a}_{11} - a_{11})\, x_1 + (\widehat{a}_{12} - a_{12})\, x_2]$ and $D_2(.) = [(\widehat{a}_{21} - a_{21})\, x_1 + (\widehat{a}_{22} - a_{22})\, x_2]$

The conclusion can be drawn from (6.22) that, to make $\frac{dV}{dt}$ *negative definite*, the condition can be expressed as:

$$\begin{aligned} |\lambda_1\, e_1^2| &> |e_1\, D_1(.)| \\ |\lambda_2\, e_2^2| &> |e_2\, D_2(.)| \end{aligned} \tag{6.23}$$

If the parameters λ_1 and λ_2 are selected as:

$$\begin{aligned} \lambda_1 &> \frac{|D_1(.)|_{max}}{e_b} \\ \lambda_2 &> \frac{|D_2(.)|_{max}}{e_b} \end{aligned} \tag{6.24}$$

Both the errors, e_1 and e_2 converge to the error bound e_b, which is selected to be sufficiently close to 0. Satisfying (6.24) ensure the robustness of the proposed *Lyapunov function* based controller to the parameter uncertainty of the overall system.

6.4 Implementation of the Lyapunov function based controller

6.4.1 Implementation of the proposed control system using the four-switch (b-4) inverter power circuit

The control inputs u_1 and u_2 are found instantly by using (6.13) and the line voltage references v_{iac} and v_{ibc} are calculated using (6.7) to track the reference inverter phase currents, i_{Ca} and i_{Cb}. It can be understood that (6.13) and (6.7) provide constraint on the inverter line voltages v_{iac} and v_{ibc} but there is no constraint on phase voltages of the inverter with respect to the DC link mid point **O** (as shown in Figure 6.2). If the phase to DC link mid-point voltages of each phase of the inverter is called v_{iaO}, v_{ibO} and v_{cO} for three phases respectively. The inverter line voltages can be written in terms of inverter phase voltages as shown:

$$\begin{aligned} v_{iac} &= v_{iaO} - v_{icO} \\ v_{ibc} &= v_{ibO} - v_{icO} \end{aligned} \tag{6.25}$$

As there is no constraint on the inverter phase voltages, so the phase voltages of the inverter with respect to the DC link mid-point, **O** can be made as:

$$\begin{aligned} v_{iaO} &= v_{iac} \\ v_{ibO} &= v_{ibc} \\ v_{icO} &= 0 \end{aligned} \tag{6.26}$$

If the inverter is operating in Sine PWM, the control signals for the upper switches (S_1, S_3 and S_5) as shown in Figure 6.2 are shown as:

$$\begin{aligned} v_{cona} &= \frac{2\, v_{iac}}{V_{dc}} \\ v_{conb} &= \frac{2\, v_{ibc}}{V_{dc}} \\ v_{conc} &= 0 \end{aligned} \tag{6.27}$$

The switching signals of the lower switches, S_2, S_4 and S_6 are found as:

$$\begin{aligned} S_4 &= \overline{S_1} \\ S_6 &= \overline{S_3} \\ S_5 &= \overline{S_2} \end{aligned} \tag{6.28}$$

It can be noted as the requirement of pole voltages of the inverter is such that $v_{icO} = 0$, so phase C terminal can be directly connected to the DC link mid point **O** as shown in Figure 6.4. This power circuit configuration is designated as *b-4* topology in the literature [111]-[112]. Detailed experimental results as well as different problems associated with *b-4* structure are also described and the detailed solutions by the proposed control strategy are discussed in Chapter 8.

6.4.2 Implementation of the proposed control system using the six-switch (b-6) inverter power circuit

The proposed control structure can also be implemented using traditional *b-6* three-phase inverter power circuit. However, the implementation method is little different from just mentioned above.

For three-phase generalized grid system, the following relation is considered:

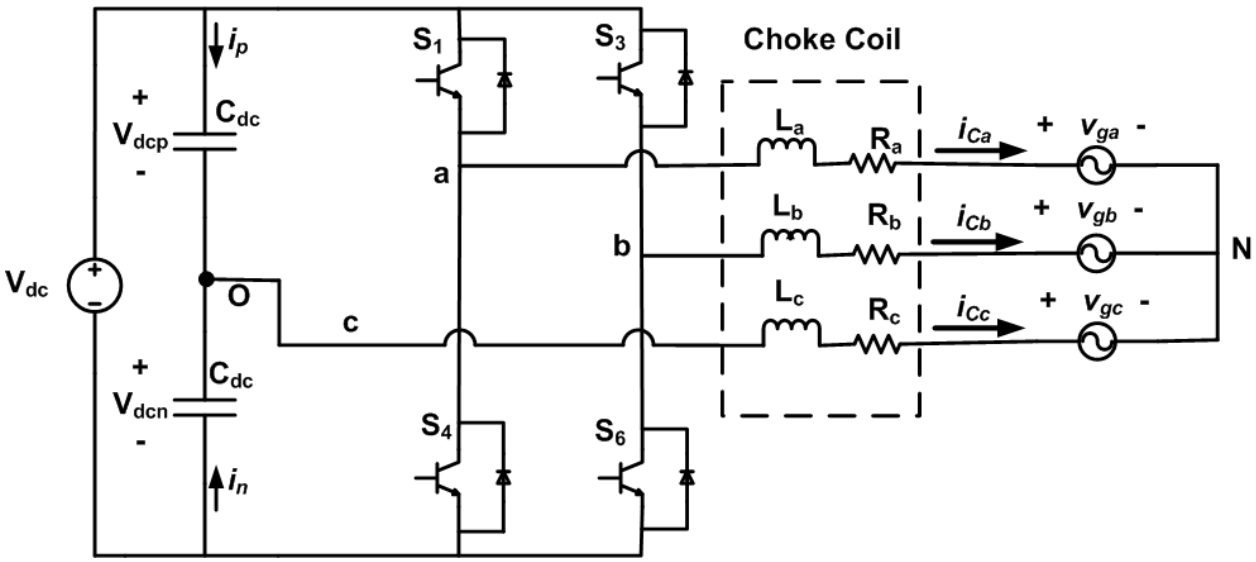

Figure 6.4: Modified power circuit of the three-phase grid connected inverter *with two IGBT legs*

$$v_{iaO} + v_{ibO} + v_{icO} = x \tag{6.29}$$

where, x is a value provided so that each of the inverter phase are under the influence of similar voltage and current stress. This is facilitated to optimize the operation of each of the inverter legs. As mentioned before, control strategy does not put any constraint on each individual pole voltages but only on two of the line voltages.

Utilizing (6.29) in (6.25), the inverter phase to DC link mid point voltage references can be calculated as:

$$\begin{aligned} v_{aO} &= \frac{x}{3} + \frac{2v_{iac} - v_{ibc}}{3} = \frac{1}{3}(x + 2v_{iac} - v_{ibc}) \\ v_{bO} &= \frac{x}{3} + \frac{2v_{ibc} - v_{iac}}{3} = \frac{1}{3}(x + 2v_{ibc} - v_{iac}) \\ v_{cO} &= \frac{x}{3} - \frac{1}{3}(v_{iac} + v_{ibc}) = \frac{1}{3}(x - v_{iac} - v_{ibc}) \end{aligned} \tag{6.30}$$

In the case of Sine PWM, the control signals for the upper switches (S_1, S_3 and S_5

as shown in Figure 6.2 are shown as:

$$\begin{aligned} v_{cona} &= \frac{2}{3\,V_{dc}}\left(x\ +\ 2v_{iac}\ -\ v_{ibc}\right) \\ v_{conb} &= \frac{2}{3\,V_{dc}}\left(x\ +\ 2v_{ibc}\ -\ v_{iac}\right) \\ v_{conc} &= \frac{2}{3\,V_{dc}}\left(x\ -\ v_{iac}\ -\ v_{ibc}\right) \end{aligned} \tag{6.31}$$

It can be remarked from (6.31), if x increases, each phase control signal value unnecessarily goes towards overmodulation. So, for the present case of experimental study, $x\ =\ 0$ is maintained.

6.4.3 Implementation of the proposed controller in digital system

The control system shown in Figure 6.3 is implemented inside DS1104 dSPACE controller board with sampling frequency $f_{sample}\ =\ 10\,kHz$. The SPWM switching frequency is taken as $f_s\ =\ 10\,kHz$. The first time derivative terms in the control signals are replaced by its backward approximation rule. The *Lyapunov function* based control (modifying (6.17)) law portion for PWM (control input) at k^{th} sampling instant can be written as,

$$\begin{bmatrix} u_{lf1}(k) \\ u_{lf2}(k) \end{bmatrix} = \begin{bmatrix} \frac{x_1^*(k)\,-\,x_1^*(k-1)}{T_s}\ -\ a_{11}x_1(k)\ -\ a_{12}x_2(k)\ +\ \lambda_1\left[x_1^*(k)\ -\ x_1(k)\right] \\ \frac{x_2^*(k)\,-\,x_2^*(k-1)}{T_s}\ -\ a_{21}x_1(k)\ -\ a_{22}x_2(k)\ +\ \lambda_2\left[x_2^*(k)\ -\ x_2(k)\right] \end{bmatrix} \tag{6.32}$$

where, $T_s\ =\ \frac{1}{f_{sample}}$.

In the experimental study, the *Lyapunov function* based control law is implemented with the estimated average inductor parameters, $\widehat{L}_a\ =\ \widehat{L}_b\ =\ \widehat{L}_c\ =\ L\ =\ 5\,mH$ and $\widehat{R}_a\ =\ \widehat{R}_b\ =\ \widehat{R}_c\ =\ R\ =\ 1\,\Omega$. The design of λ_1 and λ_2 is done using the $\pm 10\%$ uncertainty of the phase inductor parameters. It is considered that, the

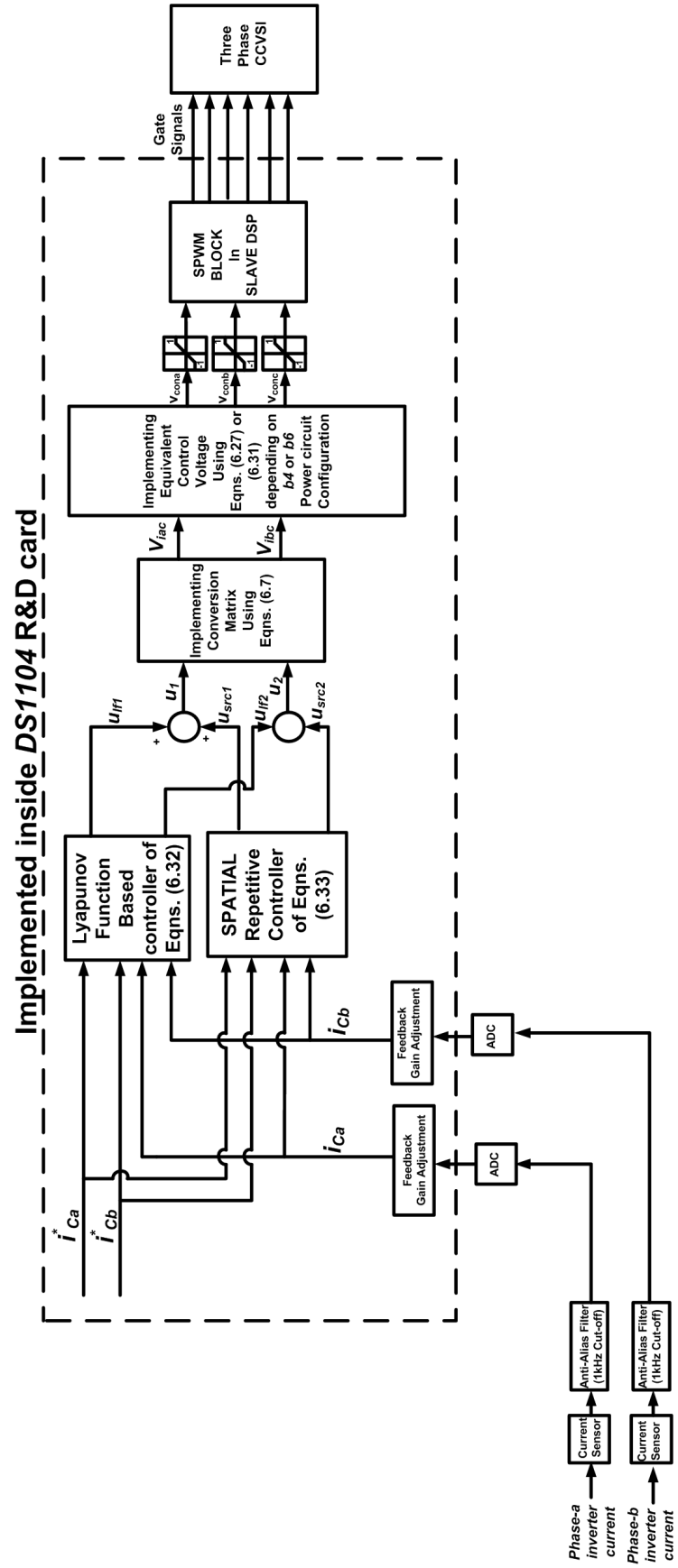

Figure 6.5: Details of the implementation method of the proposed control strategy.

actual phase inductances are: $L_a = 5\,mH$, $L_b = (1+\frac{10}{100})\ L_a = 5.5\,mH$ and $L_c = (1-\frac{10}{100})L_a = 4.5\,mH$. Similarly, the actual phase resistances are considered as: $R_a = 0.1\,\Omega$, $R_b = (1+\frac{10}{100})R_a = 0.11\,\Omega$ and $R_c = (1-\frac{10}{100})R_a = 0.09\,\Omega$. The actual system parameters, a_{11}, a_{12}, a_{21}, a_{22} are calculated based on the considered actual inductor parameters of the system and the estimated system parameters $\widehat{a}_{11}$, $\widehat{a}_{12}$, $\widehat{a}_{21}$, $\widehat{a}_{22}$ are calculated based on the estimated inductor parameters of the system. Thus by calculating the value of $D_1(.)$ and $D_2(.)$ (following (6.22)) using the maximum value of both the currents (x_1 and x_2) to be 10 A and using (6.24) (as also done in Chapter 2 for the single phase case), the values of λ_1 and λ_2 are found as $\lambda_1 = \lambda_2 = \lambda = 300000$ and are used for experimental study.

Both the SRC control law portion at k^{th} position sample, θ_k and at i^{th} iteration cycle, (implemented on fundamental grid phase θ as mentioned in Chapters 2 and 4) (as can be refereed to (6.18) are implemented as:

$$\begin{bmatrix} u_{src1}(i,\theta_k) \\ u_{src2}(i,\theta_k) \end{bmatrix} = \begin{bmatrix} u_{src1}(i-1,\theta_k) + K_{src}\, e_1(i-1,\theta_{k+N_1}) \\ u_{src2}(i-1,\theta_k) + K_{src}\, e_2(i-1,\theta_{k+N_1}) \end{bmatrix} \tag{6.33}$$

The parameters of both the SRCs are designed based on the transfer function analysis done in (6.20) and following the analysis already given in details in Chapter 2. The design methodology is not further elaborated in this Chapter. The values of the parameters of the SRCs are used are, the gains, $K_{src} = 100$ (the value is calculated considering the convergence criterion of SRC as discussed in Chapter 2) and the phase sample advancement, $N_1 = 6$ (the value is calculated considering the phase delay compensation in the control loop as discussed in Chapter 2). The detailed control system implementation is shown in Figure 6.5. The rapid prototyping DSP dSPACE ds1104 card makes it possible to implement the proposed control strategy efficiently.

A performance comparison of the proposed *Lyapunov function* based current controller with the state-of-art PI+fundamental frame multiple PR controller is done and the comparing results are provided in Appendix H.

6.5 Experimental Results

6.5.1 Hardware details of the experimental power circuit

The proposed controller is validated by extensive testing on a developed prototype. The overall control system is implemented in DS1104 dSPACE card. The switching frequency of the SPWM, f_s as well as the sampling frequency of the overall control system, f_{sample} is set at $10kHz$ during the course of the experiments. Experimental grid voltages are formed using ***Lx3000 California Instrument*** three-phase programmable power supply. The non-linear load is taken to be a three-phase rectifier terminated to a resistive, capacitive assembly. In this control topology, the parallel inverter (operating in CCVSI mode) is not only controlling the active and reactive power flow from the grid but also compensating for the non-linear current drawn by the load from the grid terminal. So, inverter current consists of both sinusoidal power current and the inverse non-linear load current. The non-linear load current has substantial $\frac{di}{dt}$ across the inverter line side inductors necessitates higher DC link voltage requirement as also reported in the single phase case in Chapter 4. For the present case of experiment, the maximum DC link voltage is taken as $V_{dc} = 250V$ and the maximum value of the grid line voltage is restricted to $100V\,rms$ for *b-6* inverter power circuit configuration. Application of the proposed control structure on the *b-4* topology inverter as well as other power circuit related

problems in the *b-4* topology are addressed in Chapter 8. This report provides the experimental results related to *b-6* topology only. The details of the power circuit utilizing *b-6* topology, is shown in Figure 6.6.

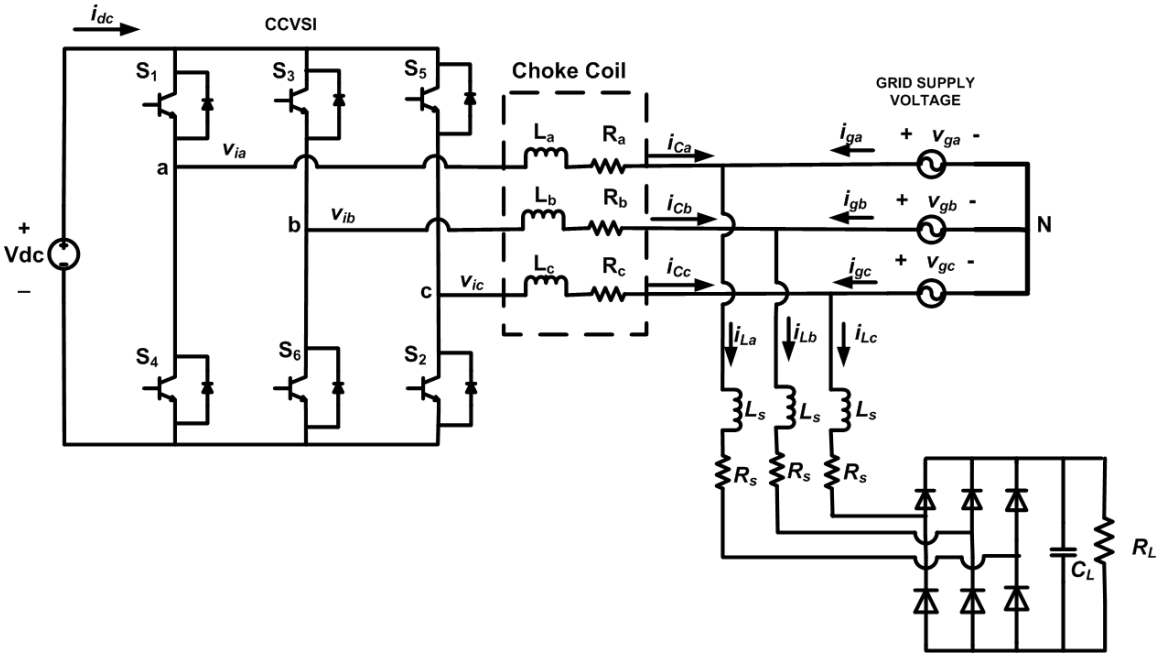

Figure 6.6: Details of the power circuit of the experiment using *b-6* inverter structure.

The parameters of the power circuit are also given in Table 6.1. The current

Table 6.1: Parameters of the experimental power circuit

Parameter	Value
maximum DC link voltage, V_{dc}	$300\,V$
maximum value of RMS of grid line voltage, v_{gll}	$100\,V$
CCVSI choke inductance, L_a, L_b, L_c	$5\,mH$
CCVSI choke resistance, R_a, R_b, R_c	$0.1\,\Omega$
Rectifier link inductance, L_s	$400\,\mu H$
Rectifier link resistance, R_s	$0.1\,\Omega$
Rectifier DC side capacitor, C_L	$3300\,\mu F$
Rectifier DC side resistance, R_L	$100\,\Omega$

reference of the CCVSI is calculated in such a way that, there is control on the part of active power drawn by the load from the grid along with maintaining the grid current to be sinusoid with unity *displacement power factor*. Hence, the CCVSI

current reference is calculated as:

$$i^*_{Cx} = i_{Lx} - i^*_{gx}, x \in a, b, c \tag{6.34}$$

where, i^*_{Cx}, i_{Lx} and i^*_{gx} are the CCVSI current reference, load current and grid current reference for phase-x. In this chapter the grid phase current references are calculated using p-q theory based method to ensure minimum possible DC link ripple due to positive and negative sequence voltage and current interaction. Different grid current reference generation methods are explained in details in Chapter 7. The focus of the present Chapter is to test the feasibility of the proposed CCVSI current tracking controller.

6.5.2 Steady state results for the *b-6* topology of there-phase inverter

The schematic of the experimental arrangement for the three-phase inverter with *b-6* topology connected to the unbalanced grid is shown in Figure 6.6. The steady state experimental results are shown in Figures 6.7 and 6.8. The grid condition is maintained with the three-phase controllable power supply (as mentioned earlier) as shown in Figure 6.7(a). It can be analyzed from Figure 6.7(a) that the grid is contaminated with 20% negative sequence and each of the phase voltages are contaminated with 5^{th}, 7^{th} and 11^{th} order voltage harmonics of 10%, 7% and 5% of the fundamental magnitude respectively. For this system, the grid voltage expression

can be represented as:

$$\begin{aligned}
v_{ga}(t) &= V_p\cos(\theta) + V_n\cos(\theta) \\
&+ 0.1\,V_p\cos(5\theta) + 0.1\,V_n\cos(5\theta) \\
&+ 0.07\,V_p\cos(7\theta) + 0.07\,V_n\cos(7\theta) \\
&+ 0.05\,V_p\cos(11\theta) + 0.05\,V_n\cos(11\theta) \\
v_{gb}(t) &= V_p\cos(\theta - \frac{2\pi}{3}) + V_n\cos(\theta + \frac{2\pi}{3}) \\
&+ 0.1\,V_p\cos(5\theta - \frac{10\pi}{3}) + 0.1\,V_n\cos(5\theta + \frac{10\pi}{3}) \\
&+ 0.07\,V_p\cos(7\theta - \frac{14\pi}{3}) + 0.07\,V_n\cos(7\theta + \frac{14\pi}{3}) \\
&+ 0.05\,V_p\cos(11\theta - \frac{22\pi}{3}) + 0.05\,V_n\cos(11\theta + \frac{22\pi}{3}) \\
v_{gc}(t) &= V_p\cos(\theta + \frac{2\pi}{3}) + V_n\cos(\theta - \frac{2\pi}{3}) \\
&+ 0.1\,V_p\cos(5\theta + \frac{10\pi}{3}) + 0.1\,V_n\cos(5\theta - \frac{10\pi}{3}) \\
&+ 0.07\,V_p\cos(7\theta + \frac{14\pi}{3}) + 0.07\,V_n\cos(7\theta - \frac{14\pi}{3}) \\
&+ 0.05\,V_p\cos(11\theta + \frac{22\pi}{3}) + 0.05\,V_n\cos(11\theta - \frac{22\pi}{3}) \qquad (6.35)
\end{aligned}$$

where, θ is the fundamental phase of grid voltage. As set in the three-phase controllable power supply, the fundamental of grid voltage has positive sequence peak magnitude is about $V_p = 49.3\,V$ and negative sequence peak magnitude is about $V_n = 9.86\,V$ and for phase-a the positive sequence and negative sequence voltage align on the same phase (total RMS of phase-a voltage is $42.2\,V$ and that of phase-b and phase-c is $32.3\,V$). The analysis of the sequence components are addressed in Chapter 8. The experiment is carried out with DC link voltage. $V_{dc} = 200\,V$. The non-linear load as described in the previous Section draws active power $P_L = 75\,W$ under this grid condition.

Initially, the total power along with the non-linear current harmonic is com-

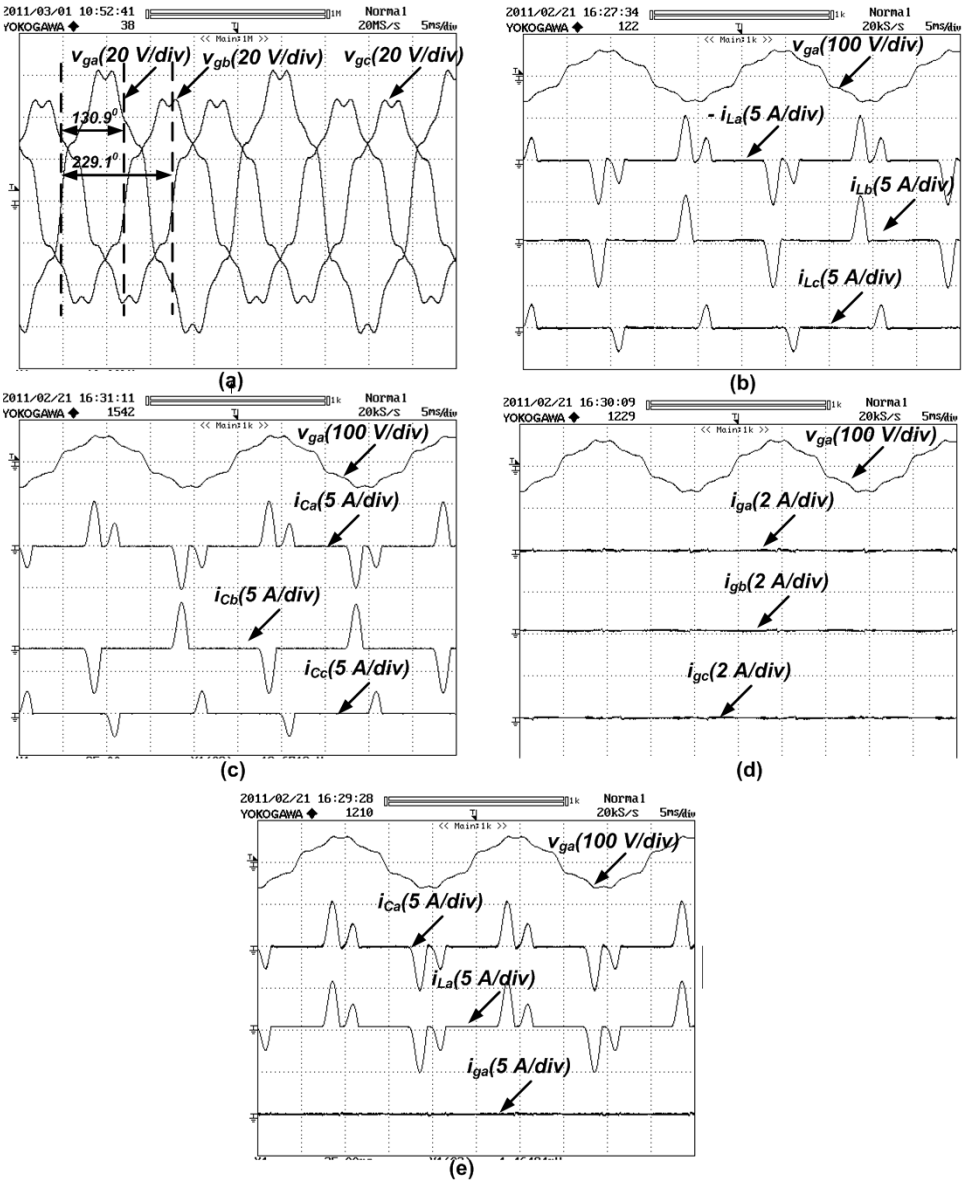

Figure 6.7: Experimental results of (a) grid voltages, v_{ga}, v_{gb} and v_{gc}, (b) phase-a grid voltage, v_{ga}, three-phase load currents, i_{La}, i_{Lb} and i_{Lc}, (c) phase-s grid voltage, v_{ga}, three-phase CCVSI currents, i_{Ca}, i_{Cb} and i_{Cc}, (d) phase-a grid voltage, v_{ga}, three-phase grid currents, i_{ga}, i_{gb} and i_{gc}, (e) phase-a grid voltage, v_{ga}, phase-a CCVSI current, i_{Ca}, phase-a load current, i_{La}, phase-a grid current, i_{ga} at grid power command, $P_g = 0\,W$ and $Q_g = 0\,Var$ with non-linear load with $P_L = 75\,W$ with *b-6* topology of inverter and $V_p = 49.3\,V$ and $V_n = 9.86\,V$.

pensated by the CCVSI with the command $P_g = 0W$ and $Q_g = 0var$. This enables the CCVSI currents (i_{Ca}, i_{Cb} and i_{Cc}) to follow the load currents, (i_{La}, i_{Lb} and i_{Lc}) as can be concluded from Figure 6.2. The experimental results in this condition

are shown in Figure 6.7. Figure 6.7(b) shows that because of the unbalance in the grid voltage, the load currents, are also asymmetrical. However, because of the *a-b-c* frame proposed control methodology, the inverter currents, i_{Ca}, i_{Cb} and i_{Cc} follow the asymmetrical load currents, i_{La}, i_{Lb} and i_{Lc}, resulting the grid currents i_{ga}, i_{gb} and i_{gc} to be zero as can be seen from Figure 6.7(c)-(e).

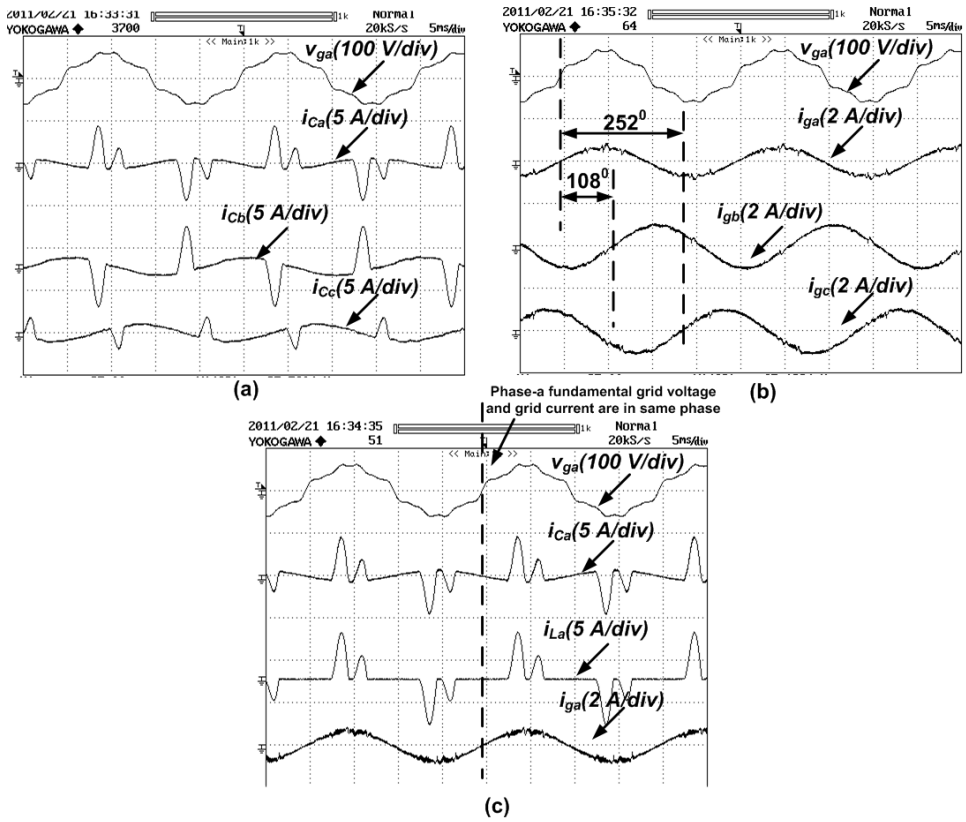

Figure 6.8: Experimental results of (a) phase-s grid voltage, v_{ga}, three-phase CCVSI currents, i_{Ca}, i_{Cb} and i_{Cc}, (b) phase-a grid voltage, v_{ga}, three-phase grid currents, i_{ga}, i_{gb} and i_{gc}, (c) phase-a grid voltage, v_{ga}, phase-a CCVSI current, i_{Ca}, phase-a load current, i_{La}, phase-a grid current, i_{ga} at grid power command, $P_g = 60\,W$ and $Q_g = 0\,Var$ with non-linear load with $P_L = 75\,W$ with *b-6* topology of inverter and $V_p = 49.3\,V$ and $V_n = 9.86\,V$.

The controller is further tested with grid current consumption command, $P_g = 60\,W$ and $Q_g = 0\,Var$. It is explained in Chapter 7 that even if the grid voltage has harmonics, the current drawn is sinusoidal with the following

mathematical form:

$$\begin{aligned} i_{ga}(t) &= I_p \cos(\theta) + I_n \cos(\theta) \\ i_{gb}(t) &= I_p \cos\left(\theta - \frac{2\pi}{3}\right) + I_n \cos\left(\theta + \frac{2\pi}{3}\right) \\ i_{gc}(t) &= I_p \cos\left(\theta + \frac{2\pi}{3}\right) + I_n \cos\left(\theta - \frac{2\pi}{3}\right) \end{aligned} \tag{6.36}$$

where, $I_p = \frac{2}{3} P_g \frac{V_p}{V_p^2 - V_n^2}$ and $I_n = -\frac{2}{3} P_g \frac{V_n}{V_p^2 - V_n^2}$

As can be predicted from Chapter 7 that, under this condition, the phase-a grid current (i_{ga}) has the peak value of $\frac{2}{3}\frac{P_g((V_p - V_n)}{V_p^2 - V_n^2}$ (for this case about 0.67 A) and each of phase-b and phase-c grid currents (i_{gb} and i_{gc}) have the peak value of $\frac{2}{3}\frac{P_g\sqrt{V_p^2 + V_n^2 + V_p V_n}}{V_p^2 - V_n^2}$ (for this case 0.94 A). It is also discussed that, phase-b grid current i_{gb} lags phase-a grid current i_{ga} by and angle $180^0 - tan^{-1}\left(\frac{\sqrt{3}\,(V_p + V_n)}{(V_p - V_n)}\right)$ (for this case about 108^0) and phase-c grid current, i_{gc} lags phase-a grid current, i_{ga} by an angle $180^0 + tan^{-1}\left(\frac{\sqrt{3}\,(V_p + V_n)}{(V_p - V_n)}\right)$ (for this case about 250^0). The experimental results for this condition are shown in Figure 6.8. It can be seen from Figure 6.8(a)-(c) that, in the presence of the non-linear load currents, the grid currents, i_{ga}, i_{gb} and i_{gc} are sinusoidal and following the property as discussed above to ensure perfect power flow control from the grid side to ensure P_g. The actual power drawn from the grid can be recalculated (by considering fundamental grid voltages) as: $P_{gactual} = \left(41.8 \times \frac{0.67}{\sqrt{2}}\right) + \left(32.02 \times \frac{0.94}{\sqrt{2}} \cos(130^0 - 108^0)\right) + \left(32.02 \times \frac{0.94}{\sqrt{2}} \cos(250^0 - 229^0)\right) \simeq 60\,W$

6.5.3 Transient results for the proposed control system

The controller is tested during transient change condition and the experimental results for the *b-6* topology of three-phase grid connected inverter is shown in

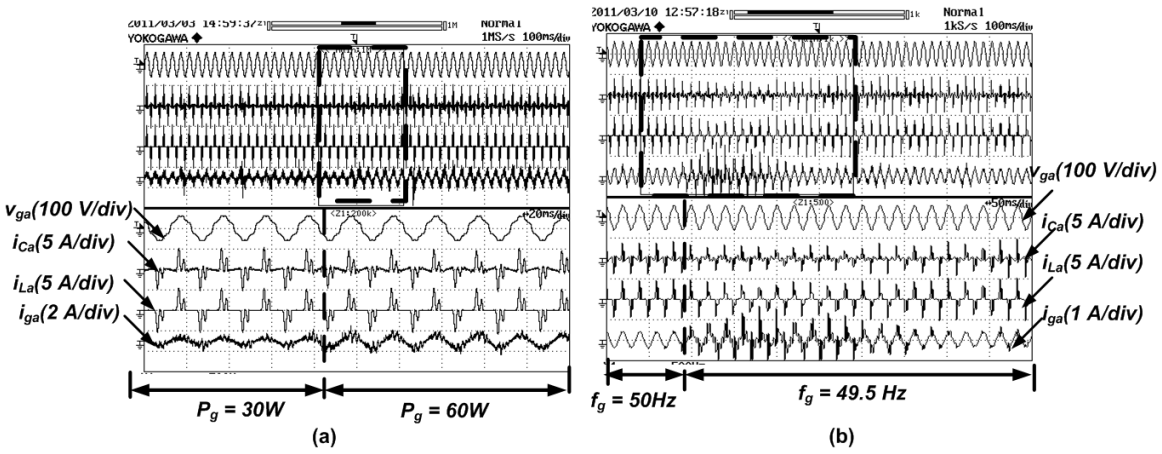

Figure 6.9: Transient experimental waveform of phase-a grid voltage, v_{ga}, phase-a CCVSI current, i_{Ca}, phase-a load current, i_{La}, phase-a grid current, i_{ga} with (a) sudden grid active power command change P_g from $30\,W$ to $60\,W$, (b) grid fundamental frequency, f_g sudden change from $50\,Hz$ to $49.5\,Hz$ with non-linear load with $P_L = 75W$ with *b-6* topology of inverter and $V_p = 49.3V$ and $V_n = 9.86$.

Figures 6.9. It can be seen from Figure 6.9(a) that, when there is a change in command of grid active power P_g from $30\,W$ to $60\,W$, the phase-a current i_{ga} peak is changed from about $0.33\,A$ to $0.64\,A$ as predictable from the discussion provided before while maintaining the proper phase relation with the phase-a grid voltage, v_{ga}. Some sampling noise can be observed in the zoomed waveform during the high sampling rate of the data acquisition of the oscilloscope. Figure 6.9(b) shows the dynamics associated with sudden change in grid fundamental frequency from $50\,Hz$ to $49.5\,Hz$. It can be seen during the frequency change the load undergoes some transients but sequentially the system is stabilized to the new frequency of the grid system. The corresponding transient can also be seen in the phase-a grid current, i_{ga} but subsequently the system settles to the new frequency with desired phase relations and shape. However, it can be noted from Figure 6.9(b) that, when there is a sudden change in the fundamental grid frequency, the load currents undergo transient because of the inductance presence in the load connecting junction, which can be visible in phase-a load current, i_{La} waveform in Figure 6.9(b), causing the

delay of the overall system. The response time of the control system is negligible with respect to this load transient delay as can be predicted from the analysis provided before.

6.5.4 THD reduction capability of the proposed control system

The robustness of the proposed controller is checked and the related experimental results are provided for the *b-6* topology of the inventer. To check the robustness of the proposed controller a linear resistive load is added with the non-linear load such that the total active load power consumption becomes $P_L = 300\,W$. The grid power command is given as $P_g = 250\,W$ and $Q_g = 0\,Var$. The experimental results are shown in Figures 6.10 and 6.11.

Figure 6.10 shows the experimental results of different current waveforms. It can be observed from Figure 6.10(a) that, because of the paralleling of linear load with the non-linear load; the load currents, i_{La}, i_{Lb} and i_{Lc} also contain significant amount of lower order harmonics. However, because of the proposed controller tracking the CCVSI currents, the grid currents are sinusoidal with phase-a grid current, i_{ga} peak about $2.8\,A$ and phase-b and c currents (i_{gb} and i_{gc}) peak both are about $4\,A$ with respective phase relation as can be seen from Figure 6.10(c).

The THD improving capability is further investigated by analyzing the FFT of phase-a grid voltage v_{ga}, phase-a load current, i_{La}, phase-a grid current, i_{ga} and phase-a CCVSI current, i_{Ca} as can be seen from Figure 6.11. It can be seen that the v_{ga} FFT is normalized with its fundamental value to show the harmonic percentage

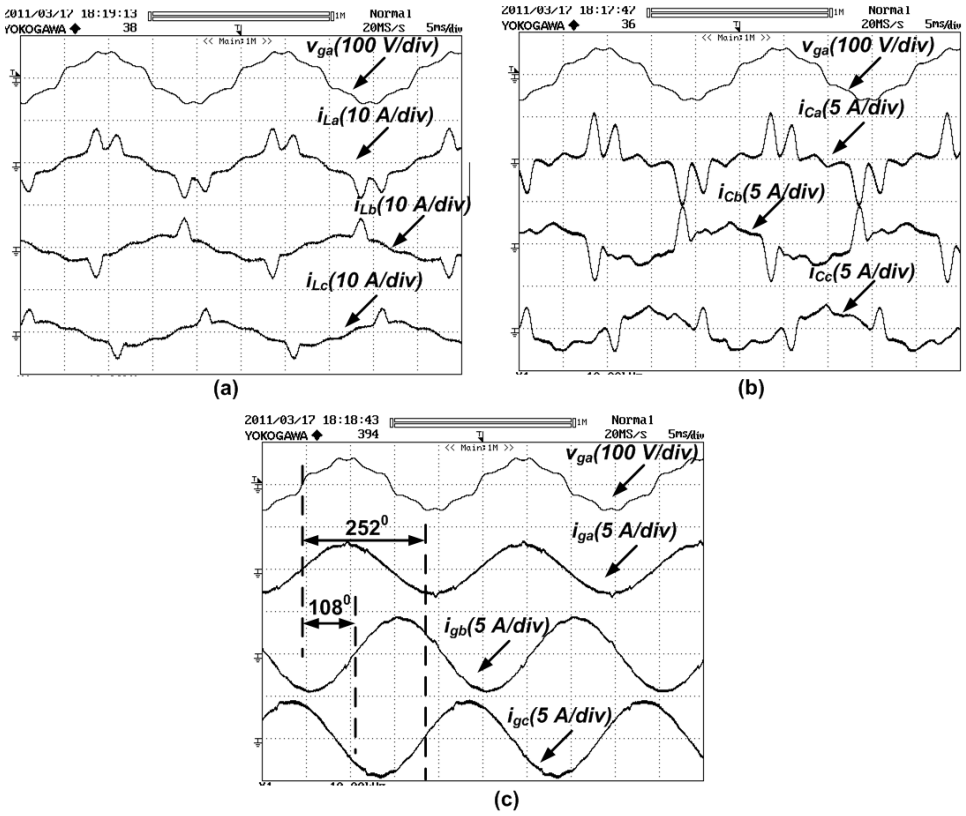

Figure 6.10: Experimental results of (a) phase-s grid voltage, v_{ga}, three-phase load currents, i_{La}, i_{Lb} and i_{Lc}, (b) phase-a grid voltage, v_{ga}, three-phase CCVSI currents, i_{Ca}, i_{Cb} and i_{Cc}, (c) phase-a grid voltage, v_{ga}, phase-a grid current, i_{ga}, i_{gb}, i_{gc} at grid power command, $P_g = 250\,W$ and $Q_g = 0\,Var$ with hybrid linear and non-linear load with $P_L = 300\,W$ with *b-6* topology of inverter and $V_p = 49.3\,V$ and $V_n = 9.86\,V$.

of the grid voltage. The FFT of i_{La}, i_{ga} and i_{Ca} are normalized with respect to the fundamental value of load current, i_{La}. It can be remarked from Figure 6.11 that, all the harmonics of the i_{La} are canceled by the reverse harmonics of i_{Ca} resulting almost no harmonics in i_{ga}. It can also be noticed that, grid current i_{ga} only contributes to the fundamental current value of the load current i_{La} along with the fundamental current of CCVSI, i_{Ca}. It can also be seen from Figure 6.11 that, the FFT of phase-a load current, i_{La} shows the presence of 3^{rd} and other triplen harmonics because of the interaction of full bridge diode rectifier with severe unbalanced grid voltage (it can be noted from the FFT of phase-a grid voltage in

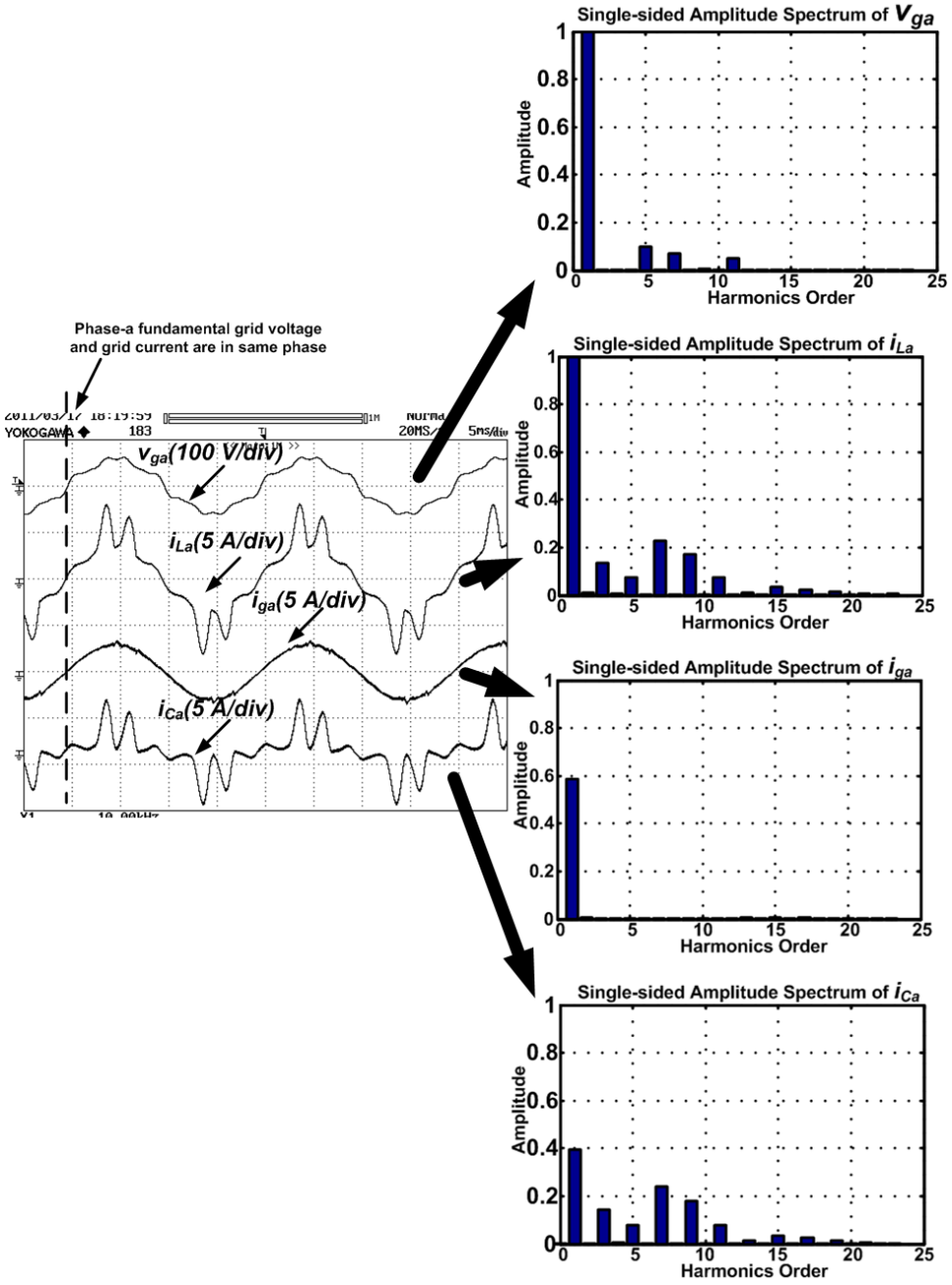

Figure 6.11: Experimental results of phase-a grid voltage, v_{ga}, Phase-a load current, i_{La}, phase-a grid current, i_{ga}, phase-a CCVSI current, i_{Ca} and FFT plot of each variable at grid power command, $P_g = 250\,W$ and $Q_g = 0\,Var$ with hybrid linear and non-linear load with $P_L = 300\,W$ with *b-6* topology of inverter and $V_p = 49.3\,V$ and $V_n = 9.86\,V$.

Figure 6.11 that grid voltage does not contain triplen harmonics either); however, the proposed current controller is also able to compensate for those triplen current

harmonics leading to pure sinusoidal grid current waveform. It can be noted that, the traditional *dual frame* controller cannot be utilized to compensate for triplen current harmonics as later does not form any space vector. The proposed controller can compensate these triplen current harmonics as it works on the *a-b-c* frame directly.

6.6 Summary

A new current control strategy for a parallel connected three-phase renewable energy source based inverter to connect to the generalized micro-grid is proposed. The control strategy is implemented directly in the *a-b-c* frame and is able to take care of unbalance conditions in both the grid voltage as well as line side inductances and load. The proposed method also reduces the THD of the grid current along with the proper grid active as well as reactive power control. The proposed control method is simple to implement in digital controller and requires no Park's transformation block unlike the conventional method where multiple controllers are implemented in *synchronously rotating dual* reference frame and gives superior performance. Thus the proposed method works without the necessity of the Phase Lock Loop (PLL). The proposed controller is also capable of rejecting the effect of grid voltage harmonics in the grid currents. The proposed controller is also shown to be independent of grid frequency. The stability of the proposed control system is described with the help of *Lyapunov's* first principle hence the name of the controller. A modeling method of the three-phase grid connected inverter under unbalanced connection condition is also presented to facilitate the proposed control action. The proposed control strategy is applied on conventional six switch

topology (*b-6* configuration) of three-phase inverter and presented experimental results show the effectiveness of the controller.

Chapter 7

Derivation of instantaneous current references for multi-phase PWM inverter to control active and reactive power flow from a renewable energy source to a generalized multi-phase micro-grid system

The previous Chapter deals with the designing of the controllers to track the currents in the renewable energy based three-phase inverter to ensure a specific amount of active and reactive power flow from the common AC bus with controlling the THD of the current drawn from the common AC bus in the presence of the non-linear load at the point of common coupling (PCC). Now, the current reference derivation for the inverter to ensure active and reactive power flow along with controlling THD of the current drawn from the PCC is another interesting aspect of this report.

In this Chapter a generalized n-phase micro-grid system is considered along with an n-phase common AC bus interconnected to a renewable energy system with a n-phase inverter system. A general n-phase non-linear load is also connected at the common AC bus. Different power theories namely, p-q based approach and *FBD* based approach are used to find the current reference for the inverter to ensure proper power control with grid current THD control capability. The effect of each of the approach on the DC link side ripples is also investigated using an *instantaneous power balance* analysis on both the sides of the inverter. The theoretical basis is established for a n-phase micro-grid system. However, experimental results are provided for a typical three-phase generalized micro-grid system to test the feasibility of the proposed methodologies of deriving the current reference of the inverter phase currents.

7.1 General description of the load and inverter interface with the grid

Figure 7.1 shows the schematic of an 'n'-phase multi-bus micro-grid system connected to the grid at the *point of common coupling* (PCC). The inverter interfacing the grid and the load is also interfaced with the renewable energy source to the *Local Bus* of the micro-grid. Analysis provided in Chapter 6 shows that the voltage source inverter (VSI) operates in current control mode (as CCVSI) to manage the harvested energy from the renewable energy sources not only to share the load active power (P_L) between power consumption from the *Local Bus* (P_g) and power supplied by CCVSI (P_{inv}) but also the reactive power and harmonic power drawn by the load are also compensated by the CCVSI to ensure that the cur-

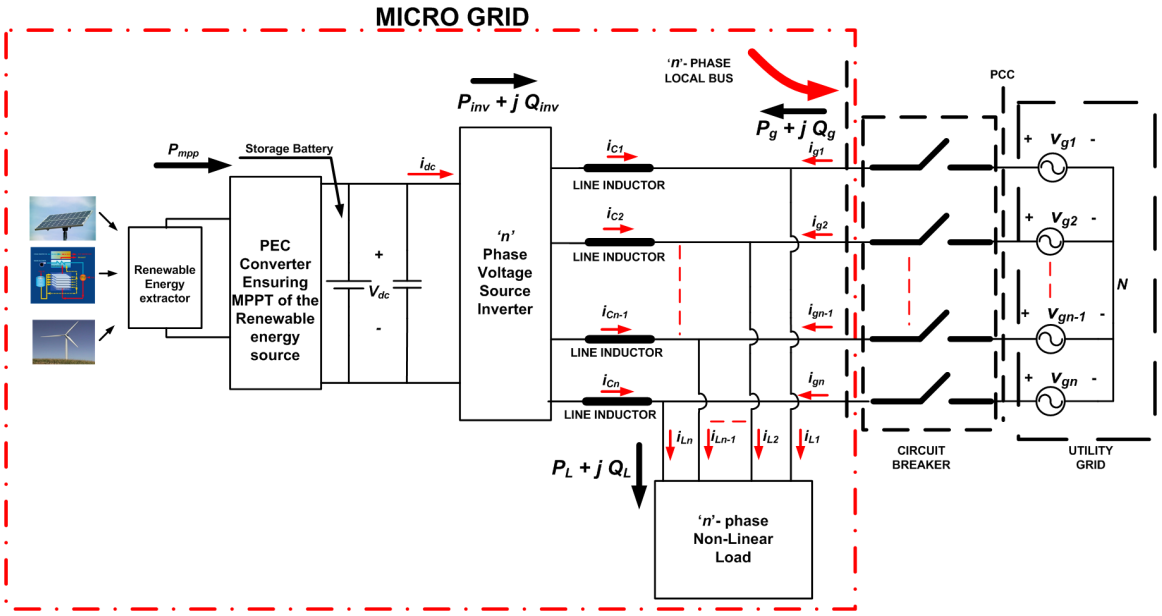

Figure 7.1: Typical configuration of a renewable energy fed 'n'- phase micro-grid.

rent drawn from the *Local Bus* (i_{g1}, i_{g2} ..... i_{gn}) to be sinusoidal and with unity displacement power factor. The thesis considers the generalized analysis for current reference generation scheme of a typical 'n'-phase generalized grid connected micro-grid CCVSI system. The utility grid neutral N is electrically isolated from the DC link mid-point of the VSI. The 'n' phase *Local Bus* voltage with respect to utility grid neutral N is marked as v_{g1}, v_{g2}.....v_{gn} as shown in Figure 7.1. From this stage onwards, the *Local Bus* voltages are referred to as *grid* voltages. The implementation method is described for a typical three-phase system with supported experimental results.

7.2 *p-q* theory based CCVSI current reference derivation

7.2.1 *p-q* theory based current references generation scheme

The 'n'-phase generalized grid is considered to have unbalance in the voltages. Because of the absence of electrical connection between utility grid neutral N and CCVSI DC side, the zero sequence current is not present in the inverter. Thus, zero sequence components of grid voltages do not contribute any active power drawn in the system interaction. Hence, the presence of zero sequence component in the grid voltage is neglected as also done in [30]and [129]. The grid voltages contain both positive and negative sequence components. The grid voltages can be written as:

$$\begin{aligned} v_{g1}(t) &= V_p \cos(\theta_1) + V_n \cos(\theta_2) \\ v_{g2}(t) &= V_p \cos\left(\theta_1 - \frac{2\pi}{n}\right) + V_n \cos\left(\theta_2 + \frac{2\pi}{n}\right) \\ \vdots &= \quad \vdots \qquad\qquad + \quad \vdots \\ v_{gn}(t) &= V_p \cos\left(\theta_1 - (n-1)\frac{2\pi}{3}\right) + V_n \cos\left(\theta_2 + (n-1)\frac{2\pi}{3}\right) \end{aligned} \quad (7.1)$$

where, V_p and V_n are the peak values of positive and negative sequence grid voltages respectively. The positive and negative sequence grid phase angles are θ_1 and θ_2 respectively and related to grid frequency (ω rad/s) as : $\theta_1 = \int \omega dt + \delta_1$ and $\theta_2 = \int \omega dt + \delta_2$.

The reference 'n'-phase grid currents are taken as:

$$\begin{aligned}
i^*_{g1}(t) &= I_p \cos(\theta_1 + \beta_1) + I_n \cos(\theta_2 + \beta_2) \\
i^*_{g2}(t) &= I_p \cos\left(\theta_1 + \beta_1 - \frac{2\pi}{n}\right) + I_n \cos\left(\theta_2 + \beta_2 + \frac{2\pi}{n}\right) \\
\vdots &= \quad \vdots \qquad\qquad\qquad + \quad \vdots \\
i^*_{gn}(t) &= I_p \cos\left(\theta_1 + \beta_1 - (n-1)\frac{2\pi}{n}\right) + I_n \cos\left(\theta_2 + \beta_2 + (n-1)\frac{2\pi}{n}\right)
\end{aligned} \tag{7.2}$$

where, I_p and I_n are the peak of positive and negative sequence reference grid currents respectively and β_1 and β_2 are the power factor angles of the respective reference grid currents respectively.

The grid voltage space vector can be written as:

$$\begin{aligned}
\overrightarrow{V_g} &= \frac{2}{n}\left[v_{g1}(t) + v_{g2}(t)\, e^{j\frac{2\pi}{n}} + ... + v_{gn}(t)\, e^{j(n-1)\frac{2\pi}{n}} \right] \\
&= V_p\, e^{j\theta_1} + V_n\, e^{-j\theta_2}
\end{aligned} \tag{7.3}$$

Similarly grid reference current space vector can be written as:

$$\begin{aligned}
\overrightarrow{I^*_g} &= \frac{2}{n}\left[i^*_{g1}(t) + i^*_{g2}(t)\, e^{j\frac{2\pi}{n}} + ... + i^*_{gn}(t)\, e^{j(n-1)\frac{2\pi}{n}} \right] \\
&= I_p\, e^{j(\theta_1 + \beta_1)} + I_n\, e^{-j(\theta_2 + \beta_2)}
\end{aligned} \tag{7.4}$$

The instantaneous grid active and reactive power are p and q and can be expressed as:

$$\begin{aligned}
p(t) &= \frac{n}{2}\, Re\left[\overrightarrow{V_g} \bullet \overrightarrow{I^{*C}_g}\right] \\
q(t) &= \frac{n}{2}\, Re\left[\overrightarrow{V_g} \times \overrightarrow{I^{*C}_g}\right]
\end{aligned} \tag{7.5}$$

where, $\overrightarrow{I^{*C}_g}$ is the complex conjugate of the grid reference space vector $\overrightarrow{I^*_g}$. '$\bullet$' and '$\times$' are dot and cross products of respective quantities. Putting (7.3) and (7.4) into

(7.5), the modified equations are:

$$\begin{aligned} p(t) &= P_0 + P_C \cos(\theta_1 + \theta_2) + P_S \sin(\theta_1 + \theta_2) \\ q(t) &= Q_0 + Q_C \cos(\theta_1 + \theta_2) + Q_S \sin(\theta_1 + \theta_2) \end{aligned} \tag{7.6}$$

where, P_0, P_C and P_S are the DC, cosine oscillatory and sine oscillatory components of active power respectively. Similarly Q_0, Q_C and Q_S are the DC, cosine oscillatory and sine oscillatory components of reactive power respectively. The constants can be expressed as:

$$\begin{pmatrix} P_0 \\ Q_0 \\ P_S \\ Q_S \end{pmatrix} = \frac{n}{2} \begin{pmatrix} V_p & 0 & V_n & 0 \\ 0 & -V_p & 0 & -V_n \\ 0 & -V_n & 0 & -V_p \\ V_n & 0 & V_p & 0 \end{pmatrix} \begin{pmatrix} I_p \cos(\beta_1) \\ I_p \sin(\beta_1) \\ I_n \cos(\beta_2) \\ I_n \sin(\beta_2) \end{pmatrix} \tag{7.7}$$

Additionally, other expressions can be found as: $P_C = Q_S$ and $P_S = -Q_C$.

To minimize the DC link voltage ripples P_C and P_S are made zero [30, 130]. In addition the Q_0 is made zero to make grid current displacement power factor (DPF) to be unity. Now, putting $P_0 = P_g$, grid reference active power, $Q_0 = P_C = P_S = 0$, (7.7) are solved as:

$$\begin{aligned} I_p &= \frac{P_g V_p}{\frac{n}{2}(V_p^2 - V_n^2)} \\ I_n &= -\frac{P_g V_n}{\frac{n}{2}(V_p^2 - V_n^2)} \\ \beta_1 &= \beta_2 = 0 \end{aligned} \tag{7.8}$$

If the phase angles of positive as well as negative sequence grid voltages θ_1 and θ_2 respectively along with the respective peak values (V_p and V_n) are known, the grid currents references can be found using (7.2) and (7.8). Now, the CCVSI three-phase current references (variables are shown in Figure7.1) are found using

KCL at PCC as:

$$\begin{aligned} i^*_{C1}(t) &= i_{L1}(t) - i^*_{g1}(t) \\ i^*_{C2}(t) &= i_{L2}(t) - i^*_{g2}(t) \\ \vdots &= \vdots - \vdots \\ i^*_{Cn}(t) &= i_{Ln}(t) - i^*_{gn}(t) \end{aligned} \tag{7.9}$$

where, $i_{L1}(t)$, $i_{L2}(t)$.....$i_{Ln}(t)$ are the 'n'-phase currents drawn by the non-linear load connected from PCC.

In the next Section it is explained how the grid voltage phase angles (θ_1 and θ_2) and magnitudes (V_p and V_n) can be obtained instantaneously without employing *PLL* or *Park's transformation*.

7.2.2 Implementation of the *p-q* theory based CCVSI current reference calculation method

This sub-section is directed towards the description of the implementation of the discussed method. The implementation is carried out for a general three-phase ($n = 3$) *a-b-c* frame. In this special case, the instantaneous grid voltages are referred as v_{ga}, v_{gb} and v_{gc}. The corresponding reference currents are referred as i^*_{ga}, i^*_{gb} and i^*_{gc}. Now, assuming the three-phase load currents are i_{La}, i_{Lb} and i_{Lc}, the three-phase CCVSI current references can be written as,

$$\begin{aligned} i^*_{Ca}(t) &= i_{La}(t) - i^*_{ga}(t) \\ i^*_{Cb}(t) &= i_{Lb}(t) - i^*_{gb}(t) \\ i^*_{Cc}(t) &= i_{Lc}(t) - i^*_{gc}(t) \end{aligned} \tag{7.10}$$

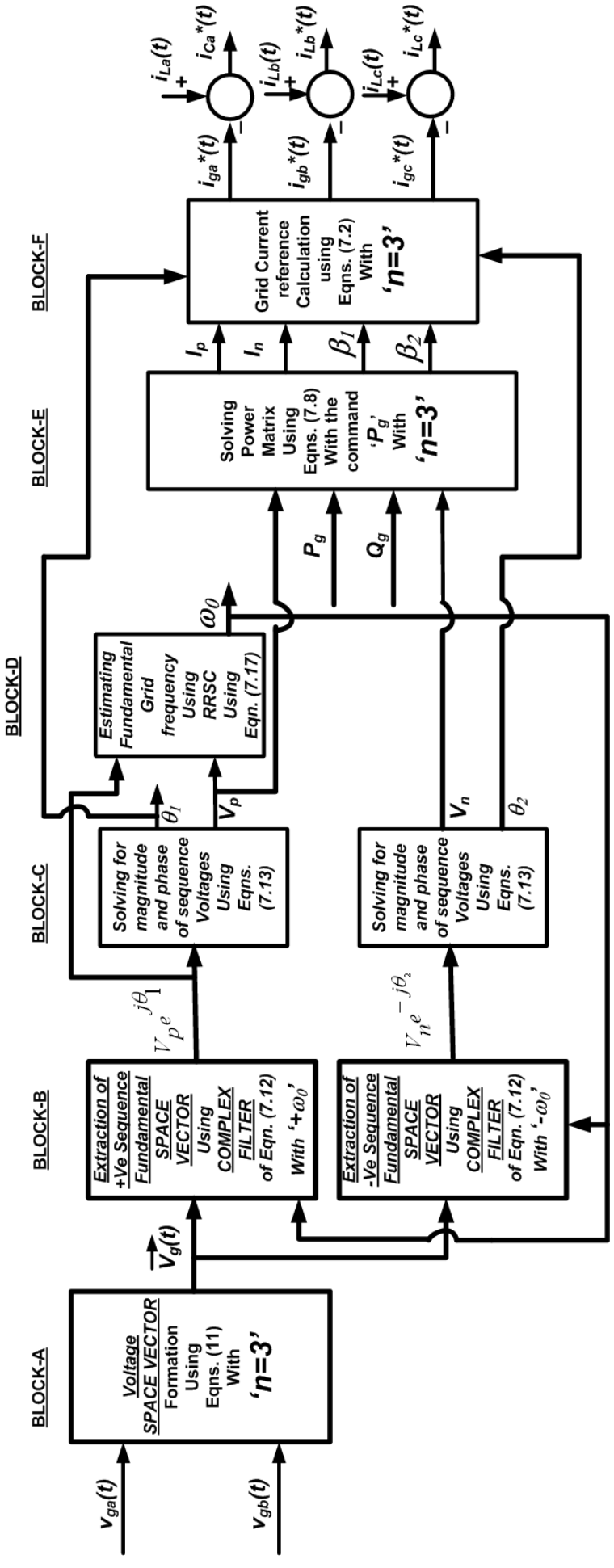

Figure 7.2: Schematics of the CCVSI current reference estimation block using p-q method.

The implementation of the overall estimation system is shown in Figure 7.2. Different instantaneous mathematical operations are carried out in the transmission path to calculate the current references for the CCVSI. The operation of the overall system is divided into six blocks (BLOCK-A to BLOCK-F) as can be seen from Figure 7.2. Each of the blocks are explained separately.

7.2.2.1 BLOCK-A

In this block, the real unbalance grid voltages (v_{ga}, v_{gb} and v_{gc}) are transformed to complex grid voltage *space vector* using, (7.3) with $n = 3$. It can be seen from (7.3) that, the real(V_{gR}) and imaginary (V_{gI}) components of the grid voltage *space vector* can be calculated as:

$$\begin{aligned} V_{gR} &= \left[\frac{2}{3}\left[v_{ga}(t) - 0.5\left(v_{gb}(t) + v_{gc}(t)\right)\right]\right] \\ V_{gI} &= j\,\frac{2}{3}\left[\frac{\sqrt{3}}{2}\left(v_{gb}(t) - v_{gc}(t)\right)\right] \end{aligned} \tag{7.11}$$

7.2.2.2 BLOCK-B

In this block, the fundamental grid positive and negative sequence *space vectors* are extracted using a *complex notch filter* (CNF) [126]. The filter is characterized to work on complex signals (i.e. space vectors) to extract *space vectors* of the rotational frequency, which is the tuned frequency of the filters. The digital transfer function (in 'z'-domain) of the complex filter can be expressed as:

$$H(z) = \frac{1 - a}{z - a\,e^{j\,\Delta\theta}} \tag{7.12}$$

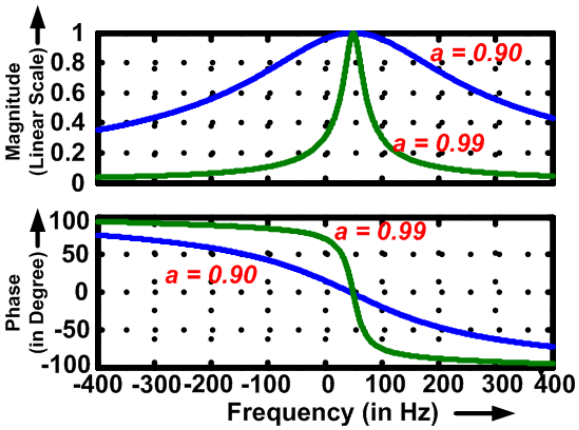

Figure 7.3: The amplitude and phase plot of the *Complex Notch Filter* for different frequencies with two different values of a with $\omega_0 = 2\pi 50$ rad/s and $T_s = 0.1$ms.

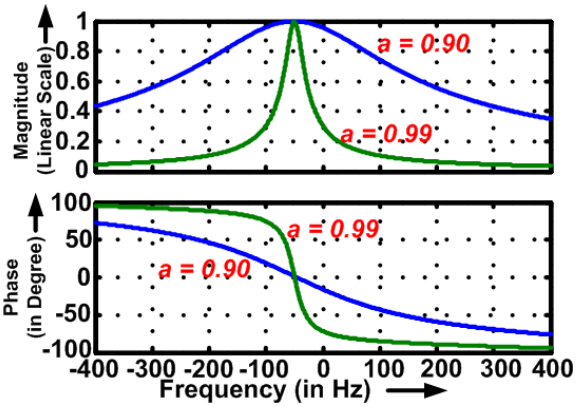

Figure 7.4: The amplitude and phase plot of the *Complex Notch Filter* for different frequencies with two different values of a with $\omega_0 = -2\pi 50$ rad/s and $T_s = 0.1$ms.

where, a is the constant ($a < 1$) of the filter controlling the bandwidth of the filter and if $\Delta\theta = \omega_0 T_s$ (T_s is the sampling time of the discrete system), the filter extracts fundamental of '+ve sequence' grid *space vector* (rotating at the speed 'ω_0' rad/s) otherwise, if $\Delta\theta = -\omega_0 T_s$, the filter extracts fundamental of '-ve sequence' grid space vector (rotating at the speed '-ω_0' rad/s). At tuned frequency, the gain of the filter is unity and at all other frequencies (+ve,-ve fundamental or harmonic depending on the setting of '$\Delta\theta$'), the gain of the filter is less than unity. The characteristics of the CNF can be explained using the simulation plot provided in Figures 7.3 and 7.4. The frequency characteristic of the filter explains that the filter is capable of removing all the harmonics present in the grid voltage and along with that, the extraction of the '+ve' and '-ve' sequence of the fundamental grid is possible with the help of this CNF. It should be emphasized that, the proposed method does not use *Fortescue's* method or its derivative to estimate the '+ve' and '-ve' sequence components of the fundamental grid voltages. In the actual implementation, initially $a = 0.90$ is used to make the transient time shorter, then after few sampling instants $a = 0.99$ is used to make the filtering more efficient.

There is a scope of optimizing the value of a to improve the performance of CNF but it is not investigated in this paper.

7.2.2.3 BLOCK-C

In this block, the magnitude and phase of both the positive and negative sequence grid voltages are found. The mathematical operation of getting the magnitude (X_M) and phase (X_ϕ) of a *space vector* $\overrightarrow{X(t)} = X_{Re} + j\,X_{Im} = X_M\,e^{j\,X_\phi}$ are shown as follows:

$$\begin{aligned} X_M &= \sqrt{X_{Re}^2 + X_{Im}^2} \\ X_\phi &= \tan^{-1}\left(\frac{X_{Im}}{X_{Re}}\right) \end{aligned} \tag{7.13}$$

In Block-C all the parameters V_p ,θ_1 ,V_n and θ_2 are extracted using (7.13) on both '+ve' and '-ve' sequence *space vector*.

7.2.2.4 BLOCK-D

In this block, the fundamental frequency of the grid voltage is estimated and the frequency information is used to re-tune the CNF to improve the filtering performance in the case of change of fundamental grid frequency as can be seen from Figure 7.2. A *Rotating Reference Signal Characterizer* (RRSC) is proposed to estimate the fundamental grid frequency accurately. The method can be explained using the analysis shown in Figure 7.5. The reference *Space Vector* $\overrightarrow{X_{ref}}$ has known frequency $\omega_{ref}\,rad/s$ and unity magnitude ($\overrightarrow{X_{ref}} = e^{j\,\alpha_{ref}} = e^{j\,\omega_{ref}\,t}$), where t is the time. The unknown frequency *space vector* is depicted as $\overrightarrow{X} = X_M\,e^{j\,\alpha} = X_{Re} + j\,X_{Im}$ with rotation speed ω_0 rad/s. As seen in Figure 7.2, the magnitude, X_M of the *space*

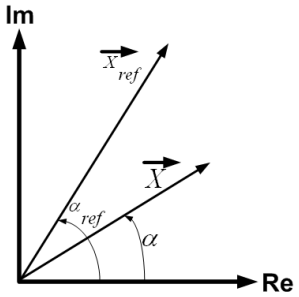

Figure 7.5: Rotating *Space Vectors*, to estimate the frequency of the grid fundamental voltage.

vector is known from the previous stage, i.e BLOCK-C. As the real and imaginary parts of both the vectors $\overrightarrow{X}$ and $\overrightarrow{X_{ref}}$ are known instantaneously, the dot and cross product values of the two vectors can be calculated at each sampling instant as a and b. The mathematical relations can be written as:

$$\begin{aligned} a &= X_M \cos(\alpha_{ref} - \alpha) = (X_{Re} \cos(\alpha_{ref}) + X_{Im} \sin(\alpha_{ref})) \\ b &= X_M \sin(\alpha_{ref} - \alpha) = (X_{Re} \sin(\alpha_{ref}) - X_{Im} \cos(\alpha_{ref})) \end{aligned} \quad (7.14)$$

At two consecutive instants, the values of a and b are stored as a_1, a_2 and b_1, b_2 respectively, Now, the angular difference is regarded as $\alpha_{ref} - \alpha = \gamma$. The two consecutive samples of γ are regarded as γ_1 and γ_2. Now, using (7.14), *sine* and *cosine* of γ at two consecutive sampling instants can be known as:

$$\begin{aligned} \cos\gamma_1 &= \frac{a_1}{X_M}; \quad \cos\gamma_2 = \frac{a_2}{X_M} \\ \sin\gamma_1 &= \frac{b_1}{X_M}; \quad \sin\gamma_2 = \frac{b_2}{X_M} \end{aligned} \quad (7.15)$$

So, the difference of two angles γ_1 and γ_2 can be expressed as:

$$\cos(\Delta\gamma) = \cos(\gamma_1 - \gamma_2) = \cos(\gamma_1)\cos(\gamma_2) + \sin(\gamma_1)\sin(\gamma_2) \quad (7.16)$$

Using (7.15) in (7.16), followed by the inverse *cosine* on (7.16), $\Delta\gamma$ is extracted. Now, because of the two consecutive sampling, the following equations also hold in

this process:

$$\begin{aligned} \Delta\gamma &= (\omega_{ref} - \omega_0)\, T_s \\ \Rightarrow \omega_0 &= \omega_{ref} - \frac{\Delta\gamma}{T_s} \end{aligned} \tag{7.17}$$

where, ω_0 is the frequency of the vector $\overrightarrow{X}$ and T_s is the sampling time of the overall system. So the fundamental angular frequency of the grid ω_0 is estimated by this method. This method is much more accurate in comparison with other methods. In the experimental studies $\omega_{ref} = 2\pi 100$ rad/s is taken. It should be noted that, for accurate operation, the only condition, needs to be satisfied, can be expressed as: $\omega_{ref} > \omega_0$.

7.2.2.5 BLOCK-E

Now, V_p and V_n are passed to BLOCK-E, in which (7.8) are solved to find I_p, I_n, β_1 and β_2 characterizing parameters of grid current reference shown in (7.2).

7.2.2.6 BLOCK-F

Sequentially, in BLOCK-F, using the parameters solved by BLOCK-E and utilizing (7.2), the instantaneous grid current references are obtained. Hence, using (7.23), the CCVSI current references are found as shown in Figure 7.2. The CCVSI current references are used to run the CCVSI to ensure proper grid active power flow, P_g.

7.3 *FBD* theory based CCVSI current reference derivation

7.3.1 *FBD* theory based current reference generation scheme

The grid is considered to be a generalized 'n'-phase system as described in (7.1). As mentioned before, the grid neutral N is electrically isolated from the inverter, following the analysis given in [104]-[106], equivalent phase voltage of phase-h, v_h, can be written with respect to the other relevant line voltages as:

$$v_h \;=\; \frac{1}{n}\sum_{\mu=1}^{n} v_{h\mu} \tag{7.18}$$

where, h can take values of $1, 2, 3.....n$ and $v_{h\mu}$ $(=\; v_{gh} \;-\; v_{g\mu})$ is the grid line voltage of phase-h with respect to phase-μ. The collective RMS voltage of all the 'n' phases can be expressed as:

$$v_\Sigma \;=\; \sqrt{\sum_{h=1}^{n} v_h^2} \tag{7.19}$$

Traditionally, M samples of v_Σ^2 are taken over half cycle of the fundamental grid voltage and the average of all the M values are defined as:

$$\overline{v_\Sigma^2} \;=\; \frac{1}{M}\sum_{M} v_\Sigma^2 \tag{7.20}$$

The term $\overline{v_\Sigma^2}$ is calculated as an instantaneous running average over the half cycle of fundamental grid voltage. The equivalent active conductance, G is calculated as:

$$G \;=\; \frac{P_g}{\overline{v_\Sigma^2}} \tag{7.21}$$

where, P_g is the grid active power flow to be ensured by CCVSI current control. Hence, the instantaneous grid current references can be found as:

$$i_{gh}^{*} \;=\; G \,.\, v_h \tag{7.22}$$

Now, the CCVSI three-phase current references (variables are shown in Figure 7.1) are found using KCL at PCC as:

$$\begin{aligned} i^*_{C1}(t) &= i_{L1}(t) - i^*_{g1}(t) \\ i^*_{C2}(t) &= i_{L2}(t) - i^*_{g2}(t) \\ \vdots &= \vdots - \vdots \\ i^*_{Cn}(t) &= i_{Ln}(t) - i^*_{gn}(t) \end{aligned} \tag{7.23}$$

where, $i_{L1}(t)$, $i_{L2}(t)$.....$i_{Ln}(t)$ are the 'n'-phase currents drawn by the non-linear load connected at the PCC.

If the sampling frequency of the overall system is f_s Hz and the fundamental grid frequency is f_0 Hz, where $f_0 = \frac{\omega_0}{2\pi}$, the number of samples are related as:

$$M = \frac{f_s}{2\, f_0} \tag{7.24}$$

Now, if the fundamental grid frequency, f_0 changes with time and it does not have an integral relation with sampling frequency, f_s, number of samples, M, becomes a fraction and term $\overline{v^2_\Sigma}$ contains oscillation, resulting in the oscillation in the reference grid currents, i^*_{gh} as can be explained using (7.22). To avoid this problem, a *position sampling* based *FBD* method is proposed and implemented in this thesis. In this method, M is kept at a fixed value and the sampling of the quantity, v^2_Σ is carried out at discrete instants when the '+ve' sequence fundamental grid phase assumes the values, θ with the relation represented as:

$$\theta = m\, \frac{\pi}{M} \tag{7.25}$$

where, m assumes the values of $0, 1, 2, ...(M-1)$.

7.3.2 Implementation of the *FBD* theory based CCVSI current reference calculation method

This sub-section is directed towards the description of the implementation of the discussed method. The implementation is carried out on a general three-phase ($n = 3$) *a-b-c* frame. In this special case, the instantaneous grid voltages are referred as v_{ga}, v_{gb} and v_{gc}. The corresponding reference currents are referred as i^*_{ga}, i^*_{gb} and i^*_{gc}. Now, assuming the three-phase load currents are i_{La}, i_{Lb} and i_{Lc}, the three-phase CCVSI current references can be written as,

$$\begin{aligned} i^*_{Ca}(t) &= i_{La}(t) - i^*_{ga}(t) \\ i^*_{Cb}(t) &= i_{Lb}(t) - i^*_{gb}(t) \\ i^*_{Cc}(t) &= i_{Lc}(t) - i^*_{gc}(t) \end{aligned} \tag{7.26}$$

The implementation of the overall estimation system is shown in Figure 7.6. The total implementation method is carried out in seven blocks (BLOCK-A to BLOCK-G). The implementation of the overall estimation system is shown in Figure 7.6. The total implementation method is carried out in seven blocks (BLOCK-A to BLOCK-G).

7.3.2.1 BLOCK-A to BLOCK-D

The details of BLOCK-A to BLOCK-D are same as also done in the case of *p-q* based implementation. So, They are not repeated here anymore.

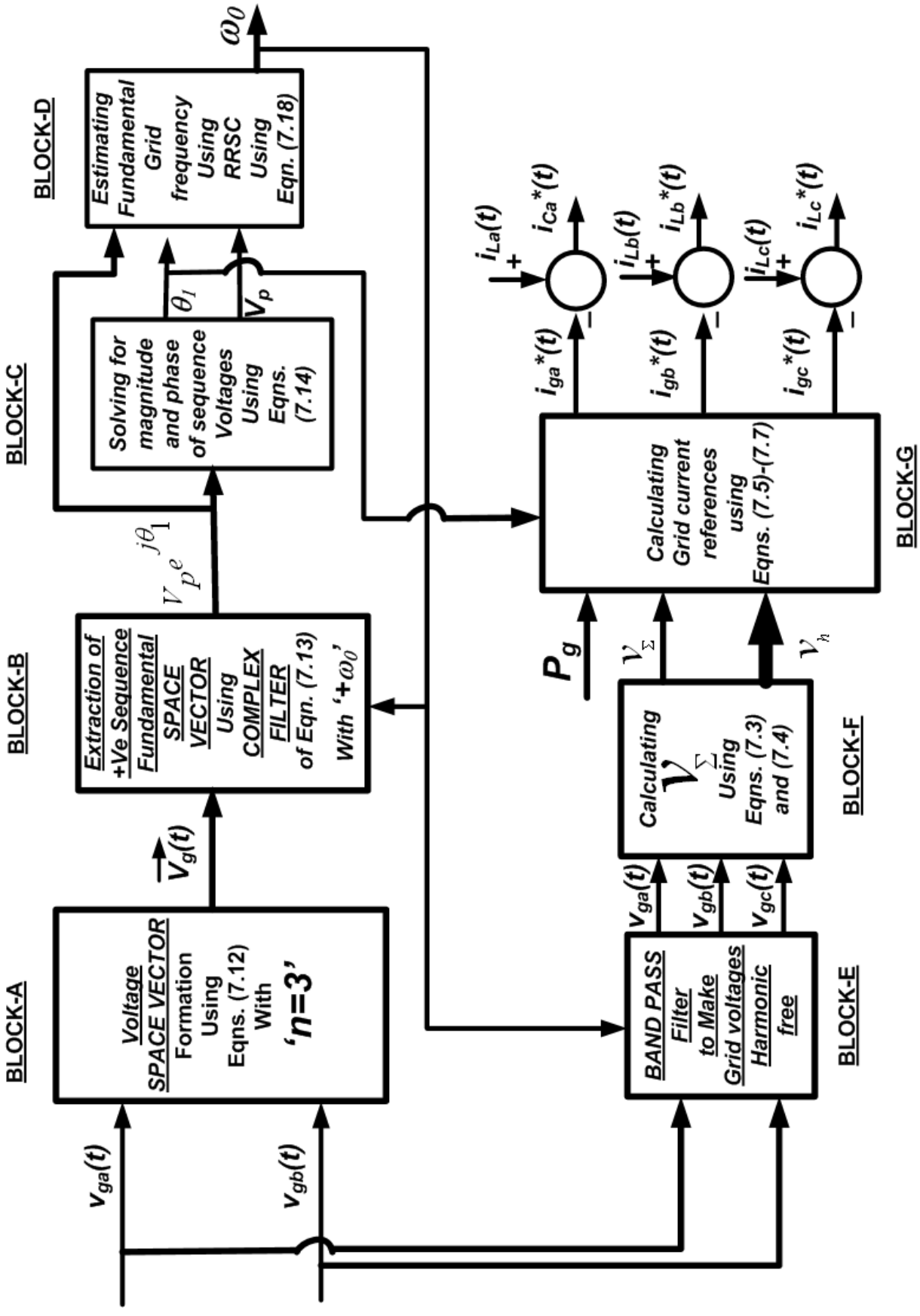

Figure 7.6: Schematics of the CCVSI current reference estimation block using FBD method.

7.3.2.2 BLOCK-E

In this block, the instantaneous grid voltages are filtered using *band pass* filter tuned at fundamental frequency, ω_o rad/s (as found from BLOCK-D) and the filtered three-phase grid voltages are used for further processing. This filtering is carried out to make the grid reference current harmonic free as also done in [108].

7.3.2.3 BLOCK-F

In this block, the instantaneous quantities v_h for all three phases and v_Σ are calculated utilizing (7.18) and (7.19) and passed to next block for further processing.

7.3.2.4 BLOCK-G

In this block, the instantaneous quantity, v_Σ is sampled at different fundamental '+ve' sequence grid phase θ_1 (as found out from BLOCK-C) according to (7.25) to find the moving average $\overline{v_\Sigma}$ and further G is calculated using (7.21). The grid current references are calculated using (7.22) for all three phases. Thereafter, CCVSI current references are calculated as shown in Figure 7.6. In the experimental implementation the half cycle of fundamental grid voltage is split into $M = 100$ samples.

It can be noted from Figure 7.6 that, from BLOCK-A to BLOCK-D are used to find out the fundamental grid frequency, $\omega_0\, rad/s$ (which is used for tuning the filters) and the fundamental positive sequence grid phase, θ_1 (which is used for *position sampling*). To facilitate this +ve sequence of grid voltages is extracted.

However, BLOCK-E to BLOCK-G, which are the core blocks from *FBD* based CCVSI current reference calculation do not use the information +ve fundamental sequence grid voltage magnitude, V_p. If any other user likes to use another method for ω_0 estimation and uses any other position synchronized with grid fundamental phase for this method, is expected to have no difference on current reference calculation in steady-state. However, if PLL is used to find the fundamental grid phase and frequency, the delay associated with PLL transient during sudden change of grid fundamental frequency can hamper the CCVSI current estimation process in dynamic condition.

7.4 Instantaneous power theory based CCVSI current reference derivation

7.4.1 Calculation of instantaneous power for an 'n'-phase grid connected system

Considering the 'n'-phase grid connected system, the instantaneous power interchange between inverter and grid due to the grid currents only can be derived as (assuming actual grid current is following the reference grid currents, i.e. $i_{gh} = i^*_{gh}$ for $h = 1, 2, 3.....n$):

$$p_g = \sum_{h=1}^{n} v_{gh}\, i_{gh} = \sum_{h=1}^{n} v_{gh}\, i^*_{gh} \tag{7.27}$$

Plugging-in the voltage and current expressions in (7.1)-(7.2) in (7.27) and considering that each phase instantaneous power consists of instantaneous power due to '+ve' sequence voltage interaction with '+ve' sequence current, '-ve' sequence voltage interaction with '-ve' sequence current and mutual interactions between

'+ve' and '-ve' sequence quantities as follows:

$$\begin{aligned} p_g &= \sum_{h=1}^{n} V_p I_p \cos\left(\theta_1 - (h-1)\frac{2\pi}{n}\right) \cos\left(\theta_1 + \beta_1 - (h-1)\frac{2\pi}{n}\right) \\ &+ \sum_{h=1}^{n} V_n I_n \cos\left(\theta_2 + (h-1)\frac{2\pi}{n}\right) \cos\left(\theta_2 + \beta_2 + (h-1)\frac{2\pi}{n}\right) \\ &+ \sum_{h=1}^{n} V_p I_n \cos\left(\theta_1 - (h-1)\frac{2\pi}{n}\right) \cos\left(\theta_2 + \beta_2 + (h-1)\frac{2\pi}{n}\right) \\ &+ \sum_{h=1}^{n} V_n I_p \cos\left(\theta_2 + (h-1)\frac{2\pi}{n}\right) \cos\left(\theta_1 + \beta_1 - (h-1)\frac{2\pi}{n}\right) \end{aligned} \quad (7.28)$$

Each of the terms in (7.28) can be expanded to elaborate as:

$$\begin{aligned} p_g &= \frac{n}{2} V_p I_p \cos(\beta_1) + \sum_{h=1}^{n} V_p I_p \cos\left(2\theta_1 + \beta_1 - (h-1)\frac{4\pi}{n}\right) \\ &+ \frac{n}{2} V_n I_n \cos(\beta_2) + \sum_{h=1}^{n} V_n I_n \cos\left(2\theta_2 + \beta_2 + (h-1)\frac{4\pi}{n}\right) \\ &+ \frac{n}{2} V_p I_n \cos(\theta_1 + \theta_2 + \beta_2) + \sum_{h=1}^{n} V_p I_n \cos\left(\theta_1 - \theta_2 - \beta_2 - (h-1)\frac{4\pi}{n}\right) \\ &+ \frac{n}{2} V_n I_p \cos(\theta_1 + \theta_2 + \beta_1) + \sum_{h=1}^{n} V_n I_p \cos\left(\theta_2 - \theta_1 - \beta_1 + (h-1)\frac{4\pi}{n}\right) \end{aligned} \quad (7.29)$$

Using trigonometric property that

$$\sum_{h=1}^{n} \cos\left(\lambda \pm (h-1)\frac{4\pi}{n}\right) = 0 \quad (7.30)$$

(with λ to be any trigonometric angle), (7.29) can be restructured as:

$$\begin{aligned} p_g &= \frac{n}{2}\left[V_p I_p \cos(\beta_1) + V_n I_n \cos(\beta_2)\right] \\ &+ \frac{n}{2}\left[V_p I_n \cos(\beta_2) + V_n I_p \cos(\beta_1)\right] \cos(\theta_1 + \theta_2) \\ &- \frac{n}{2}\left[V_p I_n \sin(\beta_2) + V_n I_p \sin(\beta_1)\right] \sin(\theta_1 + \theta_2) \end{aligned} \quad (7.31)$$

Simplifying the DC and oscillating components of instantaneous power, (7.31) can be restructured as:

$$p_g = P_0 + P_c \cos(\theta_1 + \theta_2) + P_s \sin(\theta_1 + \theta_2) \quad (7.32)$$

Considering that each phase sequence current is interacting with corresponding sequence voltage to form the DC component of reactive power , Q_0, hence utilizing single-phase reactive power definition, it can be expressed as:

$$Q_0 \;=\; \frac{n}{2}\;[V_p I_p \sin(\beta_1) \;+\; V_n I_n \sin(\beta_2)] \tag{7.33}$$

Referring to Figure 7.1, it can be concluded that, the DC side instantaneous power can be expressed as:

$$p_{dc} \;=\; v_{dc}\, i_{dc} \tag{7.34}$$

When both the sides of the inverter are concerned, there must be instantaneous power balance. The inverter current is constituted by load current and the grid current as depicted in (7.23). So, the instantaneous power at the inverter output can be expressed as (as can be classified from Figure 7.1):

$$\begin{aligned} p_{ac} &= \sum_{h=1}^{n}\left[R_h\, i_{Ch}^2 \;+\; \frac{d}{dt}\left(\frac{1}{2}\, L_h\, i_{Ch}^2\right) \;+\; v_{gh} i_{Ch}\right] \\ &= \sum_{h=1}^{n}\left[R_h\, i_{Ch}^2 \;+\; \frac{d}{dt}\left(\frac{1}{2}\, L_h\, i_{Ch}^2\right) \;+\; v_{gh}\,(i_{Lh} \;-\; i_{gh})\right] \\ &= p_{CR} \;+\; p_{CL} \;+\; p_L \;-\; p_g \end{aligned} \tag{7.35}$$

where, instantaneous power caused due to load current, p_L,

$$p_L \;=\; \sum_{h=1}^{n} v_{gh}\, i_{Lh}$$

p_{CR} is the instantaneous power caused by the resistance of the line side inductors as,

$$p_{CR} \;=\; \sum_{h=1}^{n} R_h\, i_{Ch}^2$$

and p_{CL} is the instantaneous power caused by the inductance of the line side inductors as,

$$p_{CL} \;=\; \sum_{h=1}^{n} \frac{d}{dt}\left(\frac{1}{2}\, L_h\, i_{Ch}^2\right)$$

whereas, for the h^{th} phase (as can be referred to Figure 7.1), the line side inductor consists of the resistance, R_h and inductance, L_h.

In practical cases, the typical line side inductors are designed in such a way that, both R_h and L_h assume small values (of the order of $m\Omega$ and mH range), facilitating the assumption that, values of p_{CR} and p_{CL} can be neglected in comparison with values of p_L and p_g. So, (7.35) can be modified as:

$$p_{ac} \approx p_L - p_g \tag{7.36}$$

It can be mentioned that, p_L cannot be controlled because of the nature of the load. However, p_g can be controlled in such a way that the harmonic power due to grid current can be controlled. Using (7.32) in (7.36) and using $p_{dc} = p_{ac}$, the DC link current expression can be written as:

$$i_{dc} = \frac{p_L}{v_{dc}} - \frac{P_0}{v_{dc}} - \frac{P_c}{v_{dc}}\cos(\theta_1 + \theta_2) - \frac{P_s}{v_{dc}}\sin(\theta_1 + \theta_2) \tag{7.37}$$

7.4.2 Extracting the solution provided by *p-q* theory

To make the oscillatory component of instantaneous power, p_g to be zero (terms associated with $\cos(\theta_1 + \theta_2)$ and $\sin(\theta_1 + \theta_2)$), if each of the components of P_s and P_c are equated to zero($P_c = 0$ and $P_s = 0$), (7.32) and (7.33) give the same solution as derived by p-q theory as shown in (7.7). From (7.37), it can be observed that grid current reference generated using p-q theory ensures minimum possible DC link current ripple presence of the terms with $\cos(\theta_1 + \theta_2)$ and $\sin(\theta_1 + \theta_2)$. So, the resulting DC link current expression becomes:

$$i_{dc} = \frac{p_L}{v_{dc}} - \frac{P_g}{v_{dc}} \tag{7.38}$$

7.4.3 Analysis of the solution provided by *FBD* theory

(7.18) can be restructured as:

$$\begin{aligned} v_h &= \frac{1}{n}\sum_{\mu=1}^{n} v_{h\mu} \\ &= \frac{1}{n}\sum_{\mu=1}^{n} [v_{gh} - v_{g\mu}] \\ &= v_{gh} - \frac{1}{n}\sum_{\mu=1}^{n} v_{g\mu} = v_{gh} \end{aligned} \tag{7.39}$$

This simplification is followed by substituting (7.1) in (7.18) and using the trigonometric relation in (7.30). Using (7.19), the following quantity can be reframed as:

$$\begin{aligned} {v_\Sigma}^2 &= {V_p}^2 \sum_{h=1}^{n} \cos^2\left(\theta_1 - (h-1)\frac{2\pi}{n}\right) \\ &+ {V_n}^2 \sum_{h=1}^{n} \cos^2\left(\theta_2 + (h-1)\frac{2\pi}{n}\right) \\ &+ 2\,V_p\,V_n \sum_{h=1}^{n} \cos\left(\theta_1 - (h-1)\frac{2\pi}{n}\right)\cos\left(\theta_2 + (h-1)\frac{2\pi}{n}\right) \end{aligned} \tag{7.40}$$

(7.40) can be further modified as follows:

$$\begin{aligned} {v_\Sigma}^2 &= \frac{1}{2}{V_p}^2 \sum_{h=1}^{n} \left[1 + \cos\left(2\,\theta_1 - (h-1)\frac{4\pi}{n}\right)\right] \\ &+ \frac{1}{2}{V_n}^2 \sum_{h=1}^{n} \left[1 + \cos\left(2\,\theta_2 + (h-1)\frac{4\pi}{n}\right)\right] \\ &+ V_p\,V_n \sum_{h=1}^{n} \left[\cos(\theta_1 + \theta_2) + \cos\left(\theta_1 - \theta_2 - (h-1)\frac{4\pi}{n}\right)\right] \end{aligned} \tag{7.41}$$

Using (7.30), (7.41) can be modified as:

$${v_\Sigma}^2 = \frac{n}{2}\left[{V_p}^2 + {V_n}^2 + 2\,V_p\,V_n\cos(\theta_1 + \theta_2)\right] \tag{7.42}$$

Now, (7.20) can be rewritten as:

$$\overline{{v_\Sigma}^2} = \frac{1}{M}\sum_{M}\left[\frac{n}{2}\left({V_p}^2 + {V_n}^2 + 2\,V_p\,V_n\cos(\theta_1 + \theta_2)\right)\right] \tag{7.43}$$

However, $\cos(\theta_1 + \theta_2)$ has a frequency of double the fundamental frequency of grid. Hence, theoretically, the average value of $\cos(\theta_1 + \theta_2)$ over half cycle of fundamental grid frequency is 0. Hence, (7.43) can be modified as:

$$\overline{v_\Sigma{}^2} = \left[\frac{n}{2}\left(V_p{}^2 + V_n{}^2\right)\right] \tag{7.44}$$

Now, using (7.21) and (7.22), the grid current equation can be written as:

$$\begin{aligned} i^*_{gh} &= \frac{P_g}{\left[\frac{n}{2}\left(V_p{}^2 + V_n{}^2\right)\right]} v_{gh} \\ &= \frac{2\,P_g\,V_p}{n\left(V_p{}^2 + V_n{}^2\right)} \cos\left(\theta_1 - (h-1)\frac{2\pi}{n}\right) + \frac{2\,P_g\,V_n}{n\left(V_p{}^2 + V_n{}^2\right)} \cos\left(\theta_2 + (h-1)\frac{2\pi}{n}\right) \end{aligned} \tag{7.45}$$

for $h = 1, 2, 3....n$. Comparing this with (7.2), the conclusions can be inferred as:

$$\begin{aligned} I_p &= \frac{2\,P_g\,V_p}{n\left(V_p{}^2 + V_n{}^2\right)} \\ I_n &= \frac{2\,P_g\,V_n}{n\left(V_p{}^2 + V_n{}^2\right)} \\ \beta_1 &= \beta_2 = 0 \end{aligned} \tag{7.46}$$

Hence, using (7.46) in (7.31) can be modified as:

$$p_g = P_g + P_g \frac{2\,V_p\,V_n}{V_p{}^2 + V_n{}^2} \cos(\theta_1 + \theta_2) \tag{7.47}$$

It can also be calculated from (7.33) that the DC component of the reactive power is: $Q_0 = 0$. However, because of the double harmonic instantaneous power presence, the DC current expression can be re-written as (using (7.37)):

$$i_{dc} = \frac{p_L}{v_{dc}} - \frac{P_g}{v_{dc}} - \frac{P_g}{v_{dc}} \frac{2\,V_p\,V_n}{V_p{}^2 + V_n{}^2} \cos(\theta_1 + \theta_2) \tag{7.48}$$

So, if DC voltage, v_{dc} is stabilized with DC link capacitor, the DC current, i_{dc} gets an increment in second harmonic ripple due to the term with $\cos(\theta_1 + \theta_2)$ as can be seen in (7.48).

7.4.4 Derivation of the grid current reference for a typical three phase unbalance system ($n = 3$)

If a typical three phase unbalanced grid voltage is considered with phase-a positive and negative sequence voltage are in same phase such as:

$$\begin{aligned} v_{ga}(t) &= V_p \cos(\theta) + V_n \cos(\theta) \\ v_{gb}(t) &= V_p \cos\left(\theta - \frac{2\pi}{3}\right) + V_n \cos\left(\theta + \frac{2\pi}{3}\right) \\ v_{gc}(t) &= V_p \cos\left(\theta + \frac{2\pi}{3}\right) + V_n \cos\left(\theta - \frac{2\pi}{3}\right) \end{aligned} \tag{7.49}$$

where $\theta_1 = \theta_2 = \theta$ as modified in the (7.1). Now, for the grid power command active power, P_g and reactive power, $0\,Var$, by plugging in solution by p-q theory based estimator ((7.8)) in (7.2) for the three phase system ($n = 3$) the grid current references can be derived as:

$$\begin{aligned} i^*_{ga}(t) &= \frac{2}{3}\frac{P_g(V_p - V_n)}{V_p^2 - V_n^2}\cos(\theta) \\ i^*_{gb}(t) &= \frac{2}{3}\frac{P_g\sqrt{V_p^2 + V_n^2 + V_pV_n}}{V_p^2 - V_n^2}\cos\left(\theta - 180^0 + tan^{-1}\left(\frac{\sqrt{3}(V_p + V_n)}{V_p - V_n}\right)\right) \\ i^*_{gc}(t) &= \frac{2}{3}\frac{P_g\sqrt{V_p^2 + V_n^2 + V_pV_n}}{V_p^2 - V_n^2}\cos\left(\theta - 180^0 - tan^{-1}\left(\frac{\sqrt{3}(V_p + V_n)}{V_p - V_n}\right)\right) \end{aligned} \tag{7.50}$$

Similarly, plugging in (7.46), in (7.2), the grid current reference solutions for the grid power command active power, P_g and reactive power $0\,Var$ for a typical three

phase system ($n = 3$) in solution by *FBD* theory based estimator can be found as:

$$\begin{aligned} i^*_{ga}(t) &= \frac{2}{3}\frac{P_g(V_p + V_n)}{V_p^2 + V_n^2}\cos(\theta) \\ i^*_{gb}(t) &= \frac{2}{3}\frac{P_g\sqrt{V_p^2 + V_n^2 - V_pV_n}}{V_p^2 + V_n^2}\cos\left(\theta - 180^0 + tan^{-1}\left(\frac{\sqrt{3}(V_p - V_n)}{V_p + V_n}\right)\right) \\ i^*_{gc}(t) &= \frac{2}{3}\frac{P_g\sqrt{V_p^2 + V_n^2 - V_pV_n}}{V_p^2 + V_n^2}\cos\left(\theta - 180^0 - tan^{-1}\left(\frac{\sqrt{3}(V_p - V_n)}{V_p + V_n}\right)\right) \end{aligned} \tag{7.51}$$

(7.50) and (7.51) are used to verify that the magnitudes and relative phase angles of the reference grid currents and actual grid currents in the experimental results, follow the property of the *p-q* and *FBD* theory based current reference calculator respectively.

7.5 Experimental Results

The grid current reference generation method is validated by extensive testing on a developed prototype. The overall control system is implemented in DS1104 dSPACE card. The switching frequency of the SPWM, f_s as well as the sampling frequency of the overall control system, f_{sample} is set at $10\,kHz$ during the course of the experiments. Experimental grid voltages are formed using ***Lx3000 California Instrument*** three phase programmable power supply.

7.5.1 Experimental results to show the performance of the *complex notch filter*

To test the feasibility of the CNF (BLOCK-B) and the RRSC (BLOCK-D) of Figure 7.2, experiments are carried out with the asymmetrical and harmonic distorted

grid voltages controlled by the three-phase programmable AC power supply. It can be analyzed from Figure 7.7(a) that the grid is contaminated with 20% negative sequence and each of the phase voltages are contaminated with 5^{th}, 7^{th} and 11^{th} order voltage harmonics of 10%, 7% and 5% of the fundamental magnitude respectively. The grid voltages can be expressed as:

$$\begin{aligned}
v_{ga}(t) &= V_p\cos(\theta) + V_n\cos(\theta) \\
&+ 0.1\,V_p\cos(5\theta) + 0.1\,V_n\cos(5\theta) \\
&+ 0.07\,V_p\cos(7\theta) + 0.07\,V_n\cos(7\theta) \\
&+ 0.05\,V_p\cos(11\theta) + 0.05\,V_n\cos(11\theta) \\
v_{gb}(t) &= V_p\cos(\theta - \frac{2\pi}{3}) + V_n\cos(\theta + \frac{2\pi}{3}) \\
&+ 0.1\,V_p\cos(5\theta - \frac{10\pi}{3}) + 0.1\,V_n\cos(5\theta + \frac{10\pi}{3}) \\
&+ 0.07\,V_p\cos(7\theta - \frac{14\pi}{3}) + 0.07\,V_n\cos(7\theta + \frac{14\pi}{3}) \\
&+ 0.05\,V_p\cos(11\theta - \frac{22\pi}{3}) + 0.05\,V_n\cos(11\theta + \frac{22\pi}{3}) \\
v_{gc}(t) &= V_p\cos(\theta + \frac{2\pi}{3}) + V_n\cos(\theta - \frac{2\pi}{3}) \\
&+ 0.1\,V_p\cos(5\theta + \frac{10\pi}{3}) + 0.1\,V_n\cos(5\theta - \frac{10\pi}{3}) \\
&+ 0.07\,V_p\cos(7\theta + \frac{14\pi}{3}) + 0.07\,V_n\cos(7\theta - \frac{14\pi}{3}) \\
&+ 0.05\,V_p\cos(11\theta + \frac{22\pi}{3}) + 0.05\,V_n\cos(11\theta - \frac{22\pi}{3}) \qquad (7.52)
\end{aligned}$$

where, θ is the fundamental phase of grid voltage. As set in the three-phase controllable power supply, the fundamental of grid voltage has positive sequence peak magnitude is about $V_p = 49.3\,V$ and negative sequence peak magnitude is about $V_n = 9.86\,V$ and for phase-a the positive sequence and negative sequence voltage align on the same phase (total RMS of phase-a voltage is $42.2V$ and that of phase-b and phase-c is $32.3\,V$). The fundamental positive and negative sequence of phase-a voltages are refereed as v_{gafP} and v_{gafN} respectively as:

$$\begin{aligned} v_{gafP} &= V_p \cos(\theta) \\ v_{gafN} &= V_n \cos(\theta) \end{aligned} \tag{7.53}$$

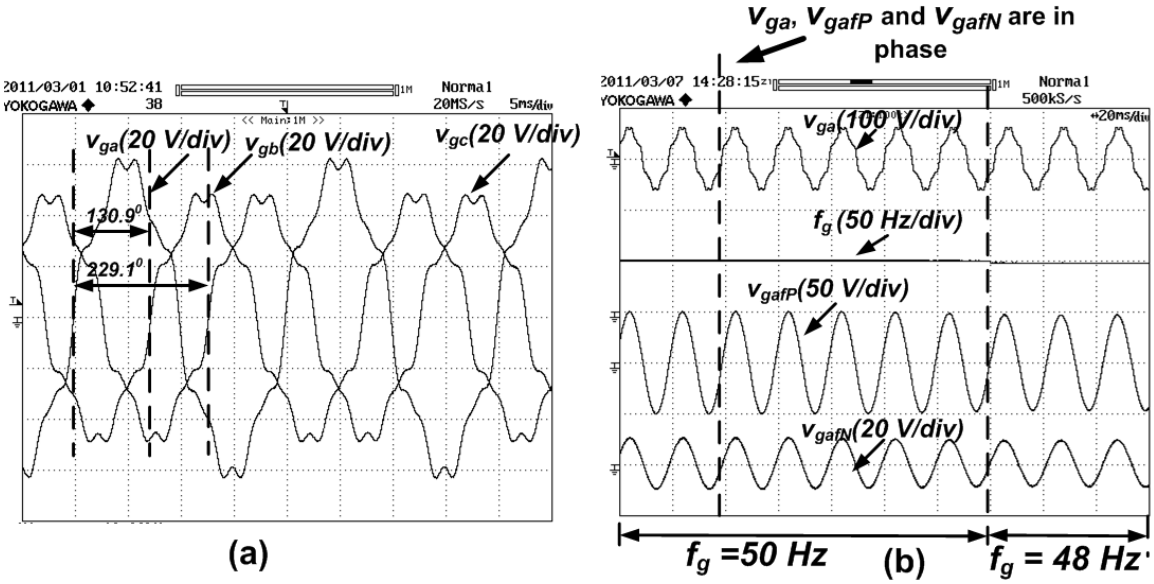

Figure 7.7: Experimental results (a) three phase grid voltages, v_{ga}, v_{gb} and v_{gc} at fundamental grid voltage frequency, $f_g = 50\,Hz$, (b) phase-a grid voltage, v_{ga}, fundamental grid frequency, f_g, fundamental positive sequence phase-a voltage, v_{gafP}, fundamental negative sequence phase-a voltage, v_{gafN} under sudden change in fundamental grid frequency, f_g from 50 Hz to 48 hz.

It can be observed from Figure 7.7(b), that, the CNF output of v_{gafP} and v_{gafN} are concurrence with the theoretical value as discussed in (7.52) and (7.53). The filter also responses within appreciable range even in the case of sudden jump of fundamental grid frequency by 2 Hz as shown in Figure 7.7(b). It can also be noted from Figure 7.7(b) that, the frequency output of the RRSV (BLOCK-D of Figure 7.2) also follows the frequency change and tune the CNF accordingly.

7.5.2 Experimental results to show the reference current generation using *p-q* and *FBD* theory

The reference grid current generation schemes using *p-q* and *FBD* methods are experimentally tested and the experimental results are shown in Figure 7.8.

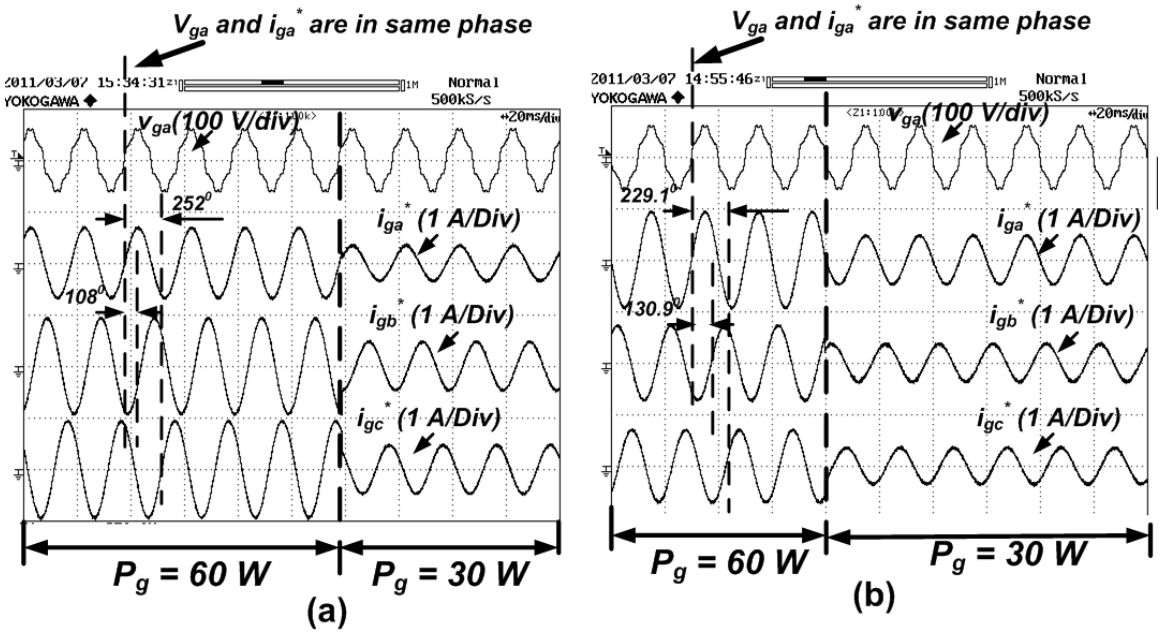

Figure 7.8: Experimental results of phase-a grid voltage, v_{ga} and three grid current references, i_{ga}^*, i_{gb}^*, i_{gc}^* for (a) *pq* theory based grid current reference estimator, (b) *FBD* theory based grid current reference estimator for a sudden change of grid active power command, P_g from 60 W to 30 W with fundamental grid sequence voltages $V_p = 49.3\,V$ and $V_n = 9.86\,V$.

Figure 7.8(a) shows the experimental waveforms of phase-a grid voltage, v_{ga} and the three grid current references, i_{ga}^*, i_{gb}^*, i_{gc}^* with a transient of sudden change of grid active power command, P_g from $60W$ to $30W$ using *p-q* method of estimation. It can be observed that when the $P_g = 60\,W$, the phase-a grid current peak is about 0.67 A and the peak of both phase-b and phase-c grid currents are about 0.94 A as can also be calculated from (7.50). The corresponding values jump to about $0.34A$ and $0.47A$ when P_g command is initiated as can be seen Figure 7.8(a). The relative phase angles between the phase grid currents are shown to be about

108^0 (between i^*_{ga} and i^*_{gb}) and 252^0 (between i^*_{ga} and i^*_{gc}) as can be observed in Figure 7.8(a). The phase angles can also in accordance to the (7.50). The grid voltage harmonics are filtered by the CNF so that the grid current references are free of any grid harmonics. Figure 7.8(b) shows the experimental waveforms of phase-a grid voltage, v_{ga} and the three grid current references, i^*_{ga}, i^*_{gb}, i^*_{gc} with a transient of sudden change of grid active power command, P_g from $60\,W$ to $30\,W$ using *FBD* method of estimation. the figure depicts that when $P_g = 60\,W$ is there the peak value of phase-a grid current reference is about $0.94\,A$ and the same for phase-b and phase-c grid current reference is $0.71\,A$. During P_g command the corresponding values attained the magnitudes of $0.47\,A$ and $0.34\,A$ respectively. It can also be observed from Figure 7.8(b) that the respective phase grid current is in phase with the respective fundamental grid phase voltage as can be confirmed with the relative phase angles of the variables in Figures 7.7(a) and 7.8(b). The magnitude and relative phase angles of the grid current reference for *FBD* method of estimation can also be confirmed with the (7.51).

Figure 7.9(a) shows the experimental waveform of the unbalanced and harmonic contaminated grid voltage waveforms. The relative phases of the respective grid voltages explain the unbalance nature also. Figure 7.9(b) shows the grid current reference waveforms, i^*_{ga}, i^*_{gb} and i^*_{gc} for fundamental grid frequency, $f_g = 50Hz$ and grid power command, $P_g = 100\,W$. It can be noted from Figure 7.9(b) that, the peak value of the reference currents are about $1.56\,A$ for phase-a and about $1.19\,A$ for phase-b and c with each of the grid current references are exactly in phase with the respective fundamental grid phases to ensure $Q_g = 0\,Var$. It can be noted that the relative magnitudes of the reference grid currents are same value as can also be predicted from (7.51). Figure 7.9(c) shows the grid current

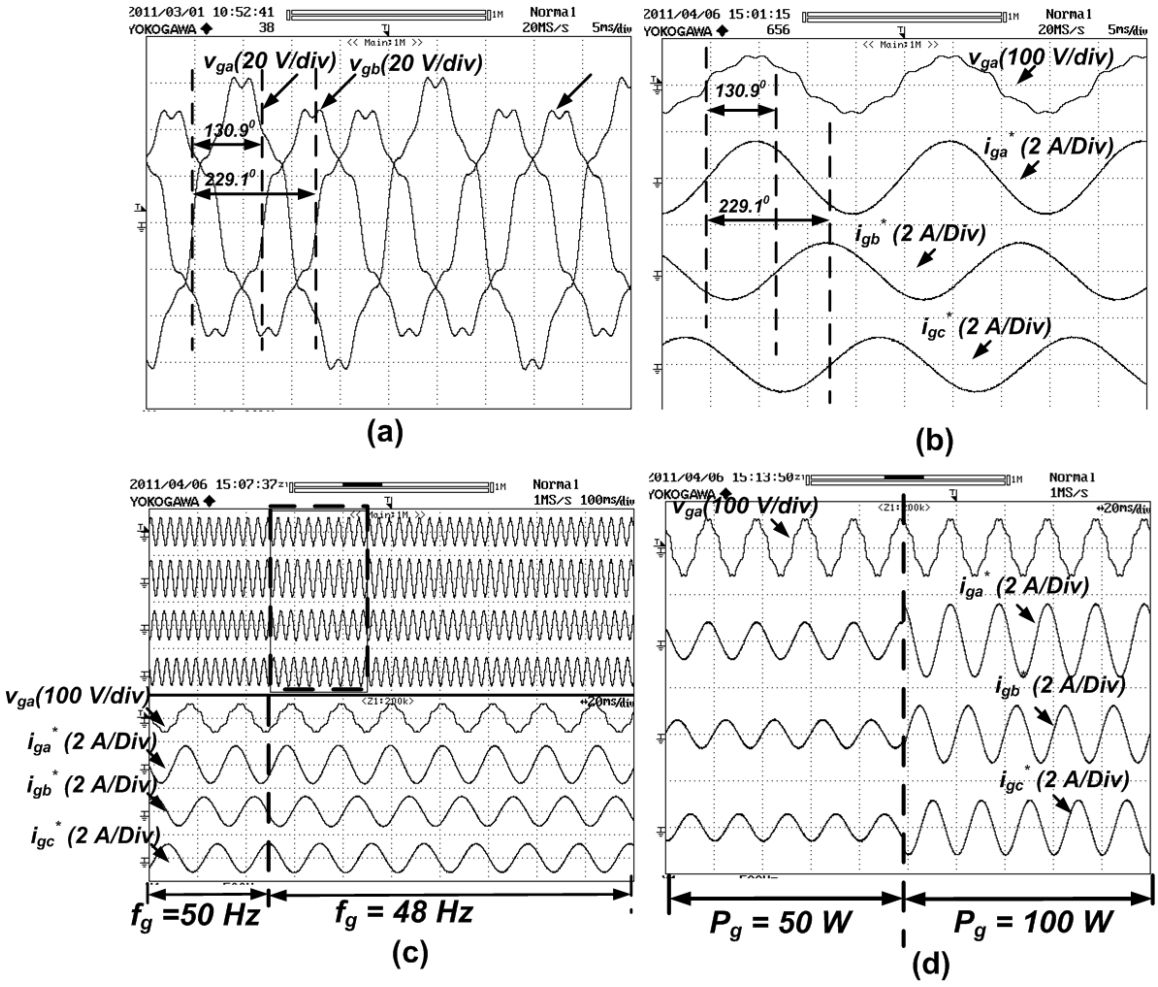

Figure 7.9: Experimental results (a) three-phase grid voltages, v_{ga}, v_{gb} and v_{gc} at fundamental grid voltage frequency, $f_g = 50\,Hz$, (b) phase-a grid voltage, v_{ga}, three-phase grid current references, i_{ga}^*, i_{gb}^*, i_{gc}^* at $50\,Hz$ with $P_g = 100\,Watts$, (c) phase-a grid voltage, v_{ga} and three grid current references, i_{ga}^*, i_{gb}^*, i_{gc}^* for a sudden change of grid frequency, f_g from $50\,Hz$ to $48\,hz$ at $P_g = 100\,W$ command, (d) phase-a grid voltage, v_{ga} and three grid current references, i_{ga}^*, i_{gb}^*, i_{gc}^* for a sudden change of grid active power command, P_g from $50\,W$ to $100\,W$ at fundamental grid voltage, $f_g = 50\,Hz$ with *FBD* method of current reference estimation and grid sequence voltages $V_p = 49.3\,V$ and $V_n = 9.86\,V$.

references during a sudden change of grid fundamental frequency from $f_g = 50$ to $f_g = 48\,Hz$ with grid active power command $P_g = 100\,W$. It can be seen from the waveform that, there are transients (magnitude and phase change of the reference currents) due to the sudden frequency change is followed by stable steady state with correct magnitude and phase relation. It can be noted that the sampling fre-

quency $f_s = 10\,kHz$ is not an integral multiple of the fundamental grid frequency $f_g = 48\,Hz$. However, because of the position sampling, the calculator is able to calculate correct and stable grid current references. Figure 7.9(d) shows the transient waveform of the grid current references during the transient active grid power command change from $P_g = 50W$ to $P_g = 100W$ with fundamental grid frequency maintained at $f_g = 50\,Hz$. It can be seen that, after issuance of the power change command, the current reference magnitudes, almost immediately jump to double the value due to the doubling of the power command with no change in the relative phase relations. It can be noted the despite of the harmonics presence in the grid voltages, the grid current references are not polluted with harmonics.

7.5.3 Experimental results to show the grid current tracking for the CCVSI

To test the impact of different grid current reference generation schemes on the real power circuit, experiments are carried out. The experimental results are presented with *b-6* topology of three phase grid connected inverter. A non-linear load is also connected at the point of common coupling of the grid. The schematic of the experimental setup is shown in Figure 6.6. Different parameters of the experimental setup is shown in Table 6.1. It is seen that with the specified unbalanced grid described in (7.52), the non-linear load draws active power amounting to P_L. The CCVSI is controlled in such a way that, $P_g = 60\,W$ is drawn from the grid and rest of the active power along with the non-linear current compensation is carried out by the CCVSI. The current of the CCVSI is controlled using the *a-b-c* frame *Lyapunov function* base current controller as described in details in Chapter 6. The current reference of the grid are calculated using *p-q* technique ((7.8)) and

FBD technique ((7.22)) and the CCVSI current references are found using (7.23) and it is tracked with the *a-b-c* frame *Lyapunov function* based controller and the experimental results are provided in Figure 7.10.

The non-linear load currents are shown in Figure 7.10(a). Figures 7.10(1b)-(1c) and 7.10(2b)-(2c) show the corresponding CCVSI currents (i_{Ca}, i_{Cb}, i_{Cc}) and the grid currents (i_{ga}, i_{gb}, i_{gc}) for the *p-q* and *FBD* method of grid current generation techniques respectively. It can be noticed that the magnitudes and relative phases of the actual grid currents shown in Figures 7.10(1c) and 7.10(2c) matches with that of the reference grid currents as shown in Figure 7.8 for both the current reference generation methods. From, Figure 7.10(1c), the actual active power drawn from the grid for the *p-q* based estimator can be recalculated (by considering fundamental grid voltages) as: $P^{pq}_{gactual} = \left(41.8 \times \frac{0.67}{\sqrt{2}}\right) + \left(32.02 \times \frac{0.94}{\sqrt{2}} \cos(130^0 - 108^0)\right) + \left(32.02 \times \frac{0.94}{\sqrt{2}} \cos(250^0 - 229^0)\right) \simeq 60\ W.$ From, Figure 7.10(2c), the actual active power drawn from the grid for the *FBD* based estimator can be recalculated (by considering fundamental grid voltages) as: $P^{FBD}_{gactual} = \left(41.8 \times \frac{0.94}{\sqrt{2}}\right) + \left(32.02 \times \frac{0.71}{\sqrt{2}}\right) + \left(32.02 \times \frac{0.71}{\sqrt{2}}\right) \simeq 60\,W.$

7.5.4 Experimental results to show the DC link ripple comparison in *p-q* and *FBD* theory based grid current estimation

The DC link ripple is an important aspect of investigation in the choice of grid current reference generation scheme. However, as can be seen from (7.38) and (7.48) that, if the DC link voltage is is maintained without ripple with DC link capacitors, the ripple manifests in the DC link current i_{dc}. The i_{dc} ripple is affected by the load

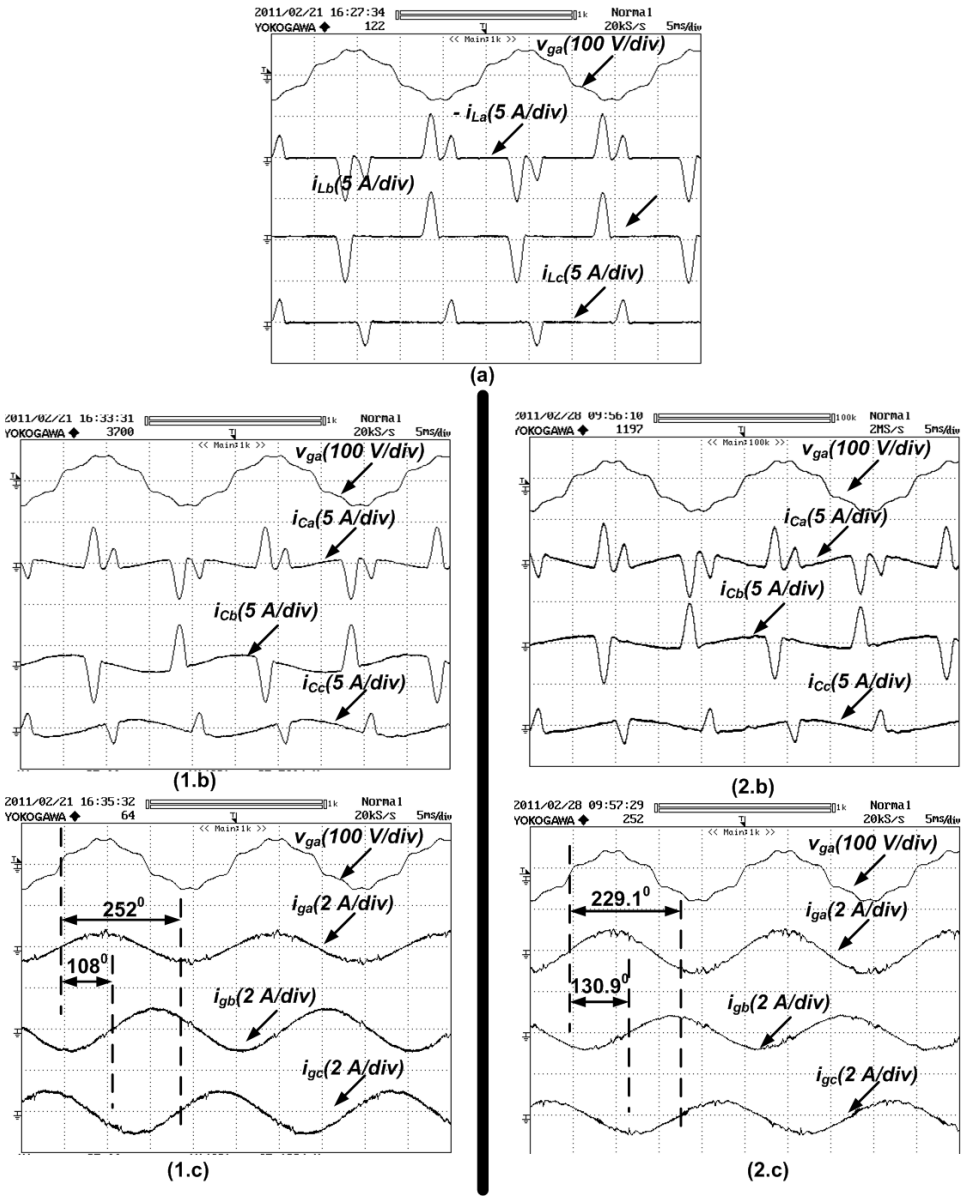

Figure 7.10: Experimental results of (a) grid phase-a voltage, v_{ga}, three phase load currents, i_{La}, i_{Lb}, i_{Lc}, (1b) Phase-a grid voltage, v_{ga}, three phase CCVSI currents, i_{Ca}, i_{Cb}, i_{Cc} with *pq* theory based grid current estimator, (2b) Phase-a grid voltage, v_{ga}, three phase CCVSI currents, i_{Ca}, i_{Cb}, i_{Cc} with *FBD* theory based grid current estimator, (1c) Phase-a grid voltage, v_{ga}, three phase grid currents currents, i_{ga}, i_{gb}, i_{gc} with *pq* theory based grid current estimator, (2c) Phase-a grid voltage, v_{ga}, three phase grid currents currents, i_{ga}, i_{gb}, i_{gc} with *FBD* theory based grid current estimator, with grid power command, $P_g = 60\,W$ and $Q_g = 0\,Var$ with non-linear load with $P_L = 75\,W$ with *b6* topology of inverter and $V_p = 49.3\,V$ and $V_n = 9.86\,V$.

ripple (as a part of p_L) and the grid voltage ripple. To test the ripple manifestation due to the current reference scheme only, the grid voltage are maintained to be pure sinusoid with 20% negative sequence contamination and the CCVSI is controlled to pump pure sinusoid current to the grid in the absence of any load at the PCC ($p_L = 0$). The schematic of the experimental setup is shown in Figure 7.11. The experimental results are shown in Figure 7.12.

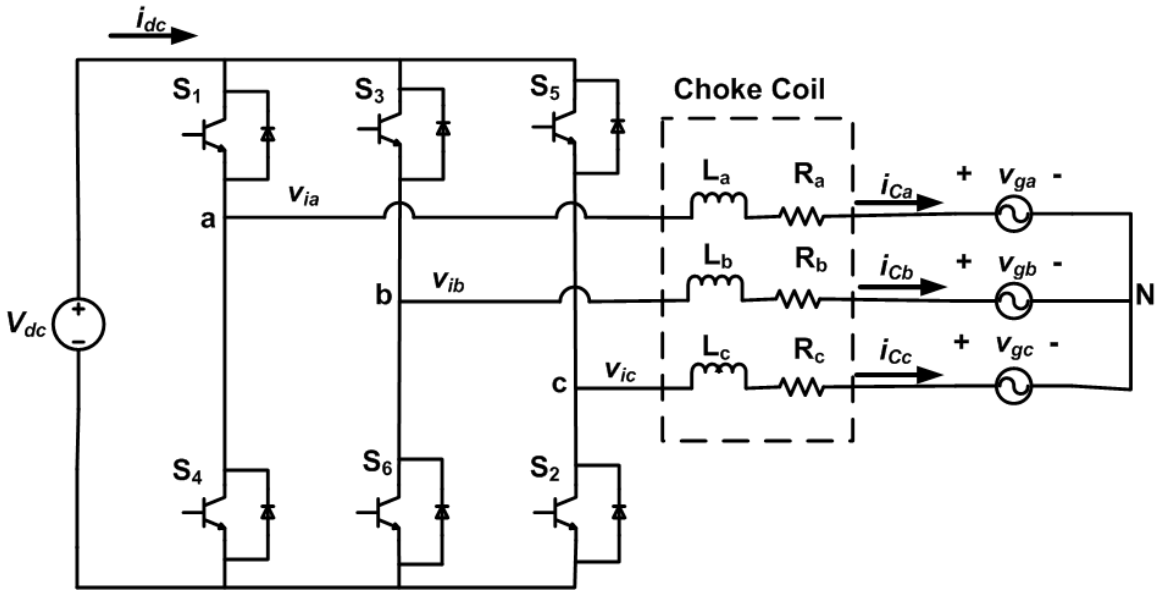

Figure 7.11: Details of the power circuit of the experiment to sink power to grid.

The grid voltages are controlled to have only fundamental with 20% negative sequence voltage as:

$$\begin{aligned} v_{ga}(t) &= V_p \cos(\theta) + V_n \cos(\theta) \\ v_{gb}(t) &= V_p \cos(\theta - \frac{2\pi}{3}) + V_n \cos(\theta + \frac{2\pi}{3}) \\ v_{gc}(t) &= V_p \cos(\theta + \frac{2\pi}{3}) + V_n \cos(\theta - \frac{2\pi}{3}) \end{aligned} \tag{7.54}$$

The fundamental of grid voltage has positive sequence peak magnitude is about $V_p = 49.73\,V$ and negative sequence peak magnitude is about $V_n = 9.95\,V$ and

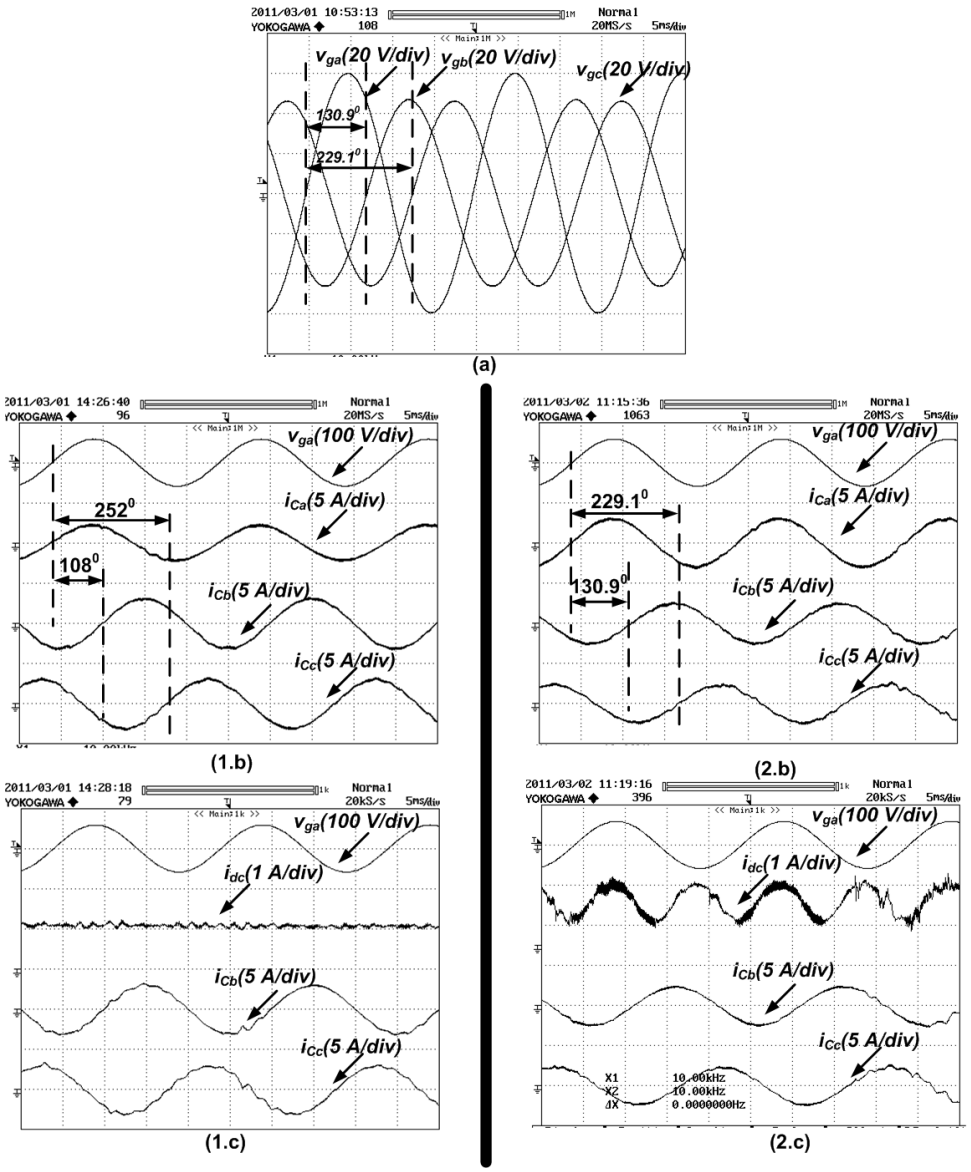

Figure 7.12: Experimental results of (a) the grid phase voltages, v_{ga}, v_{gb}, v_{gc}, (1b) Phase-a grid voltage, v_{ga}, three phase CCVSI currents, i_{Ca}, i_{Cb}, i_{Cc} with pq theory based grid current estimator, (2b) Phase-a grid voltage, v_{ga}, three phase CCVSI currents, i_{Ca}, i_{Cb}, i_{Cc} with FBD theory based grid current estimator, (1c) Phase-a grid voltage, v_{ga}, DC link current, i_{dc}, two CCVSI currents i_{Cb}, i_{Cc} with pq theory based grid current estimator, (2c) Phase-a grid voltage, v_{ga}, DC link current, i_{dc}, two CCVSI currents i_{Cb}, i_{Cc} with FBD theory based grid current estimator, with grid power command, $P_g = -200\,W$ and $Q_g = 0\,Var$ with non-linear load with $P_L = 0$ with $b6$ topology of inverter and $V_p = 49.73\,V$ and $V_n = 9.95\,V$.

for phase-a the positive sequence and negative sequence voltage align on the same phase (total RMS of phase-a voltage is still $42.2\,V$ and that of phase-b and phase-c

is 32.3 V). The sinusoidal grid voltages are shown in Figure 7.12(a). The active power sinked to the grid is amounting to $P_g = -P_{sink} = -200\,W$. The DC link voltage is maintained at the value $V_{dc} = 200\,V$. Figure 7.12(1b) shows the three phase sinusoidal CCVSI current waveforms. As can be predicted from (7.50) for p-q theory based estimator, for the CCVSI currents(which is also the negative grid currents) phase-a assumes the peak value of about 2.2 A and phase-b and phase-c assumes the peak value about 3.1 A and the specific relative phases as can be supported by Figure 7.12(1b). Similarly, from Figure 7.12(2b) for *FBD* theory based estimator, it can be seen that the phase-a CCVSI current peak is about 3.1 A and the same of phase-b and phase-c for CCVSI is about 2.4 A. The relative phase relations of the CCVSI currents are also shown in Figure 7.12(2b). The magnitudes as well as the phases are also in accordance with the (7.51). However, to compare the ripple in the DC link currents in the p-q and *FBD* method of estimator, Figures 7.12(1c) and 7.12(2c) respectively are compared. It can be seen that, for p-q theory based estimator, the DC link current is double harmonic ripple free and maintaining a steady value of about 1.1 A as can be predicted using (7.38) (putting $v_{dc}200\,V$, $p_L = 0$ and $P_g = -200\,W$). On the other hand, for *FBD* theory based estimator, the DC link current has double harmonic current ripple of peak to peak value about 0.9 A and a steady DC value of about 1.1 A (Figure 7.12(2c)). The relative values of the harmonic current to the DC value of current in the DC link can be confirmed with (7.48) with $p_L = 0$, $P_g = -200\,W$, $v_{dc} = 200\,V$, $V_p = 49.73\,V$ and $V_n = 9.95\,V$.

7.6 Summary

In this Chapter, different grid current reference generation and inverter current reference derivation methods are proposed for a parallel multi-phase renewable energy source based inverter connected to generalized multi-phase micro-grid ystem. The reference current tracking by the inverter ensures proper active and reactive grid power flow along with minimum THD of the grid currents in the presence of a non-linear load at the grid. The proposed methods are implemented in the *a-b-c* frame resulting fast dynamic response with respect to the conventional method. The proposed methods also operate without the PARK's transformation, hence usage of traditional PLL is not needed. However, the fundamental grid voltage phase is extracted using a proposed alternative method, which is less computation intensive that conventional PLL. The proposed CNF based symmetrical voltage sequence extraction block is also easier to implement than the traditional *Fortescue's* method. Different grid current reference generation schemes, i.e. *p-q* and *FBD* methods are investigated and the effect on DC link side ripples are also investigated. The proposed methods are also capable of rejecting the effect of grid voltage harmonics in the grid current references and that of change in grid frequency. A detailed analysis of the overall systems are provided for a generalized n-phase system and the proposed systems are validated in a generalized three-phase micro-grid system. Experimental results are provided to verify the feasibility of the proposed system.

Chapter 8

Application of four-switch based three-phase grid connected inverter to connect renewable energy source to a generalized micro-grid system

The three-phase renewable energy source based inverters are mostly six switch based *b-6* topology inverters connected to generalized micro-grid systems. However, the cost minimization of the overall hardware of the micro-grid system is one of the important aspect of research these days. In motor drive applications, four-switch based three-phase inverters (*b-4* topology) are commonly used as can be seen from [111]-[119]. However, different complex space vector techniques are used to reduce the phase current distortion of the four-switch based three-phase inverters because of the DC link mid-point voltage fluctuation as well as asymmetrical splitting of DC link capacitors.

In this Chapter a novel method is proposed to use four-switch based three-

phase inverter for grid connected renewable energy source based inverter application. A novel current control system is proposed to take care of the DC link mid-point voltage fluctuation as well as asymmetrical splitting of DC link capacitors using simple Sine PWM based power electric switching modulation technique. The proposed system reduces the hardware cost of the interconnecting inverter in the micro-grid due to the reduction of switch count of the inverter. Experimental results are provided to verify the feasibility of the proposed concept.

8.1 Four switch three-phase VSI (*b-4* topology) based grid connected inverter

The power circuit of a typical three-phase renewable energy source base inverter connected to generalized micro-grid is shown in Figure 6.2 and the operation of the overall circuit is described in Chapter 6. The inverter circuit is modified to form a four-switch based three-phase inverter interfacing the micro-grid system as shown in Figure 8.1. The DC voltage source, v_{dc} is assumed to be formed by the

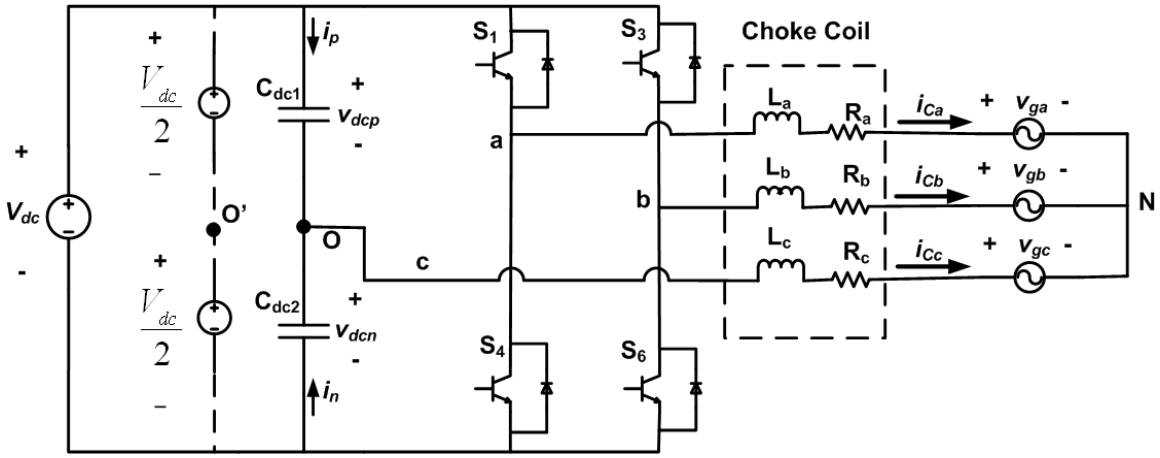

Figure 8.1: Details of the power circuit of the experiment using *b-4* inverter structure.

renewable energy sources as explained before in Figure 6.2. In the *b-4* power circuit shown in Figure 8.1, the two phases (phase-a and phase-b) are connected to the two different legs of the inverter and the phase-c is connected to the expected DC link mid-point O. Ideally, the DC link split capacitors C_{dc1} and C_{dc2} should be of exactly the same value. In practical case it is impossible to get such a symmetry in the capacitors even if from the same manufacturer and under the same batch of production. The point O' is the ideal DC link mid-point splitting the DC link voltage in exact halves. However, in reality, point O' does not exist. The inverter is connected to the three-phase grid at the PCC. At the same PCC, a non-linear three-phase rectifier load is also connected as shown in Figure 6.2.

8.2 Mathematical modeling of the *b-4* topology based grid connected inverter and description of the control structure

Figure 8.1 explains the interconnection between the grid and the inverter system. The grid neutral point N is isolated from the inverter ensuring the absence of zero sequence current in the inverter current. The three-phase line side inductances are characterized with inductance and resistance, (L_a, R_a), (L_b, R_b) and (L_c, R_c). The phase current relations of each of the phases can be written as:

$$\begin{aligned} L_a \frac{di_{Ca}}{dt} + R_a\, i_{Ca} &= v_{ia} - v_{ga} \\ L_b \frac{di_{Cb}}{dt} + R_b\, i_{Cb} &= v_{ib} - v_{gb} \\ L_c \frac{di_{Cc}}{dt} + R_c\, i_{Cc} &= v_{ic} - v_{gc} \\ i_{Ca} + i_{Cb} + i_{Cc} &= 0 \end{aligned} \tag{8.1}$$

here, v_{ia}, v_{ib} and v_{ic} are the respective inverter phase voltages with respect to the grid neutral, **N** and v_{ga}, v_{gb} and v_{gc} are the respective grid phase voltages with respect to the grid neutral, **N**. The details of the analysis are given in Chapter 6. Analyzing (8.1) in line voltage domain and taking phase-a and phase-b currents to be independent state variables ($x_1 = i_{Ca}$ and $x_2 = i_{Cb}$), the equations can be rearranged (as also done in Chapter 6) as:

$$\begin{aligned} \frac{dx_1}{dt} &= a_{11}x_1 + a_{12}x_2 + b_{11}v_{iac} + b_{12}v_{ibc} + d_1 \\ \frac{dx_2}{dt} &= a_{21}x_1 + a_{22}x_2 + b_{21}v_{iac} + b_{22}v_{ibc} + d_2 \end{aligned} \tag{8.2}$$

where, $a_{11} = -\frac{R_aL_b + R_cL_b + R_aL_c}{L_aL_b + L_bL_c + L_cL_a}$, $a_{12} = -\frac{R_cL_b - R_bL_c}{L_aL_b + L_bL_c + L_cL_a}$, $a_{22} = -\frac{R_bL_a + R_cL_a + R_bL_c}{L_aL_b + L_bL_c + L_cL_a}$, $a_{21} = \frac{R_cL_a - R_aL_c}{L_aL_b + L_bL_c + L_cL_a}$, $b_{11} = \frac{L_b + L_c}{L_aL_b + L_bL_c + L_cL_a}$, $b_{12} = -\frac{L_c}{L_aL_b + L_bL_c + L_cL_a}$, $b_{21} = -\frac{L_c}{L_aL_b + L_bL_c + L_cL_a}$, $b_{22} = \frac{L_a + L_c}{L_aL_b + L_bL_c + L_cL_a}$, $d_1 = -\frac{(L_b + L_c)v_{gac} - L_cv_{gbc}}{L_aL_b + L_bL_c + L_cL_a}$, $d_2 = -\frac{-L_cv_{gac} + (L_a + L_c)v_{gbc}}{L_aL_b + L_bL_c + L_cL_a}$. where, v_{imn} and v_{gmn} are respective inverter and grid line voltages between phase m and n respectively with $m, n \in a$, b, c and d_1, d_2 are regarded as the disturbance inputs to (8.2).

The line side inductances are designed in such a way that, $L_a \simeq L_b \simeq L_c = L$ and $R_a \simeq R_b \simeq R_c = 0$. This simplifies the (8.2) as:

$$\begin{aligned} \frac{dx_1}{dt} &= \frac{2}{3\,L}v_{iac} - \frac{1}{3\,L}v_{ibc} + d_1 \\ \frac{dx_2}{dt} &= -\frac{1}{3\,L}v_{iac} + \frac{2}{3\,L}v_{ibc} + d_2 \end{aligned} \tag{8.3}$$

The inverter line voltages can be expressed as:

$$\begin{aligned} v_{iac} &= v_{iaO'} - v_{icO'} = v_{iaO'} - v_{OO'} \\ v_{ibc} &= v_{ibO'} - v_{icO'} = v_{ibO'} - v_{OO'} \end{aligned} \tag{8.4}$$

where, point *O'* is the ideal mid-point of the DC link voltage as can be seen in Figure 8.1. The SPWM process controls the phase voltages with respect to the

ideal DC link mid-point *O'*, i.e. $v_{iaO'}$ and $v_{ibO'}$. However, for *b-4* topology, inverter phase-c voltage with respect to the ideal DC link mid-point can be expressed as:

$$v_{icO'} \;=\; v_{OO'} \;= v_{dcn} - \frac{V_{dc}}{2} \;=\; \left(V_{dcn} \;-\; \frac{1}{C_{dc2}} \int_0^t i_n \, dt\right) - \frac{V_{dc}}{2} \tag{8.5}$$

where, $v_{OO'}$ is the potential of point O with respect to the ideal DC link mod-point *O'* and V_{dcn} is the DC component of the voltage v_{dcn} and i_n is the AC component of the current flowing through the lower DC link split capacitor, C_{dc2} (as shown in Figure 8.1). Applying KCL at point O as shown in Figure 8.1, it follows:

$$i_p \;+\; i_n \;=\; i_{Ccac} \tag{8.6}$$

where, i_p and i_n are the AC component of the currents of the two DC link split capacitors and i_{Ccac} is the AC component of phase-c current (later it is explained that phase-c current, i_{Cc} contains AC component, i_{Ccac} as well as DC component) as shown in Figure 8.1. Hence, it is logical to express i_n as a proportion of AC component of the phase-c current, i_{Ccac} as:

$$i_n \;=\; k \, i_{Ccac} \tag{8.7}$$

where, k is a constant depending on the relative values of DC link split capacitors C_{dc1} and C_{dc2}. Plugging in (8.7) into (8.5), the equations can be modified as:

$$v_{icO'} \;=\; v_{OO'} \;=\; \left(V_{dcn} \;-\; \frac{V_{dc}}{2}\right) - \frac{k}{C_{dc2}} \int_0^t i_{Ccac} \, dt \tag{8.8}$$

Substituting (8.4) and (8.8) in (6.6), results in:

$$\begin{aligned} \frac{dx_1}{dt} &= \frac{2}{3\,L} v_{iaO'} \;-\; \frac{1}{3\,L} v_{ibO'} \;+\; d_1 \;-\; \frac{1}{3\,L} v_{OO'} \\ \frac{dx_2}{dt} &= -\frac{1}{3\,L} v_{iaO'} \;+\; \frac{2}{3\,L} v_{ibO'} \;+\; d_2 \;-\; \frac{1}{3\,L} v_{OO'} \end{aligned} \tag{8.9}$$

(8.9) can be restructured as:

$$\begin{aligned} \frac{dx_1}{dt} &= \frac{2}{3\,L} v_{iaO'} \;-\; \frac{1}{3\,L} v_{ibO'} \;+\; d_{1m} \\ \frac{dx_2}{dt} &= -\frac{1}{3\,L} v_{iaO'} \;+\; \frac{2}{3\,L} v_{ibO'} \;+\; d_{2m} \end{aligned} \tag{8.10}$$

where, modified disturbance terms d_{1m} and d_{2m} contain the periodic disturbances $d_1 + \frac{k}{3\,L\,C_{dc2}} \int_0^t i_{Ccac}\ dt$ and $d_2 + \frac{k}{3\,L\,C_{dc2}} \int_0^t i_{Ccac}\ dt$ respectively and the DC disturbance terms $-\frac{1}{3\,L}\left(V_{dcn} - \frac{V_{dc}}{2}\right)$ as follows (by plugging in (8.8) in (8.9)):

$$\begin{aligned} d_{1m} &= d_1 - \frac{1}{3\,L}\left(V_{dcn} - \frac{V_{dc}}{2}\right) + \frac{k}{3\,L\,C_{dc2}} \int_0^t i_{Ccac}\,dt \\ d_{2m} &= d_2 - \frac{1}{3\,L}\left(V_{dcn} - \frac{V_{dc}}{2}\right) + \frac{k}{3\,L\,C_{dc2}} \int_0^t i_{Ccac}\,dt \end{aligned} \tag{8.11}$$

It can be noticed from (8.10) and (8.11) that, the voltage fluctuation of the DC link mid-point $-\frac{k}{C_{dc2}} \int_0^t i_{Ccac}\,dt$ (as can be seen from (8.8)) is modeled as a regular periodic disturbance in the proposed control methodology.

8.3 Implementation of the control system for the *b-4* topology based grid connected inverter

Referring to (8.10), the following voltage variables are defined as:

$$\begin{bmatrix} v_1 \\ v_2 \end{bmatrix} = \begin{bmatrix} \frac{2}{3\,L} & -\frac{1}{3\,L} \\ -\frac{1}{3\,L} & \frac{2}{3\,L} \end{bmatrix} \begin{bmatrix} v_{iaO'} \\ v_{ibO'} \end{bmatrix} \tag{8.12}$$

Further, (8.10) are restructured as:

$$\begin{aligned} \frac{dx_1}{dt} &= v_1 + d_{1m} \\ \frac{dx_2}{dt} &= v_2 + d_{2m} \end{aligned} \tag{8.13}$$

For arbitrary waveform tracking in these two states, a non-linear control law is derived based on the *Lyapunov function* method, i.e. the first principle of absolute stability.

Considering the *Lyapunov function* as:

$$V = \frac{1}{2}\, e^T\, e \tag{8.14}$$

where error array e is represented as:

$$e = \begin{bmatrix} e_1 \\ e_2 \end{bmatrix} = \begin{bmatrix} x_1^* - x_1 \\ x_2^* - x_2 \end{bmatrix} \tag{8.15}$$

where, x_1^* and x_2^* are the tracking references of x_1 and x_2 respectively.

According to the property of *Lyapunov function*, $V > 0$ for all the conditions except $e = 0$ in this case. Thus, the selected V can be mentioned to be a *positive definite* function. It is required to find out control inputs $v_1(t)$ and $v_2(t)$ such that tracking error matrix $e(t)$ asymptotically converges to zero. *Lyapunov* direct method is used to find the control inputs $u_1(t)$ and $u_2(t)$ for the specific application as also done in Chapter 6. The first time derivative of V is shown as:

$$\frac{dV}{dt} = e^T \frac{de}{dt} \tag{8.16}$$

Substituting (8.13), in (8.16), the results manifest as:

$$\frac{dV}{dt} = e^T \begin{bmatrix} \frac{dx_1^*}{dt} - v_1 - d_{1m} \\ \frac{dx_2^*}{dt} - v_2 - d_{2m} \end{bmatrix} \tag{8.17}$$

From *Lyapunov function* method of finding the stability, the first derivative should be a negative definite function as:

$$\frac{dV}{dt} = -e^T \Gamma e \tag{8.18}$$

where $\Gamma = \begin{bmatrix} \lambda_1 & 0 \\ 0 & \lambda_2 \end{bmatrix}$ with λ_1 and λ_2 are to be strictly positive quantities.

Comparing (8.17) and (8.18), the control variables can be solved as:

$$\begin{aligned} v_1 &= \frac{dx_1^*}{dt} + \lambda_1 e_1 - d_{1m} \\ v_2 &= \frac{dx_2^*}{dt} + \lambda_2 e_2 - d_{2m} \end{aligned} \tag{8.19}$$

d_{1m}, d_{2m} consist not only grid voltage disturbances, DC link mid-point oscillations as well as the non-linearities due to the blanking time of the inverter semiconductor

switches. Besides these, measurement and estimation of these disturbance parts using voltage and current sensors leads to erroneous control actions because of sensor phase delay and inaccurate gain setting due to the harmonics present in circuit voltage and current quantities. Hence, d_{1m} and d_{2m} terms are estimated using a parallel SRC as also carried out in the case of Chapter 3 and Chapter 6.

The overall control system is implemented with the hybrid *Lyapunov function* based controller in parallel with the SRC as discussed in details in Chapter 6. Further detailed analysis of the hybrid control structure can be refereed in Chapter 6. In this thesis, only control law is derived following the analysis given in Chapter 6. The total voltage (v_1 and v_2), can be split into *Lyapunov function* based control law (v_{lf1} and v_{lf2}) and *Spatial Repetitive Controller* based control law (v_{SRC1} and v_{SRC2}). The *Lyapuov function* based control laws are represented as:

$$\begin{bmatrix} v_{lf1}(t) \\ v_{lf2}(t) \end{bmatrix} = \begin{bmatrix} \frac{dx_1^*}{dt} + \lambda_1 (x_1^* - x_1) \\ \frac{dx_2^*}{dt} + \lambda_2 (x_2^* - x_2) \end{bmatrix} \tag{8.20}$$

where, x_1^* and x_2^* are the reference functions of the variables x_1 and x_2 respectively and λ_1 and λ_2 are strictly +ve constants to make the the system largely stable by first principal of *Lyapunov* (the details of the convergence analysis of the specific *Lyapunov function* are given in Chapter 6. The SRC based disturbance estimator can be expressed as:

$$\begin{bmatrix} v_{src1}(i,\theta_k) \\ v_{src2}(i,\theta_k) \end{bmatrix} = \begin{bmatrix} v_{src1}(i-1,\theta_k) + K_{src}\ (x_1^*(i-1,\theta_{k+N_1}) - x_1(i-1,\theta_{k+N_1})) \\ v_{src2}(i-1,\theta_k) + K_{src}\ (x_2^*(i-1,\theta_{k+N_1}) - x_2(i-1,\theta_{k+N_1})) \end{bmatrix} \tag{8.21}$$

where, θ_k is the fundamental phase angle of the grid voltage at k^{th} position sample, $x(i,\theta_k)$ is the value of variable x at k^{th} position sample and i^{th} iteration, K_{src} is the gain of the repetitive controller and N_1 is the position sample advancement where N is the total number of position sample in one 360^0 of fundamental grid phase.

Thus the fluctuation of the DC link mid-point O is eliminated by the action of the *Spatial Repetitive Controller*, without any information about the split capacitors value or phase-c instantaneous current, i_{Cc} information.

The control signal of the SPWM for phase-a and phase-b are defined as v_{cona} and v_{conb} following:

$$\begin{aligned} v_{cona} &= \frac{2}{V_{dc}} v_{iaO'} \\ v_{conb} &= \frac{2}{V_{dc}} v_{ibO'} \end{aligned} \tag{8.22}$$

where V_{dc} is the DC link voltage of the inverter.

The control system is implemented in the rapid prototyping DSP dSPACE ds1104 card with sampling frequency $f_{sample} = 10\,kHz$ and SPWM switching frequency, $f_{switch} = 10\,kHz$. The parameters of the overall control system used are $\lambda_1 = \lambda_2 = 300,000$ (based on the convergence criterion of *Lypaunov function* as discussed in Chapter 3 and Chapter 6), total number of position sample for *SRC* implementation, $N = 200$, the number of sample advancement, $N_1 = 6$ (based on the phase delay in the control loop) and the gain of repetitive controller, $K_{src} = 100$ (based on the convergence criterion of the SRC). The design methodology to calculate the values of the parameters are discussed in details in Chapter 3 and Chapter 6. The overall schematic of the control system is shown in Figure 8.2.

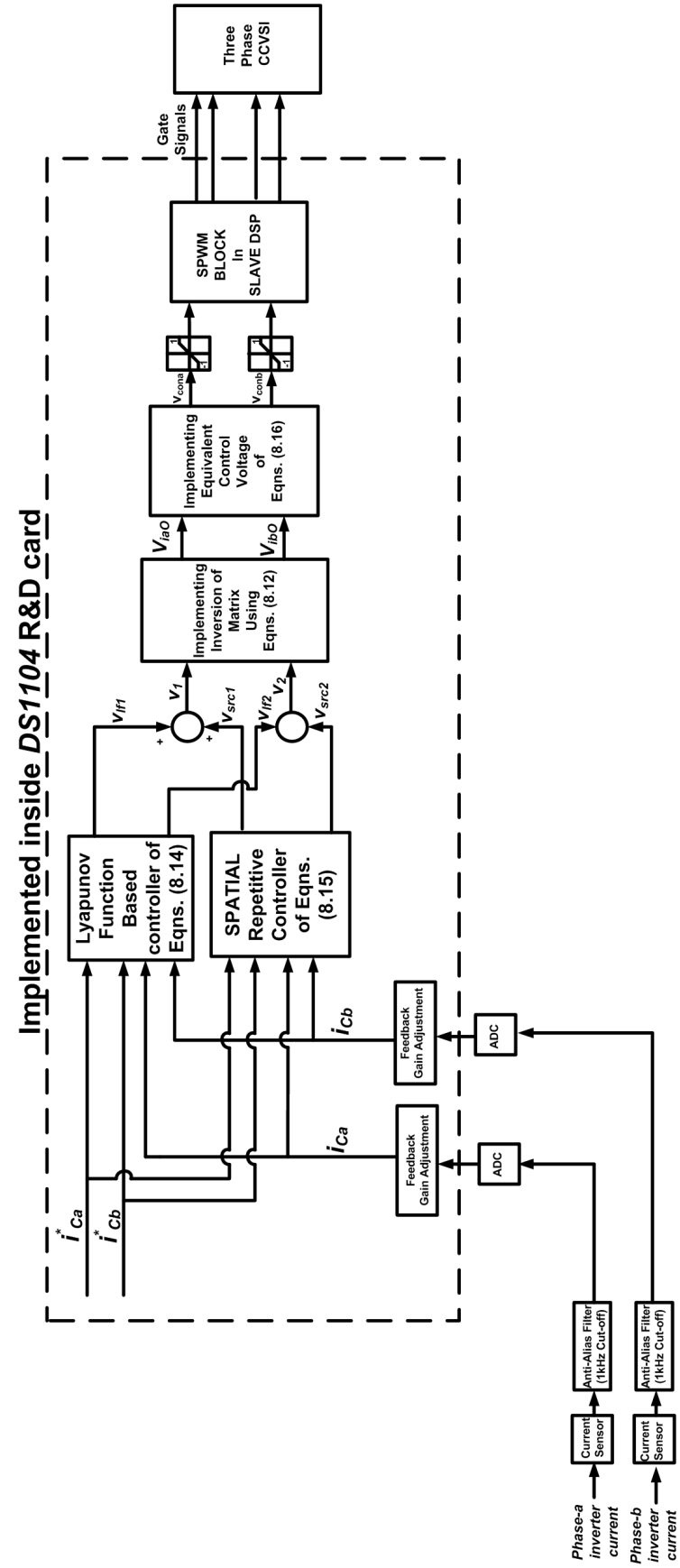

Figure 8.2: Implementation method of the proposed control strategy.

8.4 Effect of DC link split capacitor unbalance on the operation of the *b-4* topology three-phase inverter for grid connected application

Figure 8.1 depicts that the DC link mid-point O is extracted by splitting the DC link with two split capacitors C_{dc1} and C_{dc2}. Ideally, the two capacitors must be equal to ensure perfect splitting of the DC link voltage. But, in practical cases, the values are always different, i.e. $C_{dc1} \neq C_{dc2}$. Hence, the DC link capacitors are charged, the splitting of DC voltage in the capacitors becomes asymmetrical. Mathematically, the initial DC value of the voltage of the lower capacitor (V_{dcn}) is V_0 (as referred in Figure 8.1) as:

$$V_0 = \frac{C_{dc1}}{C_{dc1} + C_{dc2}} V_{dc} \tag{8.23}$$

As $C_{dc1} \neq C_{dc2}$, $V_0 \neq \frac{V_{dc}}{2}$, resulting a DC disturbance terms $\left(V_0 - \frac{V_{dc}}{2}\right)$ in the effective disturbance terms d_{1m} and d_{2m} as can be explained using (8.10) and (8.11). The DC disturbance terms tend to force a DC current in the circuit as can be explained using (8.13). However, the DC analysis can be done on the overall control system and power electronic circuit to investigate the DC effect.

The AC and DC components of corresponding currents (x_1, x_2) in the circuit are considered to be x_{1ac}, x_{1dc} and x_{2ac}, x_{2dc} respectively. It should be noted from (8.13) that, the total control voltages, v_1 and v_2 can be split as v_{1dc}, v_{1dc} and v_{2dc},

v_{2ac} respectively as:

$$\begin{aligned} x_1 &= x_{1dc} + x_{1ac} \\ x_2 &= x_{2dc} + x_{2ac} \\ v_1 &= v_{1dc} + v_{1ac} \\ v_2 &= v_{2dc} + v_{2ac} \end{aligned} \tag{8.24}$$

Using the superposition principle, it can be concluded that v_{1ac} and v_{2ac} are the part of control signals acted by *Lyapunov function* based controller and *Spatial Repetitive* controller to nullify the AC periodic disturbance and establish the AC current tracking. However, rejection of the DC disturbance is not done by *Spatial Repetitive* controller as it is ineffective on DC steady state error due to infinite period. So, the effective operation of the power circuit along with the control system in the DC disturbance ($V_{dcn} - \frac{Vdc}{2}$) can be regarded as shown in Figure 8.3.

Hence, for DC analysis, (8.13) can be modified as:

$$\begin{aligned} \frac{dx_{1dc}}{dt} &= v_{1dc} + d_{dc} \\ \frac{dx_{2dc}}{dt} &= v_{2dc} + d_{dc} \end{aligned} \tag{8.25}$$

where, $d_{dc} = -\frac{1}{3\,L}\left(V_n - \frac{V_{dc}}{2}\right)$, $v_{1dc} = \lambda_1\left(x^*_{1dc} - x_{1dc}\right)$ and $v_{2dc} = \lambda_2\left(x^*_{2dc} - x_{2dc}\right)$ with the set values: $x^*_{1dc} = x^*_{2dc} = 0$.

Figure 8.3 concludes that, because of the presence *DC internal model* $\frac{1}{S}$, the steady state value of DC component of both the state variables are zero, i.e. $x_{1dc} = x_{2dc} = 0$. Hence in steady state, $v_{1dc} = v_{2dc} = 0$. On the other hand at steady state, $\frac{dx_{1dc}}{dt} = \frac{dx_{2dc}}{dt} = 0$ resulting in $d_{dc} = 0$ as per (8.25). Thus it

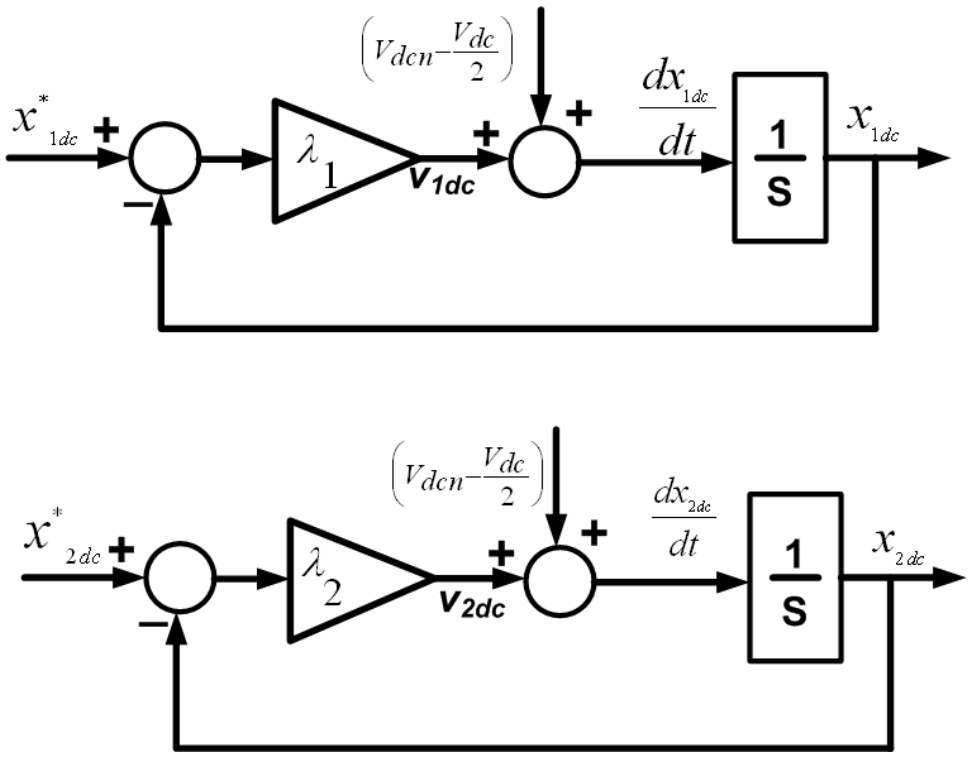

Figure 8.3: DC equivalent circuit of the *b-4* topology three-phase grid connected inverter.

can be concluded that, in steady state the DC component of voltage of the lower DC link split capacitor, $V_{dcn} = \frac{V_{dc}}{2}$, irrespective of the split capacitor unbalance. In the later part of this paper experimental results are provided to support this phenomena.

8.5 Experimental Results

To test the feasibility of the proposed *b-4* topology based three-phase inverter based grid connected systems, experiments are carried out with different operating conditions. The overall control system is implemented inside dSPACE ds1104 DSP card based control environment. The sampling frequency of the overall system is set at $f_{sample} = 10\,kHz$ and the frequency of SPWM is set at $f_{switch} = 10\,kHz$.

Experimental grid voltages are formed using ***Lx3000 California Instrument*** three-phase programmable power supply. The current reference of the CCVSI is calculated in such a way that, there is a control on the part of active power drawn by the load from the grid along with maintaining the grid current to be sinusoidal with unity *displacement power factor*. Hence, the CCVSI current reference is calculated as:

$$i^*_{Cx} = i_{Lx} - i^*_{gx}, x \in a, b, c \tag{8.26}$$

where, i^*_{Cx}, i_{Lx} and i^*_{gx} are the CCVSI current reference, load current and grid current reference for phase-x. In the paper the current references for the grid currents are calculated using *p-q* theory based method to ensure minimum possible DC link ripple due to positive and negative sequence voltage and current interactions. Different grid current reference generation methods are explained in details in Chapter 7. The focus of the present paper is to test the feasibility of the *b-4* topology based three-phase inverter for grid connected system with the proposed *a-b-c* frame *Lyapunov function* based current tracking controller discussed in Chapter 6.

8.5.1 Experimental results to show the operation of the *b-4* topology based three-phase inverter in the presence of non-linear load at the grid terminals

Firstly, the *b-4* topology based three-phase inverter is connected to the unbalanced and harmonic contaminated grid supply voltages. A non-linear load (three-phase diode rectifier terminated to the capacitor load) is also connected. The schematic of the experimental setup is shown in Figure 8.4. The three-phase grid voltage waveforms are shown in Figure 8.5. It can be analyzed from Figure 8.5 that, the

grid is contaminated with 20% negative sequence and each of the phase voltages are contaminated with 5^{th}, 7^{th} and 11^{th} order voltage harmonics of 10%, 7% and 5% of the fundamental magnitude respectively. For this system, the grid voltage expressions can be represented as:

$$\begin{aligned}
v_{ga}(t) &= V_p\cos(\theta) + V_n\cos(\theta) \\
&+ 0.1\,V_p\cos(5\theta) + 0.1\,V_n\cos(5\theta) \\
&+ 0.07\,V_p\cos(7\theta) + 0.07\,V_n\cos(7\theta) \\
&+ 0.05\,V_p\cos(11\theta) + 0.05\,V_n\cos(11\theta) \\
v_{gb}(t) &= V_p\cos(\theta - \frac{2\pi}{3}) + V_n\cos(\theta + \frac{2\pi}{3}) \\
&+ 0.1\,V_p\cos(5\theta - \frac{10\pi}{3}) + 0.1\,V_n\cos(5\theta + \frac{10\pi}{3}) \\
&+ 0.07\,V_p\cos(7\theta - \frac{14\pi}{3}) + 0.07\,V_n\cos(7\theta + \frac{14\pi}{3}) \\
&+ 0.05\,V_p\cos(11\theta - \frac{22\pi}{3}) + 0.05\,V_n\cos(11\theta + \frac{22\pi}{3}) \\
v_{gc}(t) &= V_p\cos(\theta + \frac{2\pi}{3}) + V_n\cos(\theta - \frac{2\pi}{3}) \\
&+ 0.1\,V_p\cos(5\theta + \frac{10\pi}{3}) + 0.1\,V_n\cos(5\theta - \frac{10\pi}{3}) \\
&+ 0.07\,V_p\cos(7\theta + \frac{14\pi}{3}) + 0.07\,V_n\cos(7\theta - \frac{14\pi}{3}) \\
&+ 0.05\,V_p\cos(11\theta + \frac{22\pi}{3}) + 0.05\,V_n\cos(11\theta - \frac{22\pi}{3}) \qquad (8.27)
\end{aligned}$$

where, θ is the fundamental phase angle of grid voltage. As set in the three-phase controllable power supply, the fundamental of grid voltage has positive sequence peak magnitude is about $V_p = 46.2\,V$ and negative sequence peak magnitude is about $V_n = 9.25\,V$ and for phase-a the positive sequence and negative sequence voltage align on the same phase (total RMS of phase-a voltage is $36.9\,V$ and that of phase-b and phase-c is $30.3\,V$). The analysis of the sequence components are addressed in Chapter 7. The experiment is carried out with DC link

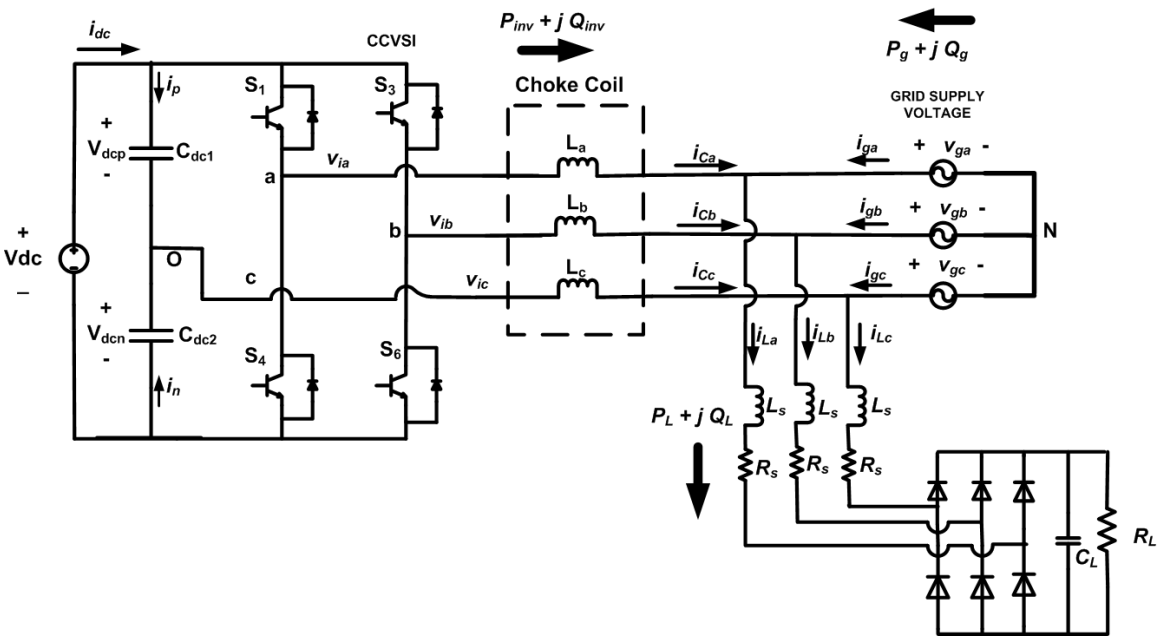

Figure 8.4: Details of the power circuit of the experiment using *b-4* inverter structure with non-linear load ar grid PCC.

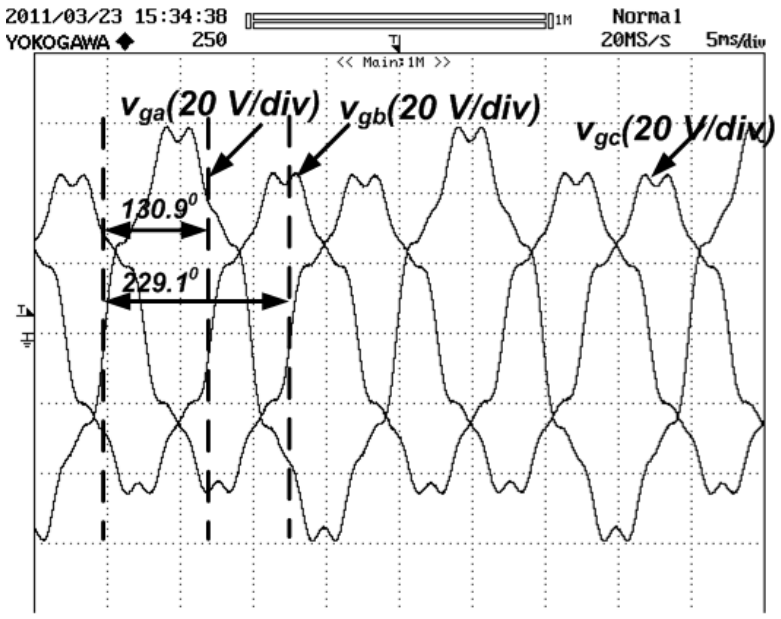

Figure 8.5: Experimental results of grid voltages, v_{ga}, v_{gb} and v_{gc} with $V_p = 49.3\,V$ and $V_n = 9.86\,V$.

voltage, $V_{dc} = 250\,V$ (the CCVSI controls the load power sharing from grid as well as compensates for the non-linear load currents, hence needs higher DC link than usual because of high $\frac{di}{dt}$ as discussed in Chapter 8. Because of the *b-4* topology,

even higher DC link is needed as discussed in [112].). The non-linear load as described in the previous Section draws the active power $P_L = 65\,W$ under this grid condition. The experimental results are shown in Figures 8.6 and 8.7. Different parameters of the experimental setup of Figure 8.4 are shown in Table 8.1.

Table 8.1: Parameters of the experimental power circuit

Parameter	**Value**
maximum DC link voltage, V_{dc}	$250\,V$
CCVSI choke inductance, L_a, L_b, L_c	$5\,mH$
Rectifier link inductance, L_s	$400\,\mu H$
Rectifier link resistance, R_s	$0.1\,\Omega$
Rectifier DC side capacitor, C_L	$3300\,\mu F$
Rectifier DC side resistance, R_L	$100\,\Omega$
DC link Splitting capacitors , C_{dc1} **and** C_{dc2}	$183\ \mu F$ and $184\,\mu F$ respectively

It can be observed from Figure 8.6(a) that, the load draws asymmetrical non-linear currents, i_{La}, i_{Lb}, i_{Lc} from the PCC. With the issuance of the grid power command $P_g = 0\,W$ and $Q_g = 0\,Vars$, the total load power $P_L = 65\,W$ as well as the non-linear currents are compensated by the CCVSI resulting in the CCVSI currents, i_{Ca}, i_{Cb} and i_{Cc} are following the non-linear load currents, i_{La}, i_{Lb}, i_{Lc} resulting in the grid currents, i_{ga}, i_{gb}, i_{gc} to be exactly zero as can be seen from Figures 8.6(b)-(d). According to the property of *b-4* topology, the current flowing through the lower DC link capacitor, i_n (as shown in Figure 8.6(e)) has the oscillating comportment due the souring of phase-c current of CCVSI, i_{Cc} as can be verified by the experimental results shown in Figure 8.6(e). As a result of this the DC link split voltage, v_{dcp} also oscillates as can be confirmed by Figure 8.6(f). The oscillation can be theoretically predicted using the mathematical relation as:

$$v_{dcp} = \frac{v_{dc}}{2} - V_0 + \frac{1}{C_{dc2}} \int_0^t i_n dt \tag{8.28}$$

However, this mid-point oscillation is rejected in the current tracking performance by the *Spatial Repetitive Controller* as discussed before.

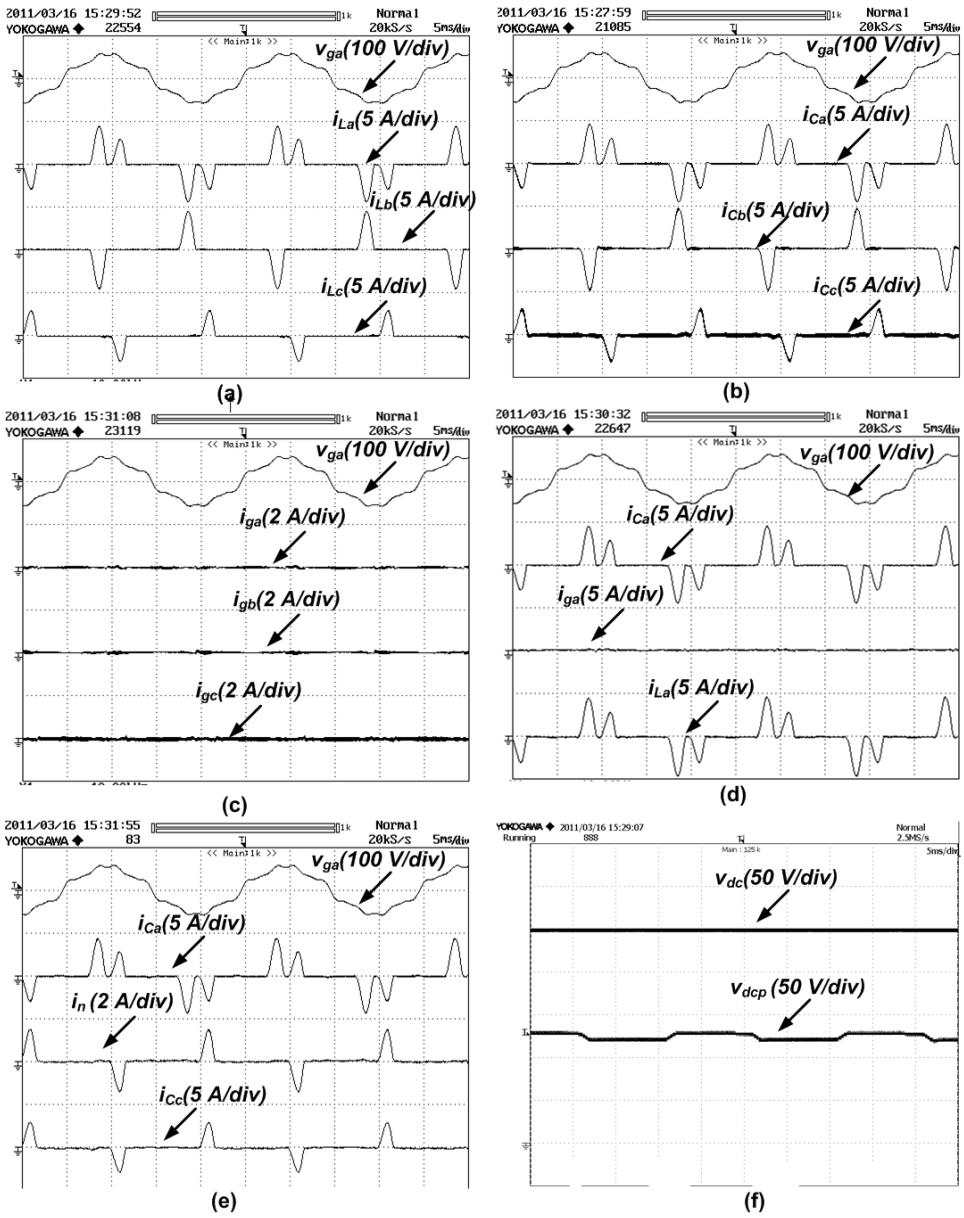

Figure 8.6: Experimental results of (a) phase-s grid voltage, v_{ga}, three-phase load currents, i_{La}, i_{Lb} and i_{Lc}, (b) phase-s grid voltage, v_{ga}, three-phase CCVSI currents, i_{Ca}, i_{Cb} and i_{Cc}, (c) phase-a grid voltage, v_{ga}, three-phase grid currents, i_{ga}, i_{gb} and i_{gc}, (d) phase-a grid voltage, v_{ga}, phase-a CCVSI current, i_{Ca}, phase-a grid current, i_{ga}, phase-a load current, i_{La}, (e) phase-a grid voltage, v_{ga}, phase-a CCVSI current, i_{Ca}, DC link lower capacitor current, i_n, phase-c CCVSI current, i_{Cc}, (f) DC link voltage, V_{dc}, DC link upper split capacitor voltage, V_{dcp} at grid power command, $P_g = 0\,W$ and $Q_g = 0\,Var$ with non-linear load with $P_L = 65\,W$ with *b-4* topology of inverter and $V_p = 46.2\,V$ and $V_n = 9.25\,V$.

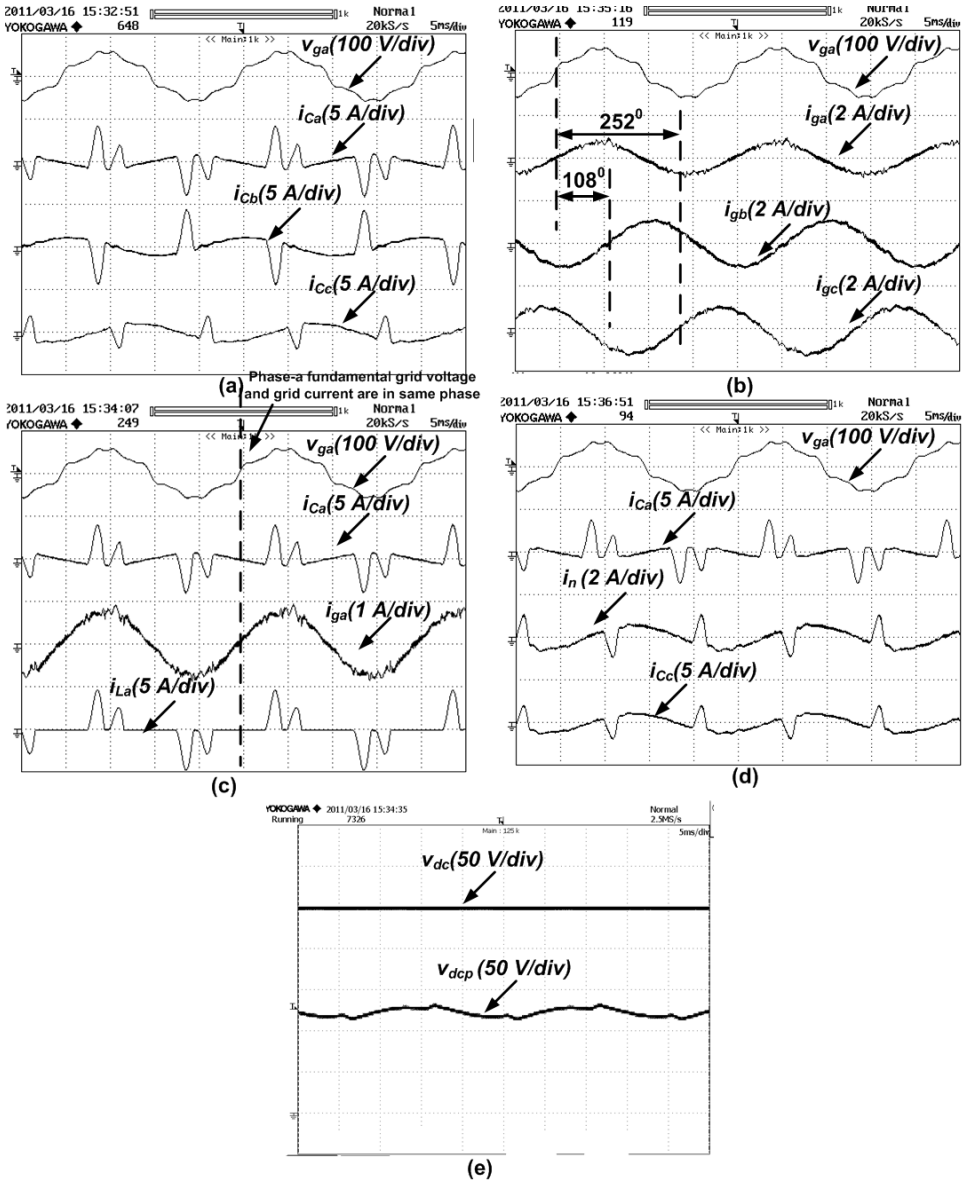

Figure 8.7: Experimental results of (a) phase-s grid voltage, v_{ga}, three-phase CCVSI currents, i_{Ca}, i_{Cb} and i_{Cc}, (b) phase-a grid voltage, v_{ga}, three-phase grid currents, i_{ga}, i_{gb} and i_{gc}, (c) phase-a grid voltage, v_{ga}, phase-a CCVSI current, i_{Ca}, phase-a grid current, i_{ga}, phase-a load current, i_{La}, (d) phase-a grid voltage, v_{ga}, phase-a CCVSI current, i_{Ca}, DC link lower capacitor current, i_n, phase-c CCVSI current, i_{Cc}, (e) DC link voltage, V_{dc}, DC link upper split capacitor voltage, V_{dcp} at grid power command, $P_g = 60W$ and $Q_g = 0Var$ with non-linear load with $P_L = 65W$ with *b-4* topology of inverter and $V_p = 46.2\,V$ and $V_n = 9.25\,V$.

Figure 8.7 shows the experimental results with the issuance of grid power command to be $P_g = 60\,W$ and $Q_g = 0\,Var$. It can be seen from Figure 8.7(b) that, the grid currents, i_{ga}, i_{gb}, i_{gc} are purely sinusoid, even in the presence of the

non-linear load currents as can be seen from Figure 8.6(a) and 8.7(c). The CCVSI currents for the three phases, i_{Ca}, i_{Cb}, i_{Cc} can be seen from Figure 8.7(a) under this operating condition. The DC link mid-point voltage fluctuation can be confirmed from Figure 8.7(e) as the voltage of the upper split capacitor v_{dcp} is oscillating due to the non-linear AC split capacitor current, i_n (according to (8.28)) as can be seen from Figure 8.7(e). However, the DC link mid-point fluctuation has no effect on the CCVSI current tracking. From Figure 8.7(b), it can be observed that, i_{ga} has a peak value of about 0.72 A and both i_{gb} and i_{gc} has peak values about 1 A. The phase relations of different grid currents are shown in Figure 8.7(b). The actual power drawn from the grid can be recalculated (by considering fundamental grid voltages) as: $P_{gactual} = \left(36.58 \times \frac{0.72}{\sqrt{2}}\right) + \left(30 \times \frac{1}{\sqrt{2}} \cos(130^0 - 108^0)\right) + \left(30 \times \frac{1}{\sqrt{2}} \cos(250^0 - 229^0)\right) \simeq 60\,W$

8.5.2 Experimental results to show the operation of the *b-4* topology based three-phase inverter sinking power to grid

Afterwards, the *b-4* topology based three-phase grid connected CCVSI is tested with sinking power to grid in the absence of any load at the PCC. The schematic of the power circuit configuration is shown in Figure 8.8.

The grid voltage is again considered to have 20% negative sequence but with-

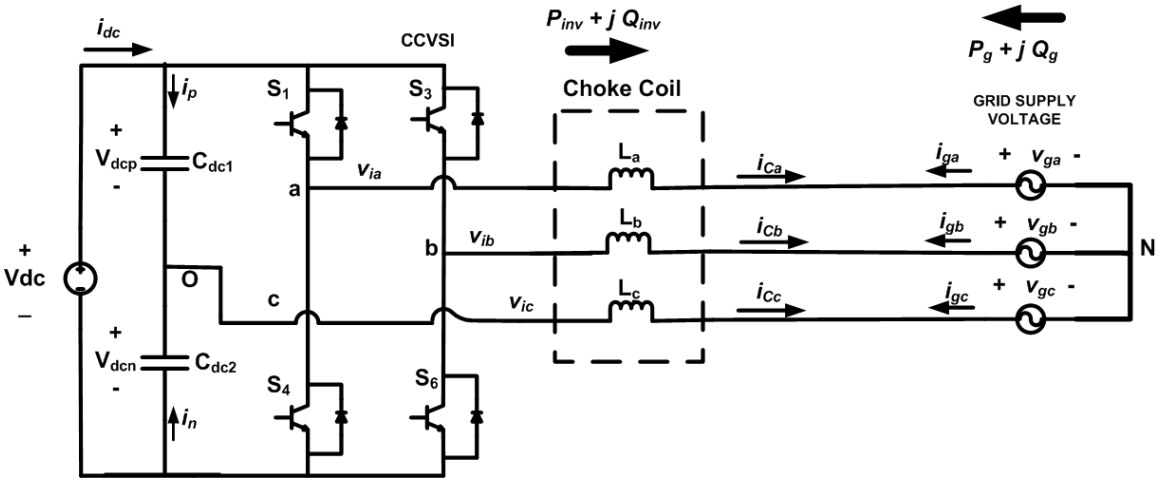

Figure 8.8: Details of the power circuit of the experiment using *b-4* inverter structure with active power sinking to grid.

out any harmonics as:

$$\begin{aligned} v_{ga}(t) &= V_p\cos(\theta) + V_n\cos(\theta) \\ v_{gb}(t) &= V_p\cos(\theta - \frac{2\pi}{3}) + V_n\cos(\theta + \frac{2\pi}{3}) \\ v_{gc}(t) &= V_p\cos(\theta + \frac{2\pi}{3}) + V_n\cos(\theta - \frac{2\pi}{3}) \end{aligned} \tag{8.29}$$

The fundamental of grid voltage has positive sequence peak magnitude is about $V_p = 46.2\,V$ and negative sequence peak magnitude is about $V_n = 9.25\,V$ and for phase-a the positive sequence and negative sequence voltage align on the same phase (total RMS of phase-a voltage is $42.2\,V$ and that of phase-b and phase-c is $32.3\,V$). Because of the absence of peaky CCVSI current (less $\frac{di}{dt}$ due to the absence of non-linear load at PCC), the DC link voltage is reduced to $v_{dc} = 200\,V$. The experimental results are shown in Figure 8.9. The three-phase grid voltages are shown in Figure 8.9(a).

It can be seen from Figure 8.9(b), that grid current of phase-a (in this case CCVSI current is negative of grid current as can be explained from Figure

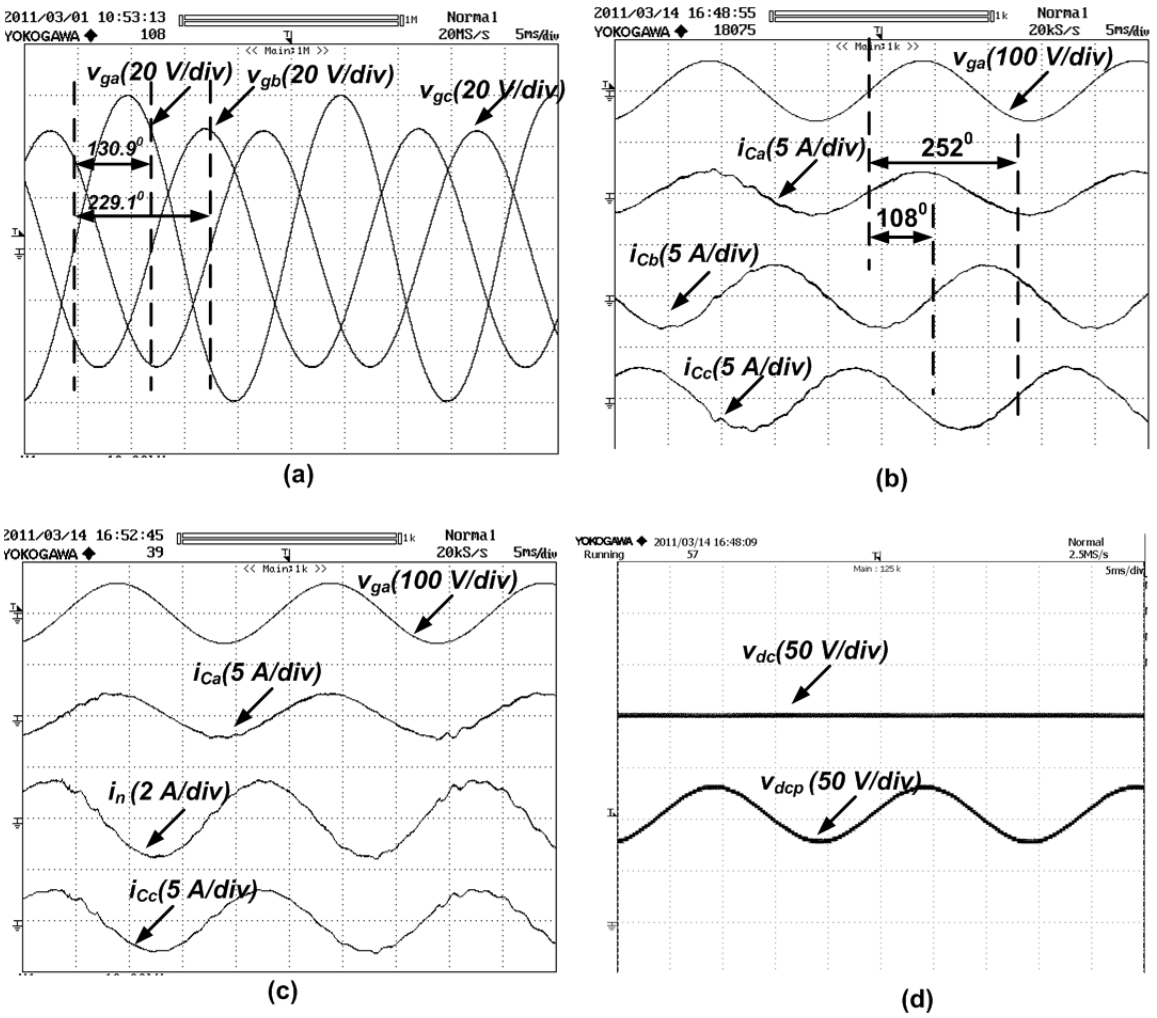

Figure 8.9: Experimental results of (a) the grid phase voltages, v_{ga}, v_{gb}, v_{gc}, (b) Phase-a grid voltage, v_{ga}, three-phase CCVSI currents, i_{Ca}, i_{Cb}, i_{Cc}, (c) phase-a grid voltage, v_{ga}, phase-a CCVSI current, i_{Ca}, DC link split capacitor current, i_n, phase-c current of CCVSI, i_{Cc}, (d) DC link voltage, v_{dc} and upper DC link split capacitor voltage, v_{pdc}, with grid power command, $P_g = -200\,W$ and $Q_g = 0\,Var$ with non-linear load with $P_L = 0$ with *b-4* topology of inverter and $V_p = 46.2\,V$ and $V_n = 9.25\,V$.

8.8) assumes the peak value of about 2.2 A and phase-b and phase-c assume the peak value about 3.1 A each with proper relative phase relations. Hence, the active power fed back to the grid can be recalculated (by considering fundamental grid voltages) as: $P^{sink}_{gactual} = -\left(42.2 \times \frac{2.2}{\sqrt{2}}\right) - \left(32.3 \times \frac{3.1}{\sqrt{2}} \cos(130^0 - 108^0)\right) - \left(32.3 \times \frac{3.1}{\sqrt{2}} \cos(250^0 - 229^0)\right) \simeq -200\,W$ It can be noted from Figure 8.9(c) that, the DC link split current, i_n is sinusoidal because of the sinusoidal nature

of CCVSI phase-c current, i_{Cc} (according to (8.28)). This results in the DC link split capacitor voltage, v_{pdc} to have 50 Hz ripple as can be confirmed with Figure 8.9(d). However, the resulted sinusoidal DC link mid-point oscillation is also eliminated from the current tracking performance of the CCVSI by the *Spatial Repetitive Controller* action.

8.5.3 Experimental results to show the effect of the control system on the DC link split capacitor unbalance for the *b-4* topology based three-phase inverter

The experimental studies are further extended to investigate the effect of the asymmetrical DC link capacitor splitting on the circuit. The DC link capacitors are split with $C_{1dc} = 360\,\mu F$ and $C_{2dc} = 180\,\mu F$. Different current waveforms under this condition are shown in Figure 8.10. If the grid current waveforms in Figure 8.10(a) and 8.9(b) are compared, it can be concluded that, the capacitor unbalance has no effect on the CCVSI current tracking. However, it can be noted, that due to asymmetrical capacitor splitting, the split capacitor currents i_p and i_n are asymmetrical as can be seen from Figures 8.10(b)-(c).

The transient of DC link mid-point voltage for the proposed control strategy on the symmetrical DC link split cap *b-4* topology based three-phase grid connected inverter is shown in Figure 8.11.

It can be seen from Figure 8.11(a) that, before, the inverter is connected to the DC link and the controller is ON, the v_{dcp} is about 66 V ($\neq 100$ V) as can be predicted from (8.23). It can also be noted that as soon as the inverter is connected with the proposed control strategy, v_{dcp} mean value settles at 100 V,

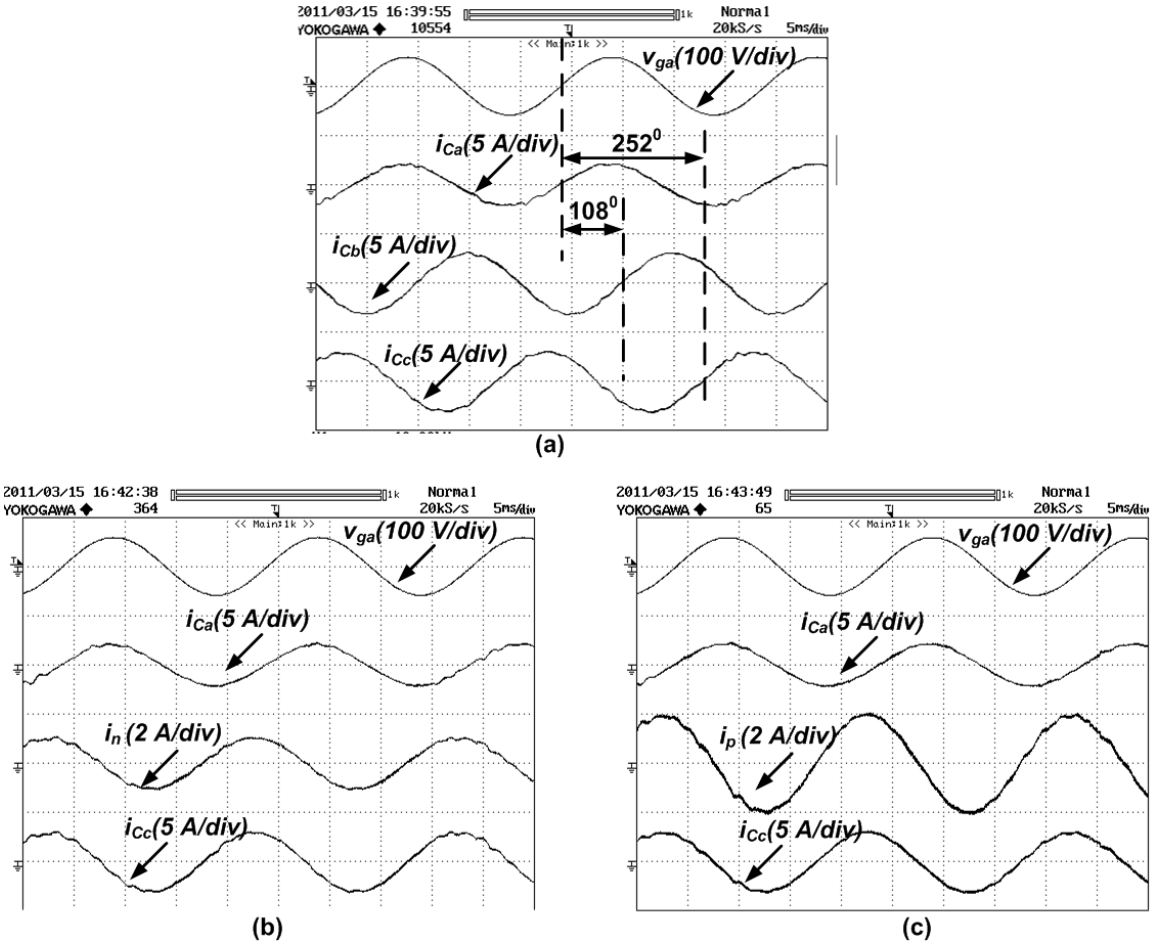

Figure 8.10: Experimental results of (a) Phase-a grid voltage, v_{ga}, three-phase CCVSI currents, i_{Ca}, i_{Cb}, i_{Cc}, (b) phase-a grid voltage, v_{ga}, phase-a CCVSI current, i_{Ca}, DC link split capacitor current, i_n, phase-c current of CCVSI, i_{Cc}, (c) phase-a grid voltage, v_{ga}, phase-a CCVSI current, i_{Ca}, DC link split capacitor current, i_p, phase-c current of CCVSI, i_{Cc} , with grid power command, $P_g = -200\,W$ and $Q_g = 0\,Var$ with non-linear load with $P_L = 0$ with *b-4* topology of inverter and $V_p = 46.2\,V$ and $V_n = 9.25\,V$.

which is as expected from the discussion from (8.25). However, the voltage v_{dcp} contains a $50Hz$ harmonics as can be seen from Figure 8.11(b)-(c) due to the reason explained before (according to (8.28)). Another important observation from Figure 8.11(c) is that, the DC link voltage, v_{dc} gets contaminated with $50\,Hz$ ripple due to the asymmetrical current splitting in i_p and i_n as the difference of the two currents flows through the DC link capacitor of the DC power supply. However, the $50\,Hz$ voltage ripple in the DC link voltage, v_{dc} also has no effect on the CCVSI

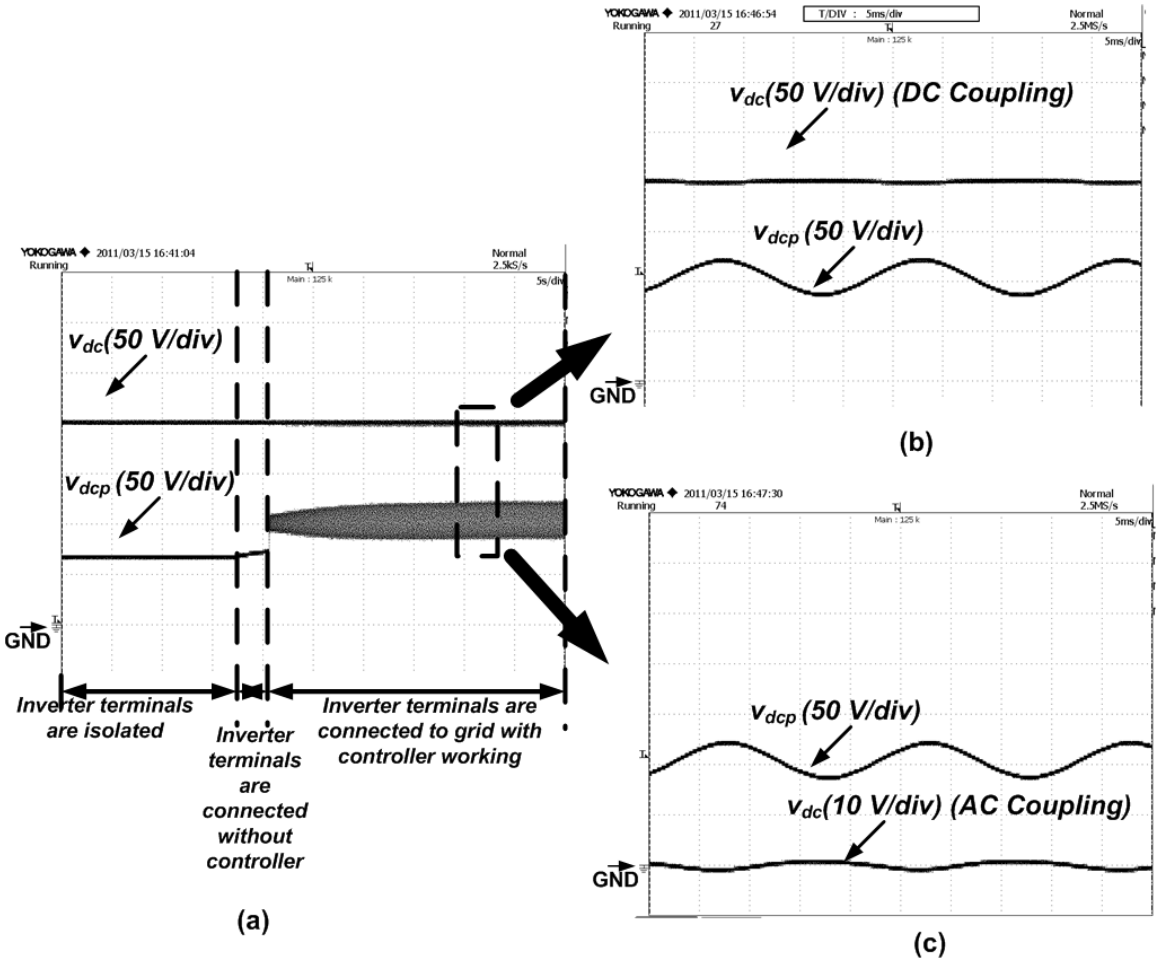

Figure 8.11: Experimental results of (a) transient DC link voltage, v_{dc} (in DC coupling), DC link split capacitor voltage, v_{dcp}, with grid power command, (b) zoomed DC link voltage, v_{dc} (in DC coupling), DC link split capacitor voltage, v_{dcp}, with grid power command, (c) b) zoomed DC link voltage, v_{dc} (in AC coupling), DC link split capacitor voltage, v_{dcp}, with grid power command $P_g = -200\,W$ and $Q_g = 0\,Var$ with non-linear load with $P_L = 0$ with *b-4* topology of inverter and $V_p = 46.2\,V$ and $V_n = 9.25\,V$: (a) time scale: 5s/div, (b)-(c) time scale: 5ms/div.

current tracking as the DC link ripple is also taken care of by the *Spatial Repetitive Controller* as one of the periodic disturbances. During the time, when inverter is connected but controller is switched off, v_{dcp} increases slowly due to leakage current through the isolator switch. It can be noted that, no such DC link voltage ripples is seen in Figures 8.9(d) as in that case, $C_{dc1} \simeq C_{dc2}$ resulting in symmetrical current splitting in i_n and i_p causing no current AC current flow though the DC

power supply DC link capacitor.

8.6 Summary

In this chapter, application of four power semiconductor switch based three-phase inverter (*b-4* topology) is proposed for renewable energy based generalized three-phase micro-grid interconnection. The proposed topology reduces the cost of the overall hardware of the inverter system as well as optimizes the hardware configuration of the grid connected renewable energy based three-phase inverter. A simple Sine PWM (SPWM) is used to control the switching of the four switches with the help of *Lyapunov function* based current controller to control the three-phase currents of the inverter directly in the *a-b-c* frame. The current control of the inverter ensures proper active and reactive power flow from the grid along with grid current THD control in the presence of the non-linear load at the grid. The DC link mid-point voltage oscillation is eliminated by the proposed technique using *Spatial Repetitive Controller*. The proposed method described is not only quite simple with respect to the conventional four switch space vector modulations of the *b-4* topology inverter but also needs no extra voltage or current sensors unlike conventional systems [111]-[113]. The proposed method is also tested to balance the voltage splitting of the DC link even in the case of asymmetry in DC link split capacitors. Experimental results are provided to support different phenomena of the *b-4* three-phase inverter hardware topology.

Chapter 9

Conclusions and Future Work

This Chapter concludes the thesis. It briefly relates the motivation behind the thesis work, the identified problem areas and the various findings in each problem area. Finally, it discusses the direction of future research in this regard.

9.1 Conclusions

This thesis covers work carried out on the development of high-performance control schemes for renewable energy based inverters connecting to micro-grid systems. The grid connected renewable energy source based inverters are very common these days for its robustness and mass production for both single-phase and three-phase applications. However, the inverter operation sufferers from high-performance power quality control because of different types of disturbances in the micro-grid voltages as well as different non-linear current present in the system. Therefore, investigation of high-performance control schemes in such application is a necessary aspect of research to operate different inverters in the micro-grid under different

unbalanced as well as distorted conditions. With the availability of affordable and powerful digital signal processors, it has become possible to use advanced non-linear control techniques to improve the performance of the inverter operation. There are numerous papers published on micro-grid connected inverter control and it would be impossible to cover all of them. However, a thorough review of various control techniques for grid connected inverters had been carried out in this thesis work.

Chapter 1, attempts to discuss the state-of-the-art for the renewable energy source based inverter as well as micro-grid research. The problems of interconnection of renewable energy source based inverter to the generalized micro-grid system have been identified. A detailed discussions are carried out to describe the pros and cons of the available control schemes of renewable energy source based inverters connected to generalized grid system. Therefore, solving those problems have been the focus of this thesis.

It is essential to have a good understanding of the plant before designing a high-performance controller. A detailed state-space modeling of a traditional single-phase parallel connected renewable energy source based inverter is carried out in Chapter 2. A single-phase p-q theory based method is also discussed to find the current reference of the inverter in the presence of a typical non-linear load at the point of common coupling with the common AC bus. The current reference is derived in such a way that the inverter operation ensures a specific amount of active and reactive power flow from the common AC bus with THD control of the current drawn from the common AC bus. This ensures the total load power is shared by the active power drawn from the common AC bus (also referred as grid) and the renewable energy sources based inverter to ensure savings of electric power

consumption by the load from the common AC bus in the micro-grid. The proposed current reference generation method ensures the single inverter to transfer active power from renewable energy source to common AC bus as well as to work as the power factor correction circuit.

The current reference of the parallel connected inverter is a typical non-sinusoidal periodic shape in the presence of the non-linear load at the point of common coupling. The tracking of such current in the actual inverter phase is discussed in Chapter 3. A *Lyapunov function* (LF) based non-linear current controller is investigated to track such arbitrary shape of current. A *Spatial Repetitive Controller* (SRC) based grid voltage and other uncertain periodic disturbances (such as inverter voltage drop due to blanking time etc.) estimator is also proposed to improvise the performance of the tracking further. Experimental results are provided to show the efficacy of the proposed system to control the active as well as reactive power flow from the grid along with the THD control of the grid current. It is also highlighted that the performance of high band-width power command changeover is also possible by the proposed method of control scheme. The implementation of the proposed controller is also shown to be much simpler with respect to the traditional multiple PI+Resonent controller structure.

If the common AC bus in the micro-grid has voltage disturbances such as sag or swell or harmonic disturbances, the load connected at the PCC has to sustain such problems in the voltage, which might damage the loads like slow poisoning. A single-phase series connected inverter topology is proposed and described in Chapter 4. The inverter is placed in series with the load and the grid. So, the inverter voltage is controlled in such a way that, the load voltage is regulated to

its nominal value in the presence of voltage disturbances at the grid with specific amount of active power flow from the renewable energy source based inverter to the load as well as grid. So, load power consumption also can be reduced leading to power savings. It is also shown that the series inverter along with the proposed control scheme has the capability to maintain leading grid power factor even at the presence of lagging power factor load.

The load voltage regulation as well as active power control is achieved by finding suitable load voltage references with nominal magnitude as specific relative phase with the grid voltage by the single-phase series inverter. Chapter 5 describes the controllers to enable such load voltage tracking. A SRC is proposed in this chapter to take care of the load voltage regulation under varied grid voltage disturbances along with sudden frequency change. A spatial sampled modeling of the whole inverter system is also provided to facilitate the design of such controller. A LF based controller is also designed to track different shape of load voltages. Experimental results are provided to show the efficacy of both the type of controllers under different operating conditions. A comparative study of the response time of the two type of controllers are also carried out for series inverter application with adequate support from the experimental verifications.

Chapter 6 describes a state-space modeling of a generalized three-phase grid connected renewable energy source based inverter. The modeling takes care of not only unbalance, disturbances in the grid voltages but also the unbalance in the inverter connecting line side inductances as well as other components. A LF based current controller is also proposed in this Chapter to control the currents of the inverter directly in the *a-b-c* frame. The proposed control method is applicable for

any arbitrary shape of current tracking. The controller is simpler to implement as it does not resolve the whole system in the +ve and -ve sequence rotating components unlike the conventional PI+resonant controller implementation without the help of dual rotating PARK's transformation. The controller controls the inverter currents in such a way that a specific amount of active as well as reactive power flow can be controlled along with the THD control of the grid currents under the presence of typical non-linear loads at the PCC. Adequate experimental results are provided to show the efficacy of the proposed control system under different operating conditions.

Chapter 7 describes different methods of deriving the current references of a multi-phase generalized grid parallel connected renewable energy source based inverter in the presence of non-linear load at the PCC. Two different methods are compared such as: *p-q* theory based approach and *FBD* theory based approach. A novel method of implementing the *p-q* theory based approach directly in the *a-b-c* frame is proposed. The proposed method utilizes a novel *Complex Notch Filter* (CNF) based approach to extract +ve and +ve sequence grid voltage space vector component in the presence of grid voltage harmonics as well as frequency variation directly in the *a-b-c* frame. The dual rotating Park's transformation is not needed in this system. Traditional PLLs are also not needed in the method of implementation. A novel method is also proposed to estimate the fundamental positive sequence grid phase. A position sampled *FBD* method is also proposed to calculate the current references of the inverter phase currents in the *a-b-c* frame. The effect of both these methods on the DC link side ripples are also investigated using the instantaneous power theory. Both the methods are verified with adequate experimental findings and the ripple manifestation aspect of each method are also

investigated experimentally on a typical three-phase generalized grid voltage system.

In the Chapter 6 and 7, the three-phase renewable energy source based inverters are considered to be traditional six switch *b-6* topology based inverters. In Chapter 8, a four-switch based three-phase inverter (*b-4* topology) is proposed for generalized grid connected renewable energy source application. The system also considers the presence of non-linear load at the PCC. The well known problems of the *b-4* inverter topology, such as DC link mid-point voltage oscillation as well as DC link capacitor asymmetrical splitting, are solved by a proposed combination of LF based current controller and SRC applied with simple Sine PWM based inverter switching directly in the *a-b-c* frame. The proposed method is much simpler to implement with respect to traditional four-switch space vector PWM not only from accuracy point of view but also the due to the reason that the proposed method does not need any extra current or voltage sensors for inverter current tracking unlike the traditional system. Adequate experimental results are provided to show the efficacy of the proposed control system for *b-4* inverter current tracking under unbalanced and distorted grid voltages, presence of non-linear load at PCC, huge unbalance of DC link split capacitors etc. The proposed control system makes it possible to control the active and reactive power flow from the grid along with controlling the THD of the current drawn from the grid by the same inverter.

In all, the main objectives as laid out Chapter 1 of this thesis have been achieved. The findings of this work have been published in international technical conferences and journals for the benefit of the future researches and renewable energy source users. The work is protected by *Intellectual Property* rights by different

US Provisional Patents. A list of the patents and publications form this thesis work is provided.

9.2 Future Work

The thesis work primarily focuses on the high-performance controller development for different single-phase as well as three-phase inverters operating in micro-grid systems to interface renewable energy source and different non-linear loads. The author has developed different non-linear controllers to achieve different control objectives. However, some further works can be undertaken in future to investigate other aspects of the renewable energy source based inverters connected to micro-grid systems.

During all the experiments undertaken in this thesis, the common AC bus (also mentioned as grid) is simulated using single-phase or three-phase programable AC power supply. The distortions and disturbances in the grid voltage are programmed in the AC power supply. However, the actual interfacing of the inverters with real micro-grid is to be carried out to test the commercialization aspect of the overall system. This process may give rise to some new types of power dynamics which is not looked into in this thesis work.

In all the experiments, it is assumed that, the DC link voltage of the inverter is stabilized by the active energy storage elements like ultra-capacitors, battery or flywheel based system. However, the development of such storage elements and charging as well as discharging of the storage elements are controlled by the same inverter or separate inverter/converter assembly. The power electronic converters

associated with the storage elements may have some power transients during charing or discharging. So, the effect of the dynamics of the energy storage system on the proposed control schemes can also be investigated.

The operations of the inverters investigated in this thesis work are basically for a condition when a specific consumer has his/her own load and some renewable energy based distributed generators. So, the benefits are investigated based on the consumers interaction with the power grid, which may be the common AC bus of a specific micro-grid. In brief, the operations are investigated in the *grid-connected* mode of the micro-grid operation. Forming the micro-grid with different distributed generator systems can also be investigated in the *stand-alone* mode or *islanded* mode of operation. Application of high-performance control in the stabilization of the overall micro-grid voltage magnitude as well as frequency can also be investigated in future.

The various algorithms have been tested on a rapid-prototyping system with a high-speed DSP. As it is commercially not feasible to use such an expensive controller for actual micro-grid system, investigations are necessary for commercially viable, cheaper controllers with similar high-performance. This step is necessary for commercialization of various findings of thesis work.

Bibliography

[1] Yong Xue, Jiamei Deng and Shuangbao Ma, "Power Flow Control of a Distributed generation Unit in Micro-grid," *in Proc. IEEE International Power Electronics and Motion Control Conf.*, 2009, pp. 2122-2125.

[2] J.F.G. Cobben, W.L. Kling and J.M.A. Myrzik, "Power Quality aspects of a future micro-grid," *in Proc. IEEE International Conf. on Future Power Systems*, 2005, pp. 1-5.

[3] N. Abdel-rahim and J.E. Quaicoe, "A single-phase voltage-source utility interface system for weak AC network applications," *in Proc. IEEE Applied Power Electronics Conference and Exposition*, 1994, pp. 93-99.

[4] Yong Xue, Yuchuan Wu, "An Adaptive Predictive Current-Controlled PWM Strategy for Single-Phase Grid-Connected Inverters," *in Proc. IEEE Annual Conference of Industrial Electronics Society*, 2007, pp. 1548-1552.

[5] D.-M.Valcan, C.Marinescu and S.Kaplanis, "Connecting a PV supplied micro-grid to the public grid," *in Proc. IEEE Conf. Rec. OPTIM*, 2008, pp. 369-374.

[6] T. Takeshita, T. Masuda and N. Matsui, "Current waveform control of distributed generation system for harmonic voltage suppression," *in Proc. IEEE Annual Power Electronics Specialists Conf.*, 2001, pp. 814-820.

[7] L.Sovannarith and N.Hoonchareon, "Stability of the Micro-Grid with Wind Power Generation," *in Proc. IEEE Conf. Rec. ICSET* 2008, pp. 1087-1093.

[8] E. Barklund, N. Pogaku, M. Prodanovic, C. H. Aramburo and T. C. Green, "Energy Management in Autononous Microgrid Using Stability-Constrained Droop Control of Inverters," *IEEE Trans. Power Electronics*, vol. 23, pp. 2346-2352, Sept. 2008.

[9] Hyosung Kim, Taesik Yu and Sewan Choi, "Indirect current control Algorithm for Utility Interactuve Inverters in Distributed generation Systems," *IEEE Trans. Power Electronics*, vol. 23, pp. 1342-1347, May 2008.

[10] J. M. Guerrero, J. C. Vasquez, J. Matas, L. G. de Vicuna and M. Castilla, "Hierarchical Control of Droop-Controlled AC and DC MIcrogrids - A General Approach Towards Standardization," *accepted for publication in IEEE Trans. Industrial Electronics*, 2010.

[11] J. M. Guerrero, J. Matas, L. G. de Vicuna, M. Castilla and J. Miret, "Decentralized Control for Parallel Operation of Distributed Generation Inverters Using Resistive Output Impedence," *IEEE Trans. Industrial Electronics*, vol. 54, pp. 994-1004, April 2007.

[12] J. M. Guerrero, J. C. Vasquez, J. Matas, M. Castilla and L. G. de Vicuna, "Control Strategy for Flexible Microgrid Based on Parallel Line-Interactive UPS Systems," *IEEE Trans. Industrial Electronics*, vol. 56, pp. 726-736, March 2009.

[13] J. M. Guerrero, J. Matas, L. G. de Vicuna, M. Castilla and J. Miret, "Wireless-Control Strategy for Parallel Operation of Distributed-Generation Inverters," *IEEE Trans. Industrial Electronics*, vol. 53, pp. 1461-1470, Oct. 2006.

[14] J. C. Vasquez, J. M. Guerrero, A. Luna, P. Rodriquez and R. Teodorescu, "Adaptive Droop Control Applied to Voltage-Source Inverters Operating in GRid-Connected and Islanded Modes," *IEEE Trans. Industrial Electronics*, vol. 56, pp. 4088-4096, Oct. 2009.

[15] J. C. Vasquez, R. A. Mastromauro, J. M. Guerrero and M. Liserre, "Voltage Support Provided by a Droop-Controlled Multifunctional Inverter," *IEEE Trans. Industrial Electronics*, vol. 56, pp. 4510-4519, Nov. 2009.

[16] J. M. Guerrero, L. G. de Vicuna, J. Matas, M. Castilla and J. Miret, "Output Impedance Design of Parallel-Connected UPS Inverters With Wireless Load-Sharing Control," *IEEE Trans. Industrial Electronics*, vol. 52, pp. 1126-1135, Aug. 2005.

[17] Robert H. Lasseter and Paolo Paigi, "Microgrid: A Conceptual Solution," *in Proc. Annul IEEE Power Elecrronics Specialists' Conf.*, 2004, pp. 4285-4290.

[18] O. Vodyakho, C. S. Edrington, M. Steurer, S. Azongha and F. Fleming, "Synchronization of three-phase converters and virtual microgrid implementation utilizing the Power-Hardware-in-the-Loop concept." *in Proc. IEEE Applied Power Electronics Conf. and Expo.*, 2010, pp. 216-222.

[19] M.H.J. Bollen, *Understanding power quality problems: voltage sags and interruptions.* IEEE Press, New York, 2000.

[20] M.F.Mc. Granaghan, D.R. Muller and M.J. Samotyj, "Voltage sags in industrial sytems," *IEEE Trans. Industy Applications*, vol. 29, pp. 397-403, 1993

[21] Fabio Carastro, Mark Sumner and Pericle Zanchetta, "Mitigation of Voltage Dips and Voltage Harmonics within a Micro-grid, using a Single Shunt Active

Filter with Energy Storage," *in Proc. IEEE Conf. Rec. IECON 2006*, pp. 2546-2549.

[22] G. Escobar, A.M. Stankovic, V. Cardenas and P. mattavelli, "A controller to compensate voltage sags and harmonic distortion using a series active filter," *in Proc. IEEE Conf. on Decision and Control*, 2002, pp.3091-3096.

[23] M.F. Schonardie, D.C. Martins, "Application of $dq0$ Transformation in Three Phase Grid-Connected PV Systems With Active And Reactive Power Control," *in Proc. IEEE International Conf. on Sustainable Energy- ICSET*, 2008, pp. 23-28.

[24] Y. Li, D. Mahinda. V. and P. C. Loh, "Design, Analysis, and Real-Time Testing of a Controller for Multibus Microgrid System," *IEEE Trans. Power Electronics*, vol. 19, pp. 1195-1204, Sept. 2004.

[25] N. Pogaku, M. Prodanovic and T. C. Green, "Modeling, Analysis and Testing of Autonomus Operation of an Inverter-Based Microgrid," *IEEE Trans. Power Electronics*, vol. 22, pp. 613-625, March 2007.

[26] Y. Li, D. Mahinda. V. and P. C. Loh, "Microgrid Power Quality Enhancement Using a Three-Phase Four-Wire Grid-Interfacing Compensator," *IEEE Trans. on Industry Applications*, vol. 41, pp. 1707-1719, Nov/Dec 2005.

[27] Y. Li, D. Mahinda. V. and P. C. Loh, "A Grid-Interfacing Power Quality Compensator for Three-Phase Three-Wire Microgrid Application," *IEEE Trans. on Power Electronics*, vol. 21, pp. 1021-1031, July 2006.

[28] A. Elmitwally and M. Rashed, "Flexible Operation Strategy for an Isolated PV-Diesel Microgrid Without Energy Storage," *accepted for publication in IEEE Trans. on Energy Conversion*, Feb 2009.

[29] M. Z. Kamh and R. Iravani, "Unbalanced Model and Power-Flow Analysis of Microgrids and Active Distribution Systems,", *IEEE Trans. on Power Delivery*, vol. 25, pp. 2851-2858, Oct. 2010.

[30] X. H. Wu, S. K. Panda, and J. X. Xu, "Analysis of the instantaneous power flow for three-phase PWM boost rectifier under unbalanced supply voltage conditions", *IEEE Trans. Power Electron*, vol. 23, no. 4, pp. 1679-1791, Jul. 2008.

[31] H. Akagi, Y. Kanazawa, A. Nabae, "Instantaneous reactive power compensators comprising switching devices without energy storage components," *IEEE Transactions on Industry Applications*, vol. IA-20, no. 3, pp. 625 630, May 1984.

[32] C.Lascu, L.Asiminoaei, I.Boldea and F.Blaabjerg, "High Performance Current Controller for Selective harmonic Compensation in Active Power Filters," *IEEE Trans. Power Electronics*, vol. 22, pp. 1826-1835, Sept. 2007.

[33] J.M. Carrasco, L.G. Franquelo, J.T. Bialasiewicz, E.G. Galvan, R.C.P. Guisado, Ma.A.M. Prats, J.I. Leon and N.M. Alfonso, "Power-Electronic Systems for the Grid Integration of Renewable Energy Sources: A Survay," *IEEE Trans. Industrial Electronics*, vol. 33, pp. 1002-1016, Aug 2006.

[34] F. Blaabjerg, R. Teodorescu, M. Liserre and A.V. Timbus, "Overview of Control and Grid Synchronization for Distributed Power Generation Systems," *IEEE Trans. Industrial Electronics*, vol. 53, pp. 1398-1409, Oct 2006.

[35] S. B. Kjaer, J. K. pedersen, F. Blaabjerg, "A Review of Single-Phase Grid-Connected Inverters for Photovoltaic Modules", *IEEE Transactions on Industry Applications, Vol. 41, No. 5, pp. 1291-1306, Sept 05.*

[36] C. Rodriguez, G. A. J. Amaratunga, "Analytic Solution to the Photovoltaic Maximum Power Point Problem", *IEEE Transactions on Circuits and Systems-I; Regular Papers, Vol. 54, No. 9, pp. 2054-2060, sept 07.*

[37] I. Agirman, V. Blasko, "A novel control method of a VSC without ac line voltage sensors", *IEEE transaction on Endustry Application, Vol. 39, no. 2, pp. 519-524, Mar./Apr. 03*

[38] R. Tepdorescu, F. Blaabjerg, U. Borup, M. Liserre, "A new control structure for grid-connected LCL PV inverters with zero steady-state eror and selective harmonic compensation", *in Proc. IEEE APEC, 2004, vol. 1, pp. 580-586*

[39] R. Tepdorescu, F. Blaabjerg, M. Liserre, P.C. Loh, "Proportional-resonant controllers and filters for grid-connected voltage-source converters", *IEEE proc. - Electr. Power Appl, vol. 153, pp 750-762, Sept. 06.*

[40] C. Rodriguez, G. A. J. Amaratunga, "Long-Lifetime Power Inverter for Photovoltaic Ac modules", *IEEE Transactions on Industrial Electronics, Vol. 55, No. 7, pp. 2593-2601, July 08.*

[41] Gilbert M. Masters, *Renewable and Efficient Electric Power Systems*, John Wiley and Sons, 2004.

[42] S. Heier, *Grid Integration of Wind Energy Conversion Systems.*, Hoboken, NJ: Wiley, 1998.

[43] G. L. Johnson, *Wind Energy Systems.*, Englewood Cliffs, NJ: Prentice- Hall, 1985.

[44] F. Blaabjerg, Z. Chen, and S. Kjaer, "Power electronics as efficient interface in dispersed power generation systems," *IEEE Trans. Power Electron., vol. 19, no. 5, pp. 11841194, Sep. 2004.*

[45] L. Helle and S. Munk-Nielsen, "Comparison of converter efficiency in large variable speed wind turbines," *in Proc. IEEE APEC, 2001, vol. 1, pp. 628634.*

[46] A. V. Rebsdorf and L. Helle, "Variable wind turbine having a matrix converter," *U.S. Patent 6,856,038, Feb. 15, 2003.*

[47] S. Barakati, M. Kazerani, and X. Chen, "A new wind turbine generation system based on matrix converter," *in Proc. IEEE Power Eng. Soc. Gen. Meeting, 2005, pp. 218224.*

[48] J. Dannehl, F. W. Fuchs and P. B. Thogersen, "PI State Space Current Control of Grid-Connected PWM Converters With LCL Filters," *IEEE Trans. Power Electronics*, vol. 25, pp. 2320-2330, Sept. 2010.

[49] M. Dai, M. N. Marwali, J. W. Jung and A. Keyhani, "Power Flow Control of a Single Distributed Generation Unit," *IEEE Trans. Power Electronics*, vol. 23, pp. 343-352, Jan. 2008.

[50] D. Zhi, L. Xu and B. W. Williams, "Improved Direct Power Control of Grid-Connected DC/AC Coverters," *IEEE Trans. Power Electronics*, vol. 24, pp. 1280-1292, may 2009.

[51] P. Rodriguez, A. Timbus, R. Teidorescu, M. Liserre and F. Blaabjerg, "Reactive Power Control for Improving Wind Turbine System Behavior Under Grid Faults," *IEEE Trans. Power Electronics*, vol. 24, pp. 1798-1801, July 2009.

[52] Y. M. Chen, H. C. Wu, Y. C. Chen, K. Y. Lee and S. S. Shyu, "The AC Line Current Regulation Strategy for the Grid-Connected PV Syatem," *IEEE Trans. Power Electronics*, vol. 25, pp. 209-218, Jan 2010.

[53] H. G. Jeong, K. B. Choi and W. Choi, "Performance Improvement of LCL-Filter-Based Grid-Connected Inverters ising PQR Power transformation," *IEEE Trans. Power Electronics*, vol. 25, pp. 1320-1330, May 2010.

[54] S. B. Kjaer, J. K. pedersen and F. Blaabjerg, "A Review of Single-Phase Grid-Connected Inverters for Photovoltaic Modules," *IEEE Trans. Industry Applications*, vol. 41, pp. 1291-1306, Sept 05.

[55] P. Rodriguez, A.T. Timbus, R. Teodorescu, M. Liserre and F. Blaabjerg, "Flexible Active Power Control of Distributed Power Generation Systems During Grid Faults," *IEEE Trans. Industrial Electronics*, vol. 54, pp. 2583-2592, OCT. 2007.

[56] P. Rodriguez, A.V.Timbus, R.Teodorescu, M.Liserre and F. Blaabjerg, "Independent PQ Control for Distributed Power Generation Systems under Grid Faults," *in Proc. IEEE Conf. Rec. IECON*, 2006, pp. 5185-5190.

[57] A.V. Timbus, R.Teodorescu, F.Blaabjerg, M.Liserre and P.Rodriguez, "Linear and Nonlinear Control of Distributed Power generation Systems," *in Proc. IEEE Conf. Rec. IAS Annual Meeting*, 2006, pp. 1015-1023.

[58] A.V. Timbus, M.Liserre, R.Teodorescu, P.Rodriguez and F.Blaabjerg, "Evaluation of Current Controllers for Distributed Power Generation Systems," *IEEE Trans. Power Electronics*, vol. 24, pp. 654-664, March 2009.

[59] X.H. Wu, S. K. Panda and J. X. Xu, "DC Link Voltage and Supply-Side Current Harmonics Minimization of Three Phase PWM Boost Rectifiers Us-

ing Frequency Domain Based Repetitive Current Controllers," *IEEE Transactions. Power Electronics*, vol. 23, pp. 1987-1997, July 2008.

[60] X.H. Wu, S. K. Panda and J. X. Xu, "Design of a Plug-in Repetitive Control Scheme for Eliminating Supply-side Current Harmonics of Three Phase PWM Boost Rectifiers Under Generalized Supply Voltage Conditions," *IEEE Trans. Power Electronics*, vol. 25, pp. 1800-1810, July 2010.

[61] K. Zhou and D. Wang, "Digital repetitive controlled three-phase PWM rectifiers," *IEEE transaction on Power Electronics*, Vol. 18. pp. 309-316, 2003.

[62] B. Zhang, K. Zhou, Y. Ye and D. Wang, "Design of linear phase lead repetitive control for CVCF PWM DC-AC converters," *In Proc. of American Control Conf.*, 2005, pp. 1154-1159.

[63] Weizhe Qian, S. K. Panda and J. X. Xu, "Speed Ripple Minimization in PM Synchronous Motor Using Iterative Learing Control," *IEEE Transactions on Energy Conversion*, Vol. 20, pp. 53-61, March 05.

[64] Richard Zhang, Mark Cardinal, Paul Szczesny and Mark Dame, "A grid simulator with control of single-phase power converters in D-Q rotating frame," *in Proc. Conf. Rec. PESC*, 2002, Vol. 3, pp.1431 - 1436.

[65] Shoji Fukuda and Takehito Yoda, "A Novel Current- Tracking Method for Active Filters Based on a Sinusoidal Internal Model," *IEEE Trans. on Industry Applications*, vol. 37, May/June 2001.

[66] Y.Xue, Y.Wu and H.Zhang, "An Adaptive Predictive Currrent-Controlled PWM Strategy for Single-Phase Grid-Connected Inverters," *in Proc. Conf. Rec. IECON*, 2007, pp.1548-1552.

[67] M.F. Schonardie, D.C. Martins, "Application of $dq0$ Transformation in Three Phase Grid-Connected PV Systems With Active And Reactive Power Control," *in Proc. IEEE International Conf. on Sustainable Energy- ICSET*, 2008, pp. 23-28.

[68] Fei Kong, Cuauhtemoc Rodriguez, Gehan Amaratunga, Sanjib Kumar Panda, "Series Connected Photovoltaic Power Inverter," *in Proc. IEEE International Conf. on Sustainable Energy- ICSET*, 2008, pp. 658-663.

[69] X.Z. Zhang, "Analysis and design of switched-mode ac/ac voltage regulator with series connected compensation," *in Proc. IEE Power Electronics and Variable-Speed Drives Conf.*, 1994, pp.181-187.

[70] Ming Tsung Tsai, "Design of a Compact Series-connected AC Voltage Regulator with an Improved Control Algorithm," *IEEE Trans. on Industrial Electronics*, vol. 51, pp. 933-936, August 2004.

[71] W. Ren, M. Steurer and T.L. Baldwin, "Improve the Stability of Power Hardware-in-the-loop Simulation by Selecting Appropriate Interface Algorithm," *IEEE Trans. on Industry Application*, vol. 44, pp. 1286-1290, July-Aug. 2008.

[72] V. Blasko, V. Kaura, "A New Mathematical Model and Control of a Three-Phase AC-DC Voltage Source Converter," *IEEE Trans. on Power Electronics*, vol. 12, pp. 116-123, Jan 1997.

[73] S. Chen, Y. M. Lai, S. C. Tan and C. K. Tse, "Analysis and design of repetitive controller for harmonic elimination in PWM voltage source inverter systems," *IET transaction on Power Electronics*, Vol. 1, pp. 497-506, February 2008.

[74] E. Koutroulis and K. Kalaitzakis, "Design of a maximum power tracking system for wind-energy-conversion applications," *IEEE Transactions on Industrial Electronics*, Vol. 53, pp. 486-494, April 2006.

[75] J. Dannehl, F. W. Fuchs and P. B. Thogersen, "PI State Space Current Control of Grid-Connected PWM Converters With LCL Filters," *IEEE Trans. Power Electronics*, vol. 25, pp. 2320-2330, Sept. 2010.

[76] M. Dai, M. N. Marwali, J. W. Jung and A. Keyhani, "Power Flow Control of a Single Distributed Generation Unit," *IEEE Trans. Power Electronics*, vol. 23, pp. 343-352, Jan. 2008.

[77] D. Zhi, L. Xu and B. W. Williams, "Improved Direct Power Control of Grid-Connected DC/AC Coverters," *IEEE Trans. Power Electronics*, vol. 24, pp. 1280-1292, may 2009.

[78] P. Rodriguez, A. Timbus, R. Teidorescu, M. Liserre and F. Blaabjerg, "Reactive Power Control for Improving Wind Turbine System Behavior Under Grid Faults," *IEEE Trans. Power Electronics*, vol. 24, pp. 1798-1801, July 2009.

[79] Y. M. Chen, H. C. Wu, Y. C. Chen, K. Y. Lee and S. S. Shyu, "The AC Line Current Regulation Strategy for the Grid-Connected PV Syatem," *IEEE Trans. Power Electronics*, vol. 25, pp. 209-218, Jan 2010.

[80] H. G. Jeong, K. B. Choi and W. Choi, "Performance Improvement of LCL-Filter-Based Grid-Connected Inverters ising PQR Power transformation," *IEEE Trans. Power Electronics*, vol. 25, pp. 1320-1330, May 2010.

[81] C. N. M. Ho, V. S. P. Cheung and H. S. H. Chung, "Constant-Frequency Hysteresis Current Control of Grid-Connected VSI Without Bandwidth Control," *IEEE Trans. Power Electronics*, vol. 24, pp. 2484-2495, Nov. 2009.

[82] B.A. Francis and W.M. Wonham, "The internal model principle of control theory," *Automatica*, Vol. 12, pp. 457-465, 1976.

[83] M. P. Kazmierkowski, L. Malesani, "Current Control Techniques for Three-Phase Voltage-Source PWM Converters: A Survay,", *IEEE Trans. on Industrial Electronics*, Vol. 45, pp.691-703, Oct. 1998.

[84] E. Twining, D. G. Holmes, "Grid Current Regulation of a Three-Phase Voltage Source Inverter With an LCL Input Filter," *IEEE Trans. on Power Electronics*, Vol. 18, No. 3, pp. 888-895, May 03.

[85] D. N. Zmood, D. G. Holmes, G. H. Bode, "Frequency-Domain Analysis of Three-Phase Linear Current Regulators", *IEEE Trans. Power Electronics*, Vol. 37, No. 2, pp. 601-610, March 2001.

[86] A. Timbus, M. Liserre, R. Teodorescu, P. Rodriguez, F. Blaabjerg, "Evaluation of Current Controllers for Distributed Power Generation Systems", *IEEE Trans. Power Electronics*, Vol. 24, No. 3, pp.654-664, March 2009.

[87] Q. Zeng, L. Chang, "An Advanced SVPWM-Based Predictive Current Controller for Three-Phase Inverters in Distributed generation Systems", *IEEE Trans. Industrial Electronics*, Vol. 55, No. 3, pp.1235-1246, March 2008.

[88] H. L. Ginn, G. Chen, "Flexible Active Compensattor Control for Variable Compensation Objectives," *IEEE Trans. on Power Electronics*, Vol. 23, No. 6, pp. 2931-2941, Nov. 2008.

[89] V. Lazarov, D. Apostolov, "PWM Inverter Power Transfer Under Unbalanced Voltage Conditions", *in Proc. Conf. Rec. IEEE ISEIMA*, pp. 254-259, July. 2006

[90] J. E. Garcia, S. Arnaltes, J. L. Amenedo, "Direct power control of voltage source inverters with unbalanced grid voltages", *IET Trans. Power Electronics*, vol. 1, pp. 395-407, April 2007.

[91] X. Song, Y. Wang, W. Hu, Z. Wang, "Three Reference Frame Control Scheme of 4 wire Grid-connected Inverter for Micro Grid Under Unbalanced Grid Voltage Conditions," *in Proc. Conf. Rec. IEEE APEC*, pp. 1301-1305, Feb. 2009

[92] P. Rodriguez, J. Pou, J. bergas, J. I. Candela, R. P. Burgoes, D. Boroyevich, "Decoupled Double Synchronous Reference Frame PLL for Power Converters Control," *IEEE Trans. on Power Electronics*, Vol. 22, Vo. 2, pp. 584-592, March 07.

[93] J. Eloy-Garcia, S. Arnaltes, J. Rodriguez-Amenedo, "Direct power control of voltage source inverters with unbalanced grid voltages," *IET Trans. on Power Electronics*, vol. 1, no. 3, pp. 395-407, Sep. 2008.

[94] L. Serpa, S. Ponnaluri, P. Barbosa, J. Kolar, "A modified direct power control strategy allowing the connection of three-phase inverters to the grid through lcl filters," *IEEE Transactions on Industry Applications*, vol. 43, no. 5, pp. 1388-1400, 2007.

[95] S. Vazquez, J. Sanchez, J. Carrasco, J. Leon, E. Galvan, "A model based direct power control for three-phase power converters," *IEEE Transactions on Industrial Electronics*, vol. 55, no. 4, pp. 1647-1657, 2008.

[96] D. Zhi, L. Xu, B. Williams, "Improved direct power control of gridconnected dc/ac converters," *IEEE Transactions on Power Electronics*, vol. 24, no. 5, pp. 1280-1292, May 2009.

[97] P. Rodriguez, A. Timbus, R. Teodorescu, M. Liserre, F. Blaabjerg, "Flexible active power control of distributed power generation systems during grid faults," *IEEE Transactions on Industrial Electronics*, vol. 54, no. 5, pp. 2583-2592, 2007.

[98] F. Wang, J. Duarte, M. Hendrix, "Design and analysis of active power control strategies for distributed generation inverters under unbalanced grid faults," *IET Transactions on Generation, Transmission and Distribution*, vol. 4, no. 8, pp. 905-916, 2010.

[99] X. Song, Y. Wang, W. Hu, Z. Wang, "Three Reference Frame Control Scheme of 4 wire Grid-connected Inverter for Micro Grid Under Unbalanced Grid Voltage Conditions," *in Proc IEEE APEC*, pp. 1301-1305, Feb. 2009.

[100] V. Lazarov, D. Apostolov, "PWM Inverter Power Transfer Under Unbalanced Voltage Conditions", *in Proc. IEEE ISEIMA*, pp. 254-259, July. 2006.

[101] S. K. Chung, "Phase-locked loop for grid-connected three-phase power conversion systems", *IEE Trans. Power Appl.*, vol. 147, pp. 213-219, May 2000.

[102] M. Aredes, H. Akagi, E. H. Watanabe, E. V. Salgado, L. F. Encarnao, "Comparisons Between the p–q and p–q–r Theories in Three-Phase Four-Wire Systems," *IEEE Transactions on Power Electronics*, vol. 24, no. 4, pp. 924-933, April 2009.

[103] H. Kim, F. Blaabjerg, B. B. Jensen, J. Choi, "Instantaneous Power Compensation in Three-Phase Systems by Using p-q-r Theory," *IEEE Transactions on Power Electronics*, vol. 17, no. 5, pp. 701-710, Sept. 2002.

[104] U. Depenbrock, "THE FBD-METHOD, A GENERALLY APPLICABLE TOOL FOR ANALYZING POWER RELATIONS,", *IEEE Transaction on Power Systems*, vol. 8, no. 2, pp. 381-387, May 1993.

[105] V. Staudt, "Fryze - Buchholz - Depenbrock: A time-domain power theory," *Nonsinusoidal Currents and Compensation, 2008. ISNCC 2008. International School on* , vol., no., pp.1-12, June 2008.

[106] M. Depenbrock, V. Staudt, "The FBD-method as tool for compensating total nonactive currents ," *Harmonics And Quality of Power, 1998. Proceedings. 8th International Conference on* , vol.1, no., pp.320-324 vol.1, Oct 1998.

[107] J. L. Willems, "Budeanu's Reactive Power and Related Concepts Revisited," *accepted for publication in IEEE Transactions on Instrumentation and Measurement*, 2010.

[108] C. Qiong, Z. Jianyong; , "The application of FBD current examination method in the three-phase power system," *Control Conference, 2008. CCC 2008. 27th Chinese*, vol., no., pp.232-235, July 2008.

[109] L.S. Czarnecki, "Orthogonal decomposition of the currents in a 3-phase nonlinear asymmetrical circuit with a nonsinusoidal voltage source," *IEEE Transactions on Instrumentation and Measurement*, vol.37, no.1, pp.30-34, Mar 1988.

[110] H.L. Ginn, C. Guangda, "Flexible Active Compensator Control for Variable Compensation Objectives," *IEEE Transactions on Power Electronics*, vol.23, no.6, pp.2931-2941, Nov. 2008.

[111] F. Blaabjerg, S. Freysson, H. Hansen, S. Hansen, "A new optimized space-vector modulation strategy for a component minimized voltage source inverter," *IEEE Trans. Power Electron.*, vol. 12, no. 4, pp. 704714, Jul. 1997.

[112] Frede Blaabjerg, Dorin O. Neacsu, John K. Pedersen, "Adaptive SVM to Compensate DC-Link Voltage Ripple for Four-Switch Three-Phase Voltage Source Inverters", *IEEE Transactions on Power Electronics*, Vol. 14, No. 4, pp. 743-752, July. 1999.

[113] J. Kim, J. Hong, K. Nam, "A Current Distortion Compensation Scheme for Four-Switch Inverters", *IEEE Trans. on Power Electronics*, Vol. 24, No. 4, pp. 1032-1040, April 09.

[114] T.B. Bashaw, T.A. Lipo, "B4 topology options for operating three phase induction machines on single phase grids," *in Conf. Rec. APEC 2005*, vol.3, no., pp.1894-1902 Vol. 3, March 2005.

[115] Heinz W. Van Der Broeck, Jacobus D. Van Wyk, "A Comparative Investigation of a Three-Phase Induction Machine Drive with a Component Minimized Voltage-Fed Inverter under Different Control Options," *IEEE Transactions on Industry Applications* , vol.IA-20, no.2, pp.309-320, March 1984.

[116] J. Klima, "Analytical investigation of an induction motor fed from fourswitch VSI with a new space vector modulation strategy," *IEEE Trans. Energy Convers.*, vol. 21, no. 4, pp. 832838, Dec. 2006.

[117] H. W. V. D. Broeck, H. Skudelny, "Analytical analysis of the harmonic effects of a PWM AC drive," *IEEE Trans. Power Electron.*, vol. 3, no. 2, pp. 216223, Mar. 1988.

[118] G. L. Peters, G. A. Covic, J. T. Boys, "Eliminating output distortion in four-switch inverters with three-phase loads," *Proc. Inst. Electr. Eng. Electr. Power Appl.*, vol. 145, no. 4, pp. 326332 , Jul. 1998.

[119] C.B. Jacobina, M.B. de Rossiter Correa, E.R.C. da Silva, A.M.N. Lima,"Induction motor drive system for low-power applications," *IEEE Transactions on Industry Applications*, vol.35, no.1, pp.52-61, Jan/Feb 1999.

[120] V. Khadkikar, A. Chandra and B. N. singh, "Generalised single-phase p-q theory for active power filtering: simulation and DSP - based experimental investigation," *IET trans. on Power Electronics*, vol. 2, pp. 67-78, 2009.

[121] Makato Saitou and Toshina Shimizu, "Generalized Theory of Instantaneous Active and Reactive Powers in Single-phase Circuits based on Hilbert Transform," *in Proc. Conf. Rec. PESC*, 2002, Vol. 3, pp.1419 - 1424.

[122] S. K. Sahoo, S. K. Panda and J. X. Xu, "Application of Spatial Iterative Learning Control for Direct Torque Control of Switched reluctance Motor Drive," *in Proc. IEEE PES General Meeting*, 2007, pp. 1-7.

[123] D. Q. Zhang, S. K. Panda, "Chattering-free and fast-response sliding mode controller," *IEE Proc.- Control Theory Appl.*, Vol. 146, No. 2, March 1999.

[124] Hung. J. Y., Gao W., Hung J. C., "Variable structure control: a survay," *IEEE Transactions on Control Systems, IE-40*, pp.2-21, 1993.

[125] Y.A.R.I. Mohamed, E.F.E. Saadany, "A Control Method of Grid-Connected PWM Voltage Source Inverters to Mitigate Fast Voltage Disturbances," *IEEE trans. on Power Systems*, Vol. 24, No. 1, Feb 2009, pp. 489-491.

[126] P.A. Regalia, "A Complex Adaptive Notch Filter," *IEEE Signal Processing Letters*, vol.17, no.11, pp.937-940, Nov. 2010.

[127] V.M. Moreno, A.P. Lopez and R.I.D. Garcias, "Reference Current Estimation Under Distorted Line Voltage for Control of Shunt Active Power Filters," *IEEE Trans. on Power Electronics*, vol. 19, pp. 988-994, July 04.

[128] Ned Mohan, T M Undeland and W P Robbins, *Power Electronics, converters, applications and design*, John Willey and Sons, Inc., Third edition, 2003.

[129] *J. J. Grainger and W. D. Stevenson, Power System Analysis. New York: McGraw-Hill, 1994*

[130] P. Rioual, H. Pouliquen, J. Louis, "Regulation of a PWM rectifier in the unbalanced network state using generalized model", *IEEE Trans. Power Electron*, vol. 11, pp. 495-502, May. 1996.

[131] M. Sakui, H. Fujita, "Calculation of harmonic currents in a three-phase convertor with unbalanced power supply conditions," *IEE Proc.*, Vol. 139, pp. 478-484, Sept 1992.

Papers and patents

Published

Journal paper

1. S. K. Sahoo, S. Dasgupta, S. K. Panda and J. X. Xu, "***A Lyapunov Function-Based Robust Direct Torque Controller for Switched Reluctance Motor Drive System***," ***IEEE Transactions on Power Electronics***, vol. 27, no. 2, pp. 555-564, February 2012.

2. S. Dasgupta, S. K. Sahoo and S. K. Panda, "***Single-Phase Inverter Control Techniques for Interfacing Renewable Energy Sources With Microgrid—Part I: Parallel-Connected Inverter Topology With Active and Reactive Power Flow Control Along With Grid Current Shaping***," ***IEEE Transactions on Power Electronics***, vol. 26, no. 3, pp. 717-731, March 2011.

3. S. Dasgupta, S. K. Sahoo, S. K. Panda and G. A. J. Amaratunga, "***Single-Phase Inverter Control Techniques for Interfacing Renewable Energy Sources With Microgrid—Part II: Series-Connected Inverter Topology to Mitigate Voltage Related Problems Along With Active***

Power Flow Control," ***IEEE Transactions on Power Electronics***, vol. 26, no. 3, pp. 732-746, March 2011.

Conference paper

1. S. Dasgupta, S. N. Mohan, S. K. Sahoo, S. K. Panda, "***Evaluation of current reference generation methods for a three-phase inverter interfacing renewable energy sources to generalized micro-grid***," at ***International Conference on Power Electronics and Drive System (PEDS)***, Singapore, pp. 316-321, Dec. 5-8, 2011.

2. S. Dasgupta, S. N. Mohan, S. K. Sahoo, S. K. Panda, "***A FBD theory based grid frequency independent current reference generation method for a three phase inverter interfacing renewable energy sources to generalized micro-grid system*** ," at ***Annual Conference of the IEEE Industrial Electronics Society (IECON)***, Melbourne, pp. 3076-3081, Nov. 7-10, 2011.

3. S. Dasgupta, S. N. Mohan, S. K. Sahoo, S. K. Panda, "***Derivation of instantaneous Current References for Three Phase PV Inverter Connected to Grid with active and reactive Power flow Control***," at ***IEEE International Conference on Power Electronics (ICPE)***, Korea, pp. 1228 - 1235, May 30-June 3, 2011.

4. S. Dasgupta, S. N. Mohan, S. K. Sahoo, S. K. Panda, "***A Lyapunov function based current controller to control active and reactive power flow in a three phase grid connected PV inverter under generalized grid voltage conditions'***," at ***IEEE International Conference***

on Power Electronics (ICPE), Korea, pp. 1110 - 1117, May 30-June 3, 2011.

5. Ko Ko Win, S. Dasgupta, S. K. Panda, "***An Optimized MPPT Circuit for Thermoelectric Energy Harvester for Low Power Applications'***," at ***IEEE International Conference on Power Electronics (ICPE)***, Korea, pp. 1579 - 1584, May 30-June 3, 2011.

6. S. Dasgupta, Freddy Wilyanto Suwandi, S. K. Sahoo and S. K. Panda, "***Dual Axis Sun Tracking System with PV Cell as the Sensor Utilizing Hybrid Electrical Characteristics of the Cell to Determine Insolation***," at ***IEEE International Conference on Sustainable Energy Technology (ICSET)***, Sri Lanka, pp. 1-5, Dec. 6-9, 2010. 6-9, 2010.

7. S. Dasgupta, K. L. Chua, S. K. Sahoo and S. K. Panda, "***A Novel Control Strategy for Fast Tracking of Photovoltaic Maximum Power Point Voltage***,"at ***IEEE International Conference on Sustainable Energy Technology (ICSET)***, Sri Lanka, pp. 1-5, Dec. 6-9, 2010. 6-9, 2010.

8. Ko Ko Win, X. H. Wu, S. Dasgupta, Jun Wen Wong, R. Kumar and S. K. Panda, "***Efficient Solar Energy Harvester for Wireless Sensor Nodes***," at ***IEEE International Conference on Communication Systems (ICCS)***, Singapore, pp. 289-294, Nov. 17-19, 2010.

9. S. Dasgupta, S.K. Sahoo, S.K. Panda and J.X. Xu, "***A Chattering free Lyapunov function based sliding mode controller applied to single phase series connected PV inverter for grid voltage compensation***," at ***Annual Conference of the IEEE Industrial Electronics Society (IECON)***, Arizona, pp. 2373-2378, Nov. 7-10, 2010.

10. S. Dasgupta, S.K. Sahoo and S.K. Panda, "***A novel current control scheme using Lyapunov function to control the active and reactive power flow in a single phase hybrid PV inverter system connected to grid***," at ***IEEE International Power Electronic Conference (IPEC)***, Japan, pp. 1701-1708, June 21-24, 2010.

11. S. Dasgupta, S.K. Sahoo and S.K. Panda, "***Design of a Spatial Iterative Learning Controller for Single Phase Series Connected PV Module Inverter for Grid Voltage Compensation***," at ***IEEE International Power Electronic Conference (IPEC)***, Japan, pp. 1980-1987, June 21-24, 2010.

12. S. Dasgupta, S.K. Sahoo and S.K. Panda, "***A New Control Strategy for Single Phase Series Connected PV Module Inverter for Grid Voltage Compensation***" at ***IEEE International Conference on Power Electronics and Drives Systems (PEDS)***, Taiwan, pp. 1317-1322, Nov 2-5, 2009.

Accepted

Journal paper

1. S. Dasgupta, S. N. Mohan, S. K. Panda and S. K. Panda, "A plug and play operational approach for implementation of an autonomous-micro-grid system," accepted for publication in ***IEEE Transactions on Industrial Informatics***, March 2012.

Conference paper

1. S. Dasgupta, S. N. Mohan, S. K. Sahoo, S. K. Panda, "***Signature voltage identification technique for implementation of a reliable autonomous-micro-grid system***," accepted for publication in the *IEEE International Symposium of Industrial Electronics*, ISIE 2012, China, May 28-31, 2012.

Submitted for Review

Journal paper

1. S. Dasgupta, S. K. Sahoo, S. K. Panda, "***Lyapunov function based current controller to control active and reactive power flow from a renewable energy source to a generalized three-phase micro-grid system***," submitted for review to the *IEEE Transactions on Industrial Informatics*.

2. S. Dasgupta, S. N. Mohan, S. K. Sahoo, S. K. Panda, "***Application of four-switch based three-phase grid connected inverter to connect renewable energy source to a generalized unbalanced micro-grid system***," submitted for review to the *IEEE Transactions on Industrial Electronics*.

Conference paper

1. S. Dasgupta, I. V. Prasanna, S. K. Panda, "***A novel four-leg three-phase inverter control strategy to reduce the Data Center thermal losses: Elimination of neutral current***," submitted for review to the in the *IEEE International Conference of Industrial Electronics*, IECON 2012, Canada.

2. S. Dasgupta, S. N. Mohan, S. K. Sahoo, S. K. Panda, "***A Sine PWM based control strategy for four-switch based three-phase inverter to connect distributed generating sources to a generalized unbalanced grid***," submitted for review to the in the *IEEE Energy Conversion Congress and Exposition*, ECCE 2012, USA.

3. S. Dasgupta, S. N. Mohan, S. K. Sahoo, S. K. Panda, "***A grid voltage sensor-less operational approach of interconnecting distributed generating source based inverter to unbalanced generalized three-phase grid together with local load at PCC***," submitted for review to the in the *IEEE Energy Conversion Congress and Exposition*, ECCE 2012, USA.

Patent: Invention Disclosures

1. S. Dasgupta, S.K. Sahoo and S.K. Panda, "***A Plug and Play Operational Approach for Implementation for an Autonomous-Smart-Micro-Grid***" Provisional US patent (registered on 5th January 2012) under serial number ***61/583,412***.

2. S. Dasgupta, S.K. Sahoo and S.K. Panda, "***A Three Phase Grid Connected PV Inverter to Control Load Power Consumption From***

Grid with Inbuilt Grid Reactive Power, Current THD and DC Link Voltage Ripples Control Capability Under Generalized Grid Voltage Conditions" Provisional US patent (registered on 28th January 2011) under serial number ***61/437,052***.

3. S. Dasgupta, S.K. Sahoo and S.K. Panda, "***A Single Phase Grid Connected PV Inverter to Control Load Power Consumption from Grid with Inbuilt Grid Reactive Power and Current THD Control Capability*** " Provisional US patent (registered on 09th December 2010) under serial number ***61/421,264***.

4. S. Dasgupta, S.K. Sahoo and S.K. Panda, "***A Single Phase Series Connected PV Inverter To Maintain rated Quality Load Voltage With Bidirectional Power Flow Control And Auto-Synchronization Facility With The Grid Frequency***" Provisional US patent (registered on 02nd February 2010) under serial number ***61/300,522***.

Appendix A

1.1 *Photo of the implemented single-phase and three-phase inverter systems*

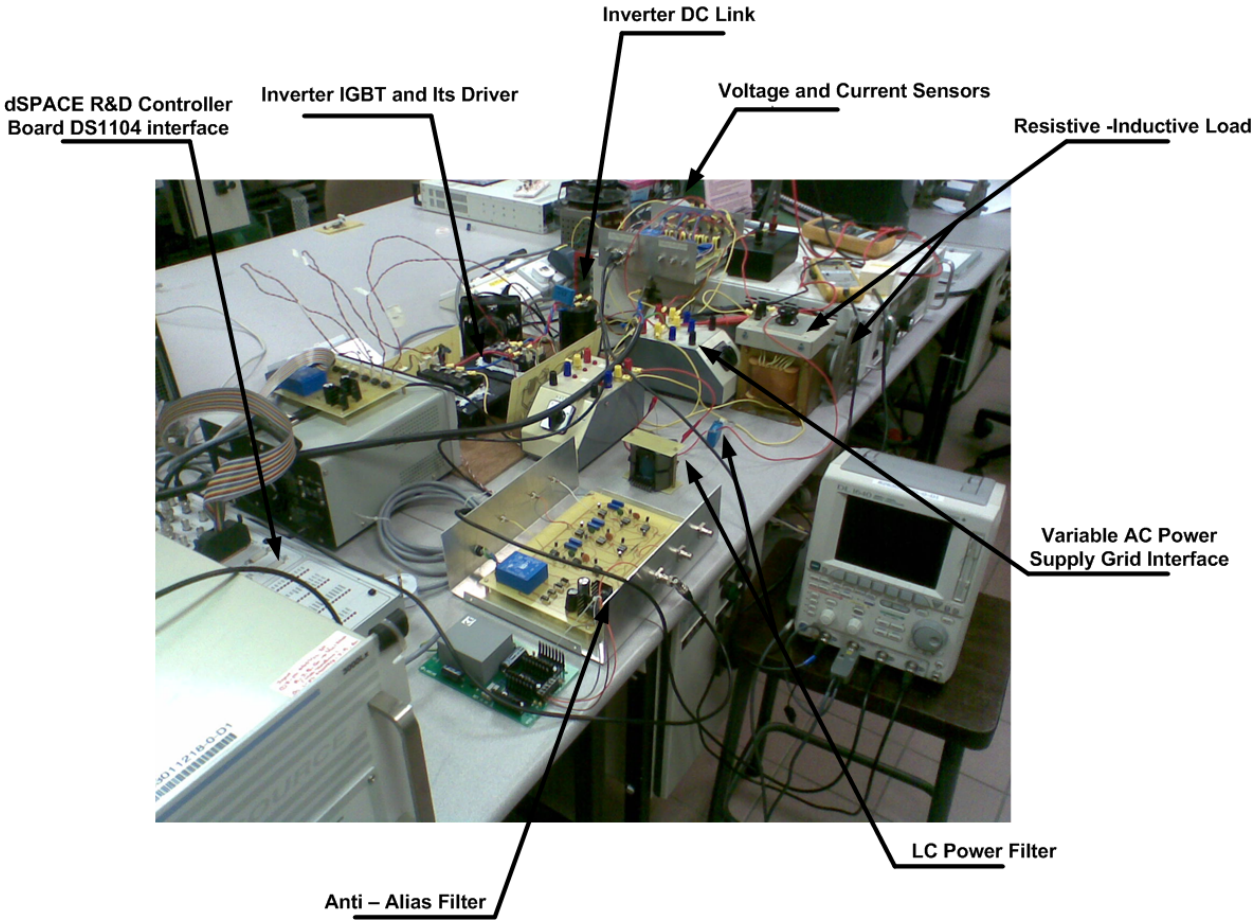

Figure A.1: Photo of the Experimental Setup for the single-phase Series Connected Inverter.

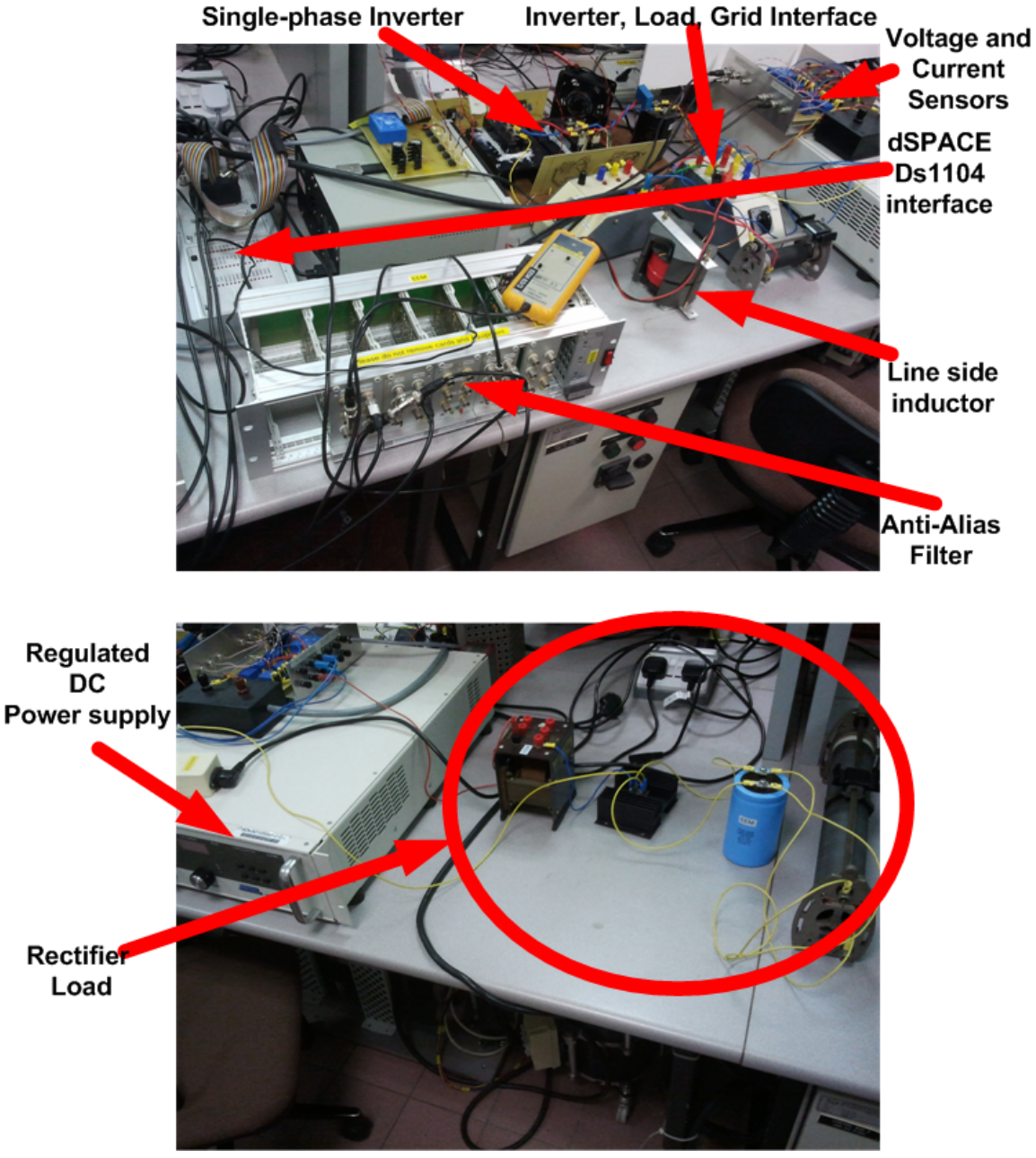

Figure A.2: Photo of the Experimental Setup for single-phase parallel Connected Inverter.

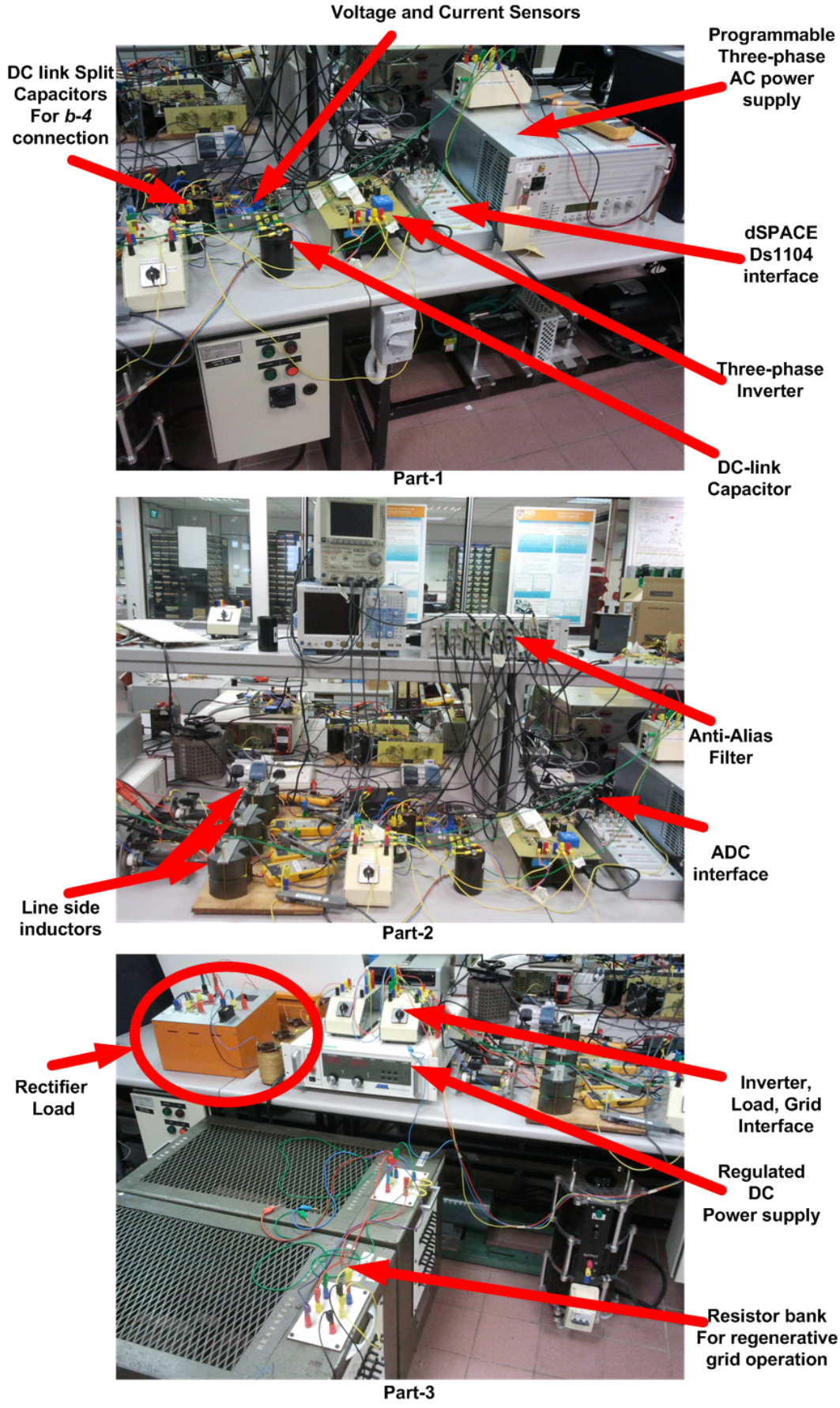

Figure A.3: Photo of the Experimental Setup for three-phase parallel Connected Inverter.

Appendix B

2.1 *Maximum Power Point operation at the presence of battery in the inverter DC link*

The power circuit of the renewable energy source based inverter shown in Figures 2.1, 4.1 and 6.1. If the renewable energy source is PV, the DC link of a typical MPPT circuit is shown in Figure B.1 in details. The proposed MPPT in this report follows the method discussed in [36]. The DC/DC converter used to track the MPPT is taken as Flyback converter. Flyback converter is chosen to have the flexibility of both voltage boosting as well as reduction. The transformer isolation in Flyback converter also helps to electrically isolate the grid side and the PV panel

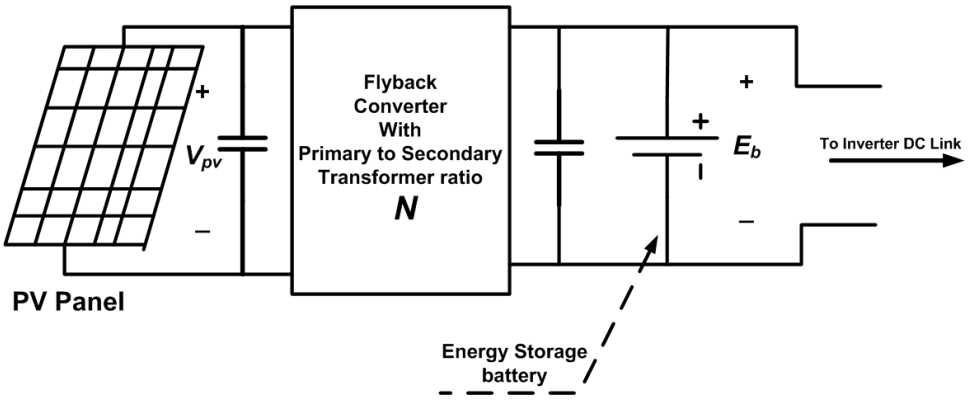

Figure B.1: Interconnection of PV panel with Inverter DC link.

side. The reverse diode of the flyback converter also prevents the reverse current flow to the PV panel in the night time when the SUN insolation becomes very low. The Flyback converter operates in continuous conduction mode (CCM)[128]. This makes the Flyback converter current less peaky reducing the current rating of the power devices. As mentioned in [36], the MPP voltage of the PV panel under the specific operating condition is found out by the information of the short circuit current and the open circuit voltage. The short circuit current and the open circuit voltage of a PV panel under any operating condition is found out by making the IGBT of the Flyback converter ON and OFF respectively for certain amount of time. This process is repeated in a specific time interval (say 1sec), to find the MPP voltage of the PV panel and the IGBT of the flyback converter is controlled in such a way that the input voltage of the Flyback converter is tracked to the calculated MPP voltage value. The primary magnetizing inductance of the transformer of the Flyback converter is designed in such a way that solar insolation from 1sun to say 0.2sun, the flyback converter operates in CCM. If the duty cycle of the IGBT of the flyback converter is D, then the relation of the input and output voltage of the Flyback converter is expressed in (B.1), under CCM [128] as:

$$\begin{aligned} \frac{E_b}{v_{pv}} &= \frac{D}{1-D}\,N \\ \Rightarrow\ v_{pv} &= \frac{1}{N}\,\frac{1-D}{D}\,E_b \\ \Rightarrow\ v_{pv} &= \frac{1}{N}\left(\frac{1}{D}-1\right)E_b \\ \Rightarrow\ v_{pv} &= k\,u_c \end{aligned} \tag{B.1}$$

where, $k = \frac{E_b}{N}$ and $u_c = \left(\frac{1}{D}-1\right)$. This results in $D = \frac{1}{1+u_c}$. Now, it can be concluded that, if the Feedback Liberalization Block , $\frac{1}{1+u}$ is used as shown in Figure B.2, simple linear PI controller can be used as the main controller for the input voltage of the Flyback converter. The control structure shown in Figure B.2

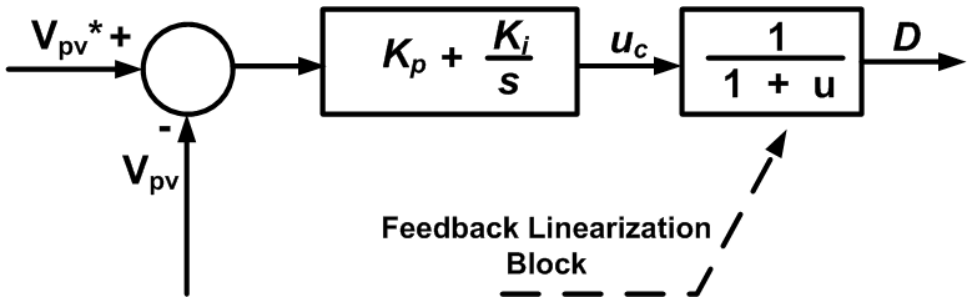

Figure B.2: MPPT voltage control of the PV panel with battery at the inverter DC link.

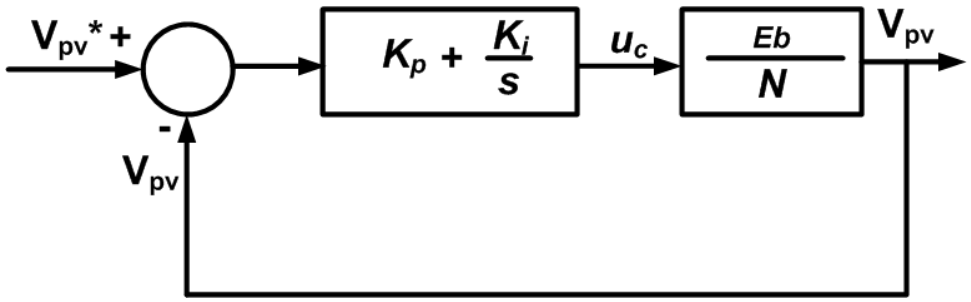

Figure B.3: Input voltage control loop of the Flyback converter with the Feedback Linearization block.

makes the total system linear, which enables the design of PI controller to control the input voltage of the flyback converter to the MPP voltage of the PV panel as shown in Figure B.3. The K_p and K_i can be easily designed to maintain a specific loop BW for the system shown in Figure B.3.

This thesis is mainly directed towards the development of high-performance control schemes for the inverters for micro-grid application. Thus, during the controller development analysis, the steady DC link is assumed (at battery terminal) while transferring a specific amount of active power through the inverter to the load/grid. However, in actual scenario, if the renewable energy is not enough to supply this amount of inverter active power reference, the balance active power comes from the battery storage causing unnecessary drain of the battery energy. Thus, based on the voltage and current of the battery (using sensors) at each con-

dition, the inverter power flow need to be decided so that if the renewable energy based system is unable to support the inverter active power reference, most of the load active power should be drawn from the grid. The intelligence should be included in the controller to make the decision of load power sharing based on battery capacity.

Appendix C

3.1 *DC link voltage control of the PV inverter at the absence of the storage element in the DC link*

The DC link of the inverter, without the energy storage element (say, battery), can be modeled as shown in Figure C.1. It can be understood that, p_{mpp} is the output power of the DC/DC converter (MPP tracker), the p_{inv} is the amount of active power transferred by the inverter and C is the value of the DC link capacitor. The energy balance at DC link can be expressed as:

$$\begin{aligned} \frac{d\left(\frac{1}{2}\,C\,v_{dc}^2\right)}{dt} &= p_{mpp} - p_{inv} \\ \Rightarrow C\,v_{dc}\,\frac{dv_{dc}}{dt} &= p_{mpp} - p_{inv} \\ \Rightarrow \frac{dv_{dc}}{dt} &= \frac{(p_{mpp}/C)}{v_{dc}} - \frac{(p_{inv}/C)}{v_{dc}} \end{aligned} \tag{C.1}$$

It can be considered that, $v_{dc} = x = State\ of\ the\ system$, $\frac{p_{mpp}}{C} = d = Uncontrolled\ input = taken\ as\ disturbance$ and $\frac{p_{inv}}{C} = u = Controlled\ input$. (C.1) can be represented as a non-linear state equation as:

$$\frac{dx}{dt} = \frac{d}{x} - \frac{u}{x} \tag{C.2}$$

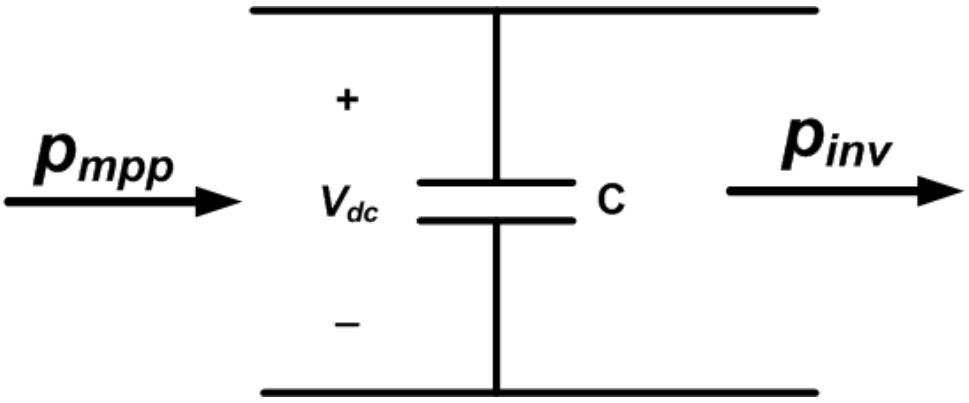

Figure C.1: DC link of the inverter without energy storage element.

It is required to have a steady DC link voltage, x^* at a particular instant. So, the DC link voltage error is defined as $e = x^* - x$ and the candidate Lyapunov function is defined as $V = \frac{1}{2}e^2$. The first time derivative of the Lyapunov function can be expressed as shown in (C.3). (C.2) is further modified as:

$$\begin{aligned} \frac{dV}{dt} &= e\,\frac{de}{dt} \\ &= e\left[\frac{dx^*}{dt} - \frac{d}{x} + \frac{u}{x}\right] \\ &= e\left[-\frac{d}{x} + \frac{u}{x}\right] \end{aligned} \tag{C.3}$$

As the time derivative of the DC link voltage reference, $\frac{dx^*}{dt}$, is zero, further modification of (C.3) is done. The control input is chosen as:

$$u = -\lambda\, e\, x \tag{C.4}$$

where, λ is a +ve number. Plugging in (C.4) in (C.3), the modified form as:

$$\frac{dV}{dt} = -\lambda\, e^2 - \frac{d\, e}{x} \tag{C.5}$$

If the steady state absolute error bound is fixed to be e_b and the value of λ is chosen as shown in (C.6), the DC link voltage error always converges to error always converges to $e = e_b$, making the first time derivative of the Lyapunov

function to be -ve within the absolute error bound, $e = e_b$.

$$\lambda > |\frac{d}{x\, e}|_{max} \tag{C.6}$$

By putting the actual expressions for the disturbance input, (C.6) is modified as:

$$\lambda > \frac{|p_{mpp}|_{max}}{x^*\, e_b\, C} \tag{C.7}$$

It can be concluded from (C.4) that, if dynamically $p_{inv} = -\lambda\, C\, (x^* - x)\, x$ is controlled, a stabilized DC link voltage can be maintained even at the absence of any kind of energy storage element(say, battery).

Appendix D

4.1 *Experimental setup*

o test the feasibility of the proposed topologies and associated control schemes, the experiments are carried out with single-phase as well as three-phase PWM DC/AC voltage sources inverters under different loading conditions as well as distorted and unbalanced operating conditions. The hardware prototype is described here.

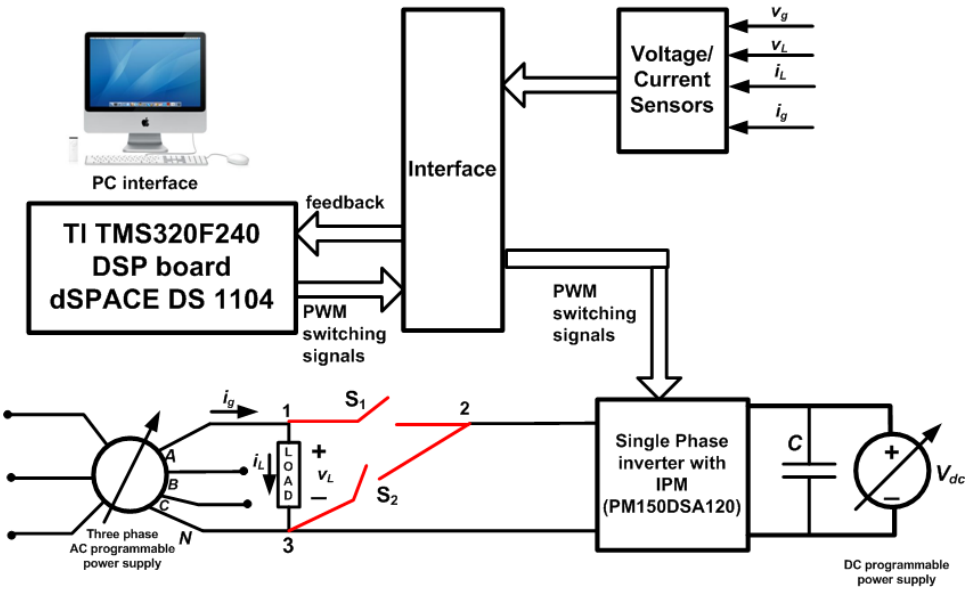

Figure D.1: Experimental Setup for single phase testings.

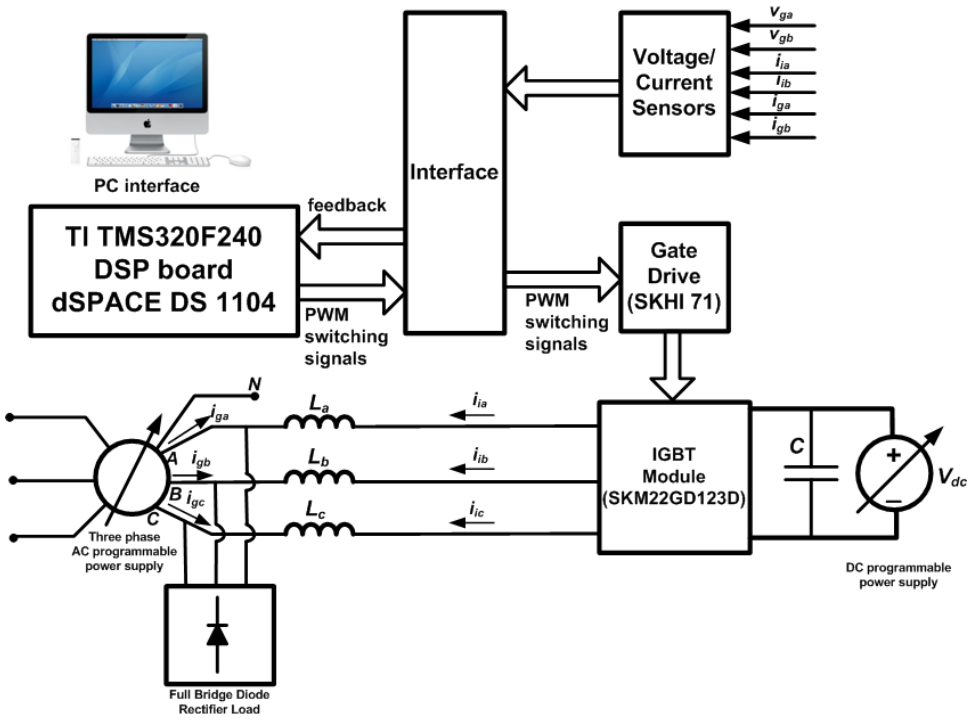

Figure D.2: Experimental Setup for three phase testings.

Figure D.1 shows the experimental set up for testing the single phase inverter topologies. The switches S_1 and S_2 are to do switching between the series and parallel topology of inverter. When S_1 is ON and S_2 is OFF, the power circuit is configured to test parallel topology and when S_1 is OFF and S_2 is ON, the power circuit is configured to test series inverter topology. Figure D.2 shows the experimental set up for testing the three phase inverter topology. The list of special modules used in the experiment can be listed as:

- Three phase programmable AC power supply (5 kW/400V)
- Digital controller for implementing the control algorithm
- Power converter and driver
- Voltage and current sensors

- Signal interface board
- Programmable DC power supply
- Load arrangements

The proposed control methodologies as shown in Figure D.1 and D.2 are implemented in the control development platform of dSPACE DSP system (DS1104), which uses a floating processor MPC8240 as the main processor, a TMS320F240 motion control DSP and ALTERA EPM3064ATC100 FPGA as rapid prototyping interface. The PC interface of the DSP controller provides an easy development environment. The DSP controller has eight A/D and D/A channels. For single phase testing, grid voltage, v_g, load voltage, v_L, grid current, i_g and load current, i_L are measured; whereas for three phase case, phase-a grid voltage, v_{ga} and phase-b grid voltage, v_{gb}, phase-a grid current, i_{ga} and phase-b grid current, i_{gb} and phase-a inverter current, i_{ia} and phase-b inverter current, i_{ib} are measured. All the signals are scaled and filtered before fed through A/D channels. All the control algorithms are developed in 'MATLAB-SIMULINK' real time implementation (RTI) toolbox and downloaded in the DSP chip. The IGBT modules in all the experiments are switched using Sine PWM strategy of $10\,kHz$ switching frequency using the Slave DSP of the control platform.

4.1.1 Three phase programmable AC power supply

California Instruments 3000Lx is used as the three phase programmable power supply to make the grid interface for the prototype three phase PWM DC/AC voltage source converter. By combining a flexible AC power source with a high-end har-

monic power analyzer, the power supply system is capable of handling applications that would traditionally have required multiple instruments. With precise output voltage regulation and accuracy, high load drive current, multi or single phase mode and built-in power analyzer measurement capabilities, this ac source addresses many application areas for AC power testing. Moreover, it provides sine and clipped sine waveforms in addition to user defined arbitrary waveforms. Harmonic waveforms can be used to test for harmonics susceptibility of a unit under test. To simulate common line disturbance occurrences, this supply offers a list of transient steps. All these setting can be programmed from the front panel or downloaded over the interface using the GUI program supplied. This supply equipped with IEEE-488 (GPIB) and RS232C remote control interfaces and support SCPI command language programming.

4.1.2 Digital controller for implementation the control system

The dSPACE R&D Controller Board (DS1104) is used for testing the control algorithms. The DSP processor TI TMS320F240 is employed with 10 kHz control loop sampling rate in the control board. Some of its special features are as follows:

4.1.2.1 Hardware Features

- It is plugged into a PCI slot of a PC.
- It is a complete real-time control system based on a 603 PowerPC floating-point processor running at 250 MHz

- Memory
  - Global memory: 32 MB SDRAM
  - Flash memory: 8 MB
- Timer
  - sample rate timer (decrementer): 32-bit down counter, reload by software, 40 ns resolution
  - 4 general purpose timer: 32-bit down counter, reload by hardware, 80 ns resolution
- Interrupt
  - 5 timer interrupts
  - 2 incremental encoder index line interrupts
- ADC
  - 4 multiplexed channels equipped with one 16-bit sample & hold ADC, 10 V input voltage range, 2 ms conversion time
  - 4 channels each equipped with one 12-bit sample & hold ADC, 10 V input voltage range, 800 ns conversion time
- DAC
  - Eight 16-bit resolution, 10 V output voltage range, 5 mA maximum output current Max. 10 ms settling time
- Digital I/O
  - 20-bit parallel I/O Single bit selectable for input or output 5 mA maximum output current TTL output/input levels

- PWM output Texas Instruments TMS320F240 DSP 16-bit fixed-point processor 20 MHz clock frequency slave DSP subsystem for timing signal generation
  - 3-phase PWM output
  - 14-bit digital I/O

4.1.2.2 Software Features

ControlDesk is dSPACEs software for carrying out experiments, a graphical user interface for managing the dSPACE boards. It provides all the functions to control, monitor and automate experiments and make the development of controllers more efficient. The dSPACE Real-Time Library, the real-time core software with a C programming interface or 'MATLAB-SIMULINK' real time workshop (RTI) interface is provided to help access the hardware I/O for implementation of the controller. Instrumentation offers a variety of virtual instruments to build and configure virtual instrument panels according the ones needs. Input instruments allow to change parameter values online. Any set of instruments can be combined to produce a virtual instrument panel that is specific to the application. In addition, Instrumentation provides data acquisition instruments from the application running on the real-time platform.

The control algorithms developed as discussed in this thesis are written in 'MATLAB SIMULINK' real time toolbox (RTI) programming environment and is verified on this experimental platform.

4.1.3 Power Converter and Driver

The single phase testing of the system (as shown in Figure D.1) is fabricated with MITSUBISHI Intelligent Power Modules (IPM) PM150DSA120. Each of the IPM contains two IGBTs making one leg of the inverter. The IPM IGBT can sustain maximum voltage of V_{CES} about $800\,V$ and the collector current, I_C about $150\ A$. The switching frequency of the IPM can reach to about $20\,kHz$. Each IPM needs a $15\,V$ isolated DC power supply to operate the driving and switching signal processing. For parallel inverter topology, the inverter is interfaced with the grid using a line side inductance of about $6\,mH$ inductance. In the series inverter topology, the inverter is followed by a L-C filter with the parameters as: value of filter inductor, $L_f = 10\,mH$, value of filter capacitor, $C_f = 3.3\,\mu F$, filter current limiting resistance, $R_f = 10\,\Omega$.

The power converter of Figure D.2, is a three phase PWM DC/AC voltage source converter, comprises a three phase IGBT bridge with three $5.5\,mH$ line side smooth inductances in series. The details of the converter modules for three phase setup is described below.

SEMITRANS Standard IGBT modules SKM 22GD123D has been adopted as the three phase IGBT bridge. This IGBT module is suitable for switched mode power supplies, three phase inverters for AC motor speed control and general power switching applications. The pulse frequencies can reach above $15\,kHz$. The maximum voltage V_{CES} is $1200\,V$ and the maximum collect current I_C is $25\ A$.

SEMIDRIVER SKHI 61 sixpack IGBT and MOSFET driver module has been

used as the three phase IGBT bridge drive. The driver module has hybrid components which may directly be mounted to the PCB. Devices for driving, voltage supply, error monitoring and potential separation are integrated in the driver. The forward voltage of the IGBT is detected by an integrated short-circuit protection, which will turn off the module when a certain threshold voltage is exceeded. In case of short-circuit or too low supply voltage the integrated error memory is set and an error signal is generated. The driver is connected to a controlled +15V supply voltage. The input signal level is $0/5\,V$. Additionally a digitally adjustable interlocking time is generated by the driver, which has to be longer than the turnoff delay time of the IGBT. The connections in between the driver board and the IGBT module are made by wires of twisted pairs.

4.1.4 Voltage and current sensors

Different voltage and current sensors are used to measure different voltage and current quantities of the circuit as mentioned previously. The multi-range (10-500V) LEM Module LV 25-P voltage transducers are employed. The conversion ratio is 2500 : 1000. The resistor on the primary side is $60\,k\Omega$ and the secondary $300\,\Omega$ resistor is connected to convert the sensed current signal into an equivalent voltage signal. With the above setting, the calibrated voltage signal is given by $0.0125\,V/V$. Finally, the circuit board containing the two voltage sensors is put inside another shielding box to minimize the EMI effect.

Here, multi-range (5-8-12-25A) LEM Module LA 25-NP current transducers are used. In this application, primary to secondary turns ratio is selected to be 1 : 1000 (thereby the current range becomes $25\,A$). Across the output, $300\,\Omega$

resistor is connected to convert the sensed current signal into an equivalent voltage signal. With the above turns ratio, the calibrated voltage signal is given by $0.3V/A$. Finally, the circuit board containing the two current sensors is put inside another shielding box to minimize the EMI effect.

4.1.5 Signal interface board

The DSP interfacing circuits consist of filters for different voltages and currents signals of the experimental circuit. Filters are required for the current and voltage signals since they generally come from noisy environment and it is necessary to minimize their noise content before feeding them into DSP for processing. They also act as anti-aliasing filters for the digital controller. According to 'Sharons Sampling Theorem', the analog input to a digital system should not contain any frequency component beyond half the sampling frequency of the digital system. The sensed signals from the line side currents and voltages contain the switching frequency $10\,kHz$, so that this switching frequency should be filtered out before the signals is fed back to digital controller. These two issues determine the cut-off frequencies for the filters. In the present implementation, second order low-pass Butterworth filters are used. The cut-off frequencies are chosen to be $1\,kHz$. Further, programmable gain amplifiers (PGAs) with a gain of 2 have been used in the filters to ensure the full load current spans the input range of the the ADC converters ($\pm 10\,V$). The outputs of the PGAs are connected to the ADC inputs of the DSP connector board.

4.1.6 Programmable DC power supply

AMREL 600 V, 10 A programmable power supply is used as the DC link of the prototype DC/AC single phase as well as three phase inverter. The DC power supply provides a precession control of the output voltage in the presence of sudden load transients as well as other dynamics. The power supply can be programmed either from the front panel nobs or remote control interfaces such as RS-232 and GPIB IEEE-488.

4.1.7 Load arrangements

Different types of electrical loads are used for the experiments during different phases of the overall verification. During the experiment of single phase parallel connected inverter, a single phase full diode bridge rectifier with capacitor termination is used as a load connected in parallel with the grid interface. The parameters of the rectifier can be expressed as: Rectifier DC side capacitor, $C_L = 2200\,\mu F$ and Rectifier DC side resistance, $R_L = 140\,\Omega$.

For, single phase series connected inverter testing, an $R - L$ combination is used as a load with the parameters as: Load resistance, $R = 150\,\Omega$, Load inductance, $L = 0.1\,H$.

During the experimental study with the three phase inverter, a three phase full bridge diode rectifier with capacitor termination is used as the non-linear load connected at the three phase grid parallel interface. The parameters of the rectifier load can be mentioned as: Rectifier DC side capacitor, $C_L = 3300\,\mu F$ and the

Rectifier DC side resistance, $R_L = 100\,\Omega$.

Appendix E

5.1 *Using modified single-phase* p-q *theory*

It can be noted from (2.8) that, if the active power P_g and the reactive power Q_g are known, the grid current reference value can be easily solved by using the conventional single phase p-q theory. Now, if the micro-grid scenario is considered, the grid voltage, v_{gr}, can be contaminated by harmonics. From the THD point of view, ideally the grid current, i_{gr}, should only contain fundamental frequency component. Now, it can be understood from (2.8) that, if real and imaginary grid voltages, v_{gr} and v_{gi} contain harmonics and the real and imaginary grid currents, i_{gr} and i_{gi} contain only fundamental component, the expression of P and Q both have a DC component and harmonic power components. On the other hand, the reference active power, P_g and the reactive power, Q_g are DC components of the actual grid power (as harmonic power magnitude can not be referred). So, if the only DC values of P_g and Q_g are used in (2.8) with grid voltage expression full of harmonics, the solution for grid current contains harmonics and the grid current becomes rich in harmonics.

To solve this harmonic power issues, a modified current expression is used to

find the current reference of the parallel CCVSI. It is considered that the real axis grid voltage, v_{gr} contains fundamental component, $v_{gr,f}$ and the harmonic component, $v_{gr,h}$. Similarly, the imaginary axis grid voltage, v_{gi} contains fundamental component, $v_{gi,f}$ and the harmonic component, $v_{gi,h}$. The real axis grid current contains only the fundamental component, $i_{gr} = i_{gr,f}$ and similarly, the imaginary axis grid current contains only the fundamental component, $i_{gi} = i_{gi,f}$. Now, from (2.7), the active and reactive power are separately written as:

$$\begin{aligned} 2\,P &= (v_{gr}\,i_{gr} + v_{gi}\,i_{gi}) \\ &= (v_{gr,f} + v_{gr,h})\,i_{gr,f} + (v_{gi,f} + v_{gi,h})\,i_{gi,f} \\ &= (v_{gr,f}\,i_{gr,f} + v_{gi,f}\,i_{gi,f}) + (v_{gr,h}\,i_{gr,f} + v_{gi,h}\,i_{gi,f}) \\ &= P_{dc} + P_h \end{aligned} \tag{E.1}$$

$$\begin{aligned} 2\,Q &= (v_{gi}\,i_{gr} - v_{gr}\,i_{gi}) \\ &= (v_{gi,f} + v_{gi,h})\,i_{gr,f} - (v_{gr,f} + v_{gr,h})\,i_{gi,f} \\ &= (v_{gi,f}\,i_{gr,f} - v_{gr,f}\,i_{gi,f}) + (v_{gi,h}\,i_{gr,f} - v_{gr,h}\,i_{gi,f}) \\ &= Q_{dc} + Q_h \end{aligned} \tag{E.2}$$

where P_{dc} and Q_{dc} are the total DC active and DC reactive power respectively, supplied from the complex grid. On the other hand P_h and Q_h are the total harmonic active and harmonic reactive power respectively, supplied from the complex grid.

From specification point if view, the user only specifies $P_g = \frac{P_{dc}}{2}$ and $Q_g = \frac{Q_{dc}}{2}$.

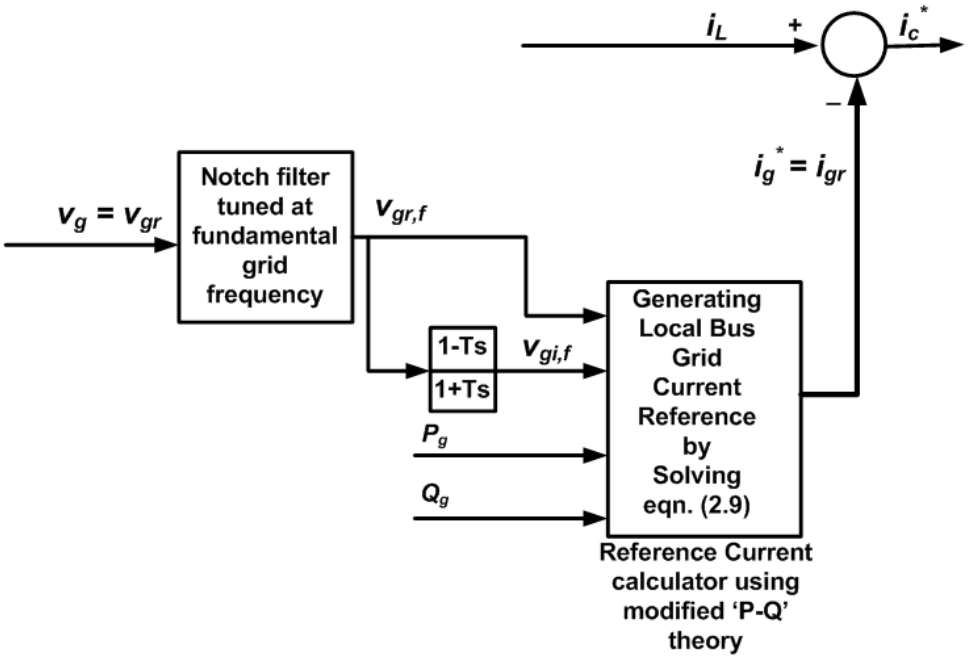

Figure E.1: Algorithm to find out the instantaneous current reference of the parallel CCVSI to ensure proper active and reactive grid power flow with grid current THD as low as possible under distorted grid voltage condition

So, using (E.1) and (E.2), the modified *p-q* equations are written as:

$$\begin{aligned}
\begin{bmatrix} 2\,P_g \\ 2\,Q_g \end{bmatrix} &= \begin{bmatrix} v_{gr,f} & v_{gi,f} \\ v_{gi,f} & -v_{gr,f} \end{bmatrix} \begin{bmatrix} i_{gr,f} \\ i_{gi,f} \end{bmatrix} \\
\Rightarrow \begin{bmatrix} i_{gr,f} \\ i_{gi,f} \end{bmatrix} &= \begin{bmatrix} v_{gr,f} & v_{gi,f} \\ v_{gi,f} & -v_{gr,f} \end{bmatrix}^{-1} \begin{bmatrix} 2\,P_g \\ 2\,Q_g \end{bmatrix} \\
&= \frac{\begin{bmatrix} v_{gr,f} & v_{gi,f} \\ v_{gi,f} & -v_{gr,f} \end{bmatrix}}{v_{gr,f}^2 + v_{gi,f}^2} \begin{bmatrix} 2\,P_g \\ 2\,Q_g \end{bmatrix}
\end{aligned} \tag{E.3}$$

It is mentioned before that the grid current only contains fundamental component. So, it can be written that $i_{gr} = i_{gr,f}$ and $i_{gi} = i_{gi,f}$. The fundamental component of any electrical quantity of imaginary axis can be found out by passing the fundamental component of the corresponding electrical quantity of real axis through the *Hilbert transformation filter* as shown in (2.4). The fundamental component of grid voltage, $v_{gr,f}$ can be found by passing the actual grid voltage, v_{gr} through the notch filter tuned to the fundamental frequency. So, the real grid current reference

can be found from (E.3) and is shown in (E.4).

$$i_g^* = i_{gr,f} = \frac{2\, v_{gr,f}\, P_g + 2\, v_{gi,f}\, Q_g}{v_{gr,f}^2 + v_{gi,f}^2} \tag{E.4}$$

Following the same logic followed in (2.10), the modified expression of the parallel CCVSI current can be found using the expression shown as:

$$i_c^* = i_L - \frac{2\, v_{gr,f}\, P_g + 2\, v_{gi,f}\, Q_g}{v_{gr,f}^2 + v_{gi,f}^2} \tag{E.5}$$

The implementation of the algorithm to find out the instantaneous current reference for the parallel CCVSI current reference discussed in this section is shown in Figure E.1.

Appendix F

6.1 *Control strategies for series inverter to pump active power to grid and charging DC link battery*

6.1.1 Control strategy of the inverter to feed power to the grid

If the operation of the inverter shown in Figure 4.1 is considered at the off-peak time the scenario is little different than the condition mentioned in previous section. The renewable energy source operates in MPPT and if the battery is considered to be totally charged, then the full MPP power needs to be transferred to the AC side. Now, if the load power requirement is less than the MPPT power at the off-peak time ($P_L < P_{mpp}$), the rest of the power ($P_{re} = P_{mpp} - P_L$) needs to be fed to the grid. Such a condition is considered in the phasor relation shown in Figure F.1. It can be noted from Figure F.1 that, the load voltage phasor, V_L, is forced to have a leading phase relation with the grid voltage phasor. V_g, in such a way that the grid phase angle, γ, is more than 90^0. This ensures a negative power flow to the grid unlike the condition as mentioned previously. It can be noted that, the load

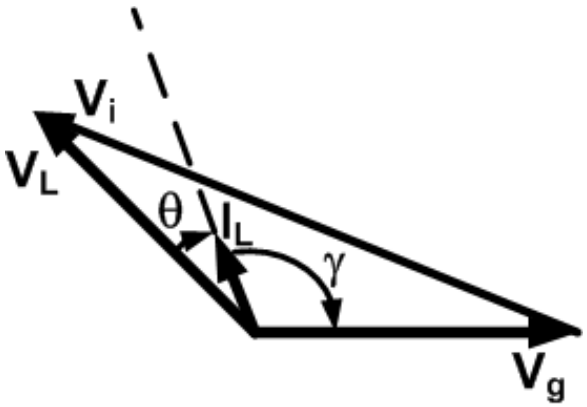

Figure F.1: Phasors diagram of the inverter quantities when $P_g = -ve$

voltage, V_L is also regulated irrespective of the grid voltage condition.

6.1.2 Control strategy of the inverter to store the power from the grid in the DC link battery

If renewable energy source is absent for a long period of time and if there is a chance that the grid may be absent for some days due to intermittent grid failure, then it is desirable to charge the DC link battery by taking extra energy from the grid along with supplying rated voltage across the load. This stored energy can be used by the load during intermittent grid failure. It can be understood that during this operating condition the renewable energy source along with its associated converter is disconnected from the DC link due to safety reason. The simplified structure of the power circuit of the series inverter when operating in *rectifier* mode is shown in Figure F.2. The inverter output voltage phasor, V_i, is adjusted in such a way that, inverter takes in the power to the DC link side. The phasor diagram of the different variables are shown in Figure F.3. It can be noted from Figure F.3 that, to utilize the grid maximally, the grid power factor, γ is maintained at 0^0 (V_g and I_g are in phase). It can also be noticed that, the phase angel relation of

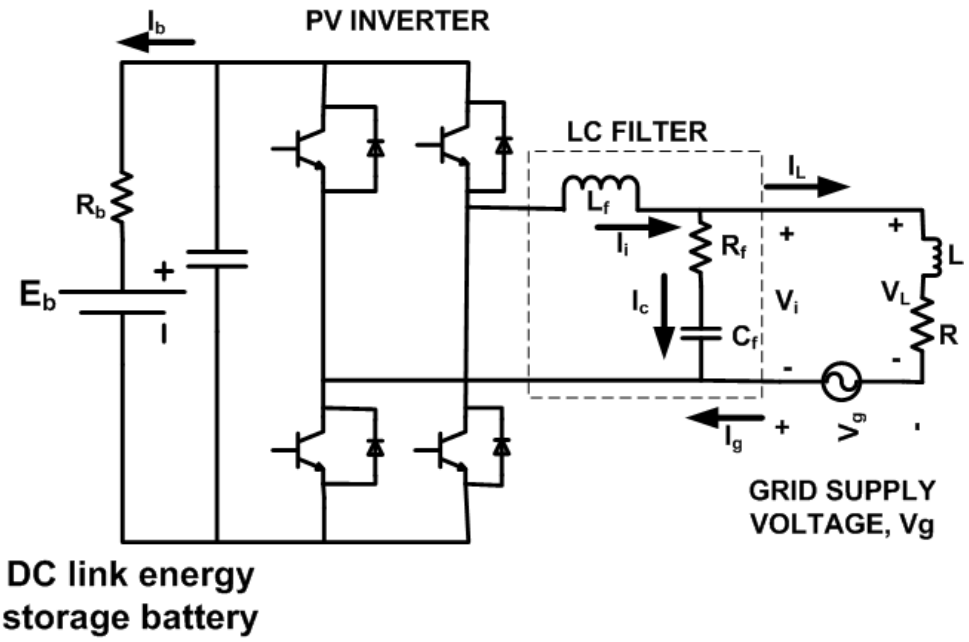

Figure F.2: Simplified power circuit of the series inverter operating in *rectifier* mode to charge the DC link battery

grid current, I_g and the inverter output voltage, V_i is maintained more than 90^0 to ensure *rectifier* mode of operation of the PV inverter.

As the grid and the load are placed in series, the load current can be written as:

$$I_L = I_g = \frac{|V_L|}{|Z|} \tag{F.1}$$

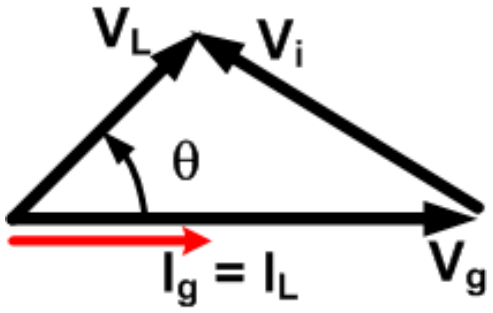

Figure F.3: Phasors diagram of the phasor quantities when inverter is working as *rectifier* to store grid power in DC link storage battery

The power drawn from the grid, P_g, is expressed as:

$$P_g = \mid V_g \mid \times \frac{\mid V_L \mid}{\mid Z \mid} \times \cos(\gamma = 0) \tag{F.2}$$

The power consumed by the load is expressed as:

$$P_L = \frac{\mid V_L \mid^2}{\mid Z \mid} \times \cos(\theta) \tag{F.3}$$

Combining (F.2) and (F.3), the power fed back through the inverter, P_{bat}, is expressed as:

$$P_{bat} = \left[\mid V_g \mid \times \frac{\mid V_L \mid}{\mid Z \mid} - \frac{\mid V_L \mid^2}{\mid Z \mid} \times \cos(\theta) \right] \tag{F.4}$$

It can be understood from (F.4) that the regeneration of grid power is possible only if the condition shown in (F.5), is satisfied.

$$\begin{aligned} P_{bat} &\geq 0 \\ \Rightarrow \mid V_g \mid &\geq \mid V_L \mid \cos(\theta) \end{aligned} \tag{F.5}$$

6.1.2.1 Charging battery when there is voltage sag in grid

Say, the amount of sag in grid voltage from nominal voltage is 'x'. The load voltage will be maintained at nominal value, $\mid V_L \mid$. Then the grid voltage magnitude can be expressed as $\mid V_g \mid = \mid V_L \mid - x$. Now using (F.5), the modified condition for regeneration can be expressed as:

$$\begin{aligned} \mid V_L \mid - x &\geq \mid V_L \mid \cos(\theta) \\ \Rightarrow x &\leq \mid V_L \mid (1 - \cos(\theta)) \\ \Rightarrow x &\leq 2 \mid V_L \mid \sin^2\left(\frac{\theta}{2}\right) \end{aligned} \tag{F.6}$$

It can be understood from (F.6) and Figure F.3 that, the control strategy is maintained in such a way that the grid power regeneration to the DC link battery is

possible along with maintaining rated load voltage under some grid voltage sag condition also.

6.1.2.2 Charging the battery when there is voltage swell as well as normal condition of grid

It can be easily understood that if there is a voltage swell in the grid or grid voltage is at normal condition, the condition mentioned in (F.5) is satisfied. Therefore, it is always possible to transfer the grid energy into the DC link battery along with maintaining the rated load voltage, in the case of grid voltage swell or the grid voltage is maintained at normal condition.

Appendix G

7.1 *Designing Lyapunov function based controller for series inverter*

7.1.1 Deriving the state-space representation of the series inverter

The circuit shown in Figure 4.2 can be seen to have two energy storage element (filter capacitor, C_f and filter inductor, L_f). Two basic governing voltage-current equations for the circuit shown in Figure G.1 are used to find out the state-space equation of the overall series converter. The filter capacitor, C_f, voltage-current equation is written using KCL at the upper terminal of the capacitor as:

$$i_i \;=\; C_f \frac{dv_{cap}}{dt} + \frac{v_L}{R} \tag{G.1}$$

The voltage-current equation for the filter inductor, L_f is shown as:

$$L_f \frac{di_i}{dt} \;=\; v_{inv} \;-\; v_{cap} \tag{G.2}$$

Due to the series connection of the inverter, grid and load, the (G.3) is also valid for this scenario.

$$v_L \;=\; v_{cap} \;+\; v_g \tag{G.3}$$

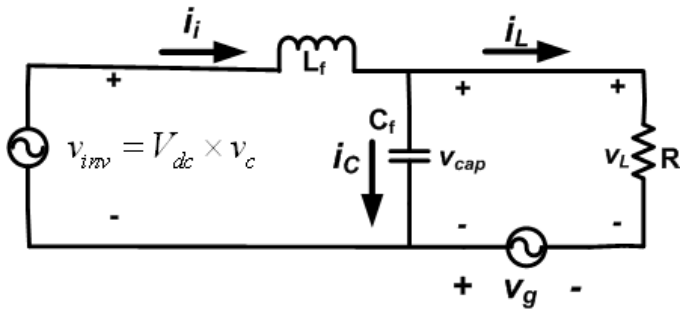

Figure G.1: Simplified representation of the power circuit of the series connected inverter

Differentiating (G.1) and also taking (G.3) into (G.2), the resultant equation becomes:

$$L_f\, C_f \frac{d^2 v_L}{dt^2} \;-\; L_f\, C_f \frac{d^2 v_g}{dt^2} \;+\; \frac{L_f}{R}\frac{dv_L}{dt} \;=\; v_{inv} \;-\; v_L \;+\; v_g \tag{G.4}$$

Now, selecting two states of the system, $x_2 = v_L$ and $x_1 = \frac{dx_2}{dt} = \frac{dv_L}{dt}$ and using (G.4), the state equation of the inverter can be written as:

$$\begin{aligned} \frac{dx_1}{dt} &= a_1 x_1 + a_2 x_2 + bu + d \\ \frac{dx_2}{dt} &= x_1 \end{aligned} \tag{G.5}$$

where, $a_1 = -\frac{1}{RC_f}$, $a_2 = -\frac{1}{L_f C_f}$, $b = \frac{1}{L_f C_f}$, control input $u = v_{inv}$ and the disturbance input $d = \frac{d^2 v_g}{dt^2} + \frac{1}{L_f C_f} v_g$. Now, two state errors are defined as $e_2 = x_2^* - x_2 = e$ and $e_1 = x_1^* - x_1 = \frac{de}{dt}$ and where x_1^*, x_2^* are the reference values of the states x_1 and x_2 respectively.

7.1.2 Designing the *Lyapunov function* based controller

The aim of the control action is such that, the errors converge to the sliding surface $\sigma(e) = c_1 e_1 + c_2 e_2 = c_1 \frac{de}{dt} + c_2 e$, where c_1 and c_2 are two user chosen +ve constants[123] and [124]. So, the Lyapunov function be:

$$V \;=\; \frac{1}{2}\,(c_1 e_1 \;+\; c_2 e_2)^2 \;=\; \frac{1}{2}\,(c_1 \frac{de}{dt} \;+\; c_2 e)^2 \tag{G.6}$$

It can be noted from (G.6) that, the chosen *Lyapunov function* is *Positive definite* anywhere in the error plane (error state plane where e_1 and e_2 moves around), except on the sliding surface $\sigma(e) = 0$.

The first time derivative of the Lyapunov function becomes:

$$\frac{dV}{dt} = (c_1e_1 + c_2e_2)(c_1\frac{de_1}{dt} + c_2\frac{de_2}{dt}) \tag{G.7}$$

7.1.2.1 Considering the case of $d = 0$ and the values of the parameters of the system are known perfectly

Using (G.5) with $d = 0$ and definitions of e_1 and e_2 in (G.7), the modified derivative of *Lyapunov function* is shown as:

$$\begin{aligned} \frac{dV}{dt} &= (c_1e_1 + c_2e_2)\left[c_1\frac{dx_1^*}{dt} + c_2\frac{dx_2^*}{dt}\right] \\ &+ (c_1e_1 + c_2e_2)\left[-(c_1a_1 + c_2)x_1 - c_1a_2x_2 - c_1bu\right] \end{aligned} \tag{G.8}$$

The goal of the control action is to converge the error dynamics to the sliding surface. Now, according to the classical definition of sliding mode control, for the convergence criterion, the first time derivative of the *Lyapunov function* should contain a term of absolute value of the sliding surface [124]. Following the definition, the first time derivative of *Lyapunov function* considered in this report is :

$$\frac{dV}{dt} = -\lambda(c_1e_1 + c_2e_2)^2 - \alpha|(c_1e_1 + c_2e_2)| \tag{G.9}$$

where, both λ and α need to be positive numbers. Equating (G.8) and (G.9), the input control law u can be written as:

$$\begin{aligned} u &= \frac{\lambda(c_1e_1 + c_2e_2)}{c_1b} + \frac{\alpha Sgn(c_1e_1 + c_2e_2)}{c_1b} \\ &+ \frac{c_1\frac{dx_1^*}{dt} + c_2\frac{dx_2^*}{dt}}{c_1b} - \frac{c_1a_1 + c_2}{c_1b}x_1 - \frac{a_2}{b}x_2 \end{aligned} \tag{G.10}$$

where $Sgn(\sigma(e))$ is the switching function over the sliding surface variable.

It can be observed from (G.9) that, the selected control input, works in such a way that the first time derivative of *Lyapunov function* (as shown in (G.9) is *negative definite* any where in the error plane (error state plane where e_1 and e_2 moves around), except on the sliding surface $\sigma(e) = 0$. Thus it can also be concluded, from the (G.9) and (G.10) that, the control input selected in (G.10) forces, the errors ($e_2 = e$ and $e_1 = \frac{de}{dt}$) to slide to the sliding surface.

7.1.2.2 Considering the presence of disturbance $d \neq 0$ with parameter uncertainty of the system

Putting the (G.5) in (G.7), the equation can be rewritten as:

$$\begin{aligned}\frac{dV}{dt} &= (c_1e_1 + c_2e_2)\left[c_1\frac{dx_1^*}{dt} + c_2\frac{dx_2^*}{dt}\right] \\ &+ (c_1e_1 + c_2e_2)\left[-(c_1a_1 + c_2)x_1 - c_1a_2x_2\right] \\ &+ (c_1e_1 + c_2e_2)\left[-c_1bu - c_1d\right] \end{aligned} \tag{G.11}$$

Considering the case where, the actual parameters of the system (a_1, a_2 and b etc) are not known. It is also considered that the estimated values of the parameters of the systems are $\widehat{a_1}$, $\widehat{a_2}$ and $\widehat{b}$. In this case the control input equation shown in (G.10) is modified to be (G.12).

$$\begin{aligned} u &= \frac{\lambda(c_1e_1 + c_2e_2)}{c_1\widehat{b}} \\ &+ \frac{\alpha Sgn(c_1e_1 + c_2e_2)}{c_1\widehat{b}} \\ &+ \frac{c_1\frac{dx_1^*}{dt} + c_2\frac{dx_2^*}{dt}}{c_1\widehat{b}} - \frac{c_1\widehat{a_1} + c_2}{c_1\widehat{b}}x_1 - \frac{\widehat{a_2}}{\widehat{b}}x_2 \end{aligned} \tag{G.12}$$

Using the input, u as defined in (G.12) in (G.11), the first derivative of the *Lyapunov function* can be written as shown in (G.13).

$$\begin{aligned}\frac{dV}{dt} &= -\frac{b}{\widehat{b}}\lambda(c_1e_1 + c_2e_2)^2 - \frac{b}{\widehat{b}}\alpha|(c_1e_1 + c_2e_2)| \\ &- (c_1e_1 + c_2e_2)\left[c_1d + \left(a_1 - \frac{b}{\widehat{b}}\widehat{a_1}\right)c_1x_1\right] \\ &- (c_1e_1 + c_2e_2)\left[\left(1 - \frac{b}{\widehat{b}}\right)c_2x_1\right] \\ &- (c_1e_1 + c_2e_2)\left[c_1\left(a_2 - \widehat{a_2}\frac{b}{\widehat{b}}\right)x_2\right] \end{aligned} \quad \text{(G.13)}$$

(G.13) can be rewritten in the form shown as:

$$\begin{aligned}\frac{dV}{dt} &= -\frac{b}{\widehat{b}}\lambda(c_1e_1 + c_2e_2)^2 - \frac{b}{\widehat{b}}\alpha|(c_1e_1 + c_2e_2)| \\ &- (c_1e_1 + c_2e_2)D(e_1, e_2, x_1, x_2, d) \end{aligned} \quad \text{(G.14)}$$

where, $D(e_1, e_2, x_1, x_2, d) = \left[c_1d + \left(a_1 - \frac{b}{\widehat{b}}\widehat{a_1}\right)c_1x_1\right] + \left[\left(1 - \frac{b}{\widehat{b}}\right)c_2x_1\right] + \left[c_1\left(a_2 - \widehat{a_2}\frac{b}{\widehat{b}}\right)x_2\right]$.

It can be understood from (G.14) that $\frac{dV}{dt}$ can be made -ve definite outside the bound of sliding surface $|\sigma(e)| = \sigma_b$ if:

$$\lambda > \left[\frac{|\ D\ |_{max}}{\frac{b}{\widehat{b}}\sigma_b} - \frac{\alpha}{\frac{b}{\widehat{b}}\sigma_b}\right] \quad \text{(G.15)}$$

where $|\ D\ |_{max}$ is the maximum possible absolute value of the expression $D(e_1, e_2, x_1, x_2, d)$ shown in (G.14).

7.1.2.3 Finite time reaching property of the Lyapunov function based sliding mode control action

Considering the condition that the parameters of the system are known and the system does not have any disturbance, i.e. $d = 0$ with the initial condition of the phase plane $\sigma_0 > 0$, the dynamics of the arbitrary sliding surface, $\sigma(e) = c_1e_1 + c_2e_2$

can be written as (using (G.6) and (G.8)):

$$\frac{d\sigma(e)}{dt} \;=\; -\lambda\,\sigma(e) \;-\; \alpha \tag{G.16}$$

Solving the differential equation in (G.16), the expression of the sliding surface $\sigma(e)$ at time t can be written as:

$$\sigma(e) \;=\; \sigma_0 e^{-\lambda t} \;-\; \frac{\alpha}{\lambda}\left(1 \;-\; e^{-\lambda t}\right) \tag{G.17}$$

Solving (G.17) algebraically to find the time taken, t_σ by the system to reach the sliding surface, $\sigma(e) \;=\; 0$ from the initial point on the phase plane $\sigma(e) \;=\; \sigma_0$ it is found as:

$$t_\sigma \;=\; \frac{1}{\lambda}\,\ln\left[\frac{\alpha \;+\; \sigma_0\lambda}{\alpha}\right] \tag{G.18}$$

It can be remarked that for any set of positive values of λ and α, the time t_σ is a finite value. So, it can be concluded from this discussions that, for a typical power electronic system if λ is made much higher than α, finite time reaching can be ensured with additional advantage of chattering free sliding mode control.

7.1.2.4 Steady state equation of the states of the system

The steady state error dynamics can be represented by the equation of the sliding surface as shown as:

$$\sigma(e) \;=\; c_1 e_1 \;+\; c_2 e_2 \;=\; \sigma_b \tag{G.19}$$

Using the state relation $e_2 \;=\; e$ and $\frac{de_2}{dt} \;=\; e_1$, the sliding surface dynamic equation shown in (G.19) can be modified as:

$$c_1\frac{de}{dt} \;+\; c_2 e \;=\; \sigma_b \tag{G.20}$$

Solving the differential equation, (G.20) for e, the error transient on the sliding surface can be written as:

$$e(t) = \frac{\sigma_b}{c_2} + \left(e(0) - \frac{\sigma_b}{c_2}\right) e^{-\left(\frac{c_2}{c_1}t\right)} \tag{G.21}$$

where $e(0)$ is the initial value of the error $e(t)$, when the error dynamics $\sigma(e)$ reaches the sliding surface $\sigma(e) = \sigma_b$. It can be understood from (G.21) that, if $\sigma_b = 0$ (which is the case when there is no parameter uncertainty as well as $d = 0$) , at $t \to \infty$, $e(t) \to 0$. It can be concluded that, λ should be selected in such a way that σ_b is sufficiently near to zero as decided by the (G.15) to ensure proper load voltage tracking.

It can also be noted from (G.21) that, the constants c_1 and c_2 control the time taken by the error e to go to zero. So, c_1 and c_2 need to be selected in such a way that, the mentioned time to reach steady state, can be controlled accordingly.

7.2 Experimental results of the proposed series inverter system with Lyapunov function based controller operation

It is mentioned in Chapter 4 that if the load voltage needs to be maintained is V_L (rms) at the grid voltage, V_g (rms) and the power flow through the inverter is to be maintained is P_{inv}, the power angle between the grid current(which is also load current) and grid voltage is γ (the details of the phase relations are also depicted in Figure 4.2(b)) can be calculated as shown:

$$\cos(\gamma) = \frac{\frac{|V_L|^2}{|Z|}\cos(\theta) - P_{inv}}{|V_g|.\frac{|V_L|}{|Z|}} \tag{G.22}$$

It is also analyzed before that, the load voltage rms phasor V_L has to lead grid voltage rms phasor V_g by an angle $\gamma + \theta$, where θ is the power factor angle and

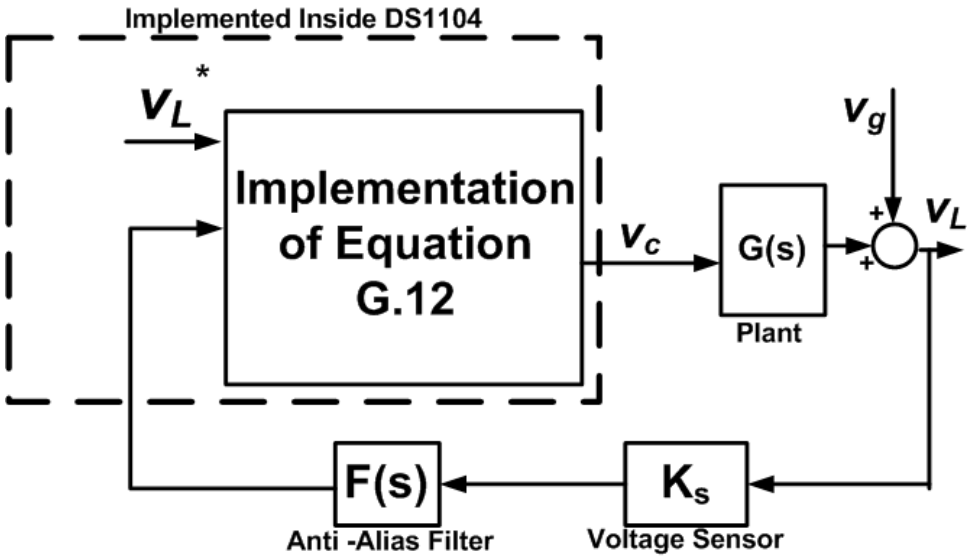

Figure G.2: Schematic of the digital implementation of the Lyapunov function based controller

γ is the grid power angle as also depicted in Figure 4.2(b). However, in this case, the focus is on the load voltage tracking process for the series inverter.

To test the feasibility of the proposed *Lyapunov function* based controller for the load voltage tracking capability of the series inverter, the controller is implemented in dSPACE **ds1104** based system and tested in a voltage scale down version of the actual series inverter system. The control system implementation diagram is shown in Figure G.2.

7.2.1 Testing of the tracking capability of the Lyapunov function based controller in the basic power circuit without disturbance

Initially, the power circuit is made without the presence of grid and different load voltages are tracked with the proposed *Lyapunov function* based controller as shown in Figures G.3 and G.4. The parameters of the power circuit considered in this

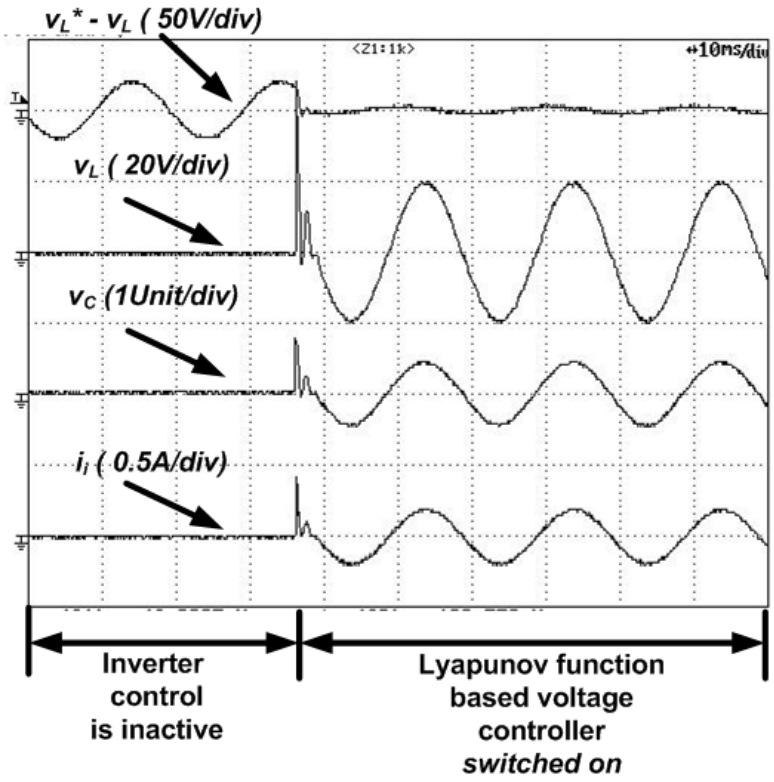

Figure G.3: Experimental waveforms of load voltage error $v_L^* - v_L$, load voltage v_L, SPWM control signal v_C and inverter current i_i to show the dynamics of *Lyapunov function* based controller to track $v_L^*(t) = 20\,Sin(2\pi 50t)$

report are: value of filter inductor, $L_f = 6\,mH$, value of the filter capacitor, $C_f = 1\,\mu F$, load resistance, $R = 100\,\Omega$. The DC link voltage is maintained at $V_{dc} = 50\,V$. By putting all the values of a_1, a_2, b and $c_1 = 1$, $c_2 = g$, in the G.10, the final form of control input is shown as

$$\begin{aligned} v_{inv} &= L_f C_f \lambda(e_1 + g\,e_2) + L_f C_f \alpha Sgn(e_1 + g\,e_2) \\ &+ L_f C_f(\frac{dx_1^*}{dt} + g\,\frac{dx_2^*}{dt}) + \frac{L_f(-g\,RC_f + 1)}{R}x_1 + x_2 \\ v_{inv} &= V_{dc} \times v_c \end{aligned} \tag{G.23}$$

where, v_c is the control signal of the SPWM process [128] to be used to run the inverter. The implementation schematic of this *Lyapunov function* based controller is shown in Figure G.2. To reduce the switching in the control signal the switching function in the control input ((G.23)) is reduced to zero by making $\alpha = 0$ and

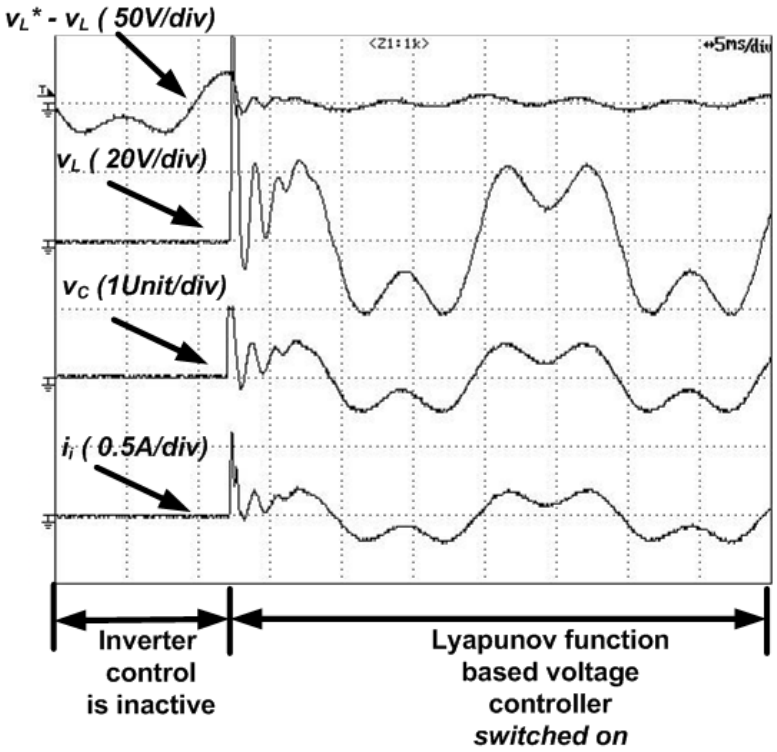

Figure G.4: Experimental waveforms of load voltage error $v_L^* - v_L$, load voltage v_L, SPWM control signal v_C and inverter current i_i to show the dynamics of *Lyapunov function* based controller to track $v_L^*(t) = 20\,Sin(2\pi 50t) + 10\,Sin(2\pi 150t)$

the other parameters are considered as : $\lambda = 10^6$, $g = 5000$ and the error bound $\sigma_b = 0.01$ in the proposed experiment. The SPWM switching frequency as well as sampling frequency of the control system are taken as $10\,kHz$.

Figure G.3 shows the experimental results of load voltage error $e = v_L^* - v_L$, load voltage v_L, SPWM control signal v_C and the inverter current i_i to track the load voltage $v_L^*(t) = 20\ Sin(2\pi 50t)V$ from zero load voltage. It can be seen that, after the *Lyapunov function* based controller is switched on, the error almost immediately reduces to minimal value with the required tracking performance. The control signal v_C can be seen to be of sinusoidal nature and free of any switching characteristics as reported in [124] and [125]. Similar performance is also seen in Figure G.4 to track the load voltage with 50% third harmonics, i.e. $v_L^*(t) = 20Sin(2\pi 50t) + 10Sin(2\pi 150t)$. Figure G.4 also shows fast tracking performance in terms of arbitrary load voltage tracking. It can be understood that, the controller parameters λ and g are chosen to take care of the parameter uncertainty of the actual power circuit during the experiment.

7.2.2 Testing of the tracking capability of the Lyapunov function based controller in the series inverter with grid

The same control input (as shown in (G.23)) can be used for the condition with the grid voltage disturbance as well. But because of the presence of grid voltage disturbance term d, the value of requirement of λ becomes very high (it can be seen that in the expression of D, the largest contribution is given by the component $c_1 d$ leading to a high value of λ from (G.15)). But it is seen during experimentation

that if the value of λ is higher than certain value, the output as well as the control signal starts to have high frequency oscillations. To avoid this problem the grid disturbance term is included in the control input (the disturbance term d in (G.5) is included in inverter voltage, v_{inv} as $L_f\ C_f\ \left[\frac{d^2v_g}{dt^2}\ +\ \frac{1}{L_f\,C_f}v_g\right]\ \approx\ v_g$ as shown below). So, (G.23) is modified to include grid disturbance as:

$$\begin{aligned} v_{inv} &= L_fC_f\lambda(e_1\ +\ g\,e_2)\ +\ L_fC_f\alpha Sgn(e_1\ +\ g\,e_2) \\ &+ L_fC_f(\frac{dx_1^*}{dt} + g\,\frac{dx_2^*}{dt}) + \frac{L_f(-g\,RC_f+1)}{R}x_1 + x_2 \\ &+ v_g \\ v_{inv} &= V_{dc} \times v_c \end{aligned} \tag{G.24}$$

The grid voltage, v_g is measured using voltage sensors and added with the controller output. Before going in the experiments with *Lyapunov function* based voltage controller some representative waveforms are shown to achieve the same tracking task with typical *learning controller* (in this case SRC).

Figure G.5 shows the experimental dynamic waveforms of grid voltage, v_g, load voltage, v_L, load voltage error, $e\ =\ v_L^* - v_L$ and the inverter current, i_i. It can be seen when *learning controller* is plugged in, it takes around 9 sec time for the load voltage v_L to reach the steady state of 20 V rms from 10V rms. The steady state waveform is shown in Figure G.6. It can be noticed from Figure G.6 that, the load voltage, v_L is maintained at 20V rms even with grid voltage v_g being maintained at $10V$ rms and both of them are in same phase.

The similar transients are tested with the proposed *Lyapunov function* based controller and the results are shown in Figures G.7 and G.8. Figure G.7 shows the dynamic transition of load voltage v_L from 14.14V rms to 20V rms (same phase with the grid voltage). Figure G.7 consists of grid voltage, v_g (maintained at 10V

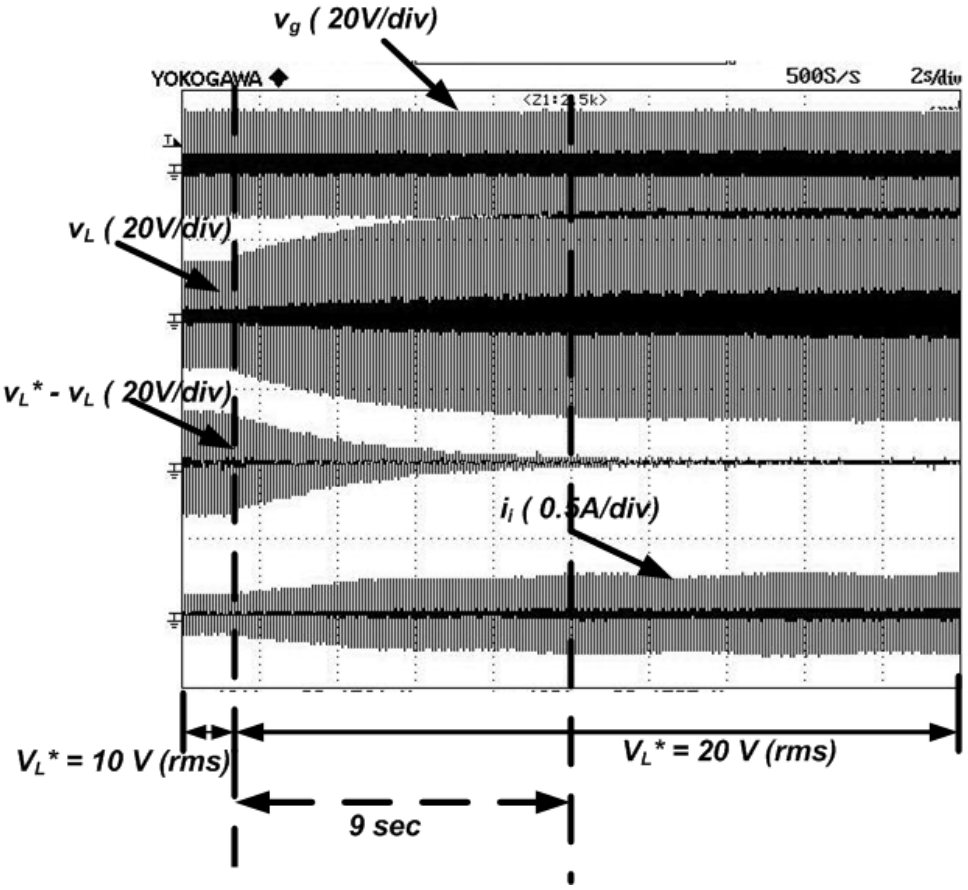

Figure G.5: Experimental dynamic waveform of grid voltage v_g, load voltage v_L, load voltage error $v_L^* - v_L$ and inverter current i_i with learning controller plugged in when load voltage reference is changed from $v_L^*(t) = 14.14\,Sin(2\pi 50t)$ to $v_L^*(t) = 28.284\,Sin(2\pi 50t)$ with the grid voltage $v_g(t) = 14.14\,Sin(2\pi 50t)$

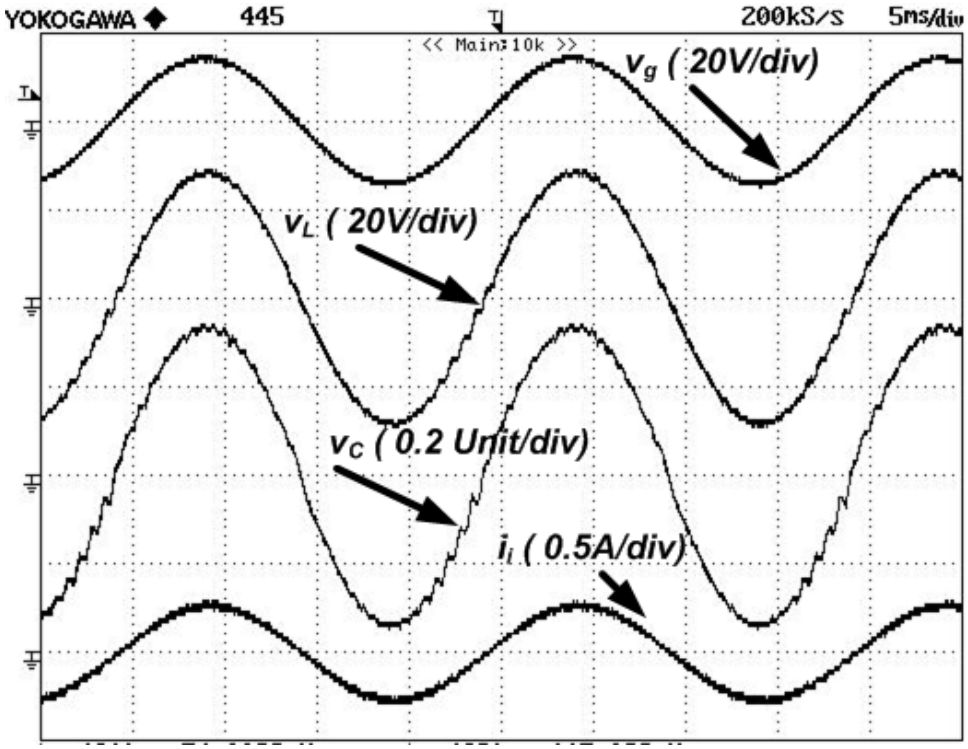

Figure G.6: Experimental steady state waveform of grid voltage v_g, load voltage v_L, load voltage error $v_L^* - v_L$ and SPWM control signal v_C with learning controller plugged in when load voltage reference is $v_L^*(t) = 28.284\,Sin(2\pi 50t)$ with the grid voltage $v_g(t) = 14.14\,Sin(2\pi 50t)$

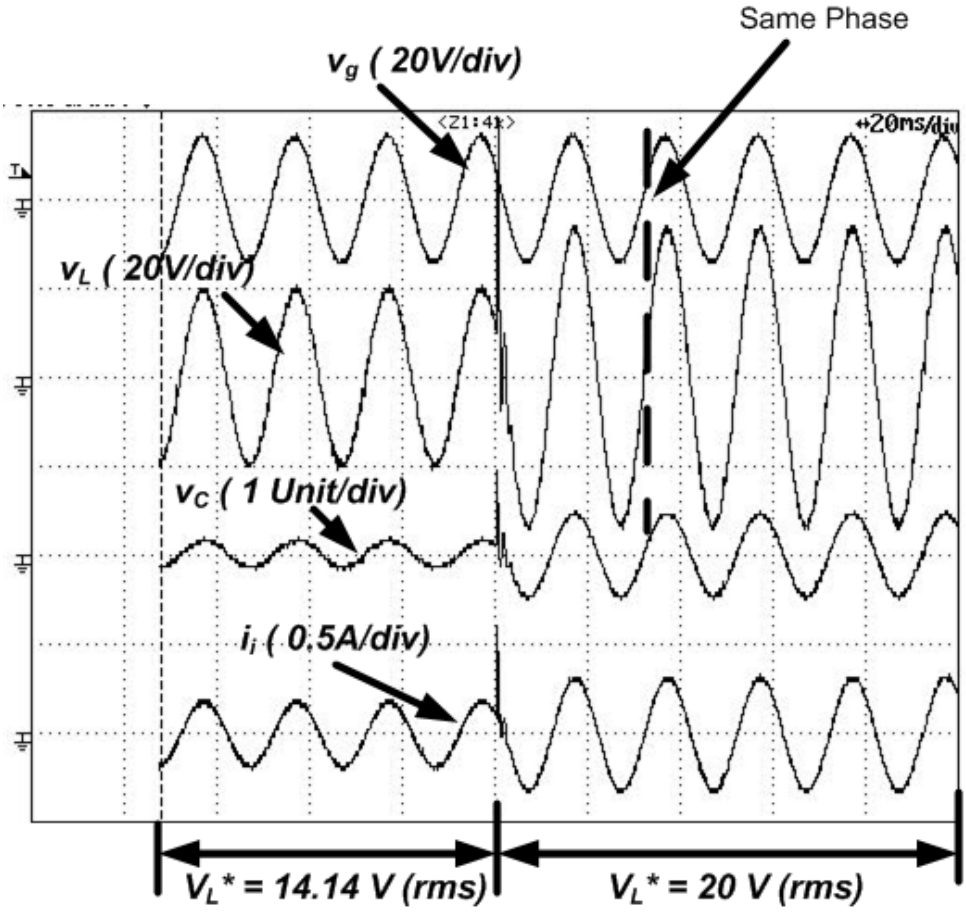

Figure G.7: Experimental dynamic waveform of grid voltage v_g, load voltage v_L, load voltage error $v_L^* - v_L$ and SPWM control signal v_c with Lyapunov function based controller plugged in when load voltage reference is changed from $v_L^*(t) = 20\ Sin(2\pi 50t)$ to $v_L^*(t) = 28.284\ Sin(2\pi 50t)$ with the grid voltage $v_g(t) = 14.14\, Sin(2\pi 50t)$

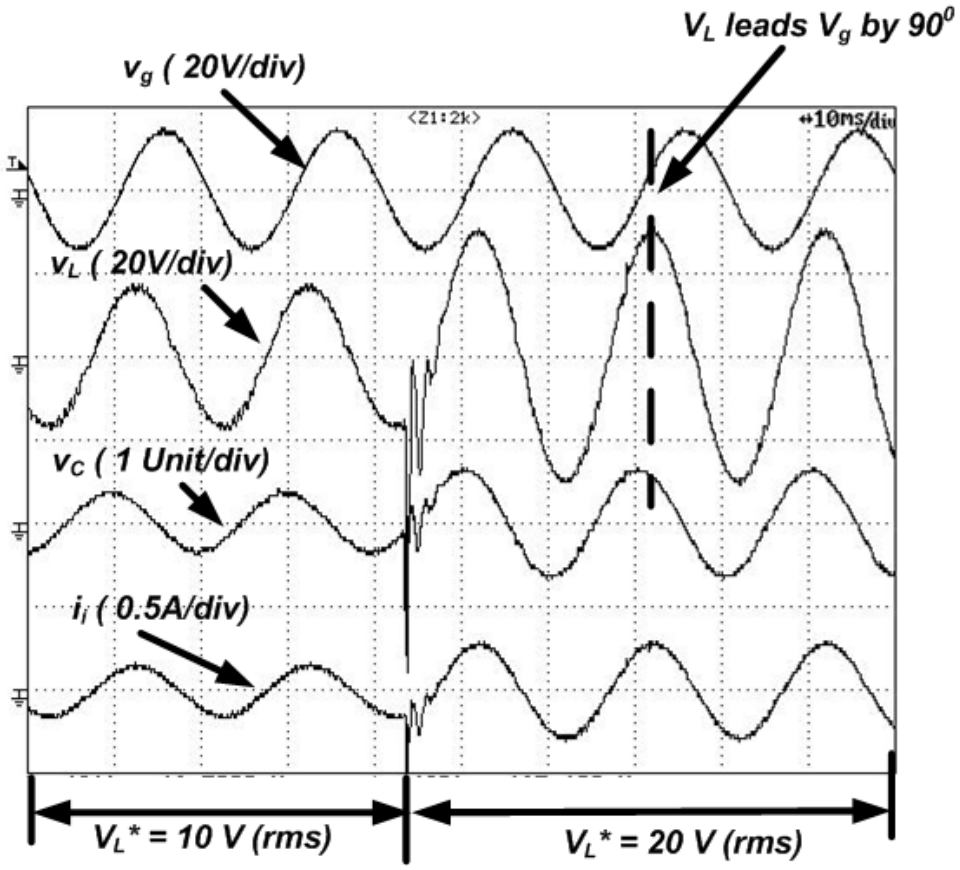

Figure G.8: Experimental dynamic waveform of grid voltage v_g, load voltage v_L, load voltage error $v_L^* - v_L$ and SPWM control signal v_c with Lyapunov function based plugged in when load voltage reference is changed from $v_L^*(t) = 14.14\,Sin(2\pi 50t + \frac{\pi}{2})$ to $v_L^*(t) = 28.284\,Sin(2\pi 50t + \frac{\pi}{2})$ with the grid voltage $v_g(t) = 14.14\,Sin(2\pi 50t)$

rms), load voltage, v_L, SPWM control signal, v_c and the inverter current, i_i with the *Lyapunov function* based controller being in operation. It can be seen that when the reference load voltage changes, the load voltage, v_L almost immediately follows the reference load voltage, v_L^*. Figure G.8 shows the dynamic transition of load voltage v_L from 10V rms to 20V rms (load voltage leads the grid voltage by 90^0 to ensure power flow condition mentioned in (G.22)). The transtion time in this case is insignificant in comparison with the time taken by *learning* controller to ensure tracking.

Appendix H

8.1 *Comparison of the performance of the proposed Lyapunov function based controller and the traditional PI+fundamental frame multiple PR controller for three-phase generalized grid connected CCVSI*

8.2 Simulation Results

The performance of the proposed controller is compared with the traditional PI+fundamental frame cascaded PR controller (as proposed in [32]) with simulation results on the power circuit shown in Figure 6.2. Both type of controller are used in a balanced grid voltages (v_{ga}, v_{gb} and v_{gc}) of peak phase value $200\,V$ as can be seen from Figure H.1(a). It can also noted (from the load currents i_{La}, i_{Lb} and i_{Lc}) the simulated three-phase rectifier load (simulated using controlled current source with triangular current notch which can be approximated as rectifier input current) consumes about $2kW$ active power (calculated using simulated power measurement device). The current reference of the inverter is devised in such a way that the CCVSI supplies $500\,W$ of active power and total harmonic power resulting the grid to

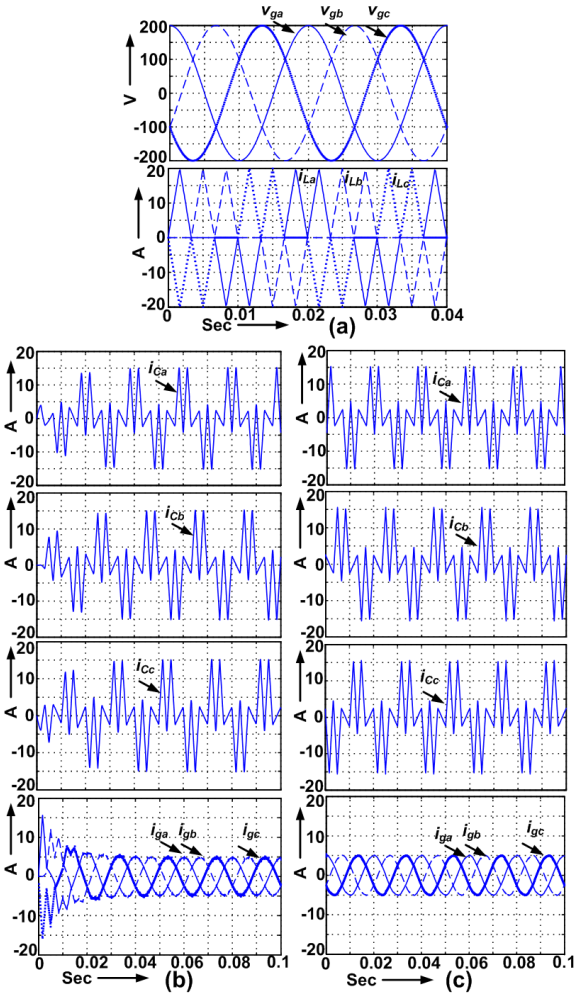

Figure H.1: Simulation results (a) Grid voltages, v_{ga}, v_{gb} and v_{gc} and load currents, i_{La}, i_{Lb} and i_{Lc}, (b) CCVSI currents, i_{Ca}, i_{Cb} and i_{Cc} and grid currents, i_{ga}, i_{gb} and i_{gc} with traditional PI+fundamental frame cascaded PR controllers (c) CCVSI currents, i_{Ca}, i_{Cb} and i_{Cc} and grid currents, i_{ga}, i_{gb} and i_{gc} with *Lyapunov function* based controller, with balanced grid voltages.

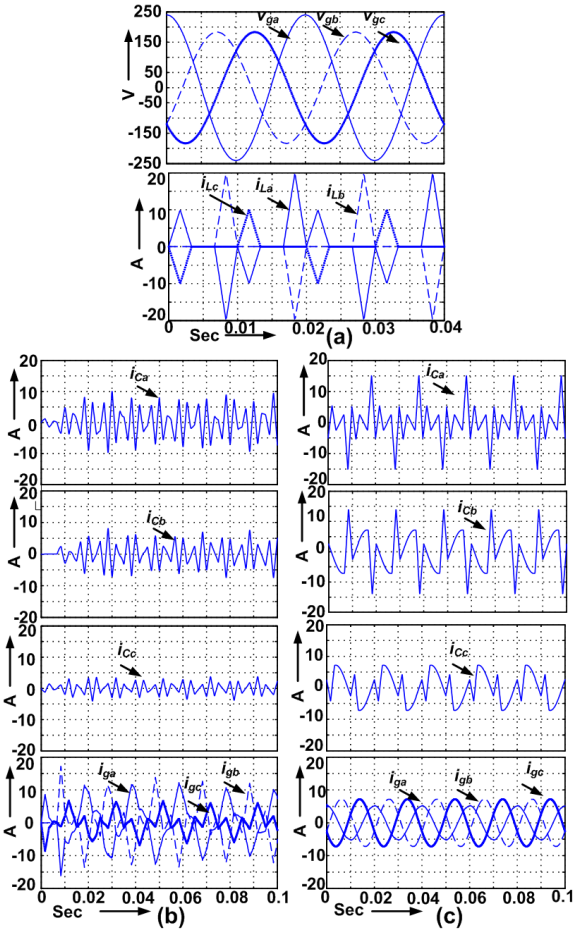

Figure H.2: Simulation results (a) Grid voltages, v_{ga}, v_{gb} and v_{gc} and load currents, i_{La}, i_{Lb} and i_{Lc}, (b) CCVSI currents, i_{Ca}, i_{Cb} and i_{Cc} and grid currents, i_{ga}, i_{gb} and i_{gc} with traditional PI+fundamental frame cascaded PR controllers (c) CCVSI currents, i_{Ca}, i_{Cb} and i_{Cc} and grid currents, i_{ga}, i_{gb} and i_{gc} with *Lyapunov function* based controller, with unbalanced grid voltages.

supply only 1.5 kW active power. The simulation results are shown in Figures H.1(b) and (c) for traditional PR controller and proposed controller respectively. It can be seen that in both the cases, the CCVSI currents (i_{La}, i_{Lb} and i_{Lc}) and the grid currents (i_{ga}, i_{gb} and i_{gc}) are the same in the steady-state; however, the proposed *Lyapunov function* based controller provides better performance during transient conditions as can be seen from Figures H.1(b) and (c). The comparison is carried out with the unbalanced grid voltages (v_{ga}, v_{gb} and v_{gc}) (20% negative sequence contamination with the balanced case mentioned earlier) as can be seen in Figure H.2(a). It can also be noted that in this condition, the load currents (i_{La}, i_{Lb} and i_{Lc}) are asymmetrical and it draws about 2.5 kW. However, the CCVSI is expected to supply about 700 W and total harmonic power of the load and the grid is expected to supply about 1.8 kW active power only. In this application, the traditional cascaded PR controller is applied in both positive and negative sequence fundamental rotating frame by splitting all the control and feedback variables in respective sequence components as discussed in [92] whereas the proposed controller structured is maintained the same as shown in Figure 6.5. It can be seen from Figure H.2(b) that, traditional PR controller is incapable of dealing with unbalance condition resulting in highly non-sinusoidal current with high THD being drawn from the grid; whereas Figure H.2(c) suggests that, the proposed controller is equally capable of dealing with unbalance condition with pure sinusoidal grid currents. For unbalanced grid voltages, the rectifier load currents contain triplen harmonics (as explained in [131] and also verified with experiments later), which does not form space vector so these current harmonics can not be taken care of by the rotating frame controllers resulting in the high THD of grid currents.

Appendix I

9.1 *Brief description of main contributions of this thesis*

9.1.1 Control methodology of single-phase parallel connected renewable energy source based inverter connecting to micro-grid to control active and reactive power flow with grid current shaping

In this thesis a control methodology of a single-phase CCVSI is investigated that enables the single inverter interfaces the renewable energy source to reduce the grid power consumption as well as controls the THD of the grid current in the presence of the non-linear load at the grid PCC. A *Lyapunov function* based current tracking controller is proposed for the single-phase micro-grid connected renewable energy sources through inverter. The proposed controller is easier to implement in comparison with other type of controllers as discussed in [57]-[58], [65]-[66]. It is directly implemented in the *real grid phase domain* ($\theta = \int \omega\, dt$) and is independent of the grid fundamental frequency. The proposed controller is shown to have fast convergence of the tracking error. The stability of the controller is derived by using the *direct method of Lyapunov*. A technique of improving the performance

of the proposed *Lyapunov function* (LF) based controller by estimating the grid and other non-linear disturbances using *Spatial Repetitive Controller* (SRC) is also proposed in this report. The inverter current reference is derived from the desired inverter output power using *single phase p-q* [120]-[121] theory. This allows control of active, reactive and harmonic power flow through the inverter to the micro-grid. The controller also leads to low THD in grid current even in presence of non-linear load. Detailed experimental results are provided to show the efficacy of the proposed current controller. The power circuit and its associated control strategy is described to work in such a way that, the proposed parallel inverter along with its control methodology can be used to interface loads with any type of renewable energy sources and the micro-grid.

9.1.2 Control methodology of single-phase series connected renewable energy source based inverter connecting to micro-grid to mitigate voltage related problems along with active power flow control

A new control strategy is proposed for series inverter to mitigate any type of grid disturbances under frequency variation along with the control of renewable energy flow to the load. In the proposed method, the renewable energy source forms the DC link. The inverter taps the DC-link and its output is also connected in series with the load and the micro-grid. In the proposed control strategy, the inverter voltage is added *vectorially* with the micro-grid voltage to have an independent control of the active power flow through the inverter along with load voltage regulation under any type of the grid (sag, swell or normal) voltage condition. It is shown in later later part of this thesis that the proposed control strategy also makes the grid power factor leading even in the presence of a lagging power factor load.

The series inverter can also eliminate the effect of the voltage harmonics across the load even if there is a voltage harmonic contamination in the micro-grid voltage. A *Spatial Repetitive Controller* (SRC), which is implemented based on grid phase sample position ($\theta = \int \omega \, dt$) domain, is proposed in this report. The proposed SRC works in a similar way as described in [122]. A design method of this SRC controller is presented in this report. A method of grid phase position domain modeling of the inverter with L-C filter assembly and grid and load interconnection is also presented to facilitate the design method. The designed SRC is used to track 110 Volts, 50 Hz rated load voltage with different phase lead angles under sag, swell or normal conditions in the micro-grid with specific amount of inverter active power flow. Experimental test results are presented to show that constant voltage is maintained across the load when there are voltage sag or swell in the grid voltage. Another set of test results are also provided to show the effectiveness of the designed SRC in eliminating grid voltage harmonics as well as maintaining rated load voltage under grid frequency variation. The proposed series inverter along with its control methodology can be used to interface loads with any type of renewable energy sources and the micro-grid. A *Lyapunov function* based tracking controller is also proposed in this report for the series inverter. Detailed analysis of the *Lyapunov function* based controller is provided in this report. The *Lyapunov function* based voltage tracking controller provides faster response with respect to SRC. It can be seen from the analysis provided, the proposed *Lyapunov function* based controller also provides well known *chattering free sliding mode* characteristics [123, 124] and [125]. Experimental results are also included to validate the efficacy of the proposed controller in the series inverter application.

9.1.3 A Lyapunov function based current controller to control active and reactive power flow from a renewable energy source to a generalized three-phase micro-grid system

A generalized model of the three-phase CCVSI in the *a-b-c* frame is presented which considers unbalanced line-side inductors with the grid. The grid can also have asymmetrical unbalance (presence of zero sequence voltage) condition. A *Lyapunov function* based controller is proposed to facilitate current control of such inverters directly in the *a-b-c* frame. The number of controllers needed for such unbalanced control is shown to be only two unlike multiple controllers as mentioned in [38]. The proposed controller is also implemented in the *a-b-c* frame which eliminates the need of *dual frame Park transformation* as well as *SPLL* in the control structure. The proposed control strategy is also invariant with respect to the fundamental frequency of the grid. The proposed control method uses the current references calculated directly in the *a-b-c* frame by the method and the successful current tracking by the CCVSI ensures proper grid active and reactive power flow along with minimum DC link voltage ripple and pure sinusoidal grid currents in the presence of non-linear load connected at the PCC in the grid. This also eliminates the need of additional *power factor correction* (PFC) circuit, which is commonly referred to as shunt compensator in literature [26]-[27]. A SRC is used to estimate the predictable and unpredictable periodic disturbances to improve the performance of the *Lyapunov function* based controller. The proposed control method is tested successfully in traditional *b-6* three-phase inverter (six semiconductor switches) or in *b-4* [111]-[112] three-phase inverter (four semiconductor switches) utilizing simple Sine PWM switching method. A detailed analysis of the proposed controller is provided and adequate experimental results are also

included to show the efficacy of the proposed control structure.

9.1.4 Derivation of instantaneous current references for multi-phase PWM inverter to control active and reactive power flow from a renewable energy source to a generalized multi-phase micro-grid system: the p-q theory based approach

A novel implementation method of *p-q* theory based reference current calculator for CCVSI for controlling both the grid active power flow and grid current THD is proposed in this report. The proposed implementation directly calculates the VSI instantaneous line current references in the *a-b-c* frame from information such as instantaneous phase or line voltages of the unbalanced grid but never resolves it into dual synchronous frame. Also, SPLL is not required in this method of reference current calculation. It is described in this report that the proposed method is able to take care of the sudden change in grid frequency and harmonic contamination in the grid voltages as well. A novel method of extracting positive-sequence and negative-sequence voltage components using *Complex Notch Filter* (CNF) [126] is also proposed to eliminate the phase shifting complications (*typically* 120^0 *phase shifting operations*) of *Fortescue's* method. A *Rotating Reference Signal Characterizer* (RRSC) method is also proposed to estimate the magnitude, frequency and phase of the positive and negative sequence voltages is also proposed. The frequency information is used to tune the CNF in the case of sudden change in grid voltage fundamental frequency. The RRSC operates much faster and accurately than traditional SPLL as tested during experimental study. Because of the reduced computational burden, the proposed method is much faster than the traditional implementation process of *p-q* based current reference calculation as can be referred

to [30]-[31], [99]-[100] and [120]-[121]. The CCVSI current references provided by the *p-q* theory based method is further analyzed with single phase instantaneous power theory based approach and the presence of second harmonic power in the DC link quantities of the inverter is also investigated. A detailed analysis and experimental results are presented in this report to show the efficacy of the proposed implementation method of calculating the current reference of the CCVSI.

9.1.5 Derivation of instantaneous current references for multi-phase PWM inverter to control active and reactive power flow from a renewable energy source to a generalized multi-phase micro-grid system: the FBD theory based approach

A novel implementation method of *FBD* theory based reference current calculator for CCVSI for controlling both the grid active power flow and grid current THD is proposed in this report. The proposed implementation directly calculates the VSI instantaneous line current references in the *a-b-c* frame from the information of instantaneous phase or line voltages of the unbalanced grid but never resolves it into dual synchronous frame. An implementation of *FBD* method is proposed based on the position sampling unlike the traditional time sampling. The position sampling is carried out in the fundamental phase of the grid voltages. The position sampling method is similar to what the present authors have proposed in the case of SRC implementation. Position sampling process enables the *FBD* to operate under dynamic change in grid fundamental frequency without changing the number of samples unlike the conventional *FBD* method. The CCVSI current references provided by the *FBD* theory based method is further analyzed with single phase instantaneous power theory based approach and the presence of second harmonic

power in the DC link quantities of the inverter is also investigated. A detailed analysis and experimental results are presented in this report to show the efficacy of the proposed implementation methods of calculating the current reference of the CCVSI.

9.1.6 Application of four-switch based three-phase grid connected inverter to connect renewable energy source to a generalized unbalanced micro-grid system

The four-switch based three-phase inverter is proposed for a generalized unbalanced grid connected system. The space vector methods for *b-4* configuration as discussed in [111]-[119] are not applicable for grid connected applications because of the absence of consideration of the unbalanced load voltage. In this report, a Sine PWM (SPWM) based control method is proposed for the four-switch inverter. The current control of the inverter phases are carried out in the *a-b-c* frame following the control methodology discussed for six-switch three-phase inverters connected to grid. In this method of control the DC link mid-point fluctuation is suppressed by the control action taken by SRC to reject periodic disturbances. The detailed mathematical analysis is also provided to explain this phenomena. It is also shown mathematically and experimentally that even if the DC link split capacitors are unbalanced , the DC link mid-point potential (with respect to ideal DC link mid-point) settles to the zero DC value during the operation of the proposed control system. Adequate experimental results are provided to show the efficacy of the overall system.

The four-switch three-phase *b-4* topology is applied in the grid connected

application in an effort to reduce the cost of the inverter. Admittedly, this topology warrants higher voltage ratings of the semiconductor devices used and the DC link split capacitors used with respect to a conventional six-switch three-phase *b-6* topology inverter for a specific set of grid voltages. The author reserves his comments on the issue of cost-effectiveness of *b-4* topology inverter over *b-6* topology inverter for they believe that it is application specific; for high voltage application it is expected that the inverter semiconductor switches cost more than capacitors and incremental increase in the voltage rating, while the low voltage application, the argument can be reversed.